Numerical Simulation of Mitral Valve Function

Kevin Daniel Lau

A Thesis submitted for the degree of Doctor of Philosophy

Department of Mechanical Engineering, University College London
and the
Centre for Mathematics and Physics in the Life Sciences and
Experimental Biology, University College London

March 6, 2012

Disclaimer

I, Kevin Daniel Lau confirm that the work presented in this thesis is my own. Where information has been derived from other sources, I confirm that this has been indicated in the thesis.

Signed KEVIN D LAU

Abstract

In the mammalian heart there are four heart valves (HV), of which the largest is the mitral valve (MV). Key components in the circulatory system, correct HV function is vital to cardiovascular health. A tethered and asymmetric structure, the MV regulates unidirectional flow between the left atrium and left ventricle. MV function is divided between systole/closure, where the MV is required to sustain a pressure load ∼120 mmHg whilst minimising flow reversal, and diastole/opening in which the MV is required to rapidly transition from closed to open in order to maximise the transport of blood. Directly affecting the heart, dysfunction of the MV can affect either opening or closing through stenoses or prolapse/regurgitation respectively.

Complementing experimental techniques, numerical simulation of the MV offers additional insights into MV function as unmeasurable variables such as the stresses can be approximated. Due to the immersed nature of the HVs, numerical simulation of the MV requires an approach that is able to model both the large deformation of the MV and non–uniform haemodynamics pressure load resulting from the blood/HV contact. In this work the finite element solver LS–DYNA has been used as it addresses both issues. Using this framework, anatomically sized MV models have been used to characterise the current methodology of reported HV simulations, showing that the fluid–structure interaction (FSI) modelling of the blood/HV contact is essential in the simulation of MV dynamics. Application of this FSI method has been applied to surgical repair technique of the MV known as the edge–to–edge repair, showing that more invasive procedures result in greater stress concentrations but impaired the flow rates. Further advances in this model have been used to examine growth and remodelling effect of the MV tissue in both normal and dysfunctional states.

Abstract word count: 299

Contents

List of Figures

List of Tables

Listings

Glossary

A

anisotropic having properties that differ according to the direction of measurement. 28

annulus fibrous base of heart valves. 18

anteropostero direction which connects the anterior and posterior portions of the valve. 27

atrioventricular valve heart valve which divides the atrium and ventricle. 17

C

chordae tendineae thin tendinous structures which support the atrioventricular valves during closure. 18

commissural direction which connects the left and right commissural portions of the valve. 19

congenital dysfunction existing at or dating from birth. 17

D

deformation gradient second order tensor which describes the deformation of a continuum body from a reference position to its current position. 36

E

edge–to–edge surgical repair technique in which the prolapsing segments of the valve are sutured together. 50

effective orifice area the area of the streamtube with the equivalent pressure gradients and fluid velocities as the valve. 22

F

fibrous trigones a triangular mass of fibrous tissue which forms the mitral and aortic annuli, the trigones mark the end of the mitral–aortic continuity. 18

fluid–structure interaction numerical method of simulating both fluid and structural dynamics and the resulting coupling between the two. 42

G

geometric orifice area geometric measurement of the visible area of the valvular orifice. 95

H

heart valve unidirectional valves that regulate the flow of blood in the heart, in the mammalian heart there are four in total. 17

K

keyword LS–DYNA input file command. 75

M

mitral valve located between the left atrium and the left ventricle the mitral valve is largest of the four heart valves. 17

O

orthotropic having properties that differ according to the direction of measurement. 41

P

papillary muscles muscular nodes to which the chordae tendineae connect to the ventricular wall, contract to support the atrioventricular valves during closure. 18

pathological state of disease. 17

percutaneous surgical procedure through which access to internal organs is performed through the blood vessels of the circulatory system. 18

principal stresses the eigenvalues of the stress tensor. 43

Q

quiescent a cellular state of of inactivity or dormancy. 121

R

rough zone localised regions of thicker leaflet tissue that correlate with leaflet contact during closure. 19

S

structural–only numerical method of simulating the structural dynamics only. 42

Z

zone of apposition localised regions of the leaflets which contact during closure. 19

Acknowledgements

I would like to give thanks to my supervisors Dr. Vanessa Díaz, Dr. Gaetano Burriesci and Prof. Peter Scambler all of whom have sacrificed their time to provide invaluable assistance that has shaped this work from its inception. Without their insight and input, the direction of my current and future work would be shapeless. I would also like to acknowledge the invaluable assistance of Dr. Daniel Einstein, without his technical advice the implementation of the LS–DYNA subroutine would never had been possible.

I would like to give special thanks to all those who have encouraged my scientific curiosity and imparted upon me the sound fundamentals which I have today, in particular all my lecturers from the Department of Aeronautics at Imperial College, Prof. Eugenio Oñate, Dr. Róberto Lopez and Dr. Prashanth Nadukandi from the International Centre of Numerical Methods in Barcelona, Marcel Bos from the National Aerospace Laboratories in The Netherlands, and my teachers Richard Rooth, Paul Goldbrum, Anthony Richards and Susan Cowell.

I would like to extend a personal thanks to my friends whose support the over the last four years has been immeasurable, in particular: Randeep Bedi, Farouk Jivraj, Elizabeth Muldown, Robert Simmons and Thomas Shelswell, fellow Mechanical Engineeing students – Gillian Munir, Giulia di Tomaso and Dave Western, visiting students Carlo Conti from Politecnico di Milano and Gaëlle Diserens from Ecole Polytechnique Fédérale de Lausanne and my fellow CoMPLEX students with whom I have had the pleasure of sharing the journey of the last four years – Max Ahmed, Arturo Araujo, Gwenan Knight, Lorette Noiret, Charles Mullon, Dorothy Kuipers and Johannes Riegler. Special thanks are reserved for Mae Woods, who helped me believe in myself again. Finally thanks to my family, Linda, Daniel and Henry, without whose love I would not have been able to get this far.

The financial support of CoMPLEX, the EPSRC and the BHF is gratefully acknowledged.

Thesis Outline

In this work several aspects relating to the numerical modelling of the mitral valve have been addressed. Divided into five main chapters, please note that each chapter is accompanied by its own bibliography and that the reference numbering is unique to each chapter. Beginning with Chapter 1, a brief review of information relevant to the multiple aspects related to the modelling of the mitral valve has been summarised. Within this work it has been chosen to focus upon three key issues related to the mitral valve, simulation of valvular dynamics, surgical repair techniques and valve growth and remodelling, as detailed in the following text and in the illustration below. In Chapter 2 an in–depth review of the methodologies used to model these three aspects is summarised in greater detail.

The foundation of valvular modelling is the method used to describe and model valve function, in Chapter 3 the current techniques available for mitral valve modelling have been examined. Previously published models of the mitral valve have either been described using the a structural–only approach of simulating the valve–only, or a fluid–structure interaction approach of simulating the valve immersed within blood. In the structural–only approach the effect of the haemodynamic load is approximated as a uniformly distributed pressure load, the effect of which has not been examined. By comparing a structural–only model directly against a fluid–structure interaction model, the effect of this approximation has been examined in several different scenarios.

Key to restoring function in diseased states, simulation of the correction of a valvular dysfunction has been addressed in Chapter 4 focussing upon the valvular repair technique known as the edge–to–edge repair. Previously reported models of this approach have been fluid or structural based models, as such no fluid–structure interaction models of this procedure exist. Using the simulation techniques described in Chapter 3, here the methodology of these approaches have been characterised by comparison with a fluid–structure interaction method. Furthermore a dysfunctional model the edge–to–edge repair has been evaluated with and without annular support (annuloplasty) reflective of traditional and percutaneous approaches currently available. Using a fluid–structure interaction model these two options have been characterised and compared in terms of the induced stresses and subsequent flow rates following the simulated procedure.

Key to valve function in both normal and dysfunctional states, in Chapter 5 the simulation of growth and remodelling of the mitral valve has been addressed. Maintained homeostatically in normal states, the biomechanical properties of the valve microstructure are vital to correct function of the valve in both opening and closing phases. However this regulation is disrupted in dysfunctional states, resulting in a degradation of the biomechanical properties. Abnormal forces have been shown experimentally to induce dysfunctional adaptation, however the role of the mechanical environment in this tissue degradation is not well understood. In order to better understand the potential mechanisms through which valvular tissue adapts a stress–based approach to tissue adaptation has been examined in both normal and dysfunctional states. Separately examining fibre reorientation and leaflet thickness, the resulting changes in the tissue microstructure and the associated changes in the stresses and strains have been examined.

Simulation of valvular dynamics (Chapter 3)
Normal State
Valve Modelling (Chapter 2)
Mitral Valve Function (Chapter 1)
Growth and remodelling (Chapter 5)
Surgical repair techniques (Chapter 4)
Dysfunctional State

Chapter 1

Literature Review

Contained within this chapter is a brief review of the multiple aspects related to the modelling of the mitral valve. This has been divided into the clinical background behind heart valve disease (Section 1.1), valvular anatomy and function in normal and pathological states (Sections 1.2 and 1.3), the biomechanical properties of the valve (Section 1.4) and numerical modelling of valve function (Section 1.5).

1.1 Clinical background

The human heart contains four heart valves: the mitral valve, aortic valve, tricuspid valve and pulmonary valve. Classified by their anatomical position and function in the cardiac cycle these valves can be divided between the atrioventricular valves (mitral and triscupid) and the semilunar valves (aortic and pulmonary), which respectively separate the left/right atria from the left/right ventricles and the left/right ventricle and the aorta/pulmonary artery. Under normal conditions these valves regulate unidirectional flow of blood through the heart, enabling the generation of pressure required to pump blood around the cardiovascular system [1]. The functional requirement of the valves are divided between its two states, open and closed. When closed the valves are required to sustain pressure loads ranging from 30 mmHg up to 150 mmHg [2], whilst minimising flow reversal. When open the valves must rapidly transition from closed to open, minimising the resistance to fluid motion and maximising the transport of blood. Dysfunctional changes in either open or closed phases directly affect the function of the heart by disrupting filling or ejection. Classification of valve dysfunction is determined from abnormal leaflet displacement during closure, the presence of abnormal retrograde flow during closure or abnormal narrowing of the valvular orifice that are respectively referred to as prolapsed, regurgitant or stenotic states.

Although the occurrence of heart valve disease is less frequent than that of coronary disease, heart failure or hypertension, heart valve disease is a potential causes of death in predominately older patient populations. A recent European wide survey focussing on heart valve disease reports that the mean age of heart valve disease patients as 61 ± 14 years [3]. Although the mean age is relatively high, younger populations are also affected in cases of congenital malformations such as the bicuspid aortic valve for which the expected incidence is reported to range from 0.4 % to 2.45 % [4]. In patients with a singular dysfunction, stenosis of the aortic valve is the most frequent (43.1%), followed by regurgitation of the mitral valve (31.5%), regurgitation of the aortic valve (13.3%) and finally stenosis of the mitral valve (12.1%). The origins of these dysfunctions have a variety of different causes, with the predominant causes rheumatic and degenerative (Table 1.1).

If the dysfunction is severe enough to impair the function of the cardiovascular system, it is possible to perform a surgical correction in order to restore normal function. Depending upon the severity of dysfunction, the existing valve anatomy is either repaired to an improved state of functionality or the

Table 1.1: Etiology (or origin) of single native left–heart valvular diseases, values after Iung et al. [3]. Labels: AO – aortic stenosis, AR – aortic regurgitation, MS – mitral stenosis and MR – mitral regurgitation.

Origin	AO [%]	AR [%]	MS [%]	MR[%]
Degenerative	81.9	50.3	12.5	61.3
Rheumatic	11.2	15.2	85.4	14.2
Endocarditis	0.8	7.5	0.6	3.5
Inflammatory	0.1	4.1	0.0	0.8
Congenital	5.4	15.2	0.6	4.8
Ischaemic	0.0	0.0	0.0	7.3
Other	0.6	7.7	0.9	8.1

valve is replaced with an artificial substitute. In cases of mitral regurgitation, the majority of cases either undergo surgical repairs (46.5%) or mechanical valve replacement (43.2%), with the remainder receiving a biological (10.3%) valve replacement [3]. The converse is reported in cases of mitral stenosis, with the majority of patients receiving a mechanical valve replacement (58.0%) and the remainder undergoing percutaneous balloon commissurotomy (33.9%), biological valve replacement (4.5%) or valvular repair (3.6%) [3]. The choice of repair or replacement is dependent on several key factors and can be affected by advanced age, infective endocarditis, patient suitability for surgical procedures, extensive calcifications of the valve and even the centre of treatment [5, 6]. The large variety of factors is reflected in the high number of operations performed without meeting pre–defined guidelines (17.5%) and conversely the number of operations not performed even though these guidelines are met (16.5%) [3]. Currently the number of heart valve operations performed annually is reported as approximately 275,000 worldwide with approximately 9,000 occurring within the United Kingdom, figures indicate that this is a trend which continues to increase [7, 8].

1.2 Valve anatomy

The focus of this work is the mitral valve, a title which has been attributed to Andreas Vesalius who noted the resemblance of the valve in its closed configuration to that of a bishop's mitre [9]. Located between the left atrium and left ventricle, the mitral valve is the largest of the four heart valves and operates in conjunction with the aortic valve to regulate the pumping of oxygenated blood into the circulatory system through the left side of the heart. The anatomy of the valve consists of four different components, the annulus, the leaflets, the chordae tendineae and the papillary muscles. The antomical details of these components are described in greater detail in the following sections. How these subcomponents all operate in synergy to ensure correct valvular function is covered in detail in Section 1.3.

1.2.1 Annulus

The mitral valve is connected to the structure of the heart through a discontinuous ring of tissue known as the annulus fibrosus, a fibrous cord–like structure that defines the perimeter of the valvular orifice and the base of the valve. Located adjacent to the aortic valve, the mitral annulus shares a fibrous continuity with the left coronary and half of the non–coronary cusps of the aortic annulus (Figure 1.1). This continuous section defines the anterior portion of the mitral annulus, the limits of which are referred to as the left and right fibrous trigones. Although considered to be a continuous structure, histology of the annulus indicate that its fibrous structure is not fully continuous in neither normal or dysfunctional states [10]. Measurement of the total length and extent of the annulus have been documented in both human and porcine valves by Kunzelman et al. [11], the results of which are summarised in Appendix A.1.

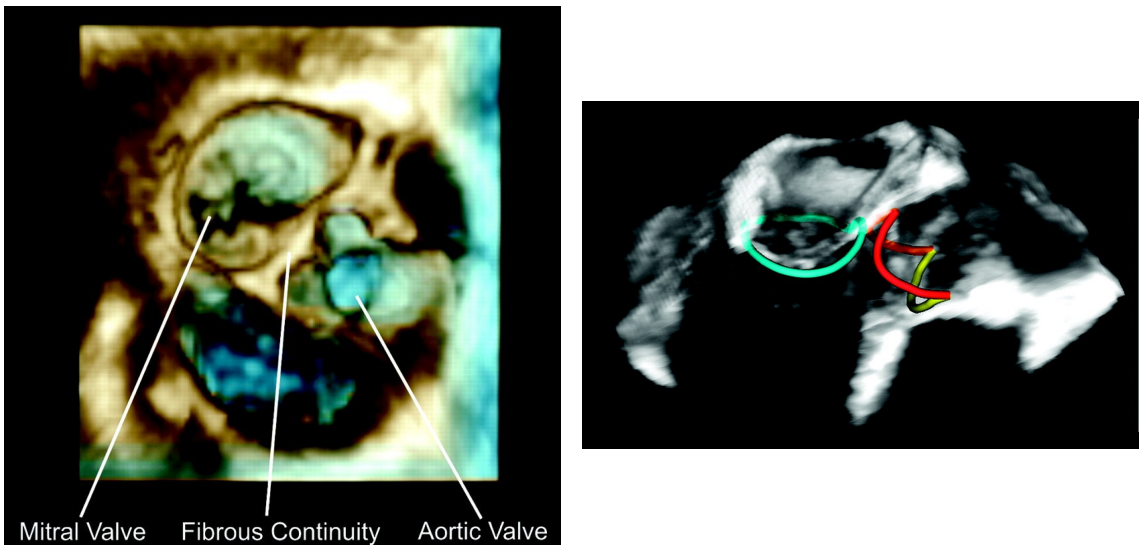

(a) Volume rendering image of the mitral annulus

(b) Mitral and aortic annuli 3D echocardiography visualistion

Figure 1.1: (a) 3D echocardiographic volume rendering of the mitral and aortic annuli as viewed form the left atrium. (b) 3D visualisation of the mitral and aortic annuli superimposed onto an echocardiographic image of the mitral and aortic annuli. Note that the mitral annulus is shaped like a "saddle", or hyperbolic paraboloid, the peak of which lies on the anterior side of the annulus adjacent to the mitral/aortic annular continuity. Images after Veronesi et al. [12].

1.2.2 Leaflets

The leaflets of the mitral valve are formed from a continuous band of tissue which extends outward from the mitral annulus and into the left ventricle cavity. Based on its geometric form and its anatomical connection to the annulus, the tissue of the leaflets can be divided into the following regions: anterior, posterior/mural and commissural (Figure 1.2). The anterior region has a trapezoidal/semicircular profile and is typically formed of a single cusp. Connected to the mitral annulus on the anterior side of the heart, this cusp occupies approximately a third of the annular circumference [11]. Separated by the commissural cusps and positioned opposite the anterior cusp are the posterior/mural cusps. Although narrower than the anterior cusp with a more scalloped profile, the posterior/mural cusps are similar in area to the opposing anterior cusp [13]. Reported measurements of the key leaflet dimensions are summarised in Appendix A.2.

The posterior leaflet is typically described as being formed by three cusps: P1, P2 and P3 (Figure 1.3). Similarly the segments of the anterior leaflet that oppose the P1, P2 and P3 cusps are labelled A1, A2 and A3 respectively. Variation in the exact number of these anterior and posterior cusps exists, with the average number of anterior and posterior scallops reported as 1.2 ± 0.4 and 3.0 ± 1.0 respectively [14]. Divisions in the posterior cusp were found to occur in the standard P1/P2 position with a frequency of 66% and in the P2/P3 position with a value of 71% [14], although extra divisions were found to occur up to 32 % in the P2 (Table 1.2). However this variation in the number of cusp divisions is limited to the posterior cusp, as the anterior cusp exhibits little variation (Table 1.2),

During closure the anterior and posterior leaflets coapt together to form a haemodynamic seal (Figure 1.3). Coapting on their atrial facing surfaces, the two anterior and posterior cusps contact each other along an area of tissue known as the zone of apposition (or rough zone) which extends 6–8 mm from the edge/free margin of the valve leaflets. Non–uniform in tissue thickness, this region is characterised as thicker and rougher than the rest of the valvular tissue [13].

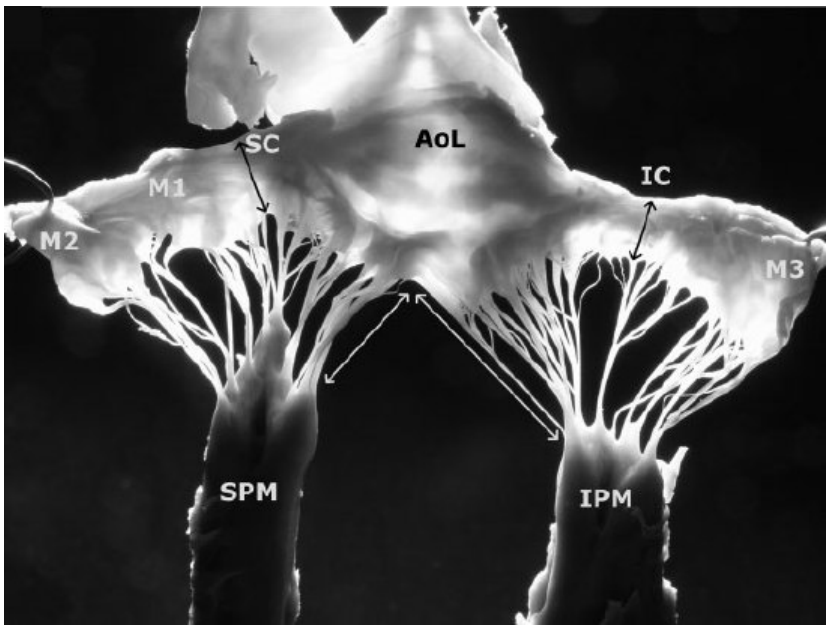

Figure 1.2: Backlit image of a cut human mitral valve displaying the valvular profile of the anterior cusp (AoL) and the posterior/mural cusps (M1,M2,M3) of the valve leaflets. Also labelled here are the inferior commissure (IC) and superior commissure (SC) regions and the inferior and superior papillary muscles (IPM and SPM respectively). Image and labels after Muresian [13].

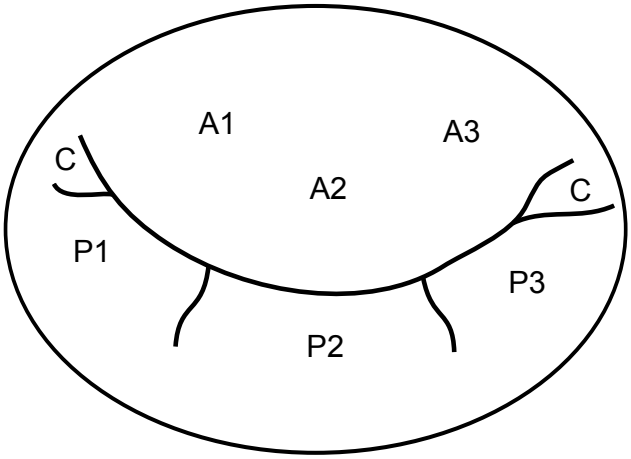

Figure 1.3: Diagrammatic representation of the mitral valve at closure. The anterior leaflet folded across the valvular orifice and the posterior and commissural scallops fold into the leaflet to form a tight seal.

Table 1.2: Extra divisions in the anterior and posterior cusps. Data after Quill et al. [14]

Anterior cusp	Occurrence [%]	Posterior cusp	Occurrence [%]
A1	5	P1	13
A2	8	P2	32
A3	13	P3	21

1.2.3 Chordae Tendineae

The chordae tendineae are thin chord–like structures that support the valve during closure and prevent the inversion of the valve into the atrium (Figure 1.4). Classified by the point of attachment to the valve and its dimensional size, the chordae can be subdivided into a variety of different classes. Earlier authors [15, 16] have classified the chordae using the terminology: first, second and third order. However more recent authors [13] have used a more functional terminology: marginal, rough zone, strut (sustain) and basal chordae (Table 1.3). It is this terminology which has been used throughout this work

The marginal chordae are the thinnest chordae and are found attached to the leaflet at the free mar-

gin. Attached below the free margin are the rough zone chordae, intermixed with the marginal chordae these structures support the position of the zone of apposition/rough zone during closure of the valve (see Section 1.2.2). Separation of the rough zone chordae from the marginal chordae is complex due to the similarity in attachment point and dimensional size. Supporting the main leaflet body and the leaflet base are the strut and basal chordae respectively (Figure1.5) [17], thicker than the marginal chordae these structures allow the valve to bear the haemodynamic load imparted during closure Reported measurement of the length and thickness of the different chordal classes have been summarised in Appendix A.3.

Table 1.3: Current and previous terminology used to classify the different classes of the chordae tendineae, including the point of attachment to the valve structure and the role in valve function.

Recent terminology [13]	Previous terminology [16]	Leaflet attachment	Function
Marginal	First order	Free margin	Leaflet coaptation
Rough zone	Second order	Rough zone	Leaflet geometry
Strut/sustain	Third order	Main leaflet body	Leaflet geometry
Basal	Third order	Leaflet base	Annular reinforcement

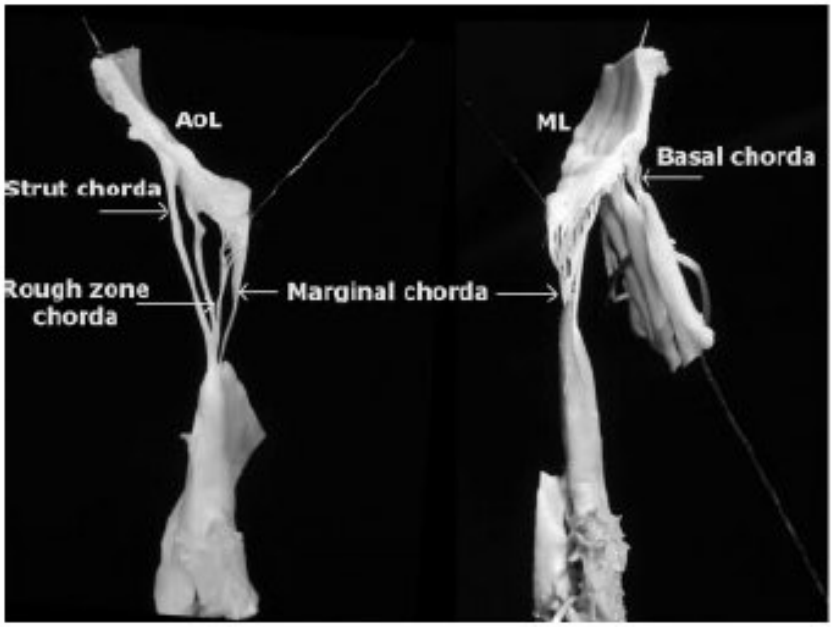

Figure 1.4: Marginal, rough zone, strut and basal chordae tendineae of the anterior and posterior/mural leaflets. Inserting into the atrial side of the leaflets, the chordae connect the valve to the papillary muscles. Image after Muresian [13]

1.2.4 Papillary muscles

The chordae connect to the ventricular wall via a set of muscular fascicles referred to as the papillary muscles (Figure 1.4). Protruding into the ventricular chamber, these fascicles are classified by their anatomical location and are grouped together as the anterolateral and posteriormedial papillary muscles. Traditionally considered as muscular extensions of the ventricular wall, X–ray imaging by Axel [18] has shown that the papillary muscles do not connect to the muscular aspect of the ventricular wall. Instead, the base of the papillary muscles connect to an intermediate layer that form part of the muscular projections into the ventricle known as the trabeculae carneae.

Anatomical measurements of the average distance of the papillary muscle tip to the valve complex have been measured in excised human hearts by Sakai et al. [19]. These measurements indicate that the

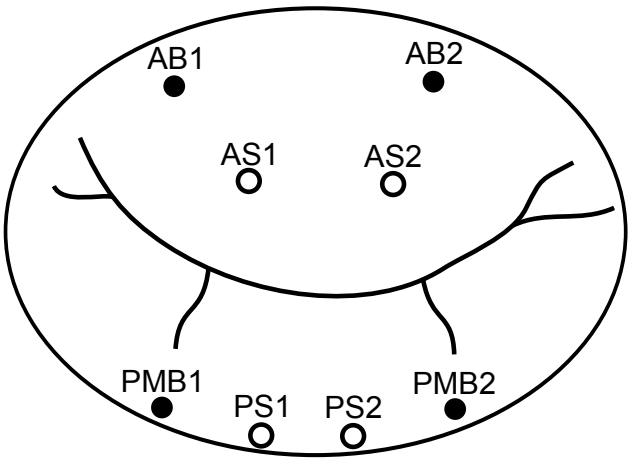

Figure 1.5: Location of the strut (○) and basal chordae (●) on the anterior and posterior ventricular surfaces. Labels: AS – anterior strut chordae, AB – anterior basal chordae, PS – posterior strut chordae and PB – posterior basal chordae. Data after Degandt et al. [17].

average distance between each papillary tip and the corresponding annular segment (anterolateral/-posteriormedial) are equal. The key points of these measurements have been summarised in Appendix A.4.

1.3 Valve function

The mitral valve has two key functions: (1) maintenance of a haemodynamic seal during ventricular ejection (systole) whilst minimising retrograde flow and (2) ensuring rapid ventricular filling (diastole) by minimising flow resistance in the transition between closed to open configurations. The ability of the valve to function optimally depends upon several factors such as the haemodynamic load imparted from the flow of blood, the biomechanical properties of the valvular tissue and the functional anatomy of the left heart. In dysfunctional states one or more of these factors are affected, resulting in suboptimal filling or ejection. These dysfunctions can be broadly classified into states which affect the passage of blood through the valve (stenosis) or those that result in abnormal deformations (prolapse) and associated retrograde flow during closure (regurgitation). In this section the normal and abnormal function of each subcomponent and the resulting valvular dysfunction (stenosis/prolapse/regurgitation) are reviewed.

1.3.1 Blood flow

Opening and closing of the valve is a predominately passive event, in that these events occur in response to the haemodynamic loads generated by the contraction and relaxation of the heart throughout the cardiac cycle rather than active valvular activity. Measurement of the haemodynamic function of the heart is the most accessible variable clinically and for this reason it has traditionally been matched to valve function through parameters such as the effective orifice area.

Normal states

In a normal state the pressure gradient across the valvular orifice is negative from ventricle to atrium during diastole, which results in the flow of oxygenated blood from the left atrium into the left ventricle (Figure 1.6). At the end of diastole the pressure gradient over the valve becomes positive as the ventricle contracts and the ventricular pressure exceeds the atrial pressure, the blood flow is reversed and the valve is closed.

Blood flow from the atrium into the ventricle during diastole consists of two pulses, with the first larger than the second [20] (Figure 1.7). Generated in response to the change in pressure between systole and diastole, the peak of flow occurs at the start of diastole and is referred to as the E–wave. Towards the end of diastole the atrium contracts, generating a smaller secondary filling motion referred to as the A–wave. Under normal conditions the fluid velocities during diastole ranges from 0.5 to 0.8 $m\,s^{-1}$ [2].

The rapid opening of the mitral valve during diastole results in the generation of a fluid jet as blood passes through the mitral orifice into the ventricle. *In vivo* imaging has shown that the mixing of the fluid jet with the blood within the ventricle generates a pair of large and small asymmetric vortices/eddies in the ventricle [21] (Figure 1.8). Further mixing of the fluid is generated through interactions of the blood with the chordae tendineae and the fascicles of the papillary muscles. The presence of these vortices are considered beneficial to the closure of the valve, as the vortex motion is thought to assist the closure of the valve leaflets [22].

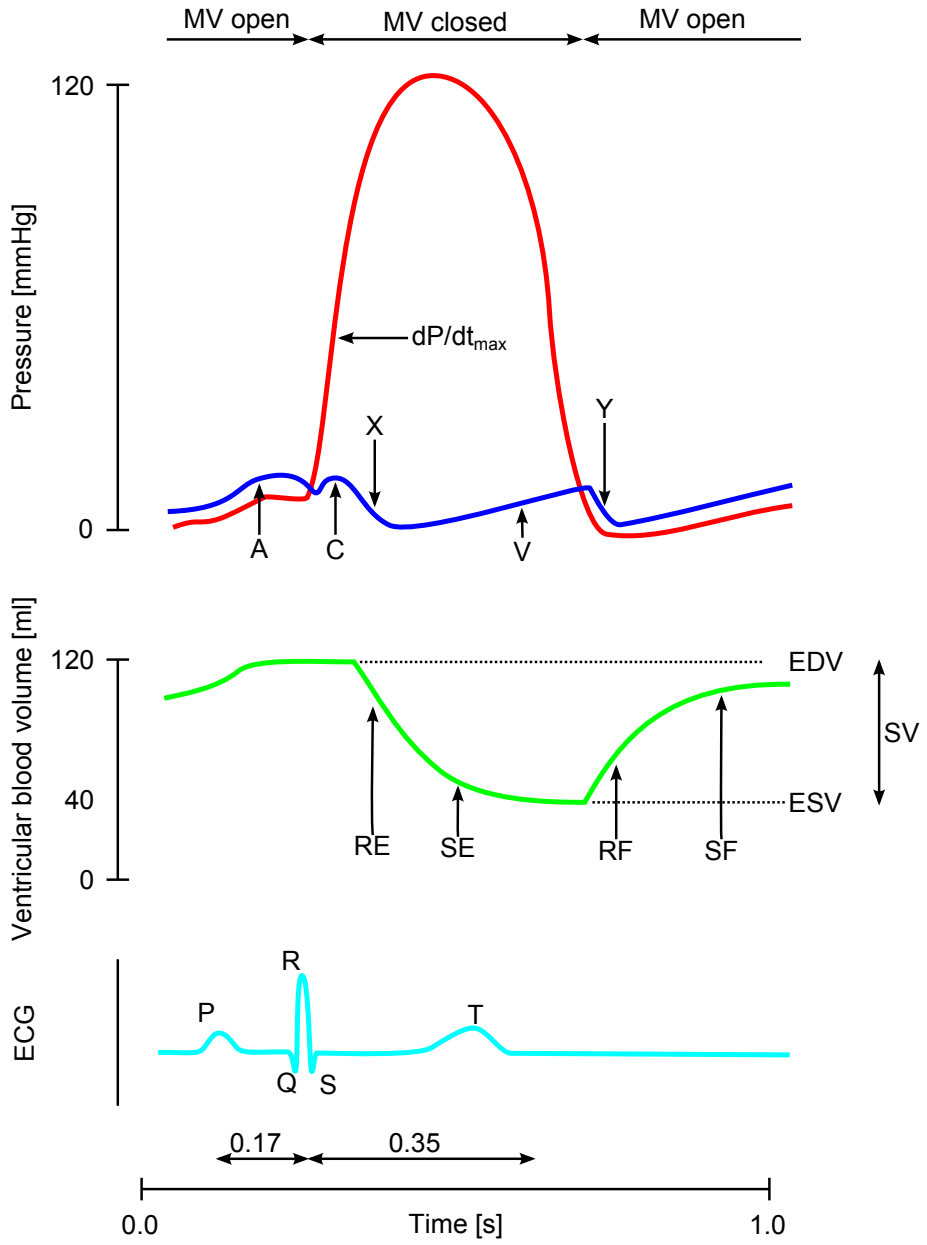

Figure 1.6: Illustration showing the change in left ventricular pressure, left atrial pressure, left ventricular blood volume and the electrocardiography (ECG) activity over a cardiac cycle. Image modified after Levick [1]. Pressure plot labels: A – A wave, C – C wave, X – X descent, V – V wave and Y – Y descent. Blood volume labels: RE – rapid ejection, SE – slow ejection, RF – rapid filling, SF – slow filling, EDV – end diastolic volume, ESV – end systolic volume and SV – stroke volume. ECG labels: – P – P wave, Q/R/S – QRS complex and T – T wave.

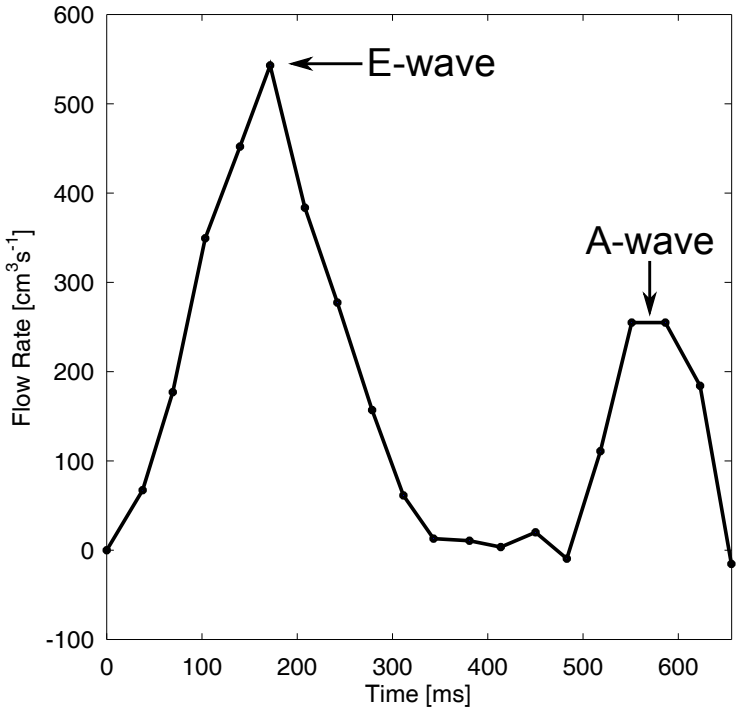

Figure 1.7: Flow rate during diastole. Values time corrected in order to define the start of diastole as t=0 ms. Data after Westenberg et al. [20].

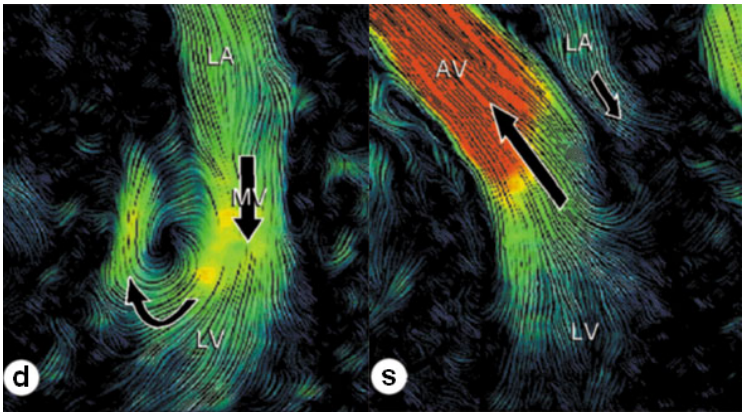

Figure 1.8: *In vivo* flow visualisation in the left ventricle depicting the fluid motion and assymetric rotation of blood flow during diastole (d) and systole (s). Labels: LA – left atrium, LV – left ventricle, AV – aortic valve and MV – mitral valve. Image after Kilner et al. [21].

The haemodynamic performance of the left heart has been traditionally linked to heart valve function through measures such as the effective orifice area (EOA) [23, 2]. Particularly useful in the assessment of stenotic valves or testing of prosthetic valves, the effective orifice area is an empirical formula derived from Bernoulli's equation of motion for a steady streamline. Based on a steady flow assumption, it is required that the effective orifice area be evaluated when the fluid is not accelerating, either under constant flow conditions or at the moment of peak flow over a open/closed cycle. At the point of peak flow over a single cycle, when considering averaged fluid variables, the sum of the inertial forces is zero as the forces induced in opening and closing are equal and opposite. Measured in units of cm^2, the effective orifice area is calculated instantaneously (Equation 1.1) or as an average over a single cycle (Equation 1.2). The instantaneous effective orifice area is evaluated using the instantaneous flow rate Q in ml·s^{-1} and the instantaneous pressure difference Δp in mmHg. Using the same units, the averaged effective orifice area is calculated using the root mean squared of the flow rate Q_{rms} and the mean transvalvular pressure difference $\overline{\Delta p}$. Here the units of pressure and velocity are mmHg and cm·s^{-1} respectively and the constant term has been defined empirically.

$$EOA = \frac{Q}{51.6\sqrt{\Delta p}} \tag{1.1}$$

$$\overline{EOA} = \frac{Q_{rms}}{51.6\sqrt{\overline{\Delta p}}} \tag{1.2}$$

More recently the non–dimensional vortex formation time has also been used to measure haemodynamic performance (Equation 1.3). A function of the average of the time varying velocity $\overline{U(t)}$, the vortex formation time t and the width of the orifice D, this non–dimensional number is essentially the ratio of the vortex length L to the orifice width D [24]. Simplified and cast in terms of ventricular parameters such as the left ventricular ejection fraction, left ventricular end–diastolic volume and the time–averaged mitral valve diameter, Gharib et al. [24] used this vortex number to analyse vortex formation in both healthy patients and diseased patients. The non–dimensional vortex formation times of normal subjects were found to be within the range from 3.3 to 5.5, significantly higher than patients suffering from dilated cardiomyopathy in which the non–dimensional vortex formation time was found to range from 1.5 to 2.5.

$$T = \frac{\overline{U(t)} \cdot t}{D} = \frac{L}{D} \tag{1.3}$$

Dysfunctional states

In cases of mitral stenosis the stiffness of the valve structure increases, resulting in an increase of the haemodynamic resistance of the valve during filling. Due to the reduction in the effective orifice area the velocity of the jet during filling increases by a factor of approximately 5, with clinical reports of severe stenoses describing peak velocities up to 2.8 m·s^{-1} [25]. Clinical assessment of the severity of the stenosis is performed through evaluating the mitral valve area and the pressure gradient [26] (Table 1.4).

In cases of mitral regurgitation the structure of the valve is not able to sustain the haemodynamic load during closure, resulting in abnormal deformation and flow reversal. As the leaflets close and are unable to coapt fully, a high velocity jet is formed as the fluid is forced through the leaflets due to the high pressure difference in systole. Maximum fluid velocities are reported to range from 4 to 6 m·s^{-1} [27]. Clinical assessment of the severity of regurgitation is performed through evaluation of the width of the regurgitant jet (vena contracta width), the regurgitant volume/volume fraction and the effective regurgitant orifice area [27] (Table 1.5).

Table 1.4: Classification of mitral stenosis based on the mitral valve area (MVA) and mean transvalvular pressure gradient (MTPG). The transvalvular pressure gradient has been approximated using the simplified Bernoulli relationship $\Delta P = 4\Delta v^2$, where $v$is the transvalular velocity. These recommendations are valid for heart rates in the range 60–80 bpm and in sinus rhythm. Values after Baumgartner et al. [26].

Severity	Mild	Moderate	Severe
MVA [cm^2]	>1.5	1.0–1.5	<1.0
MTPG [mmHg]	<5	5–10	>10

1.3.2 Annulus

The perimeter of the valvular orifice is defined by the annulus of the valve, a flexible structure that varies in size and shape during the cardiac cycle. Sharing a structural connection with the aortic annulus, the areas of the aortic and mitral annuli vary in a reciprocal manner during the cardiac cycle, with the maximum of the aortic area coinciding with the minimum of the mitral valve and vice versa [12].

Table 1.5: Classification of mitral regurgitation based on the vena contracta width (VCW), regurgitant volume (Regur. Vol.), regurgitant fraction as a percentage of the stroke volume (Regur. Frac.) and effective orifice area of regurgitation (EOAR). Values after Zoghbi et al. [27].

Severity	Mild	Moderate	Severe
VCW [cm]	<0.3	0.3–0.69	≥0.7
Regur. Vol. [ml/beat]	<30	30–59	≥60
Regur. Frac. [%]	<30	30–49	≥50
EOAR [cm^2]	<0.20	0.20–0.39	≥0.40

Normal state

During early diastole the annulus widens to its maximal size in order to maximise fluid transport into the ventricle. Conversely during systole the annulus contracts to its minimum size as the valve closes [12]. Relatively planar and circular during diastole the annulus adopts a non–planar hyperbolic paraboloid, "saddle" shaped, configuration during systole as the heart contracts (Figure 1.9).

The dynamics of the annulus can be described by decoupling the planar and non–planar contributions (Figure 1.10). In the plane of the annulus its profile is described by its eccentricity e, which is defined by the ratio of its major and minor axes a and b as $e = \sqrt{a^2 - b^2}/a$. Measurements show a reduction of ~ 0.1 in eccentricity from diastole to systole as the annulus adopts a more elliptical configuration in closure (Table 1.6) [28]. Out of the plane the annulus is described by the height of the annular "saddle". Measurements of the annular height indicate a increase of ~ 0.1 cm in height from diastole to systole as the annulus increases its non–planarity in closure (Table 1.6) [28]. However this out–of–plane motion is not uniform across the annulus, as the anterior portion adjacent to the aorta exhibits larger displacements than the centre of the posterior portion [29].

The area enclosed by the annulus is a clinical measured parameter as it is used in the classification of dysfunctions such as mitral stenosis (Table 1.4). Measurement of the annular area in human studies shows that significant variation exists between different imaging methods (Table 1.7) [30]. Estimation of the annular area is strongly dependent upon the definition of the annular border and the conversion of the non–planar geometry into a planar area [31]. However all three imaging methods listed show similar values for the maximum measured percentage change in area from diastole to systole.

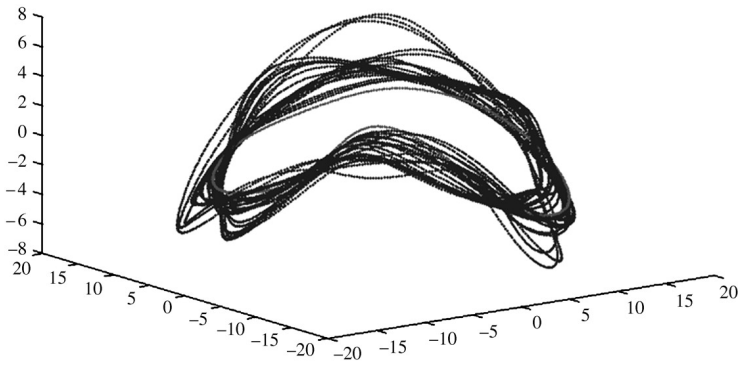

Figure 1.9: Geometric motion of the annulus throughout the cardiac cycle. Image after Votta et al. [32].

Dysfunctional state

In abnormal states the annulus is no longer as dynamic in its motion, as highlighted by measurements of the eccentricity. In cases of functional mitral regurgitation the eccentricity exhibits less variation throughout the cardiac cycle (Table 1.6). Similarly the measured annulus area reduction between diastole and systole is reduced from its normal value of 36%±6% to 19%±7% in states of functional mitral

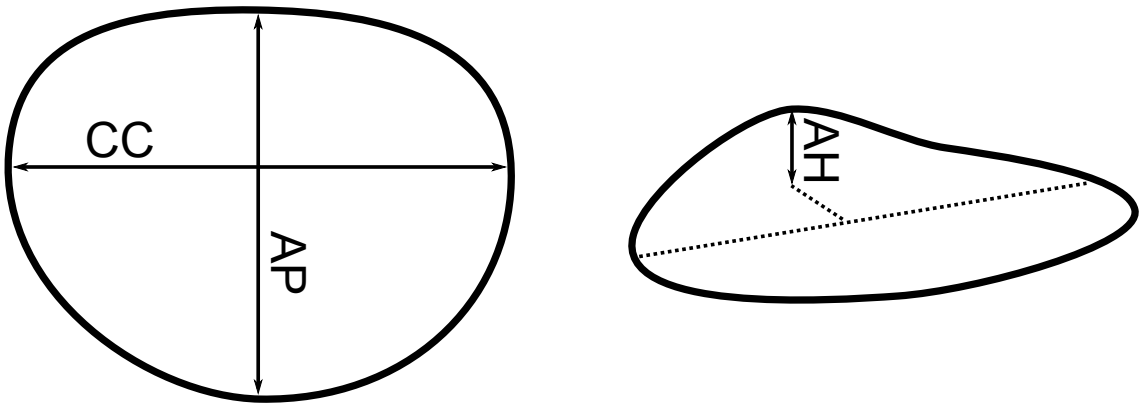

(a) Plan view **(b)** Three–dimensional view

Figure 1.10: Illustration of the characteristic geometric variables of the mitral annulus. Labels: AP – antero-postero diameter, CC – commissural diameter and AH – annular height.

Table 1.6: Annular eccentricity during the cardiac cycle in both normal and functional regurgitant states. Values after Kaplan et al. [28]. Labels: NRM – normal and FMR – functional mitral regurgitation.

	Eccentricity [–]		Height [cm]	
Phase	NRM	FMR	NRM	FMR
End diastole	0.54	0.45	0.63	0.59
Mid systole	0.57	0.50	0.74	0.63
End systole	0.49	0.42	0.73	0.59
Mid diastole	0.49	0.42	0.63	0.57

Table 1.7: Measurement of the maximum/mean enclosed annular areas and the maximum area reduction during the cardiac cycle. Values after Timek and Miller [30] Labels: 2DE – two–dimensional echocardiography, 3DE – three–dimensional echocardiography and MRI – magnetic resonance imaging.

Imaging method	Maximum area [cm^2]	Mean area [cm^2]	Reduction [%]
2DE	7.1±1.3	–	26±3
3DE	–	11.8±2.5	24±5
MRI	9.5±1.4	–	26±5

regurgitation [30]. Unable to reduce the interleaflet distance as in normal states, dysfunction of the mitral annulus results in incomplete coaptation of the leaflets that leads to prolapse and/or regurgitation.

Correction of annular dysfunction is typically performed through the reduction of the orifice size using a surgical technique known as annuloplasty. Restoration of coaptation is achieved through the reduction of the interleaflet distance by the application of an artificial ring sewn directly into the annulus [33]. There are three main approaches to annuloplasty, each offering different levels of structural support: (1) complete rigid/semi–rigid ring, (2) completely flexible ring or (3) partial (posterior) flexible ring [34]. However, uncertainty on the optimal approach to annuloplasty exists as the long–term durability of the different techniques remain unclear.

1.3.3 Leaflets

The largest components of the valve, the leaflets are primarily responsible for maintaining a haemodynamic seal during closure and preventing flow reversal. During opening the leaflets are required to transition rapidly from closed to open in order to maximise ventricular filling. Predominantly passive tissue, the leaflets respond to the haemodynamic load imposed by the transvalvular pressure gradient.

Normal state

Although the anterior and posterior leaflets are approximately equal in anatomical area, during closure the anterior leaflet covers the majority of the orifice. The posterior leaflets “tuck” into the anterior leaflet

forming a tight seal. In order to ensure full coaptation under a range of varying pressure loads and heart rates, the leaflets are formed of an excess amount of tissue that is approximately 1.5–2 times greater than the size of the mitral orifice [35]. Contact of the leaflets occurs during early systole, however the leaflets continue to deform until the load between the fluid and structure is balanced. The biomechanical strength to sustain this load without inverting is derived from the constituents of the leaflet tissue, a topic which is discussed in further detail in Section 1.4.

Traditionally the leaflet tissue has been considered as a non–contractile component of the heart, however *in vivo* experiments indicate that portions of the mitral valve contract in response to neural control [36]. Using an inverse finite element method the anisotropic stiffness of the valve was determined from recorded *in vivo* displacements and pressures. Leaflet stiffness was found to increase with sub–threshold electrical stimulation of the aortic–mitral continuity, which was subsequently abolished through the application of β–blockers during isovolumic contraction. It is reported that in the anterior leaflet the nerve density is twice that of the posterior leaflet [37].

In early diastole the leaflets rapidly transition from closed to open. The biomechanical properties which allow this rapid transition are derived from the constituents of the leaflet tissue, a topic which is discussed in further detail in Section 1.4. *In vitro* measurements of the surface stretches induced during opening have been measured in the porcine anterior leaflet by Sacks et al. [38]. Maximum principal stretches rates in excess of 1000% per second are measured in the transitions from closed to open.

Dysfunctional state

The biomechanical properties of the leaflets are key to the correct function of the valve, as abnormal changes to these properties lead to dysfunctional states such as prolapse/regurgitation and stenosis. In mitral valve prolapse the mechanical strength of the leaflets is reduced which results in abnormal deformation of the leaflets in closure as the valve prolapses. Defined by the excess deformation of the leaflets into the atrium relative to the annular line (with or without an associated regurgitation), leaflet displacements $\geq$2 mm are defined as prolapse [39]. In prolapsed states it is reported that the leaflets increase in size and the tissue microstructure becomes less organised along with associated thinning and/or elongation of the chordae tendineae. In mitral valve stenosis the mechanical stiffness of the leaflets increases, increasing the haemodynamic resistance of the valve in filling that results in the abnormal flow conditions decribed in Section 1.3.1. Caused by rheumatic infection, the leaflets are affected by thickening and calcification of the leaflets and/or commissural fusion.

Depending upon its severity, correction of these leaflet dysfunctions can be performed either by surgical repair or by replacement of the valve with an artificial prosthesis. In the case of degenerative causes of the mitral valve dysfunction it is preferred to perform valve repair over valve replacement as the long term survival rates are higher [39]. Surgical repair options include the reduction of the leaflet area, modification of the leaflet structure, repositioning of the native chordae and even the addition of artificial chordae.

1.3.4 Chordae tendineae

The chordae tendineae connect the valve to the papillary nodes, preventing the inversion of the valve during systole. Due to their relatively small size and rapid motion, the chordae cannot be visualised *in vivo* using current imaging techniques such as ultrasound and magnetic resonance imaging. Functional assessment of these valvular subcomponents requires the use of experimental *in vitro* techniques or *in vivo* animal models.

Normal state

Using a left heart simulator, Espino et al. [40] have shown that the removal of the anterior marginal chordae results in the full prolapse of the valve, as the valve does not offer any resistance during closure and inverts. However similar removal of the posterior and commissural marginal chordae resulted in localised leaflet prolapse. Compared to the intact valve, the maximum sustainable pressure load before prolapse was reduced in chordae removal scenarios.

Using the same methodology the contribution of the larger strut and basal chordae have also been assessed [40]. These secondary chordae carry a large proportion of the leaflet load during closure and act to reduce the induced leaflet strain by minimising leaflet deformation. Removal of the strut chordae does not affect leaflet coaptation or the maximum pressure load sustained. Removal of the basal chordae however reduces the maximum sustainable pressure significantly [40]. Similar *in vivo* experiments on ovine valves have also shown that the removal of the anterior strut chordae increase the deformation in the circumferential direction[1] whilst decreasing in the radial direction[2] [41].

Dysfunctional state

Similar to the leaflet tissue, changes in the biomechanical properties of the leaflets result in dysfunctional states of the valve. Loss of mechanical strength in the chordae tendineae leads to abnormal deformation of the leaflets that result in prolapse/regurgitation. Also resulting in prolapse/regurgitation is the more severe case of chordal rupture, which is also referred to as a "flail" leaflet. Traditionally rupture has been linked to rheumatic causes, however recent reports now show an increase in cases associated with myxomatous degeneration and mitral valve prolapse [42].

Correct function of the chordae has been hypothesised to play a role in the regulation of ventricular function. Dependent upon the force transmitted by chordae, in dysfunctional states this force is disrupted resulting in remodelling of the ventricle. However the clinical evidence for this is conflicting [43].

1.3.5 Papillary muscles

Connecting the ventricular wall to the valve via the chordae tendineae, the papillary muscles are muscular nodes which contract and relax throughout the cardiac cycle to ensure correct valve coaptation and maximal fluid transfer respectively. Innervated by nerves originating from the atrioventricular bundle [15], the activation of the papillary muscles are synchronised with the onset of systole [44].

Normal state

During systolic contraction the twisting motion of the ventricle displaces the apex towards the mitral annulus, simultaneously the papillary muscles contract in order to maintain tension in the chordae tendineae and maintain normal leaflet deformations. *In vivo* measurements in ovine hearts by Joudinaud et al. [44] indicate that that each papillary muscle remains at a constant distance relative to its local segment of the annulus (Figure 1.11). Maintenance of this distance arises directly from the papillary muscle contraction, as shown by the corresponding annulus–apex distance which is significantly different indicating that the muscle tips do not simply follow the ventricular motion.

Protruding into the ventricular cavity, the papillary muscles actively interact with the flow of blood. During filling the papillary muscles are relaxed and their protrusion into the ventricular cavity are minimised, however during ejection the muscles protrude significantly into the ventricle and are considered to shape the flow towards to the aortic outflow tract [43].

[1] The circumferential direction is aligned parallel to the annulus as illustrated in Figure 1.14
[2] The radial direction is orientated orthogonal to the circumferential directions as illustrated in Figure 1.14

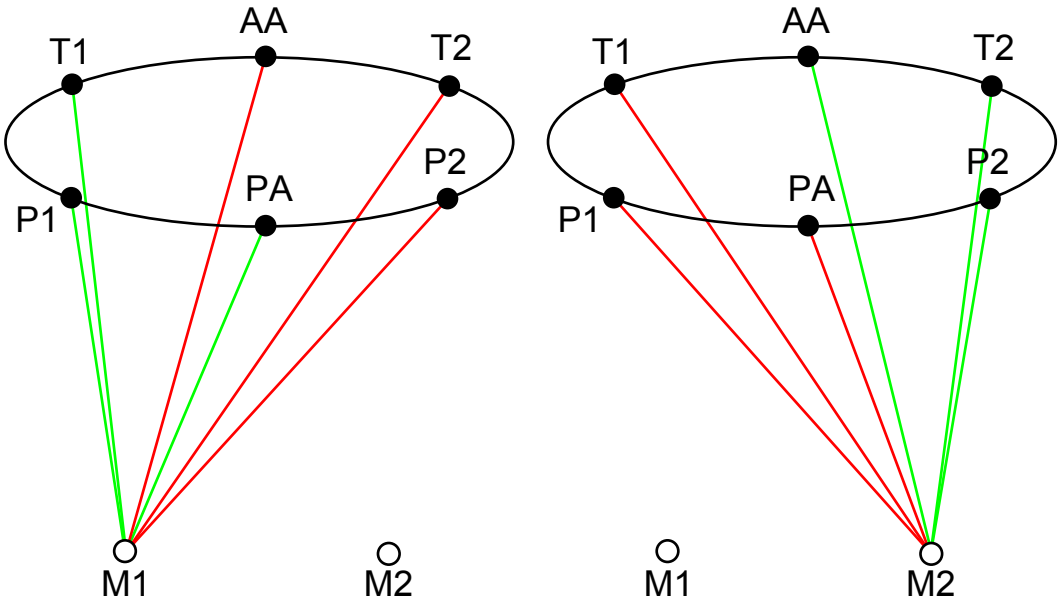

(a) Antero–lateral papillary muscle

(b) Postero–medial papillary muscle

Figure 1.11: Relative distance between the papillary muscle and the mitral annulus through the cardiac cycle. Here the red and green lines represent non–constant and constant distances during the cardiac cycle. Values after Joudinaud et al. [44] Labels: AA – mid–anterior annulus, PA – mid–posterior annulus, T1 – left trigone, T2 – right trigone, P1 – base of antero–lateral cusp of the posterior leaflet, P2 – postero–lateral cusp of the posterior leaflet, M1 – tip of the antero–lateral papillary muscle and M2 – tip of the postero–lateral papillary muscle.

Dysfunctional state

Changes in the contractility of the papillary muscle can lead to dysfunctional states of the valve. Abrupt changes in this contractility arising from rupture of a papillary muscle does result in regurgitation of the valve. In conjunction with myocardial wall damage, papillary muscle dysfunction can result in mitral regurgitation. However experimentally induced damage, ischemia or infarction of an isolated papillary muscle itself does not result in regurgitation [44].

1.3.6 Ventricle motion

Although not part of the valve complex, the function of the ventricle contribute to the function of the valve in terms of its structural motion and the motion of blood through it.

Normal state

In normal states the ventricle contracts and expands as the heart pumps and fills during systole and diastole respectively. Valve function occurs as normal.

Dysfunctional state

Loss of contractility in the ventricular myocardium results in dysfunctional states of both the ventricle and the valve. In cases of ischemia the valve (can) remain functional and mitral regurgitation can still occur. Referred to as ischemic mitral regurgitation, the loss of ventricular motion results in the leaflets being subjected to abnormal displacements during closure. Unable to coapt properly, regurgitation occurs as the leaflets adopt a configuration which is described as “tented” (Figure 1.12). Recently it has been suggested that quantitative measurement of the tenting area could be used as a measure of ventricular health [45]. Restoration of valve function is typically performed by reducing the interleaflet distance during closure through the application of annuloplasty [46].

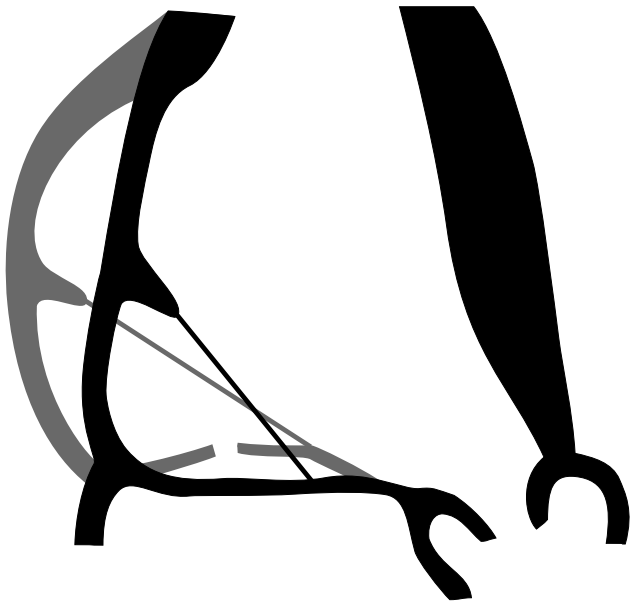

Figure 1.12: Illustration of the mitral valve closure in normal and ischemic mitral regurgitation. Here the normal contractile state is represented in **black** and the ischemic state in **grey**. In the ischemic case, regurgitation occurs as the loss of contraction results in the incomplete coaptation of the leaflets. The displaced configuration of the leaflets is commonly referred to as "tenting".

1.4 Biomechanical properties

Derived from its microstructural composition, the biomechanical properties of the different subvalvular components vary in accordance with their valvular function. Here in this section the different biomechanical characteristics of the leaflets of the valve in both normal and dysfunctional states are reviewed.

1.4.1 Leaflets

Governed by the microstructural arrangement of elastin and collagen fibres, the biomechanical response of the leaflets under tension is non–linear and anisotropic. These properties allow the leaflets to stretch and recoil freely during opening and also provide the tensile strength to withstand the haemodynamic load of closure [47]. Deviation in these properties result in dysfunctional states such as mitral prolapse/regurgitation and stenosis due to biomechanical weakening and stiffening respectively.

Normal states

As with all soft tissues, the leaflets of the mitral valve exhibit a non–linear and anisotropic biomechanical response when stretched. Divided into two phases, pre– and post–transition, the leaflets exhibit an exponential increase in stiffness with increasing stretches. The non–linearity of this response is derived from the microstructural content of collagen and elastin fibres bound together in a matrix of glycosaminoglycans (GAGs) and proteoglycans, the functional contribution of which are listed in Table 1.8.

The structure of the leaflet tissue can be divided into three distinct layers: the atrialis and/or spongiosa, fibrosa, and ventricularis (Figure 1.13) [49]. Facing the atrium, the atrialis is a thin layer composed mainly from elastic fibres and smooth muscles cells. Towards the free edge of the leaflet, the atrialis is replaced by a layer referred to as the the spongiosa. Composed of loosely arranged collagen and elastin, the spongiosa does not carry significant loads during closure but facilitates the rapid flexure of the valve during transitions between open/close and vice versa. On the opposite side of the leaflet facing the ventricle is the ventricularis; this layer is formed predominantly from elastic fibres and is the thinnest of all the layers. As the chordae tendineae insert into the leaflet surface on the ventricular side, this layer contributes to the formation of these structures [50]. Sandwiched between the atrialis/spongiosa and the

Table 1.8: Mitral valve leaflet constituents and their functional properties [48]. Information after Alberts et al. [48].

Constituent	Functional role
Collagen	Collagen is a triple helix protein that is cross–linked together to form larger fibrils which form collagen fibres. The principal load bearing constituent in the leaflets, the tensile strength of collagen under tensile stretch is comparable to steel. However collagen fibres have no compressive strength.
Elastin	Elastin is a chain like protein which is cross–linked together to form a network of elastic chains. Rubber like in behaviour, when stretched these fibres are able to return to their initial configuration upon the removal of tensile loads.
Fibrillin	Fibrillin is a protein which contributes to the microfibrils which form the sheath around the elastin core elastic fibres; bound to the elastin fibres, the microfibrils are key to the structural integrity of the elastic fibre. Key to the assembly of elastic fibres, the microfibrils are considered to form the base upon which elastin is initially deposited upon. Mutations in the gene responsible for this protein results in a degenerative state known as Marfan's syndrome.
GAGs & proteoglycans	Glycosaminoglycans (GAGs) and proteoglycans are compounds in which the collagen and elastic fibres of the tissue are bound within, this matrix lubricates the frictional forces between fibres.

ventricularis is the fibrosa. Composed of compactly arranged collagen, this layer bears the majority of the load imposed during closure [49]. The collagenous fibres of this layer also eventually give rise to the load bearing fibres which form the chordae tendineae. Both the total leaflet thickness and the thickness of the fibrosa layer are significantly thicker in the anterior leaflet than the posterior leaflet [37].

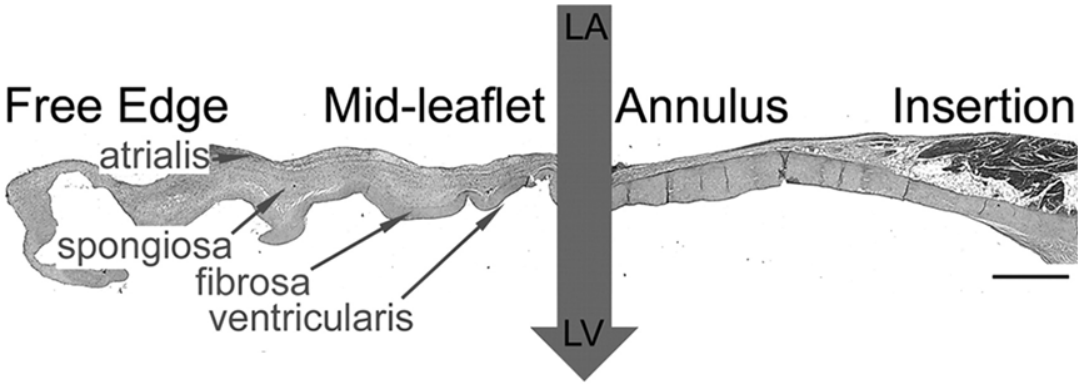

Figure 1.13: Leaflet microstructure of the anterior leaflet stained using Movat pentachrome. Image after Stephens et al. [51]. Labels: LA – left atrial side and LV – left ventricular side.

The organisation of the fibre orientation through the thickness of the leaflets has shown that the microstructure is organised relative to the valve anatomy [52]. Aligned circumferentially (parallel to the annulus) in the central portion of the valve leaflets, in the vicinity of the fibrous trigones and the anterior strut chordae this fibre orientation is found to rotate radially. Such orientation towards anatomical landmarks was not found to be the case in the posterior leaflet. Measurements on the variability of the fibre orientation was found to range from 0.58 to 0.65, where 1.0 implies perfect fibre orientation and 0.0 a totally random distribution [52].

This spread in fibre orientation is considered to be the mechanism through which the leaflet (and other soft tissues) inherit their non–linear and anisotropic properties. Defined with a particular periodicity of waviness and geometric spread, the fibres are considered to be initially slack when unloaded. At low stretches the resistance to applied loads is low, as few fibres are taut and able to bear load and/or orientated in the direction of loading. With increasing stretch the proportion of load bearing fibres in-

creases as fibres become taut and reorientated in the direction of load, increasing the overall resistance to loading. It is considered that this non–linear increase in load bearing fibres to applied stretch is the mechanism through which fibrous tissues inherit their non–linear properties [53].

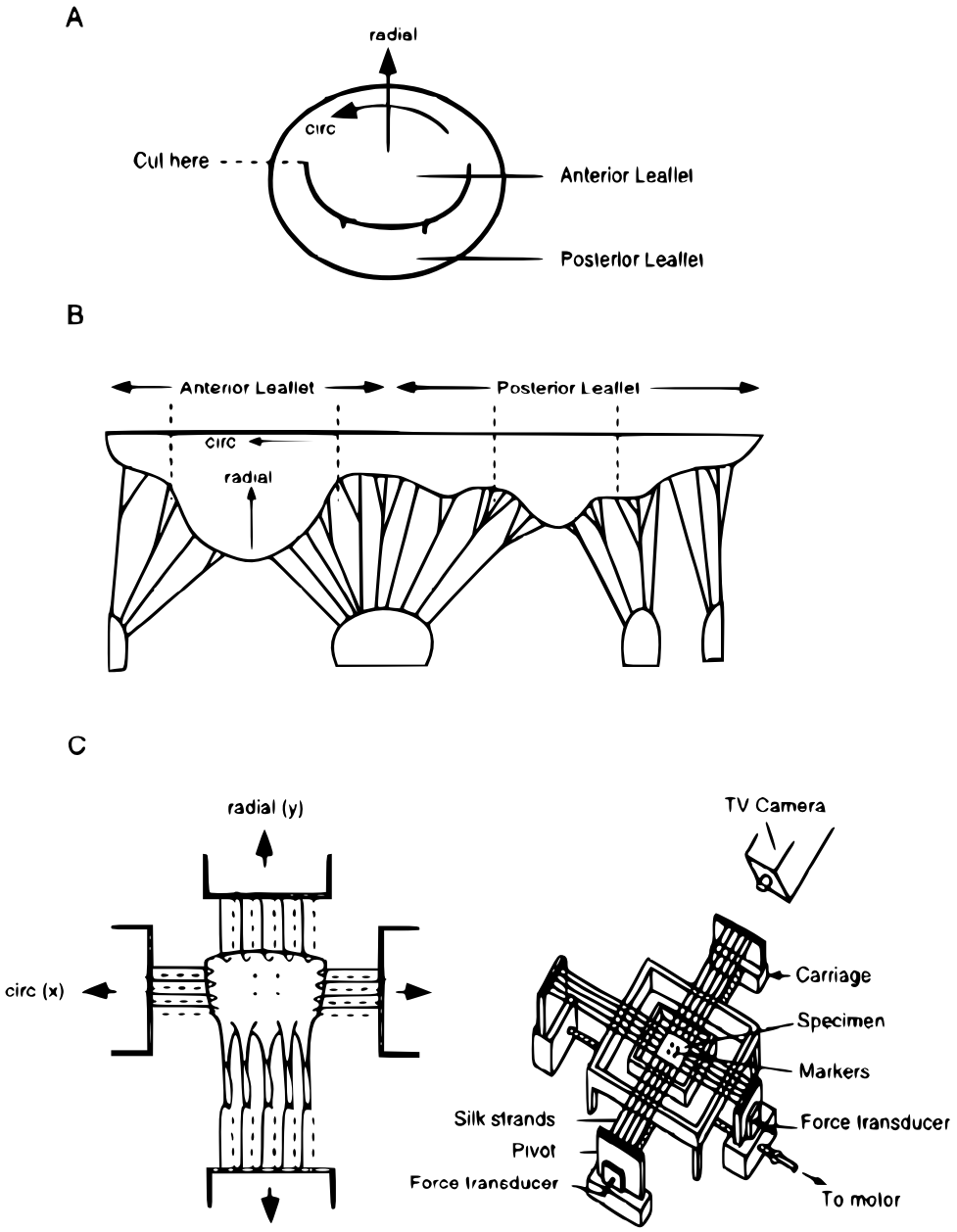

Figure 1.14: Illutration of the experimental proceedure used to characterise the leaflet biomechanical properties. The circumferential directions is defined as parallel to the annulus, with the radial direction defined orthogonal to this. Image after May-Newman and Yin [54].

The mechanical response of the mitral valve has traditionally been characterised in the circumferential and radial directions as illustrated in Figure 1.14. Experimental observations have shown that when loaded from an initially unloaded state, mitral valve tissue (like most soft tissues) exhibits a hysteretic stress–strain response in loading and unloading [54]. However if correctly preconditioned using a cyclic loading protocol (8–10 cycles) [54], the tissue produces a pseudoelastic response as the tissue adapts to its cyclic loading and the hysteretic response dissipates. Experiments on porcine anterior leaflets by Grashow et al. [55] have show that although the leaflet show significant stress relaxation under constant stretch, negligible creep was observed under constant stress tension. Over a three hour period the circumferential and radial stretch were found to vary by ∼1%. These results indicates that valvular tissue is not viscoelastic, but quasi–elastic.

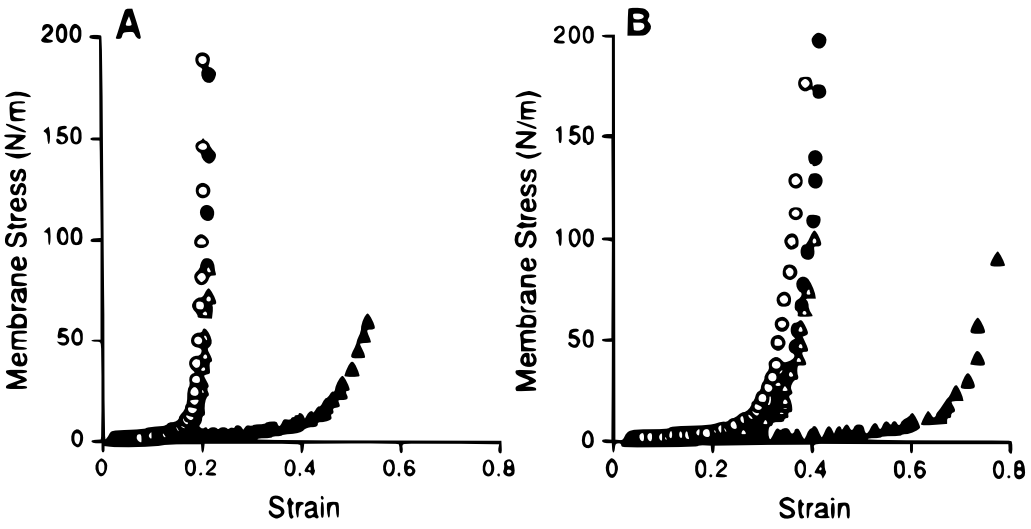

(a) Anterior leaflet **(b)** Posterior leaflet

Figure 1.15: Experimental results showing the membrane stress–strain relationship in (a) anterior and (b) posterior leaflets of an excised porcine mitral valve from May-Newman and Yin [54]. Note that under uniaxial testing the radial stress in both leaflets displays a different mechanical response when compared to the biaxial case, indicating the dependency of the radial stresses on the circumferential load. Figure labels: △ – equibiaxial radial, ○ – equibiaxial circumferential, ▲ – uniaxial radial and ● – uniaxial circumferential.

Mechanical tests on excised porcine valves have shown that the leaflets are stiffer in the circumferential directions; variation in the stiffness between leaflets are also reported, with the the posterior leaflet more isotropic in its mechanical response and more extensible than the anterior leaflet [54]. The earliest tests of leaflet tissue were performed using uniaxial testing procedures [56], however this approach is unable to account for the in–plane anisotropic coupling of the leaflet tissue. As highlighted in Figure 1.15, comparison of uniaxial and biaxial testing procedures indicate that loads in the circumferential direction strongly affect the radial response. Thus in order to correctly characterise the anisotropic in–plane behaviour of the leaflets, biaxial testing is required.

Further characterisation of the mechanical response of the leaflet tissue shows regional variation. Earlier uniaxial testing have reported that regions adjacent to chordal attachment reported have an initial elastic moduli greater than regions in the centre of the valve [57]. More recently biaxial testing has been performed on leaflet tissue in the vicinity of a chordal attachment [58]. At these locations the collagen fibres are highly directed, aligning locally to the direction of the attached chordae tendineae. Results of these mechanical tests show decreasing extensibility and increasing stiffness in radial direction with proximity to the chordae insertion.

The above experiments have all been performed upon excised valves *in vitro*. Using an inverse finite element method Krishnamurthy et al. [59] have performed an *in vivo* assessment of the post–transition stiffness. Using geometric markers applied to an ovine heart, the anisotropic stiffness of the leaflets has been approximated from the measured deformations at different points in the cardiac cycle. Results indicate that during isovolumic relaxation the stiffness of the valve is linear, with the circumferential stiffness greater than the radial. However it is not possible to measure the pre–transition phase as this approach lacks the temporal resolution required.

Dysfunctional state

Changes in the organisation of the tissue microstructure alters the biomechanical properties, resulting in dysfunctional states. In states of myxomatous degeneration, the leaflet tissue is reported to be abnormally thick with irregular regions of collagen [60] and a disorganised arrangement of the fibrosa [61]. Comparison of the collagenous content between normal and degenerate leaflets shows that collagen

content increases by 9–53%, depending upon collagen type (I, III or V) [61]. The effect of this upon the mechanical properties has been assessed in normal, myxomatous and flailing human valves by Barber et al. [62] and Mills et al. [63]. Obtained from human subjects undergoing valve repair or replacement, uniaxial measurements in both the circumferential and radial directions have been performed. The results indicate that pre–/post–transition stretch increases, as the leaflets become more extensible. Measurements of the post–transition elastic modulus show that the stiffness decreases compared to normal valves. Similar experimental measurements have been performed by Prot et al. [64], who obtained diseased valves from hypertrophic obstructive cardiomyopathic hearts. As with the myxomatous and flailing valves, biomechanical tests on these valves indicated that they were more extensible and less stiff than normal valves.

1.4.2 Chordae

Similar to the microstructure of the leaflets, the chordae tendineae are composed of a mixture of collagen and elastin [65]. The structure of the chordae is arranged with the collagen fibres in the centre of the chordae, aligned with the axis direction; surrounding this central core is a thin sheet of elastic fibres intermixed with collagen fibres (Figure 1.16). Using optical and scanning electron microscopy, it has been observed in unstretched states that the collagen fibres are arranged in a undulating pattern aligned with the axial direction [66]. Also referred to as “crimp”, this variation in the pitch of collagen fibres has been suggested as the mechanism reponsible for difference in mechanical properties [65].

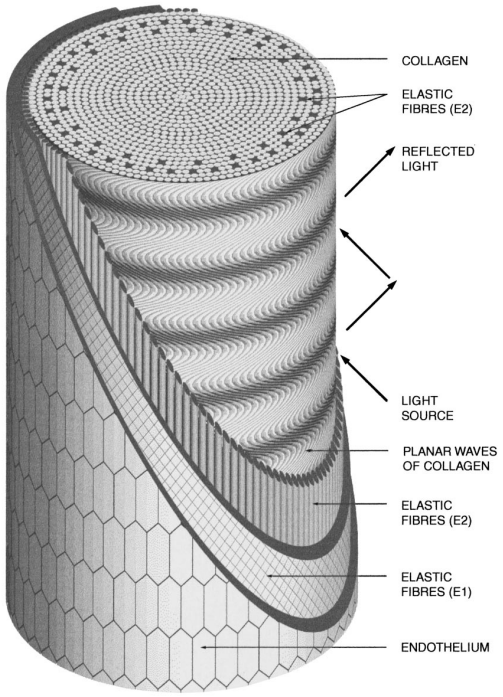

Figure 1.16: Illustration depicting the microstructure of the chordae tendineae. E1 and E2 layers refer to the outer and inner layers respectively. Image after Millington-Sanders et al. [66].

Normal state

Similar to the leaflet tissue, chordal tissue also exhibits a non–linear stress–strain response. As the fibres are aligned in a common direction, experimental measurements are simplified as uniaxial testing is sufficient. Stress–strain data reported by Kunzelman and Cochran [67] has characterised the non–linear behaviour of both the marginal and basal tendineae. Using porcine samples, these results indicate that the marginal chordae are less extensible and stiffer than the larger basal chordae. Reported in units of grams per millimetre squared, conversion to SI units is performed using $1\,\mathrm{g\,mm^{-2}} = 9806\,\mathrm{N\,m^{-2}}$.

Further measurements on porcine samples by Liao and Vesely [68] report the differences between the marginal, basal and strut chordae. Results indicate that the diametric size of the chordae is proportional to the extensibility of the chordae and inversely proportional to its elastic modulus. The mechanism of this mechanical behaviour is considered to be a function of the collagen fibre pitch, as experimental measurements show an inversely proportional relationship between the periodicity of the collagen pitch and the chordal extensibility [68].

Dysfunctional state

As with the valve leaflets, changes in the organisation of the chordae microstructure alters the biomechanical properties and results in dysfunctional states. Uniaxial tests on myxomatous chordae tendineae have been reported by Barber et al. [69], results state that myxomatous chordae are twice as large normal chordae in terms of both cross–sectional area and mass. Measurement of the post–transitions elastic moduli and the failure stress of the myxomatous chordae were less than 25% of the normal values. Similar measurements have been performed upon flailing chordae by Mills et al. [63], similarly results show that the flail chordae are more extensible than normal and ultimately fail at lower stresses.

1.4.3 Mathematical models

In the case of soft tissues where the strains are finite (i.e. large), the biomechanical response have traditionally been modelled using finite hyperelasticity theories. Using experimental data, such as that described previously in Sections 1.4.1 and 1.4.2, mathematical models can be constructed which describe the mechanical response of the tissue. The benefits of such an approach are vast as modelling provides a methodology in which the mechanical response can be assessed under *in vivo* conditions.

For more information regarding the theory of finite hyperelasticity please refer to Holzapfel [70] and the references contained therein.

Kinematics

Here the kinematics of motion are described within a Cartesian coordinate system defined by the a set of orthonormal vectors $\{\mathbf{e}_1, \mathbf{e}_2, \mathbf{e}_3\}$. In this coordinate system an elemental mass is located at the position $\mathbf{X} = [X_1, X_2, X_3]$ at an arbitrary reference time t_0. At the current time t, this mass element is located at the different position $\mathbf{x} = [x_1, x_2, x_3]$. The motion of this mass element through the coordinate space is given by the mapping $\mathbf{x} = \chi(\mathbf{X}, t)$ (Figure 1.17). This function is assumed to be continuous and differentiable, allowing for the definition of the deformation gradient tensor $\mathbf{F}$ (Equation 1.4) [71]. Here $\otimes$ is the dyadic vector product and the indices $i, j = 1, 2, 3$. In this work a membranous definition has been adopted, thus the out–of–plane response is not coupled with the in–plane motion and vice versa, i.e. $F_{13} = F_{23} = F_{31} = F_{32} = 0$ (Equation 1.5).

$$\mathbf{F}(t_0, t) = \frac{\partial \mathbf{x}}{\partial \mathbf{X}} = F_{ij}(t_0, t)\,\mathbf{e}_i \otimes \mathbf{e}_j \tag{1.4}$$

$$\mathbf{F} = \begin{pmatrix} F_{11} & F_{12} & 0 \\ F_{21} & F_{22} & 0 \\ 0 & 0 & F_{33} \end{pmatrix} \tag{1.5}$$

For soft tissues it is a typically assumed that the element mass is incompressible (i.e. volume conserving), which gives the incompressibility constraint $J = \det \mathbf{F} = 1$ [72]. Example of the deformation gradient (in an incompressible state) under uniaxial, biaxial and shearing stretches are illustrated in Figure 1.18. The corresponding values of the deformation gradient to these states are defined in Equation 1.6. Here the left and right Cauchy–Green deformation tensors are introduced, **B** and **C** respectively

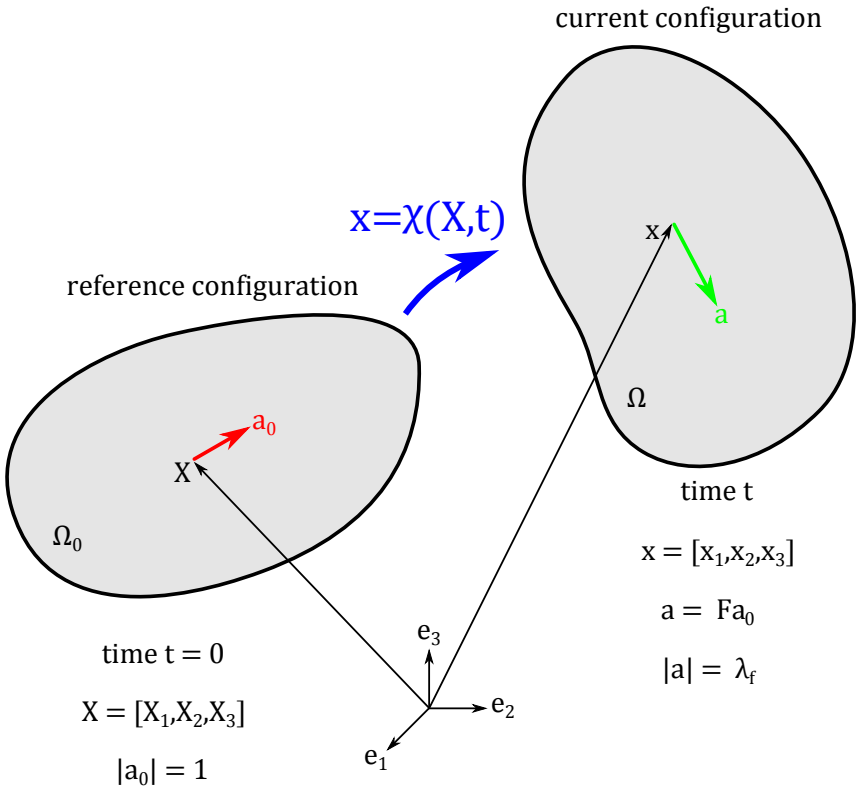

Figure 1.17: Deformation of a continuum body at position **X** at time $t = 0$ to the position **x** at time t. The mapping beween these two positions is defined as χ where $\mathbf{x} = \chi(\mathbf{X}, t)$, assumed to be a continuous function the derivative of this mapping is referred to as the deformation gradient $\mathbf{F} = \partial\mathbf{x}/\partial\mathbf{X}$. Embedded within the initial configuration γ_0 at time $t = 0$ is a vector $\mathbf{a}_0$, this vector is convected with the motion of the body such that at time t this vector adopts the orientation **a** where $\mathbf{a} = \mathbf{F}\mathbf{a}_0$.

(Equations 1.7 and 1.8). Linked to the deformation tensor, these tensors are also used to quantify the deformation of the elemental mass.

$$\mathbf{F}_{uniaxial} = \begin{pmatrix} \lambda & 0 & 0 \\ 0 & \lambda^{-1/2} & 0 \\ 0 & 0 & \lambda^{-1/2} \end{pmatrix}$$

$$\mathbf{F}_{biaxial} = \begin{pmatrix} \lambda & 0 & 0 \\ 0 & \lambda & 0 \\ 0 & 0 & \lambda^{-2} \end{pmatrix} \tag{1.6}$$

$$\mathbf{F}_{shear} = \begin{pmatrix} 1 & \gamma & 0 \\ 0 & 1 & 0 \\ 0 & 0 & 1 \end{pmatrix}$$

$$\mathbf{B} = \mathbf{F}\mathbf{F}^T \tag{1.7}$$

$$\mathbf{C} = \mathbf{F}^T\mathbf{F} \tag{1.8}$$

In order to model the effects of the anisotropy in materials such as soft tissues, it is required to provide the elemental mass with an additional directional stiffness. Using virtual fibres embedded within the material, an anisotropic stress response can be generated [72]. The initial direction of this fibre at time t_0 is defined by the unit vector $\mathbf{a}_0$, where $\mathbf{a}_0 \cdot \mathbf{a}_0 = 1$. The motion of this vector follows the motion of the elemental mass, thus at time t its current direction is given as $\mathbf{a} = \mathbf{F}\mathbf{a}_0$ (Figure 1.17). The deformation

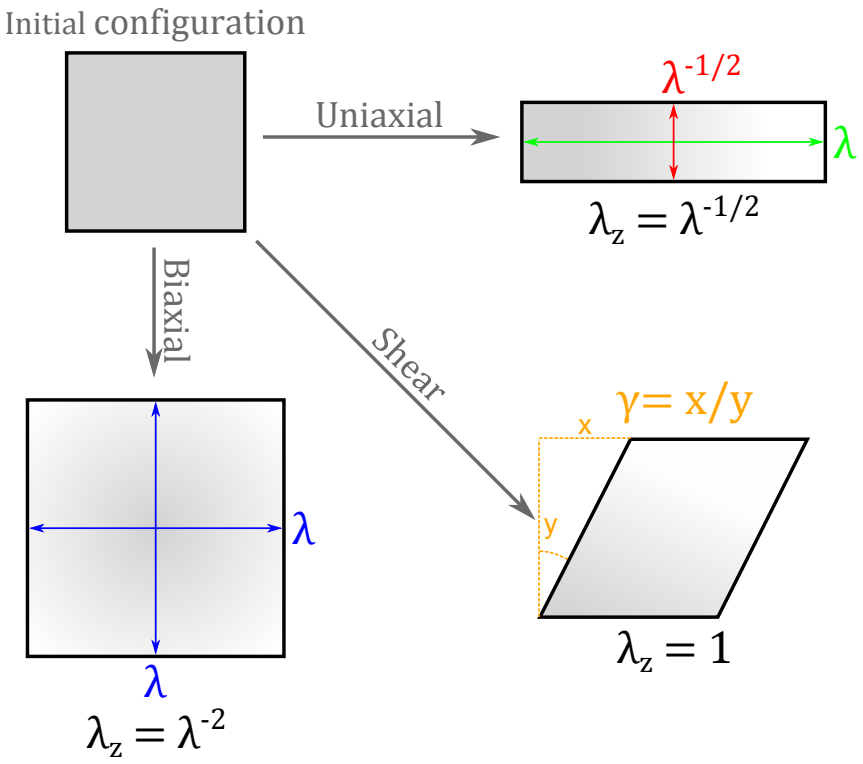

Figure 1.18: Two–dimensional illustrations of the uniaxial, biaxial and shear deformations. The values of the deformation gradient in these states are given in Equation 1.6. Here the in–plane stretches λ are labeled in color, with the associated out–of–plane stretches λ_z defined adjacent to the relevant deformation.

of this vector can be measured by the stretch of this vector, λ_f (Equation 1.9).

$$\lambda_f^2 = \mathbf{a}\cdot\mathbf{a} = (\mathbf{F}\mathbf{a}_0)^T\cdot(\mathbf{F}\mathbf{a}_0) = \mathbf{a}_0(\mathbf{C}\mathbf{a}_0) \tag{1.9}$$

Discrete fibre strain–energy functions

As stated previously, the elastic properties of soft tissues can be modelled using finite hyperelastic theories [70]. For a finite hyperelastic material the elastic properties are defined by its associated Helmholtz free–energy function ψ, which when defined solely as a function of the deformation gradient **F** (or some other strain tensor) is more commonly referred to as the strain–energy or stored–energy function. It is through the derivatives of this scalar valued function that the stresses are related to the deformation. For the mitral valve leaflets there exist two separate strain–energy functions that have been fitted to the biaxial data reported by May-Newman and Yin [54].

Reported by May-Newman and Yin [73] and Prot et al. [74], both functions are non–linear and model the anisotropic behaviour of the leaflet tissue with a single discrete embedded fibre system which lies in the plane, i.e. a $\mathbf{a_0} = [a_{01}, a_{02}, 0]$. Referred to as transversely isotropic, single fibre family materials can be described using five invariants (I_1, I_2, I_3, I_4 and I_5) of the right Cauchy–Green tensor **C** (Equations 1.10 – 1.14) [71].

$$I_1 = \mathrm{tr}(\mathbf{C}) = C_{11} + C_{22} + C_{33} \tag{1.10}$$

$$I_2 = 1/2\left(\mathrm{tr}(\mathbf{C})^2 - \mathrm{tr}\left(\mathbf{C}^2\right)\right) \tag{1.11}$$

$$I_3 = \det \mathbf{C} \tag{1.12}$$

$$I_4 = \mathbf{a_0} \cdot (\mathbf{C}\,\mathbf{a_0}) = a_{01}C_{11}a_{01} + a_{01}C_{12}a_{02} + a_{02}C_{21}a_{01} + a_{02}C_{22}a_{02} \tag{1.13}$$

$$I_5 = \mathbf{a_0} \cdot (\mathbf{C^2}\,\mathbf{a_0}) \tag{1.14}$$

The two strain–energy functions are a function of the 1st invariant I_1 (Equation 1.10) and 4th pseudo–invariant I_4 (Equation 1.13), which describe the volumetric dilation and square of the stretch in the fibre direction respectively λ_f^2 (see Equation 1.9). The May-Newman and Yin [73] and Prot et al. [74] strain–energy functions (Equations 1.15 and 1.16 respectively) are similar in form, only differing in the I_4 term. The corresponding parameter for these strain–energy functions are listed in Table 1.9.

$$\psi(I_1, I_4) = c_0\left(\exp\left[c_1(I_1-3)^2 + c_2(\sqrt{I_4}-1)^4\right] - 1\right) \tag{1.15}$$

$$\tilde{\psi}(I_1, I_4) = \tilde{c_0}\left(\exp\left[\tilde{c_1}(I_1-3)^2 + \tilde{c_2}(I_4-1)^2\right] - 1\right) \tag{1.16}$$

Table 1.9: Parameters for the strain–energy functions listed in Equations 1.15 and 1.16.

Equation/Source	Leaflet	c_0 (kPa)	c_1	c_2
1.15	Anterior	0.399	4.325	1446.5
[73]	Posterior	0.414	4.848	305.4

Equation/Source	Leaflet	$\tilde{c_0}$ (kPa)	$\tilde{c_1}$	$\tilde{c_2}$
1.16	Anterior	0.052	4.63	22.6
[74]	Posterior	0.171	5.28	6.46

Both strain–energy functions are converted to the second Piola–Kirchoff stress tensor using Equation 1.17 (note that ψ is interchangable with $\tilde{\psi}$) [74]. The derivatives of the 1st and 4th invariants are shown in Equations 1.19 and 1.20, here the term p is the internal pressure of the material. For membranes the through plane component of the stress is zero, i.e. $S_{33} = 0$, which gives the pressure constraint (Equation 1.18).

$$\mathbf{S} = 2\sum_{\substack{i=1 \\ i\neq 2,3}}^{4} \frac{\partial \psi}{\partial I_i}\frac{\partial I_i}{\partial \mathbf{C}} + p\mathbf{C}^{-1} \tag{1.17}$$

$$p = -2\sum_{\substack{i=1 \\ i\neq 2,3}}^{4} \frac{\partial \psi}{\partial I_i}\frac{\partial I_i}{\partial C_{33}}C_{33} \tag{1.18}$$

$$\frac{\partial I_1}{\partial \mathbf{C}} = \mathbf{I} \tag{1.19}$$

$$\frac{\partial I_4}{\partial \mathbf{C}} = \mathbf{a_0} \otimes \mathbf{a_0} \tag{1.20}$$

Continuous fibre strain–energy functions

Optical examination of the tissue microstructure indicates that the mean fibre orientation and standard deviation vary in the different regions of the leaflet (Section 1.4.1). In the discrete approach detailed above only the mean fibre angle is accounted for, the effects of fibre splay require a continuous approach

in which the fibre orientation is defined using a probability density function. A comparative study of the two methods by Bischoff [75] has shown that the discrete method results in large discrepancies with large standard deviations of fibre splay. In cases of uniaxial loading the two methods were found to be in close agreement, however in cases of biaxial loading, significant differences in the displacement were found in cases of fibre splay >5°.

For the mitral valve, a continuous fibre model of the valve leaflets has been reported by Einstein et al. [76]. Derived from the approach originally reported by Billiar and Sacks [77], this model is based upon a continuous distribution of fibres which are defined with a preferred mean direction and standard deviation centred on this mean with a Gaussian distribution (Figure 1.19). It is from this continuous fibre distribution that the non–linear and anisotropic mechanical response is generated.

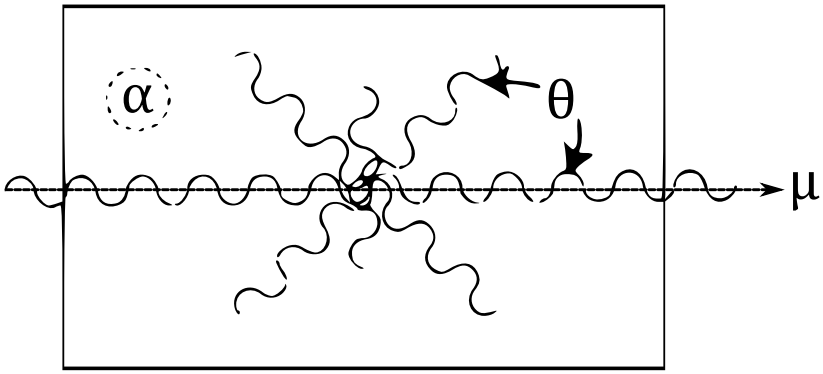

Figure 1.19: Illustration of collagen fibre arrangement in the continuous fibre model of Einstein et al. [76]. Embeded within an isotropic matrix of stiffness α, the fibres are defined with a preferred mean direction μ and a standard deviation about this mean of θ. Image after Einstein et al. [76]

In the continuous fibre model the second Piola–Kirchhoff stress **S** is calculated using Equations 1.21 – 1.25, for further details regarding the derivation of this model and the terminology used here refer to Billiar and Sacks [77] and Einstein et al. [76]. Evaluated from a continuous in–plane distribution of fibres, the key parameters in this model are the fibre stretch s_f and the angular distribution of fibres $R(\theta)$. Fitted to experimental data, the parameters used to model the mitral valve leaflets are listed in Table 1.10.

Implementation of a continuous distribution has been reported to be more computationally intensive. The evaluation of the integral term is reported to require at least 18 discrete intervals increasing the numerical cost per element by 18 times [71]. More efficient approaches of continuous fibre modelling based upon an invariant formulation is detailed in Freed et al. [71], however this has currently only been applied to aortic valves.

$$\mathbf{S} = pJ\mathbf{C}^{-1} + 2J^{-2/3}\mathrm{DEV}\left[\frac{\partial \tilde{W}}{\partial \tilde{\mathbf{C}}}\right] \tag{1.21}$$

$$\mathrm{DEV}(\bullet) = (\bullet) - \frac{1}{3}\mathrm{tr}((\bullet)\,\mathbf{C})\mathbf{C}^{-1} \tag{1.22}$$

$$\frac{\partial \tilde{W}}{\partial \tilde{\mathbf{C}}} = \alpha\mathbf{I} + \int_{-\pi/2}^{\pi/2} S_f R(\theta)\mathbf{A}\otimes\mathbf{A}\,d\theta \tag{1.23}$$

$$S_f = A\left[\exp\left[\frac{B}{2}(\mathbf{A}(\theta)\mathbf{C}\mathbf{A}(\theta) - 1)\right] - 1\right] \tag{1.24}$$

$$R(\theta) = \frac{1}{\sigma\sqrt{2\pi}}\exp\left[\frac{-(\theta-\mu)^2}{2\sigma^2}\right] \tag{1.25}$$

Table 1.10: Continuous fibre model leaflet parameters for Equations 1.21 – 1.25, values taken from Einstein et al. [76]. Labels: A – fibre volume fraction, B – fibre stiffness, σ – fibre angle standard deviation and α – isotropic matrix stiffness.

Leaflet region	A [kPa]	B [–]	σ [°]	α [kPa]
Anterior	0.070	40	20	10
Posterior	0.005	40	20	10
Commissures	0.030	40	20	10

Finite element implementation

Comparison of the two discrete fibre strain–energy functions defined in Equations 1.15–1.16 have been implemented and examined in the structural solver ABAQUS [74]. Using the fourth–order elasticity tensor, these strain–energy functions have been implemented using a implicit time integration scheme. In–plane behaviour of a single element show no significant difference between the analytical solution in both the fibre direction and cross–fibre direction. Out–of–plane behaviour was assessed by direct comparison against the numerical results of an earlier hyperelastic orthrotropic constitutive model, for which the two strain–energy functions were refitted to match the earlier hyperelastic model. Out–of–plane deformation was induced by simulating the inflation of a spherical membrane by a transverse pressure load, here the fibre aligned in the circumferential direction. Comparison of the out–of–plane displacement show similar values to the earlier hyperelastic orthotropic material model, however differences were noted between the two strain–energy functions. When pressurised the sphere adopted an ellipsoid shape, the Prot et al. [74] strain–energy function was shown to be stiffer at the centre of the ellipsoid but weaker at the tips than the May-Newman and Yin [73] strain–energy function.

A hyperelastic anisotropic finite element membrane formulation has been reported by Einstein et al. [78]. Implemented in the commercial code LS–DYNA the implementation of the strain–energy function has been performed using reduced integration corotational Hughes–Liu continuum shell elements [79, 80]. Validated by comparison to Mooney–Rivlin rubber models, with and without anisotropy, this membrane formulation avoids the numerical shear locking phenomenon through reduced integration. As the integration is reduced in the thickness direction in order to degenerate the element to a membrane, the stress is assumed to be uniform over the element. The deformation gradient is calculated and stored using a user defined subroutine. This algorithm has been used in this work and further discussion on this topic can be found in Chapter 2, Section 2.3.1.3.

Using a mixed displacement–pressure finite element formulation Weinberg and Kaazempur-Mofrad [81] have implement the strain–energy function reported by May-Newman and Yin [73]. This mixed displacement–pressure formulations has been modified in order to keep the stiffness matrix positive definite at low strains by using a small neo–Hookean contribution to the strain–energy function. Implemented in the commercial finite element solver ADINA, single element tests under uni/biaxial stretches are reported and compare well to the analytical solutions. This has been followed by an updated formulation that includes a through thickness strain calculation based upon a plane stress assumption in a three–dimensional shell element [82]. Using the same strain–energy function, this has also been implemented in ADINA 4–node element with $2\times2\times2$ Gauss point integration. Results include single elements under uni/biaxial stretch and a simple three–dimensional case [82].

1.5 Numerical models

Although advances in imaging techniques such as magnetic resonance imaging [83] and echocardiography [84] allow the extraction of anatomical detail and even the flow characteristics of blood flow, these modalities do not provide an insight into how the valves function such as stress state. In order to better understand the complexity of heart valve function it is required to supplement clinical observations with experimental and numerical techniques that allow in–depth examination of function. Although there

exist a variety of different models of the mitral valve, here in this section the focus has been applied primarily to three dimensional finite element models of the mitral valve.

1.5.1 Modelling methodologies

Simulation of mitral valve function has progressed significantly over the last 18 years since the publication of the first three dimensional model by Kunzelman et al. [85]. By modelling the valve as a solid body that satisfies the mass and momentum conservation, the equations of motion which define the dynamics of the valve can be approximated using the finite element method (Appendix B.1.2). Although differences exist in the numerical implementation of the stress, all the heart valve models described here are based upon the solution of the same equations of motion.

Depending upon how the haemodynamic load is applied to the model, simulation of mitral valve function can be divided into structural–only or fluid–structure interaction models. As the term suggests, fluid–structure interaction models includes and couples together both the fluid (blood) and structural (valve) domains, whereas structural–only models only contain the structural domain of the valve in which case the haemodynamic load must be approximated. This particular issue has been explored within Chapter 3, where the differences between these two modelling methodologies has been characterised in the context of valvular dynamics.

1.5.2 Model geometries

As detailed in Section 1.2, the anatomical form of the mitral valve is strongly asymmetric and contains significant variation in the number of cusps and chordal attachments for example. Geometric variation between the models reflects the different models interpretation of the anatomical variation of the mitral valve itself. Geometric variation also exists as determination of the *in vivo* stress–free configuration, which corresponds to the initial geometric state of the valve, is currently not possible [59]. In general features are noted across the different models such as the number of leaflets (two), however variation does exist in the number of posterior leaflet scallops modelled and the shape of the annular profile. A comparison of the different model geometries is reported by Votta et al. [32].

In order to solve the conservative equations which describe the dynamics of the structure/fluid using the finite element method, it is required to discretised the geometry. Typically the leaflets of the valve have been modelled using two–dimensional shell elements or three–dimensional solid elements. whereas the chordae tendineae are typically modelled using one–dimensional beam elements. The fluid domain is typically modelled using three–dimensional solid elements. For more details regarding finite element technology refer to Zienkiewicz et al. [86].

1.5.3 Valve function

Numerical models enable the study of scenarios which cannot be measured (i.e. stress) or not possible to be tested experimentally either *in vivo* or *in vitro*. The use of mitral valve models has permitted the examination of the different subcomponents of the valve, giving an insight into the contribution of each subcomponent to the overall function of the valve. Here in this section the different mitral valve models have been grouped together broadly by the class of material model used to describe the biomechanics of the valve, beginning with linear elastic materials followed by hyperelastic non–linear elastic materials.

Linear elastic models

Kunzelman et al. [85] and Kunzelman et al. [87] and Kunzelman et al. [88]

The earliest structural 3D finite element model of the mitral valve was developed in 1993 by Kunzelman et al. [85]. Using the finite element structural solver ANSYS, simulation of closure in a symmetrical

valve model has been simulated. The results of this model show that the largest principal stresses in the valve are tensile in closure, with larger stresses induced in the anterior leaflet than the posterior leaflet. Principal stress directions were found to correspond to the local collagen fibre direction defined in the model.

The geometry of this model was based upon anatomical resin casts taken from porcine heart, with the leaflets, chordae tendineae and the papillary muscles defined in their open positions. Idealised using constant thickness shell elements, the leaflets have been modelled using an anisotropic linear elastic material model and constant thickness whereas the chordae have been modelled as linearly elastic beam elements. In the leaflets, the anisotropic material properties are orientated with respect to the collagen fibres with the largest value of stiffness defined in this direction; in the model this has been defined locally in each shell element following experimental mapping of the fibres. The material properties of each leaflet have been defined independently, with the anterior leaflet modelled as more anisotropic; the ratio of stiffness in the anterior leaflet are 6.2/2.1 MPa compared to 2.4/1.9 MPa in the posterior leaflet. The effects of bending in valvular tissue have been assumed to be negligible, minimal bending stiffness was applied to the shell elements. Simulated in the absence of blood, the inertial effect of blood in this structural–only model has been approximated by increasing the density of the full structure by a factor of ten.

Using the model described previously, the effect of annular dilation on the valve has been assessed [87]. Simulation of dysfunction has been performed by increasing the annular circumference by 18%. Closure of the valve occurs with delayed coaptation when compared to the normal model, with the incomplete coaptation observed. The magnitude of the principal stress was shown to increase by a factor of two in both leaflets.

Salgo et al. [89]

The effect of a non–planar saddle shaped annulus on the predicted values of stress in a structural–only model has been investigated by Salgo et al. [89]. The results of this model have shown that both the curvature and non–planarity of the annulus independently reduce the maximum predicted Von Mises stress and in combination further reduce the stress.

Based upon an elliptic shaped annulus, the valve has been defined in a closed state with the free margin of the two leaflets joined together. Using shell elements, the leaflets have been modelled as a linearly elastic orthotropic material which was defined with a larger elastic modulus in the fibre direction. In this model the fibre direction is oriented in the direction of the commissural–to–commissural direction. Implemented in the finite element solver Algor, structural–only simulations of systole have been performed by applying a pressure load of 16 kPa. A set of different models have been created which are characterised by the annular height to commissural width ratio, ranging from 0 to 20%. The predicted Von Mises stresses were found to be minimised at an annular height to commissural width ratio of 15–20%. *In vivo* measurements performed by the authors of this model support these results, with the average value of this ratio reported as 15% in humans, sheep and baboons.

Lim et al. [90]

The effect of the 3D annular displacements on the mitral valve have been examined in an asymmetrical model of the valve by Lim et al. [90]. The effect of this dynamic motion was shown to reduce the stress concentration in the posteriormedial commissural region when compared to the anterolateral commissural region due to the asymmetric skewing of the leaflets.

The geometry of the model was generated from *in vivo* data obtained from 12 ultrasonic transceiver crystals embedded into the structure of an ovine heart taken at diastole; accordingly the geometry of the valve is asymmetric and contains a saddled shaped annulus. Modelled using shell and beam elements,

the anisotropy of the leaflets has been neglected as the leaflet material has been assumed to be isotropic. Applying the experimentally measured pressure loads and the displacements of the annulus and papillary muscles throughout the cardiac cycle, a structural–only simulation of the full cardiac cycle has been performed using the structural solver ANSYS v5.7. The results of these simulations indicate that the highest stresses are located in the commissural region between the anterior and posterior leaflet and at the leaflet free margin. Due to the asymmetry of the valve geometry the stresses are also asymmetric, with a larger stress concentration on the anterolateral side.

Non–linear elastic models

As reviewed in Section 1.4, the biomechanical properties of the valve tissue are both non–linear and anisotropic. The linear simplification results in underestimation of the deformation, as non–linear materials are able to deform more freely than a linear material given the same magnitude of stress. Here the latest hyperelastic models are reviewed, which include features such as the non–linear anisotropic behaviour of the valve tissue and fluid–structure interaction.

Prot et al. [74], Prot and Skallerud [91], Prot et al. [92], Prot et al. [64] and Skallerud et al. [93]

The effect of annular motion, chordal support and the material properties of the leaflet tissue have been examined through a family of structural models by Prot et al. [74], Prot and Skallerud [91], Prot et al. [92, 64], Skallerud et al. [93]. All of these models have been implemented in the finite element structural solver ABAQUS and all feature a hyperelastic, anisotropic membrane, strain–energy function material model [74].

The earliest of these models reports the simulation of valve closure with and without the thicker strut chordae tendineae[74]. Unlike other models, the geometry of the model only contains the anterior and posterior leaflets, attached to a circular annulus; the connective tissue of the commissural regions has not been included. Coaptation of the leaflets has been ensured by the positioning of the two leaflet segments on opposing sections of the circular annulus. In this model the leaflets and chordae tendineae have been represented using shell and beam elements respectively. Using this model, the elongation or rupture of the strut chordae has been simulated through the modelling of the valve with and without the basal chordae. Simulating only closure with a transvalvular pressure ramp of 80 mmHg, as obtained *in vivo* from a porcine heart, the numerical results have been compared against *in vivo* ultrasound measurements from a human subject. The results of these simulations indicate that with the additional support of the strut chordae, the displacement of the valve during closure better matches the physiological displacements exhibited by a normal valve when directly compared to a marginal chordae–only model.

Using the same material model, this geometry of the previous model was updated to include anatomical measurement of a porcine valve, local collagen fibre directionality and a saddle shaped annulus (Figure 1.20) [92]. Using *in vivo* ultrasound measurements from a porcine heart the saddle–shapped annulus has been simulated as both static and dynamic; in the dynamic case the motion of the annulus was mimicked by changes in the anterior portion of the annulus, whilst the posterior side remained fixed. The material anisotropy in each shell element has been defined locally following experimental measurements. Simulation of the valve closure was performed using a transvavular pressure ramp which has now been scaled to a peak pressure of 120 mmHg. As in the previous model the effect of the strut chordae were examined by simulating the valve with and without these secondary chordae. The resulting simulations indicated that these chordae are responsible for approximately 30% of the papillary muscle load during closure and without these structures the tensile load in the marginal chordae doubles. From the simulations of static and dynamic annular motion it was found that increases in the height of the saddle does not significantly modify the chordal forces or stresses induced in the leaflets.

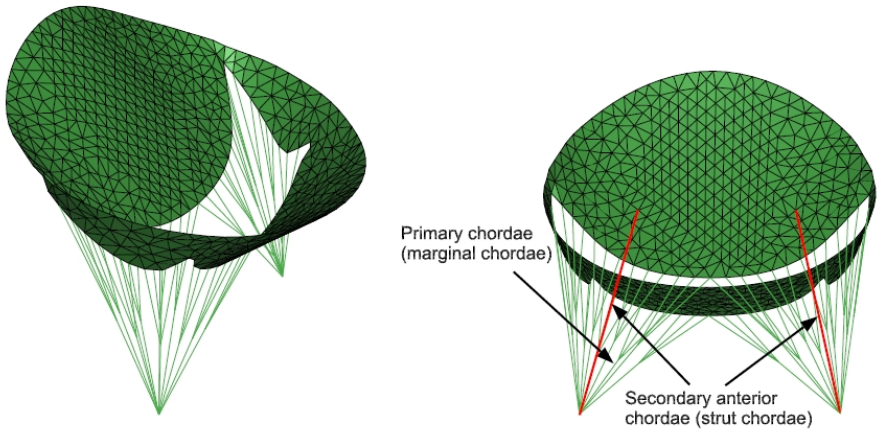

Figure 1.20: 3D model geometry of Prot et al. [92].

A solid element version of the previous model has been used to examine the effect of modelling the leaflets as a transversely heterogeneous material upon the valve deformation [91]. Unlike past and present models which have all assumed transverse isotropy through the leaflet thickness, this model has been defined with three different sections to represent the atrialis, fibrosa and ventricularis of the valve leaflets. As with the previous model, the model includes anatomical measurements taken from porcine samples, a saddle shaped annulus and local collagen fibre directionality. However here the leaflets have been discretised into three sections of solid brick elements, which represent the three different sections of the leaflet (atrialis/fibrosa/ventricularis). By varying the stiffness in the fibre direction in each layer, the behaviour of the leaflet as a one/two/three layered structure has been examined.

As before, simulation of valve closure was performed with using a transvalvular pressure ramp of 120 mmHg. Results show that the heterogenous modelling of the leaflet layers does not change the deformed configuration at closure, as all three variations exhibit identical behaviour. However increases in the stresses in the central section of the anterior leaflet were observed in the heterogenous layer models, with larger magnitude stress on the atrial side when compared to the ventricular side. The effect of the attachment of the strut chordae was also investigated by varying the area covered by the chordae in the radial and circumferential directions of the leaflet surface. Additional support in the circumferential direction was shown to result in a flatter deformed profile with a reduced displacement above the annular line during closure. Comparison of the valve deformation was performed against echocardiographic recordings taken from a porcine heart, from these measurements it was found that the simulated valve is displaced further into the atrium than observed *in vivo*.

Using the single layer solid element model described above, the effect of a normal and dysfunctional biomechanical state has been examined in a three–dimensional model [64]. Experimental tests on normal and dysfunctional leaflet tissue have been performed and are reported; these results show that the biomechanical response of both the normal and dysfunctional tissue is anisotropic, however the dysfunctional tissue is weaker and exhibits larger stretches at equivalent loads (Section 1.4.1). This data was then extrapolated and fitted to the strain–energy function used to describe the leaflet material properties (Equation 1.16). As in the previous model a localised preferred fibre orientation has been used, this has been assumed to remain constant between normal and dysfunctional states. As before simulation of closure has been performed with a transvalvular pressure load of 120 mmHg. Comparison of the valve deformation between the normal and dysfunctional states show that the weakened biomechanical properties of the dysfunctional model result in larger deformation, with the valve protruding above the annular line. Comparison to the porcine strain–energy function used in previous models was also performed, with the dysfunctional state still exhibiting greater deformation.

More recently an update to these models has been reported which includes active muscle con-

traction of the leaflet tissue [93]. Following experimental observations highlighting the contractile behaviour in the leaflets, the strain–energy function previously used to model the material properties of the leaflets has been modified to include an additional contractile fibre to the existing collagen fibre (refer to Skallerud et al. [93] for more details). Based upon anatomical descriptions and observations, the distribution and orientation of the muscle fibres have been assumed. Also assumed is the level and directionality of contractility, different levels of maximum contractile stress have been examined (100/200/300 kPa) along with contractile contribution in the collagen fibre direction which results in an orthotropic response. Modifying the two layer model solid element variant of the previous models, simulation of closure with a transvalvular pressure load of 120 mmHg has been performed with different levels of contractility, maximum contractile stress: 0, 100, 200 and 300 kPa. The deformation of the normal and contractile models has been compared, with the results showing reduced deformation in the central region of the leaflets. Comparison to *in vivo* experimental measurements have shown that the predicted deformation of the active model is significantly closer to the experimental results, suggesting that the contractility of the leaflets may have a strong physiological role.

Votta et al. [32] and Stevanella et al. [94]

The effect of the leaflet material properties and the motion of the annulus and papillary muscles have been examined in a family of models by Votta et al. [32] and Stevanella et al. [94]. Based upon the geometry of earlier linear elastic models [95], here the material properties have been updated and defined as non–linear. Implemented in the structural solver ABAQUS, the leaflets have been defined using the hyperelastic strain–energy function reported by Prot et al. [74].

The first model in this family has been used to examine the effect of annular and papillary muscle motion [32]. In this model the preferred fibre direction has been defined globally as circumferential, following the annulus around the orifice. The base of the model is a saddle shaped annulus which has been determined from *in vivo* measurements, simulations of valve closure has been performed with a transvalular pressure load of 120 mmHg, with and without dynamic annular motion. With dynamic annular motion, the time dependent displacement of the annulus has been applied as boundary condition during the simulation. The results of these simulations show that prior to coaptation the stress distributions are similar, however following coaptation the stresses are lower in the static model than in the dynamic model, with stresses in the anterior leaflet 67% higher in the dynamic model than the static model. The most highly stressed regions were the areas adjacent to the attachment of the strut and marginal chordae, with peak stresses reported as 1200 kPa. In the dynamic model an asymmetrical tension was shown in the anterolateral papillary muscle which experienced a lower load than the posteromedial side, however this difference was not observed in the static model.

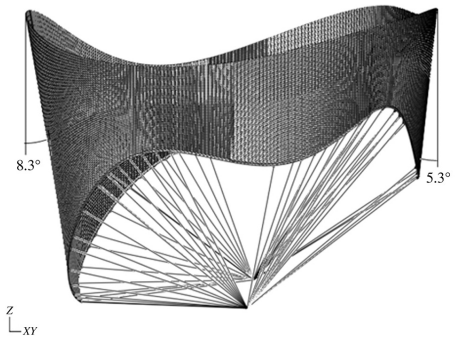

Figure 1.21: Initial valve geometry of the mitral valve model of Votta et al. [32].

An update of this model further examines the effect of the subcomponent motion on the stress state of the valve under closure [94]. The key features of the previous model have been adopted here (saddle

shaped annulus, non–linear anisotropic material behaviour, etc.), the only significant change is in the material properties in the leaflet tissue at the insertion of the strut chordae. Here the shell elements in the vicinity of the strut chordae insertion have been been defined as isotropically elastic with a Young modulus of 60 MPa and a Poisson modulus of 0.48 rather than hyperelastic. The peak stresses observed in the previous model are therefore reduced to 300 kPa from 1200 kPa. The results of these simulations show that while the anterior leaflet experiences tensile strains, the posterior leaflet undergoes compressive strains as the tissue folds during closure.

Einstein et al. [76],Einstein et al. [96],Einstein et al. [97] and Kunzelman and et al. [98]

The effect of haemodynamic loading and tissue dysfunction on the mitral valve component of the first heart sound have been examined in a family of models [76, 96, 97, 98]. Updating earlier linear elastic models, these models are implemented in the finite element solver LS–DYNA and include both non–linear anisotropic material models. Uniquely these models also include the predicted acoustic radiation, linking the function of the valve to the generation of the first heart sound in both normal and dysfunctional states. As such these model are the only fluid–structure interaction models of the native mitral valve reported within the literature. The results of the two studies detailed here have are also contained in the reviews by Einstein et al. [97] and Kunzelman and et al. [98].

The first model in these series examines the effect of haemodynamic loading on the acoustic radiation, varying the amplitude (p_{max}) and the time derivative (dp/dt) of the transvalvular load [76]. Based upon a valve geometry described in previous studies this model is also symmetrical along the anteropostero axis, a factor which simplifies and reduces the computational time required (Figure 1.22). Defined as a non–linear elastic structure, the leaflets have been discretised using shell elements which have been defined as an anisotropic non–linear hyperelastic membrane governed by a continuous fibre distribution. The localised leaflet thickness and collagen fibre direction have been defined from experimental data. In order to perform fluid–structure interaction, it is required for the valve model to be immersed in a fluid domain, which has been defined here as a cuboid surrounding the valve complex (Figure 1.22). Coupling of the valve geometry to the resulting fluid flow was performed using a constrained acceleration and velocity method. The key parameters of this model are listed in Table 1.11.

In this model valve closure has been simulated by applying experimental measurements of the haemodynamic pressure to the atrial and ventricular portions of the fluid domains over a period of 150 ms. The simulated flow rates and regurgitant volumes of the base model are in agreement with *in vitro* experimental data from a left heart simulator. In order to assess the effect of different haemodynamics loads on the acoustic radiation, the maximum amplitude of the pressure and the time derivative have been scaled and the difference in acoustic pressure assessed. The acoustic radiation has been evaluated by sampling of the simulated pressure above the valve and from the normal velocity of the belly region of the anterior and posterior leaflets. In close proximity to the source the acoustic radiation from the velocity and the pressure are in phase, thus the sampling of the two leaflets will show how each contributes of the first heart sound. The results of these simulations show that the amplitude to the acoustic radiation is linear with both increases in amplitude and time derivative of the pressure. However the frequency of the radiation was shown to be non–linear with respect to both amplitude and the time derivative, increasing steeply then stabilising. This behaviour is attributed to the material properties of the leaflets which stiffen more rapidly with increases time derivatives, reducing the deformation and thus the acoustic radiation. From assessing the normal velocity of the two leaflets, it is shown majority of the acoustic power generated in these cases are from the anterior leaflet. However once the two leaflet coapt the points of maximum acoustic radiation shift to the commissural areas.

The model described above has also been used to examine the effect of microstructural variation in the leaflets upon valve function, mimicking dysfunctional changes in leaflet structure linked to degeneration [96]. Using the same continuous material model described previously, the effect on valve function

Table 1.11: Structural and fluid properties used in Einstein et al. [76].

Variable	Value
Structural density [kg mm^{-3}]	1.04×10^{-6}
Structural bulk modulus [kPa]	2.5×10^{4}
Fluid density [kg mm^{-3}]	1×10^{-6}
Fluid dynamic viscosity [kg mm^{-1} s]	0.045
Fluid bulk modulus [kPa]	2.5×10^{4}

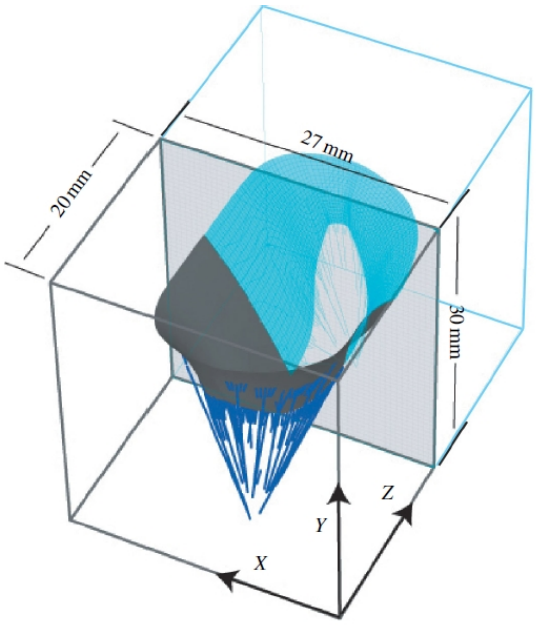

Figure 1.22: 3D geometry of the fluid structure interaction model of Kunzelman and et al. [98].

from independent variation in the fibre volume fraction, fibre stiffness, fibre splay and matrix stiffness have been assessed. Fitting the reference material model to biaxial stress–strain data, these parameters have been perturbed independently and the effect on regurgitant flow, coaptation time, leaflet stress and accoustic radiation have been assessed. As before, valve closure has been simulated from applying the haemodynamic load to the fluid volume and the resulting flow has been coupling to the structure of the valve.

Changes in the microstructure that maintain the anisotropy of the leaflet do not impact upon the function of the valve. However changes that affect the anisotropy of the leaflets have a significant affect upon the function of the valve, causing regurgitation of the blood and tenting of the leaflets during closure. Increasing isotropic matrix stiffness was found to increase coaptation time, such that at large values the valve was unable to close and the valve was regurgitant. Reduction in the acoustic radiation peak frequency was also observed with increasing matrix stiffness. Changes in the volume fraction of the collagen were found not to alter the flow rates significantly, with regurgitant volumes decreasing and increasing in response to increasing and decreasing volume fractions. The peak stresses were found to increase with increasing volume fraction and to decrease with decreasing volume fraction, however the stress distribution exhibited in both cases were similar to the normal model. When considering the two leaflets combined, the acoustic radiation peak frequency was shown to decrease; however when each leaflet was analysed individually it was found that both increases and decreases in the the volume fraction decreased the individual acoustic radiation peak frequency. Changes in the collagen fibre stiffness did not change transmitral flow rates significantly, however the peak principle stresses were increased and decreased with increasing and decreasing fibre stiffness respectively. These changes did not affect coaptation of the valve, however the peak frequency of the acoustic radiation was found to vary non–linearly with increasing fibre stiffness; at low values of stiffness the increase in peak frequency was found

to rise rapidly, flattening at higher values of stiffness. Variation in the degree of fibre splay caused pronounced changes in the peak stress, with increases in the splay of the collagen fibres leading to a more uniform distribution of stress in the bellies of the two leaflets. Conversely, decreases in the degree of splay increased the peak stress significantly with the peak stresses shifted to the strut chordae and the free margins of the leaflets. Decreases in the splay also resulted in transmitral regurgitation of the flow and billowing of the leaflets during closure of the leaflets. The peak acoustic frequencies were found to increase in the posterior leaflet with increase splay, however the peak frequencies in the anterior leaflet and acoustic pressure decreased in cases of increased and decreased fibre splay.

1.5.4 Surgical applications

Models of the mitral valve have also been used to simulate surgical techniques in order to understand the functional changes between a dysfunctional and repaired valve.

Chordal replacement

The functional effect on the stress state of the valve in the case of chordal rupture where a native chordae is replaced with a stiffer artificial substitute has been addressed in a series of finite element studies [99, 100, 101]. Described using shell elements and the same linear elastic anisotropic material model as described previously in Section 1.5.3, closure of the mitral valve has been performed using the structural solver ANSYS. Simulations of the normal valve have been compared to a dysfunctional and repaired states, where several chordae have been first removed then replaced with stiffer substitutes. The results of these simulations show that in the dysfunctional state of chordal rupture the principal stresses are comparable to the normal state, however the posterior leaflet is displaced further towards the annulus than in normal states. Replacement of the chordae with a stiffer artificial substitutes restores the magnitude of the principal stress to the normal state however stress concentrations are induced at the location of the chordae due to a mismatch in stiffness. These localised peaks have been shown to be minimised by increasing the number of artificial replacements.

Annuloplasty

The functional effect annuloplasty on the stress state of the valve in cases where annular dilation requires the implantation of an annular ring has been examined in independent numerical studies [88, 102]. Using an anisotropic linear elastic model, the effect of ring annuloplasty on the dynamics of a valve with a dilated mitral annulus have been simulated in a structural only model [88]. As annuloplasty directly affects the motion generated from the structural contraction of the heart, the motion of the annulus has been prescribed in this model using a linear time dependent force on the posterior segment of the annulus. Implemented using the structural solver ANSYS, closure of the valve has been simulated with both rigid and flexible ring annuloplasty have been performed with the results compared against a simulation of an uncorrected dilated valve. The application of the flexible ring was found to return stresses and the dynamics of closure closer to the levels of the normal scenario than the rigid annuloplasty ring.

In a separate study based upon earlier anisotropic linear elastic models, the functional effect of two different designs of annuloplasty ring have been examined [102]. Implemented in the structural solver ABAQUS using shell elements, this model utilises the same valve geometry as previous versions but includes updated definitions for the anisotropic material properties of the two leaflets. In order to simulate correction of dysfunction, the model was first put into a dysfunctional state by displacing the papillary muscles by 1/3/5 mm away from the annular plane. Simulated application of planar and non–planar annuloplasty rings was then performed by displacing the annulus to conform with the ring profile. In order to assess the difference between different size mitral valve orifices, three different diam-

eter annuloplasty rings and valve geometries have been assessed. From comparisons of the regurgitant areas in each model it was found that both rings reduced the value of the regurgitant area, with the non–planar annuloplasty ring reducing the size of the area more than the planar ring in all three sizes. Another measure of the effectiveness, the length of leaflet coaptation at the free margin, was found to increase with the non–planar ring. However the value of peak stress was found to be higher in the non–planar ring at large values of papillary muscle displacement (5 mm), at the lower values (1 mm and 3 mm) the induced stresses were similar in magnitude.

Percutaneous balloon inflation

The functional effect upon the mitral valve from the dynamic effect of percutaneous balloon inflation in stenosed mitral valves has been examined in single and double balloon configurations in a numerical model by Schievano et al. [103]. Geometrically derived from the fluid–structure interaction model by Einstein et al. [76], this model has been implemented in the structural–only solver of LS–DYNA. The leaflets of the valve have been modelled as a linearly elastic anisotropic material which interact with a single/double balloon object which is inflated and presses against the valve structure (Table 1.12). The results of this model have shown that the double balloon method imparts a more uniform stress distribution on the valve during deployment compared to a single balloon, which is less likely to damage the leaflets of the mitral valve.

Table 1.12: Linear orthotropic structural properties used in Schievano et al. [103]. Labels: E_x – elastic modulus in the fibre direction and E_y – elastic modulus in the off–fibre direction.

Leaflet	Anterior	Posterior
E_x [MPa]	6.233	2.080
E_y [MPa]	2.350	1.887
Poison ratio [–]	0.45	0.45
Shear modulus [MPa]	1.369	0.694
Density [kg·mm^{-3}]	10.4×10^{-6}	10.4×10^{-6}

Edge–to–edge repair

The functional effect of the edge–to–edge surgical repair, a technique which used to correct regurgitant valves, has been examined independently in several different models [95, 104, 105]. Correction of prolapse is accomplished by directly connecting the prolapsing leaflets together with a suture, therefore minimising the intersegment distance during opening which ensures improved copatation during closure (Figure 1.23). However as this restricts the valve during opening and reduces the effective/geometric orifice areas, this repair alters the stress of the valve during diastole. The models listed here are all structural–only models and as such there are no fluid–structure interaction of the edge–to–edge repair.

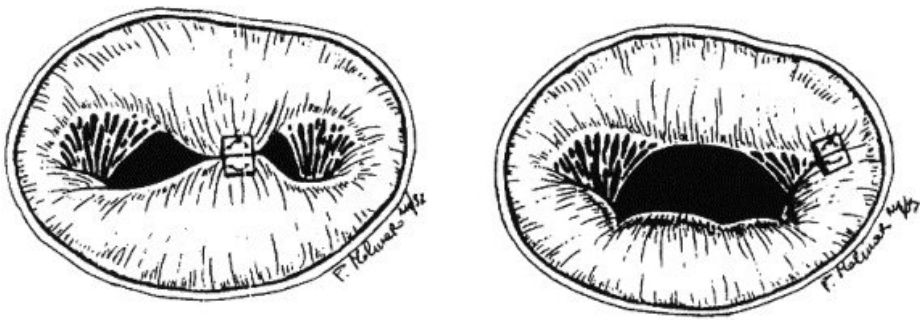

(a) Double orifice. **(b)** Single orifice.

Figure 1.23: Illustration of the the edge–to–edge repair technique, with a (a) double and (b) single orifice. Image after Dal Pan et al. [104]

The first study of this surgical correction modelled the effect of the suture has been by constraining several nodes to act in synchrony, effectively joining the nodes together [95]. Implemented in the structural solver ABAQUS, the leaflets have been discretised using shell elements defined with anisotropic linear elastic properties. The effect of the edge–to–edge has been examined by varying the suture length in a family of models with different levels of annular dilation. Systole and diastole have been simulated by applying of a uniform transvalvular pressure of 120 mmHg and 15 mmHg respectively. The results of the simulations (without the valve correction) showed that under the application of the systolic pressure the valve was not able to close, however this was attributed to the linear elastic properties and complex valve geometry. With the application of the surgical suture to the model it was found that the principal stresses at systole did not differ significantly from correct to uncorrected model. However during diastole the peak principal stresses in the corrected model were found to be similar in magnitude to the uncorrected model in systole, which essentially double the frequency of systolic loading during each cardiac cycle.

More recently non–linear hyperelastic models of the edge–to–edge repair technique have been reported [104, 105]. Using a hyperelastic non–linear material model, the effect of the lateral suture positioning, length of the suture and severity of annular dilation have been examined. Both models have been implemented in the structural solver ABAQUS and use shell elements defined with an isotropic Mooney–Rivlin material model which has been fitted to the myxomatous mitral valve biomechanical data. These models have been defined with the leaflet in a semi–closed configuration, with the free margin of the leaflet constrained simulating the effect of a suture. Dysfunctional states have been generated by scaling the dimension of full valve to model annular dilation. Simulation of diastole has been performed in structural–only simulations, with the transvalvular pressure drop derived by Redaelli et al. [106] using an orifice area based relationship determined from a fluid–only model of the edge–to–edge repair. Results of these simulations have shown that the lateral positioning and length of the suture both have a positive effect in reducing the magnitude of stress induced. Both models also show that the uncorrected dilation of the annulus in a simulated dysfunctional state result in a higher value of stress during diastole.

1.5.5 Valveless models

The heart valves assist in the pumping of blood in the left ventricle, however all of the models presented in Section 1.5.3 have not addressed the dynamics of ventricular filling. Several different authors have addressed the fluid dynamics of this problem, with the effect of the valves modelled using a variety of different methodologies. The majority of the left ventricular models existing in literature model only the ventricular chamber and have neglected the full, three dimensional, coupled dimensional representation of the valves. The only work, to the the author's knowledge, which has attempted to address this issue are the immersed boundary method models of McQueen and Peskin [107] and McQueen et al. [108]. However the structural models of the valves are simplified by representing the valve as a network of fibres and not a continuous material. These techniques are also not able to handle self–contact conditions and thus are limited to diastole only. A review of this area of research is outside the scope of this work, however one example of this field has been selected in order to summarise efforts in fluid–only modelling of the the mitral valve and its role in ventricular filling.

Using a fluid–only model, the fluid dynamics in the ventricular chamber during the cardiac cycle have been modelled in order to examine the dynamic of filling into a expanding volume [109]. Volumetric changes in the ventricular chamber have been modelled by prescribed displacements of the boundary positions determined from *in vivo* measurements from a human subject with the mapped mesh of the ventricle expanding and contracting as required. Using a non–Newtonian description of the fluid viscosity to represent the properties of blood, the numerical solution of the Navier–Stokes equations of fluid motion have been resolved on a moving mesh using the arbitrary Lagrangian–Euler method in

the computation fluid dynamics code Star–CD. The valves have been modelled as two–dimensional orifices at the inlet and outlet of the model, opening and closing of the valves was modelled by variation of the effective orifice area throughout the simulation. In order to better represent the fluid interaction of the valve, an intermediate area around the orifice centre was defined where the resistance to flow was non–zero (see Figure 1.24). The value of this non–zero pressure drop was selected by comparison of the numerical values of the flow rate to experimental measured values at both the aortic and mitral positions. The effect of the leaflets of the mitral valve on the flow have been neglected, with the anterior leaflet in particular assisting the directionality of the fluid flow before entering the left ventricular outflow tract, a fact acknowledged by the authors themselves. Analysis of the numerical results have shown that the model presents with flow rotation and velocities similar to those measured *in vivo* for the purpose of this study.

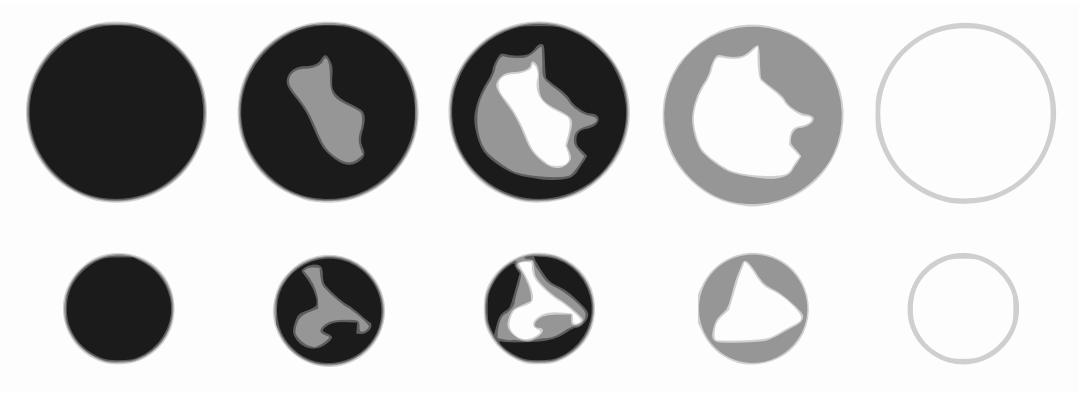

Figure 1.24: Two dimensional representation of the aortic and mitral valves in the model of Schenkel et al. [109]. The black areas represents a no flow boundary, the grey a transition pressure drop (defined by the authors) and the white a zero pressure drop.

Chapter 2

Mitral Valve Model

Contained within this chapter is an in–depth review of the methods used to model valve function in the proceeding chapters. Although sharing common features, the exact details of the model in each chapter have been tailored towards the specific aim of the chapter itself. These three models are referred to as:

(1) Isotropic – Introduced in Chapter 3, the aim of this model was to examine the effect of haemodynamic loading differing fluid volumes and also between structural–only and fluid–structure interaction methods. For this reason the material properties of the valve have been simplified and represented as isotropic and linearly elastic.

(2) Orthotropic – Introduced in Chapter 4, the aim of this model was to examine the effect of a corrective surgical procedure on valvular stress state and the corresponding fluid dynamics. For this reason the material properties of the valve leaflets was updated to an orthotropic material definition.

(3) Hyperelastic – Introduced in Chapter 5, the aim of this model was to examine changes in the microstructure of the valve in response in scenarios of remodelling and growth. For this reason the material model of the valve leaflets was updated to a hyperelastic fibre based definition.

Divided between structural and fluid aspects of the mitral valve model, this chapter begins with a comparison of the main differences in terms of the the valve geometry (Section 2.1) and material definitions of the leaflet and chordae (Sections 2.3.1 and 2.3.2). Following this is a comparison of the different fluid geometries (Section 2.2.1) and the material model used to represent the fluid (Section 2.3.3) Also included are details of the different aspects used in the numerical simulation of the structural dynamics (Section 2.4.1) and fluid dynamics (Section 2.4.2).

2.1 Valve model geometry

As in reality, the models presented here all contain the four different subcomponents of the mitral valve, the geometry of which are based upon a mixture of *in vivo* and *ex vivo* measurements reported within the literature. In this section the differences between the three models are compared against each other.

2.1.1 Annulus

Although the annulus is a dynamic substructure of the valve, here the geometrical form of the annulus has been constricted to a fixed planar geometry in order to reduce the numerical complexity of the problem. The profile of the annulus has been defined as D–shaped orifice, which was selected to represent the configuration of the valve during systole (Figure 2.1). This profile has been used in the isotropic, orthotropic and hyperelastic models.

Since the annulus is fixed, as in the case of annuloplasty, the ratio of the anteroposterior and commissural diameters has been based upon the design of the "Carpentier–Edwards Physio Annuloplasty Ring"[1]. Reported as 4:3, here the commissural and anteroposterior diameters are defined as 30.0 mm and 22.5 mm respectively. The resulting annular perimeter and area are measured as 86.7 mm and 554 mm^2 respectively, with the enclosed annular area in agreement with the reported range at systole (Table 1.7).

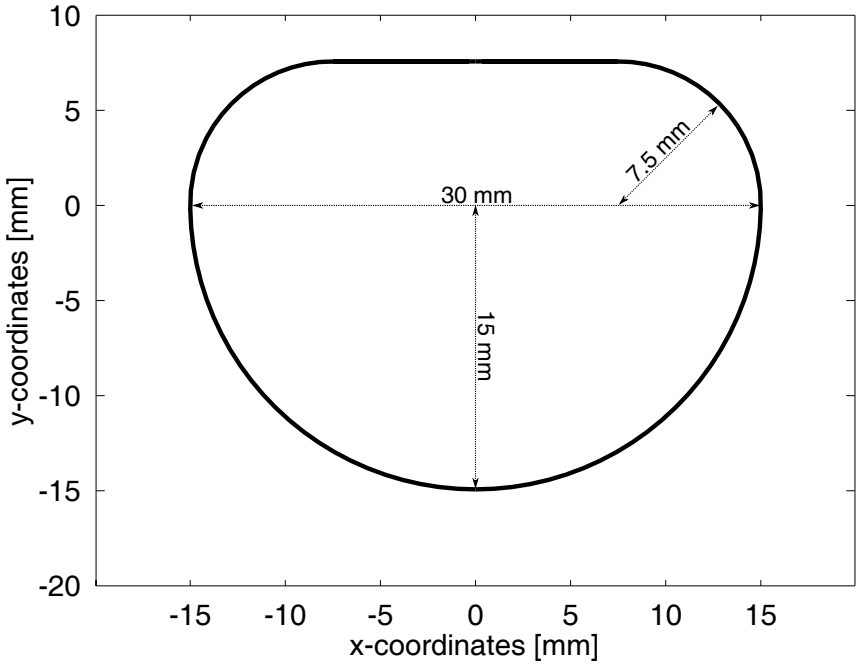

Figure 2.1: Planar profile of the valve annulus which is defined as symmetrical in the anteropostero axis. The anteropostero and commissural diameters are defined as 22.5 and 30.0 mm respectively.

2.1.2 Leaflet profile

In all three models the leaflets have been modelled as a continuous band of tissue that extends outwards from the annulus. Attachment to the annulus is divided into anterior and posterior segments scaled from anatomical measurements to the model annulus described in the previous section [19, 11]. However the three models differ in the profile used to represent the leaflets, as the meshes generated from the resultant geometries were found to be unstable when applied to more advanced material models (see Section 2.1.5). Here the different leaflet profiles used in the isotropic, orthotropic and hyperelastic models are presented as shown in Figure 2.2.

Isotropic model

In the isotropic model the leaflets have been represented using a scalloped profile for the anterior, posterior and commissural regions (Figure 2.2). Using the anteropostero/symmetry axis as the geometric reference point, the annular extent of the individual cusps are defined using the same annular proportions as the human anatomical data reported by Sakai et al. [19]. The peak of each cusp is defined by its maximal height at the centre of its annular portion which is also taken from the anatomical data, also reported by Sakai et al. [19]. The undulating free margin of the leaflet profile is then define by fitting a B–spline through these points. Using this B–spline curve and the annular profile, the surface area of the leaflets is formed from fitting a Coons patch to the region contained between these two lines (Figure 2.3). The total leaflet areas is measured as 936 mm^2 with the anterior and posterior contributing 444 and 492 mm^2 respectively (Table 2.1).

[1] http://ht.edwards.com/resourcegallery/products/rings/pdfs/2188update.pdf

Orthotropic model

In the orthotropic model the leaflet profile has been simplified by combining the commissural cusps with the closest posterior cusp (Figure 2.2). As in the isotropic model the annular extent of the individual cusps are defined using the same annular proportions as the human anatomical data reported by Sakai et al. [19]. In this model the peak of each cusp is defined by its maximal height at the centre of its annular portion taken from the porcine anatomical data reported by Kunzelman et al. [11]. As previously the undulating free margin of the leaflet profile is defined by fitting a B–spline through these points and the surface area is formed from a Coons patch of the region contained between this line and the annulus (Figure 2.3). The total leaflet areas is measured as 912 mm^2 with the anterior and posterior contributing 414 and 498 mm^2 respectively (Table 2.1).

Hyperelastic

In the hyperelastic model the leaflet profile has been further simplified by representing the multiple cusps of the posterior leaflet as a single cusp (Figure 2.2). Here the annular extent of the anterior and posterior cusps are defined using the same annular proportions as the porcine anatomical data reported by Kunzelman et al. [11]. As in the orthotropic model, the peak of each cusp is defined by its maximal height at the centre of its annular portion taken from the porcine anatomical data reported by Kunzelman et al. [11]. As before, the undulating free margin of the leaflet profile is defined by fitting a B–spline through these points and the surface area is formed from a Coons patch of the region contained between this line and the annulus (Figure 2.3). The total leaflet areas is measured as 872 mm^2 with the anterior and posterior contributing 412 and 460 mm^2 respectively (Table 2.1).

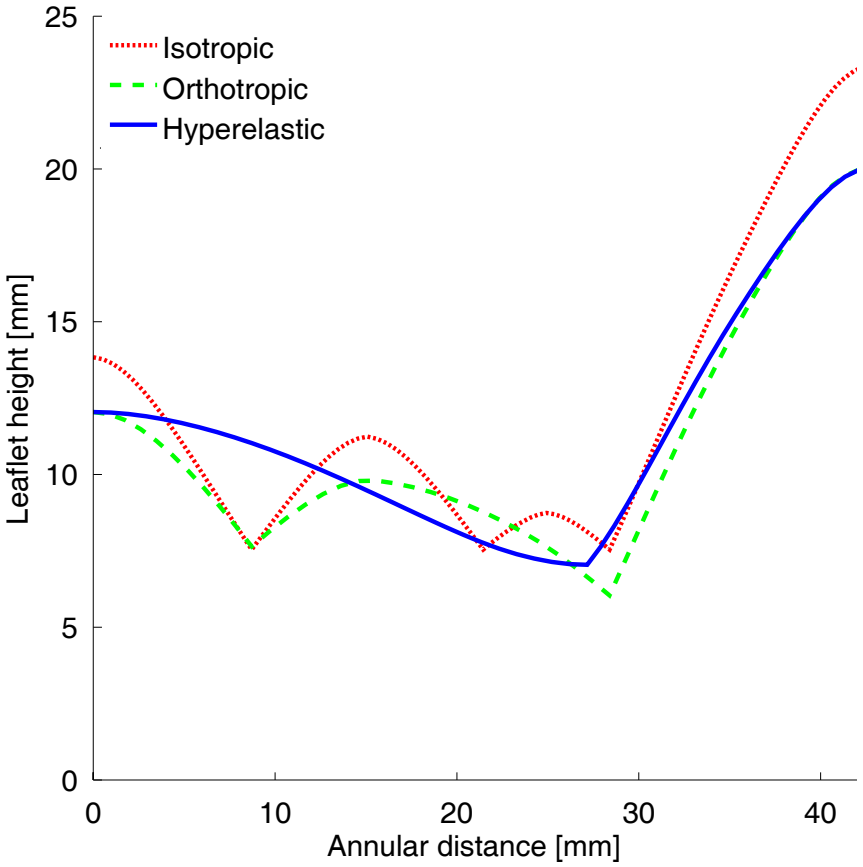

Figure 2.2: Comparison of the isotropic, orthotropic and hyperelastic model leaflet profiles against the circumferential distance from the centre of the posterior leaflet. Note that only half the leaflet profile is shown here as the profile is symmetrical.

Figure 2.3: Three–dimensional comparison of the isotropic, orthotropic and hyperelastic models. As the models are all symmetrical, only half the geometry in each model is shown.

Table 2.1: Comparison of the leaflet areas in the isotropic, orthotropic and hyperelastic models. Note that in the isotropic model the commissural areas are included in the posterior areas.

	Leaflet areas [mm^2]		
Model	Anterior	Posterior	Total
Isotropic	444	492	936
Orthotropic	414	498	912
Hyperelastic	412	460	872

2.1.3 Chordae tendineae

In the different models a variety of different chordal arrangements have been used to support the valve during closure, the chordae used in each model are listed in Table 2.2. The configuration of the chordae tendineae network has been defined to allow proper coaptation under physiological conditions and to also minimise numerical instabilities generated by distortion of the mesh. In all models the geometry of the chordae branches before attaching to the leaflet surface, at each bifurcations the current area of each chordae is conserved over the number of branches such that $A_{\text{postbranch}} = A_{\text{prebranch}}/N$ where N is the number of divisions.

Table 2.2: Comparison of the different chordal classes in the isotropic, orthotropic and hyperelastic models

	Chordal class		
Model	Marginal	Basal	Strut
Isotropic	☑	☐	☐
Orthotropic	☑	☑	☐
Hyperelastic	☑	☑	☑

Isotropic model

In the isotropic model only the marginal chordae, which support the free margins of the leaflets, have been represented (Figure 2.4). The structures emit from the papillary muscle node and subsequently branch out as they approach the free margin of the leaflets where they ultimately attach to the leaflet. The chordae have been distributed equally in order to support the leaflets in closure and to prevent mesh instabilities.

Orthotropic model

In the orthotropic model the marginal chordae have been supplemented with the basal chordae, as both the free margins and the basal regions of the leaflets are supported (Figure 2.4). As before the chordae emit from the papillary muscle after which they split and branch before connecting the surface of the leaflets. The chordae have been distributed equally in order to support the leaflets in closure and to prevent mesh instabilities.

Hyperelastic model

In the hyperelastic model, in conjunction with the marginal and basal chordae, the valve is supported by the strut chordae which is inserted into the centre of the anterior leaflet (Figure 2.4). As in both the isotropic and orthotropic models, the chordae emit from the papillary muscle and split before connecting with the leaflet surface. The chordae have been distributed equally to support the leaflets and to prevent mesh instabilities, with the exception of the strut chordae which is a singular structure.

2.1.4 Papillary muscle

In all three models the structure of the papillary muscles have been represented as a single tip, to which the chordae are attached to (Figure 2.4). These tips have been modelled as static, as *in vivo* measure-

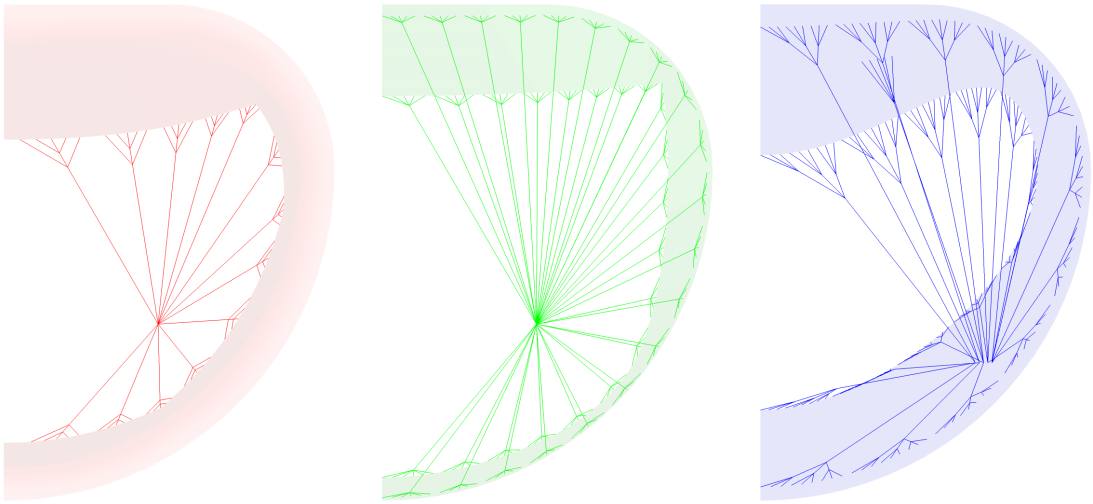

Figure 2.4: Comparison of the chordal attachments in the isotropic, orthotropic and hyperelastic models as viewed from the ventricular side of the valve. The chordae are shown to initiate at the papillary muscle tip, before branching and subsequently inserting into the leaflet surface. Here the leaflets have been illustrated as translucent in order to aid visualisation of the chordae. Note that only half the model is shown here as the geometry is symmetrical.

ments indicate that the distance between the tip and the annular plane remains constant throughout the cardiac cycle. As the model is symmetrical, the location of the papillary muscle tip is mirrored in the anteropostero plane.

Isotropic model

The location of the papillary muscle tips in the isotropic model has been defined using the measurements reported by Sakai et al. [19]. Using the distances relative to the left and right fibrous trigones on the annulus, the location of the papillary muscle tip has been defined as 22 mm above the plane of the annulus. The lateral position of the papillary muscle has been adjusted in order to ensure correct coaptation and to minimise numerical instabilities during closure.

Orthotropic model

The location of the papillary muscle tip in the orthotropic model has been defined in the same manner as the isotropic model. However the vertical height of the papillary muscle tip has been reduced to 20 mm in correspondence with the reduction in leaflet height (Section 2.1.2). This value corresponds to measurements reported *in vivo* from normal porcine samples [110].

Hyperelastic model

The distance between the muscle tips in the hyperelastic model has been defined using *in vivo* measurements from normal porcine subjects reported by Jensen et al. [110]. This interpapillary distance has been scaled relative to the commissural diameter using the *in vivo* measurements in which the distance between the papillary muscles is measured as 23±1 mm, with a commissural diameter of 33±1 mm. Using a ratio of 0.7, the interpapillary distance has been defined ranging from 19.5 mm to 21.0 mm. The vertical height of the papillary muscle tips has been set as 20 mm, following the same set of *in vivo* measurements. The positioning in the anteroposterior direction was adjusted in order to ensure correct coaptation and minimise numerical instability during closure.

2.1.5 Finite element meshes

In order to solve the equations of motion, the geometry of the valve must be first discretised into a suitable mesh of elements and nodes. Here the leaflets have been discretised using a structured approach, dividing the surface area into a series of 4–node rectangular elements (Figure 2.5). Defined as a three–dimensional line, here the chordae tendineae have been discretised using 2–node beam elements. All the meshes described in this work have been prepared using the software package ANSYS Release 11.0.

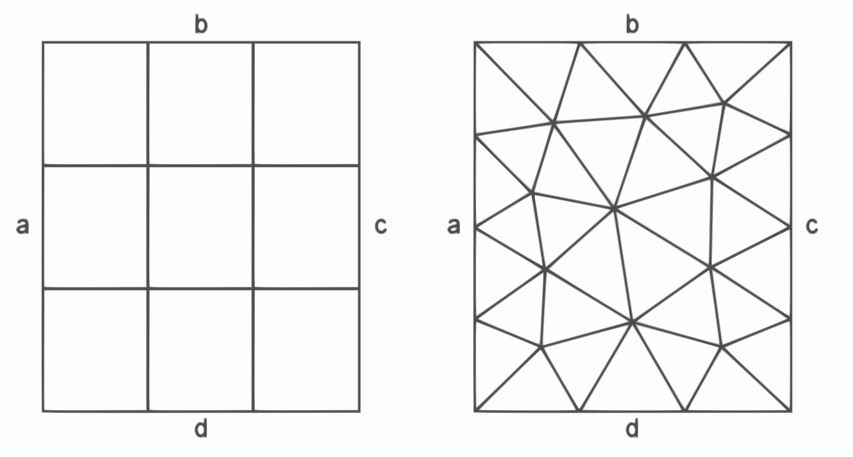

Figure 2.5: Comparison of structured and unstructured approaches to meshing. Here the element size parameter selected is the same, in the structured approach the area is defined as a quadrilateral and the opposing line segments (a/c and b/d) are defined with equal number of divisions and the elements are formed from the resulting line intersections. In an unstructured approach the area is divided into many triangular elements which satisfy the sizing parameter, as shown here the edges a and c contain a different number of divisions when compared to the structured case.

Isotropic model

In the isotropic model the leaflets are represented using 2688 shell elements in total, with 896 in the anterior leaflet and 1792 in the posterior/commissural leaflets (Figure 2.6). The marginal chordae are represented using 333 beam elements in total.

Orthotropic model

In the orthotropic model the leaflets are represented using 4000 shell elements in total, with 1600 in the anterior leaflet and 2400 in the posterior/commissural leaflets. Updated with an orthotropic material model, it was found that the previous isotropic mesh was no longer adequate as numerical instabilities were generated when using this mesh. By reducing the elemental skew at the commissural regions of the leaflets, these instabilities were stabilised (Figure 2.6). In total the chordae are represented using 1663 beam elements with 670 marginal and 993 basal chordal elements.

Hyperelastic model

In the hyperelastic model the leaflets are represented using 3920 shell elements in total, with 1680 in the anterior leaflet and 2240 in the posterior/commissural leaflets. As with the orthotropic model it was required to further reduce the elemental skew at the leaflet junction between the anterior and posterior leaflets (Figure 2.6). In this model the chordae have been represented using 292 beam elements with 143 marginal, 143 basal and 6 strut chordal elements. The number of beam elements is significantly smaller in the third generation model as the mesh used to define the chordae has been simplified. In the isotropic and orthotropic models the chordae have been defined using multiple elements, whereas

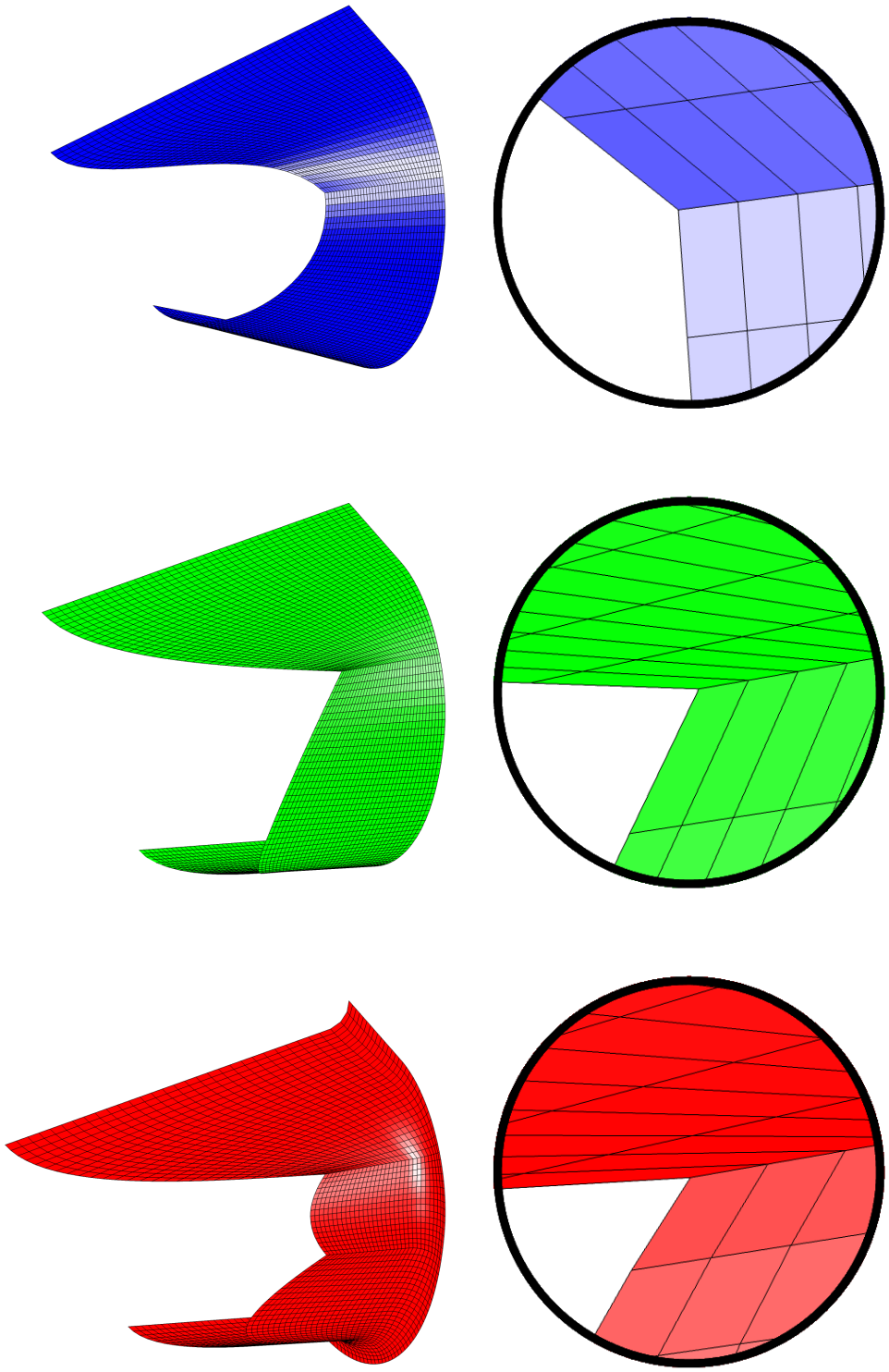

Figure 2.6: Comparison of the isotropic, orthotropic and **blue**hyperelastic model meshes and the elemental skew in the commissural regions.

in the hyperelastic model this has been simplified to a single beam up to the point where the chordae branch.

2.2 Fluid domain model

2.2.1 Geometry

In order to simulate the haemodynamic environment of the valve, it is required to immerse the valve in a suitable fluid volume. Here the geometrical details of the different fluid volumes used in this work are described.

2.2.1.1 Isotropic model

Used to assess the geometric effect upon diastolic filling and systolic closure, the isotropic model contains both a tubular and a ventricular shaped fluid volume (Figure 2.7). These volumes have been sized based upon the total volume of the heart, 120 ml. The size of the ventricle has been taken as the average between diastole and systole, 85 ml. The atrium forms the remaining 35 ml. The only difference between the tubular and ventricular models is the aortic outflow.

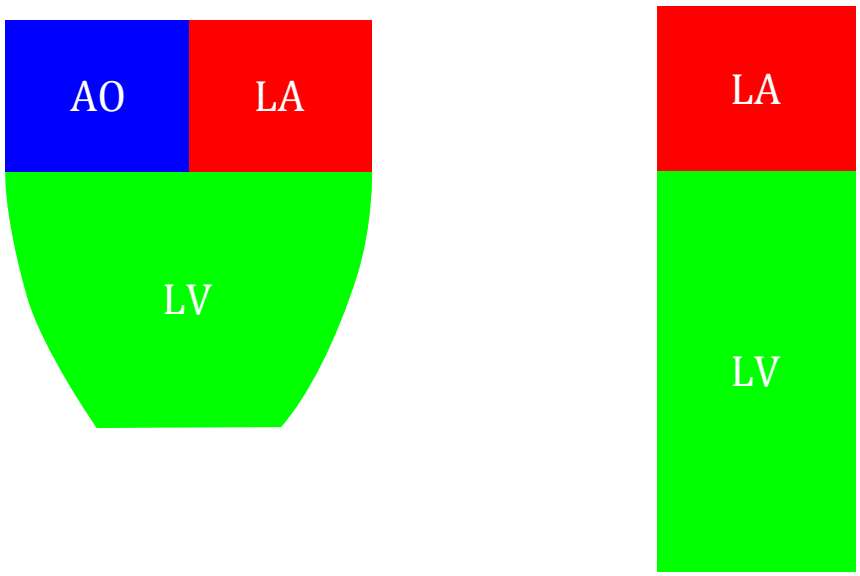

Figure 2.7: Comparison of the ventricular and tubular fluid volumes used in the isotropic model. Label: LA – left atrium, LV – left ventricle and AO – aortic outflow.

2.2.1.2 Orthotropic models

In the orthotropic model two different model geometries have been used with the linear and non–linear variants of the valve model.

Linear

Used in the analysis of steady flow conditions, the fluid volume used in the linear orthotropic model is a semi–infinite chamber (Figure 2.8). The dimensions of the ventricular outflow section have been defined by using an accompanying valveless computation fluid dynamic simulation. Here the outflow width has been defined from the point at which the ratio of the velocity magnitude to the maximum fluid velocity was reduced to less than 1% (results not shown). As in the isotropic model, the left atrium has been sized as 35 ml.

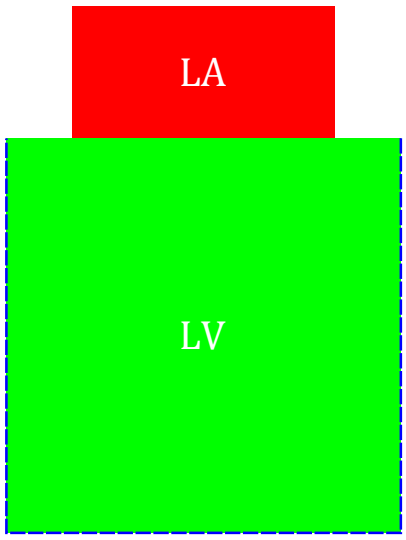

Figure 2.8: Semi–infinite fluid volumes used in the linear orthoropic model. Here the infinite boundaries are marked with a blue broken line. Label: LA – left atrium and LV – left ventricle.

Non–linear

Used in the analysis of diastolic filling, the fluid volume used in the non–linear orthotropic model has been defined as a ventricular shaped fluid volume (Figure 2.9). Using the same sizing principals as the isotropic model (left ventricle = 85 ml, left atrium = 35 ml), here the fluid volume has been modified to reduce the level of element skew in order to maximise the element size, and therefore the maximum permitted time step (see Equation 2.23).

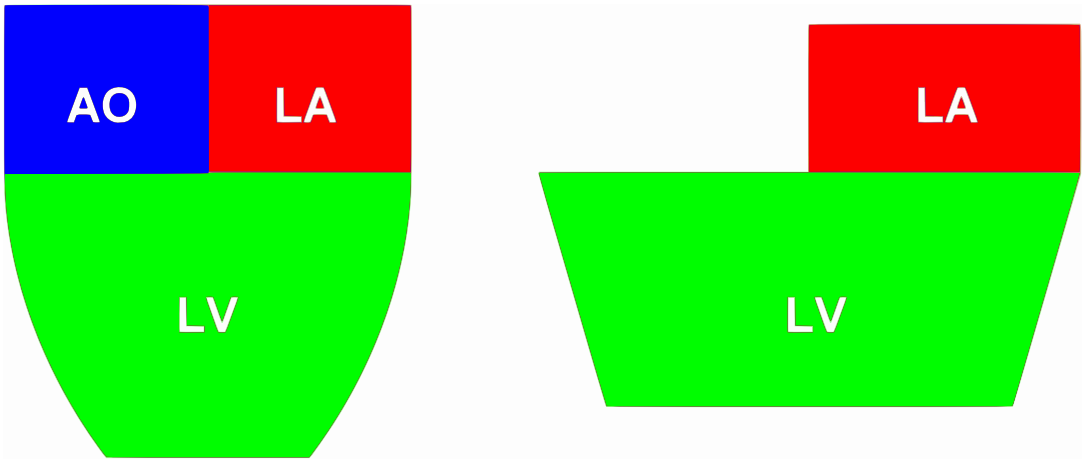

Figure 2.9: Comparison of the ventricular fluid volumes used in the isotropic (left) and orthotropic non–linear (right) models. Label: LA – left atrium, LV – left ventricle and AO – aortic outflow.

2.2.2 Finite element meshes

All the fluid meshes have been created using a structured meshing method (see Figure 2.5 for the two–dimensional analogue). This is a requirement of the fluid dynamic solver used in LS–DYNA (see Section 2.4.2.1)

Isotropic model

The tubular and ventricular volumes contain of 81,920 and 43,008 solid elements respectively (Figure 2.10). These element density of these models has been determined by dividing each solid element into eight further elements (similar to the shell element division in Figure 2.19). The mesh density has been

assessed by applying a velocity boundary condition to the inlet of each model equal to 1 m·s^{-1}. The subsequent variation in velocity across the valve plane (without the valve) has been measured and the mesh deemed sufficiently refined when the difference between the maximum magnitude of the fluid velocity became less than 5%. Note that the orifice has been embedded into the mesh design.

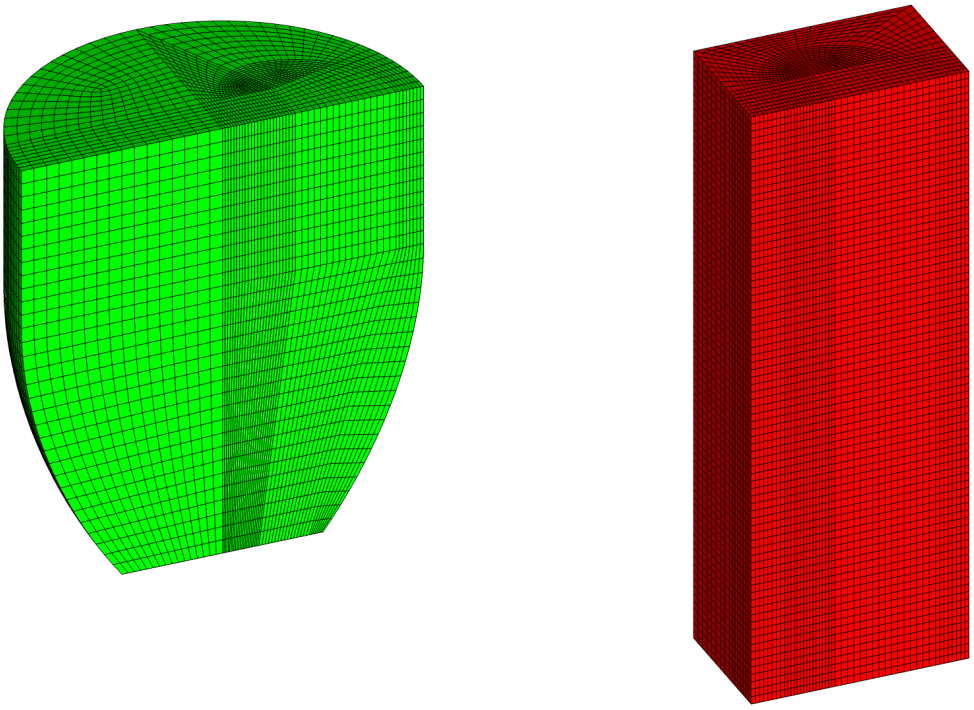

Figure 2.10: Comparison of the ventricular and tubular isotropic model fluid meshes.

Orthotropic model

The fluid mesh used in the linear orthotropic model consist of 23,200 solid elements (Figure 2.11). Using the mesh density increasing approach described above, the mesh density has been assessed by applying a velocity boundary condition to the inlet equal to 1 m·s^{-1}. As in the previous isotropic model, the variation in velocity across the valve plane (without the valve) has been measured and the mesh deemed sufficiently refined when the difference between the maximum magnitude of the fluid velocity became less than 5%.

The non–linear orthotropic model geometry described previously has been meshed in two separate approaches, defining a normal and dysfunctional state of the valve (see Section 4.3.4, Page 111). However the geometry/volume remains constant in both cases, here only the normal meshed volume has been presented (Figure 2.11). The normal and dysfunctional fluid volumes consisted of 20,430 and 30,618 solid elements respectively. Using the approach described above, the mesh density has been assessed by applying a pressure boundary condition corresponding to the maximum value sustained during diastole (∼1 kPa).

2.3 Material models

2.3.1 Leaflet material models

In this section the different material models used to represent the leaflets in the isotropic, orthotropic and hyperelastic models are described in further detail. Defined with linear and non–linear elastic moduli, a mixture of standard and custom material models have been implemented in the finite element solver LS–DYNA (Table 2.3).

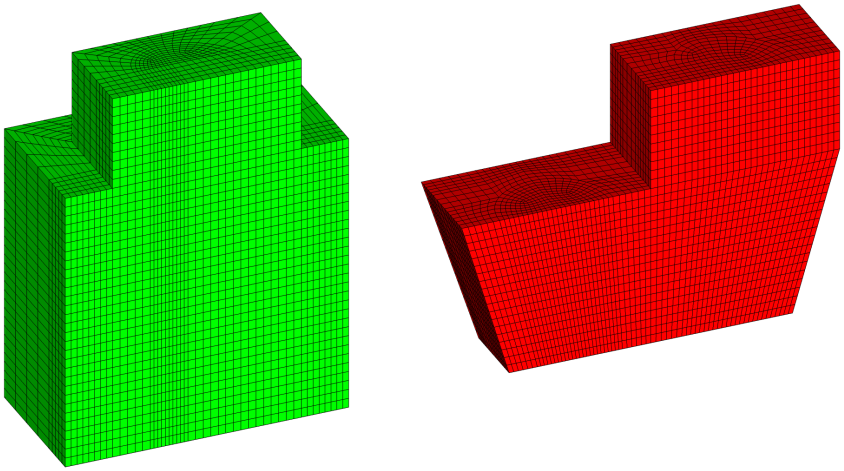

Figure 2.11: Comparison of the linear (left) and non–linear (right) orthotropic fluid volumes. Here only the normal non–linear orthotropic fluid mesh has been visualised, for the dysfunction fluid mesh refer to Figure 4.7 on Page 113.

Table 2.3: Comparison of the key features of the different material models used to represent the leaflets.

Model	Linear	Non–linear	Standard	Custom
Isotropic	☑	☐	☑	☐
Orthotropic	☐	☑	☑	☐
Hyperelastic	☐	☑	☐	☑

2.3.1.1 Isotropic model

In the isotropic model the leaflets have been defined as isotropic and linearly elastic. As the focus of this model was to determine the difference between structural–only and fluid–structure interaction approaches, it was chosen to approximate the material behaviour of the leaflets with the simplest possible material model. This has been implemented within LS–DYNA using the standard material model `MAT_ELASTIC` in conjunction with the Belytschko–Lin–Tsay finite element shell with three integration points in the thickness direction (Table 2.4) [79, 80].

Table 2.4: Material parameters for the isotropic model. Labels: E – elastic modulus, ν – Poisson's ratio and t – shell thickness.

	Leaflet	
Variable	Anterior	Posterior
E [MPa]	3.0	3.0
ν [–]	0.45	0.45
t [mm]	0.75	0.75

2.3.1.2 Orthotropic model

In the orthotropic model the leaflets have been defined orthotropic with both linear and non–linear material properties. As the focus of this model was to determine the effect of a fluid load upon the mitral valve in a corrected state, it was required to use a more advanced material model to represent the leaflets than the isotropic model described previously.

Linear

The linear orthotropic material model has been implemented in LS–DYNA using the standard material model `MAT_ORTHOTROPIC_ELASTIC` in conjunction with the Hughes–Liu finite element shell, defined with a single integration point in the thickness direction. The in–plane (x/y) properties of the leaflets

have been defined from a previously reported finite element study reported by Votta et al. [102]. Although the out–of–plane (z) response is uncoupled from the in–plane (x/y) response of the material, the elastic and shear moduli in the out–of–plane direction are still required in this material model. Used in the calculation of the contact force calculation with both the structure and the fluid, this value has been defined in conjunction with the contact stiffness to minimise numerical leakage in fluid–structure interaction scenarios (Table 2.5).

Table 2.5: Material parameters for the linear orthotropic model, here the x– and y–directions refer to the circumferential and radial directions respectively. Labels: E_x – circumferential elastic modulus, E_y – radial elastic modulus, E_z – out–of–plane elastic modulus, G_{xy} – circumferential/radial shear modulus, G_{yz} – out–of–plane shear modulus, G_{zx} – out–of–plane shear modulus, ν_{xy} – in–plane Poisson's ratio and t – shell thickness.

	Leaflet	
Variable	Anterior	Posterior
E_x [MPa]	6.2	2.4
E_y [MPa]	2.1	1.8
E_z [MPa]	10.0	10.0
G_{xy} [MPa]	1.4	0.7
G_{yz} [MPa]	1.4	0.7
G_{zx} [MPa]	1.4	0.7
ν_{xy} [–]	0.45	0.45
t [mm]	1	1

Non–linear

The non–linear orthotropic material has been implemented in LS–DYNA using the standard material model `MAT_NONLINEAR_ORTHOTROPIC` in conjunction with the Belytschko–Lin–Tsay finite element shell, defined with a single integration point in the thickness direction. In this material model the non–linear behaviour must be pre–defined by the user, here the in–plane non–linear stress–strain response has been defined using the experimental data reported by May-Newman and Yin [54] (Figure 2.12). Although non–linear in the plane of the material, as in the case of the linear model this material model requires the input of the out–of–plane elastic and shear moduli in order for the contact force calculation. As before in the linear model, these values have been defined in conjunction with the contact stiffness in order to minimise numerical leakage in fluid–structure interaction scenarios (Table 2.6). Based upon a finite–strain formulation, this material model is reported in the user manual as unstable and is not recommended for general use [80, 79].

Table 2.6: Additional parameters of the orthotropic material model, here the x– and y–directions refers to the circumferential and radial directions respectively. Labels: E_x – circumferential elastic modulus, E_y – radial elastic modulus, E_z – out–of–plane elastic modulus, G_{xy} – circumferential/radial shear modulus, G_{yz} – out–of–plane shear modulus, G_{zx} – out–of–plane shear modulus, ν_{xy} – in–plane Poisson's ratio and t – shell thickness.

	Leaflet	
Variable	Anterior	Posterior
E_x [MPa]	17.1	5.6
E_y [MPa]	6.7	3.4
E_z [MPa]	20.0	20.0
G_{xy} [MPa]	1.37	1.37
G_{yz} [MPa]	1.37	1.37
G_{zx} [MPa]	1.37	1.37
ν_{xy} [–]	0.45	0.45
t [mm]	1	1

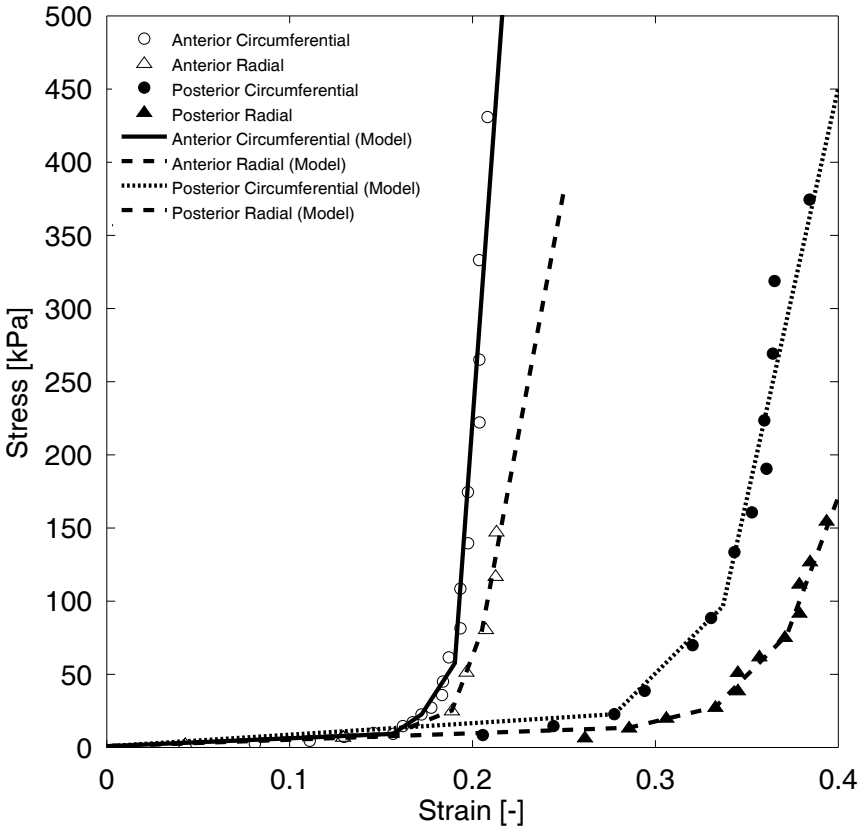

Figure 2.12: Comparison of the stress–strain curves used to define the circumferential and radial elastic moduli in the orthotropic material model. Here the experimental data of May-Newman and Yin [54] is represented using the following figure labels: ○ – anterior circumferential, △ – anterior radial, ● – posterior circumferential and ▲ – posterior radial.

2.3.1.3 Hyperelastic model

In the hyperelastic model the leaflets have been represented using a hyperelastic, anisotropic, non–linear, discrete fibre material model. As the focus of this model was to determine the effect of remodelling and growth upon the dynamics of the valve, it was required to use a material model that included microstructural aspects such as the fibre orientation. Using the strain–energy function described previously in Section 1.4.3, a material model has been implemented in LS–DYNA using a user defined subroutine in conjunction with the co–rotational Hughes–Liu finite element shell, defined with a single integration point in the thickness direction. The numerical implementation of this particular material model has described in further detail in the following section.

Although non–linear in its in–plane response, this material model requires the input of the bulk and shear moduli for the calculation of both the contact force and timestep size (Table 2.7).

Table 2.7: Additional parameters of the hyperelastic material model. Labels: K – bulk modulus, G – shear modulus and t – thickness.

	Leaflet	
Variable	Anterior	Posterior
K [MPa]	100	100
G [MPa]	50	50
t [mm]	1	1

Numerical implementation

The hyperelastic, non–linear, anisotropic, discrete fibre material model described previously in Section 1.4.3 has been implemented following the numerical approach reported by Einstein et al. [78]. Defined

in LS–DYNA through a user defined material subroutine, the `FORTRAN77` source code for this user defined material model can be found in the Appendix B.5. This material model has been implemented using the co–rotational Hughes–Liu finite element shell. Reported as being computationally more efficient [78], this particular element utilises a local coordinate system which rotates with the element as it deforms (Figure 2.13 and Equation 2.1) [79, 80].

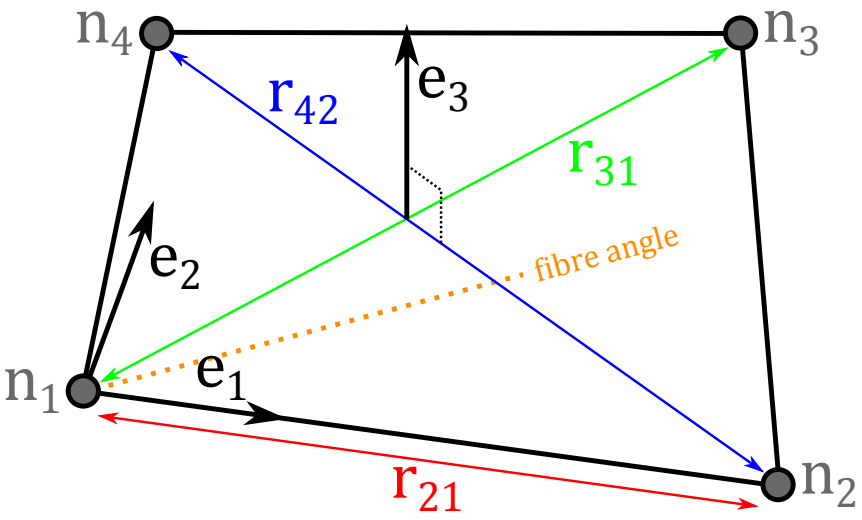

Figure 2.13: Illustration of the local basis of the co–rotational Hughes–Liu element, which is characterised using two key vectors: the shell normal $\mathbf{e}_3$ and the local x–axis $\mathbf{e}_3$ (Equation 2.1). Here the fibre angle in the deformed configuration is illustrated by the dashed line. Labels: $\mathbf{n}_1$ – first node, $\mathbf{n}_2$ – second node, $\mathbf{n}_3$ – third node, $\mathbf{n}_4$ – fourth node, $\mathbf{r}_{21}$ – vector connecting second and first nodes, $\mathbf{r}_{31}$ – vector connecting third and first nodes, $\mathbf{r}_{42}$ – vector connecting fourth and second nodes, $\mathbf{e}_1$ – first orthonormal vector, $\mathbf{e}_2$ – second orthonormal vector and $\mathbf{e}_3$ – third orthonormal vector.

$$
\begin{aligned}
\mathbf{e}_3 &= \frac{\mathbf{s}_3}{\sqrt{\mathbf{s}_3 \cdot \mathbf{s}_3}} \\
\mathbf{s}_3 &= \mathbf{r}_{31} \times \mathbf{r}_{42} \\
\mathbf{e}_1 &= \frac{\mathbf{s}_1}{\sqrt{\mathbf{s}_1 \cdot \mathbf{s}_1}} \\
\mathbf{s}_1 &= \mathbf{r}_{21} - (\mathbf{r}_{21} \cdot \mathbf{e}_3) \times \mathbf{e}_3 \\
\mathbf{e}_2 &= \mathbf{e}_3 \times \mathbf{e}_1
\end{aligned}
\tag{2.1}
$$

From the co–rotational element it is possible to extract the in–plane incremental displacement gradients $\Delta\mathbf{G}$, which defines the change in the incremental element displacement $\Delta\mathbf{u} = [u_1, u_2, u_3]^{\mathrm{T}}$ with respect to the current deformed coordinates $\mathbf{y} = [y_1, y_2, y_3]^{\mathrm{T}}$, at each time step (Equation 2.2). It is from these incremental displacement gradients that the deformation gradient has been manually assembled. As the material has been defined as a membrane, the out–of–plane components are uncoupled to the in–plane components, i.e. $\Delta G_{13} = \Delta G_{23} = \Delta G_{31} = \Delta G_{32} = 0$ (Equation 2.3).

$$
\Delta G_{ij} = \partial \Delta u_i / \partial y_j \tag{2.2}
$$

$$
\Delta\mathbf{G} = \begin{pmatrix} \Delta G_{11} & \Delta G_{12} & 0 \\ \Delta G_{21} & \Delta G_{22} & 0 \\ 0 & 0 & \Delta G_{33} \end{pmatrix} = \begin{pmatrix} \partial \Delta u_1 / \partial y_1 & \partial \Delta u_2 / \partial y_1 & 0 \\ \partial \Delta u_2 / \partial y_1 & \partial \Delta u_2 / \partial y_2 & 0 \\ 0 & 0 & \partial \Delta u_3 / \partial y_3 \end{pmatrix} \tag{2.3}
$$

By definition the incremental displacement and deformation gradients are related through the identity tensor $\mathbf{I}$ (Equation 2.4). Modelled as an incompressible material, the incremental deformation gra-

dient is defined as volume preserving (Equation 2.5).

$$\Delta\mathbf{F} = \mathbf{I} + \Delta\mathbf{G} \tag{2.4}$$

$$\det \Delta\mathbf{F} = 1 \tag{2.5}$$

From this incompressibility constraint, the out–of–plane incremental displacement gradient can be defined as a function of the in–plane increments (Equation 2.6).

$$\Delta G_{13} = \frac{1}{(\Delta G_{11}+1)(\Delta G_{22}+1) - \Delta G_{21}\Delta G_{12}} \tag{2.6}$$

Calculation of the deformation gradient from the incremental deformation gradient is an additive operation, as the incremental deformation gradient at the current time t is related to the deformation gradient at time t by using the deformation gradient at some previous time $t - \Delta t$ (Equation 2.7).

$$\mathbf{F}(t) = \Delta\mathbf{F}(t)\,\mathbf{F}(t-\Delta t) \tag{2.7}$$

However in the co–rotational element, the incremental displacement gradients are returned in the current co–rotational basis at the time t and are referred to as $\Delta\tilde{\mathbf{G}}$. It is required to rotate these incremental displacement gradients back to the initial basis of the element before updating the deformation gradient as detailed in Equations 2.4, 2.5 and 2.7 (Figure 2.14).

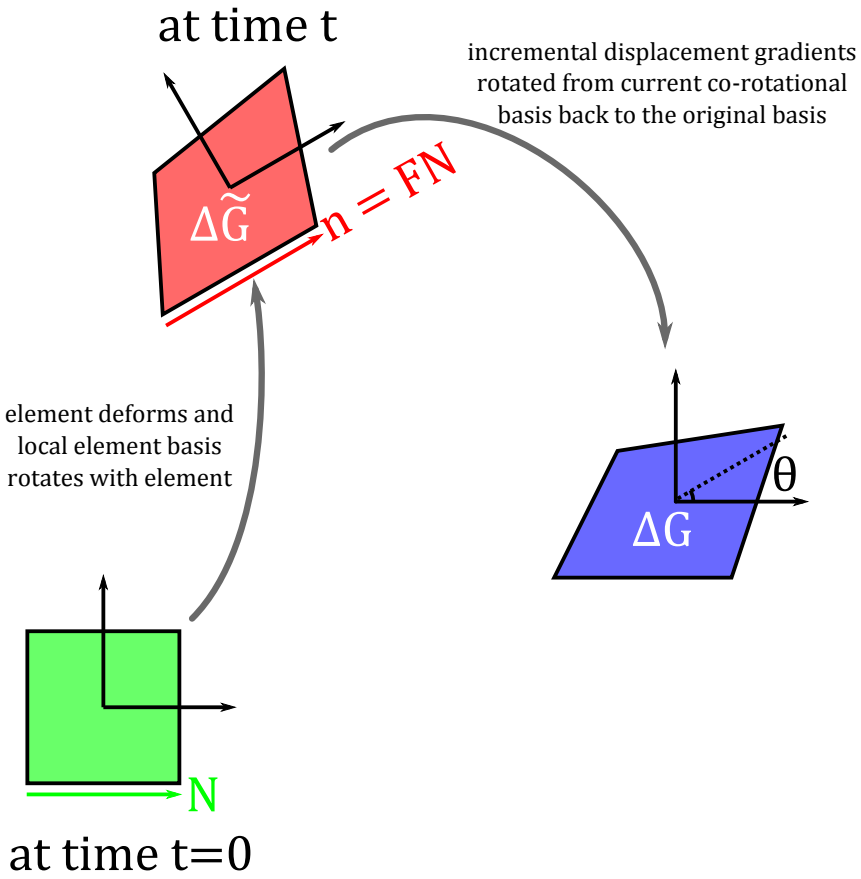

Figure 2.14: At time t the incremental displacement gradients $\Delta\tilde{\mathbf{G}}$ are given in the current co–rotational basis. In order to assemble the deformation gradient correctly, $\Delta\tilde{\mathbf{G}}$ gradient must be rotated by the angle θ to give the incremental displacement gradient in the original basis $\Delta\mathbf{G}$. Labels: $\Delta\tilde{\mathbf{G}}$ – incremental displacement gradients in co–rotational basis, $\Delta\mathbf{G}$ – incremental displacement gradients in original basis, θ – angle of rotation, $\mathbf{N}$ – initial x–axis vector and $\mathbf{n}$ – x–axis vector in the deformed configuration.

The angle θ through which the current element basis must be rotated back is determined directly

using the deformation gradient (Figure 2.14). At $t = 0$, the local x–axis of each element is defined in the initial elemental basis with the unit vector $\mathbf{N} = [1,0,0]^{\mathrm{T}}$. At time t, following the deformation gradient $\mathbf{F}$ the vector $\mathbf{N}$ has the deformed configuration $\mathbf{n} = \mathbf{F}\mathbf{N}$ which is also defined in the initial elemental basis.

$$\mathbf{n} = \mathbf{F}\mathbf{N} = \begin{pmatrix} n_1 \\ n_2 \\ 0 \end{pmatrix} = \begin{pmatrix} F_{11} & F_{12} & 0 \\ F_{22} & F_{22} & 0 \\ 0 & 0 & F_{33} \end{pmatrix} \begin{pmatrix} 1 \\ 0 \\ 0 \end{pmatrix} = \begin{pmatrix} F_{11} \\ F_{21} \\ 0 \end{pmatrix} \tag{2.8}$$

The orientation of the vector $\mathbf{n}$ with respect to $\mathbf{N}$ gives the angle of rotation θ and is calculated by taking the dot product of the corresponding normalised vectors (Equations 2.9 and 2.10).

$$|\mathbf{n}| = \sqrt{(\mathbf{F}\mathbf{N})^{\mathrm{T}} \cdot \mathbf{F}\mathbf{N}} = \sqrt{\mathbf{N}^{\mathrm{T}}\mathbf{F}^{\mathrm{T}}\mathbf{F}\mathbf{N}} = \sqrt{C_{11}} \tag{2.9}$$

$$\cos\theta = \frac{\mathbf{N}\cdot\mathbf{n}}{|\mathbf{n}|} = \frac{F_{11}}{\sqrt{C_{11}}} \tag{2.10}$$

The incremental displacement gradients in the current co-rotational basis $\Delta\tilde{\mathbf{G}}$ are rotated back to the initial basis by using the rotation matrix $\mathbf{Q}$ (Equations 2.11 and 2.12).

$$\mathbf{Q} = \begin{pmatrix} \cos\theta & -\sin\theta & 0 \\ \sin\theta & \cos\theta & 0 \\ 0 & 0 & 1 \end{pmatrix} \tag{2.11}$$

$$\Delta\mathbf{G} = \mathbf{Q}\Delta\tilde{\mathbf{G}}\mathbf{Q}^{\mathrm{T}} \tag{2.12}$$

Once in the initial basis, the incremental displacement gradient $\Delta\mathbf{G}$ are used to calculate the incremental deformation gradient and the corresponding deformation gradient at the time t (Equations 2.4 and 2.7). Using the deformation gradient $\mathbf{F}$, the stress response of the material is evaluated using the discrete fibre approach described previously in Section 1.4.3. Omitted here for brevity, the second Piola–Kirchhoff stress tensor $\mathbf{S}$ is calculated as a function of the deformation gradient $\mathbf{F}$ and the chosen strain–energy function (for more details see Pages 39 to 41). The second Piola–Kirchhoff stress tensor is subsequently pushed forward to the Cauchy stress tensor $\boldsymbol{\sigma}$ using the deformation gradient (Equation 2.13).

$$\sigma = \mathbf{F}\mathbf{S}\mathbf{F}^{\mathrm{T}} \tag{2.13}$$

Defined in the initial elemental basis, it is required to rotate the Cauchy stress tensor $\boldsymbol{\sigma}$ stress back to the current co–rotational basis in order to be consistent with the expected stress in LS–DYNA. Using the same rotation matrix defined previously (Equation 2.11), the Cauchy stress tensor in the initial elemental basis $\boldsymbol{\sigma}$ is rotated to $\tilde{\boldsymbol{\sigma}}$ which is defined in the current co–rotational basis (Equation 2.14).

$$\tilde{\boldsymbol{\sigma}} = \mathbf{Q}^{\mathrm{T}}\boldsymbol{\sigma}\mathbf{Q} \tag{2.14}$$

In the co–rotational basis the transverse stresses σ_{13} and σ_{23} are updated using a Lagrangian approach. These stresses are calculated using the the value of stress in the previous time step σ_{ij}^{t-1}, the current strain increments $\Delta\epsilon_{ij}^{t}$ and the transverse stiffness c (Equation 2.15).

$$\sigma_{ij}^{t} = \sigma_{ij}^{t-1} + c\Delta\epsilon_{ij}^{n} \quad \text{where i=1,2 and j} = 3 \tag{2.15}$$

The complete process through which each element is processed is shown in Figure 2.15. Validation

of this the correct calculation of **F** was performed by using the approach adopted by Einstein et al. [78], in which the strain–energy function was changed to that of a Mooney–Rivlin membrane and the resulting dynamics of its inflation have been compared against its corresponding analytical solution (results not shown). Numerical tests on the mitral valve strain–energy function are performed in the following section.

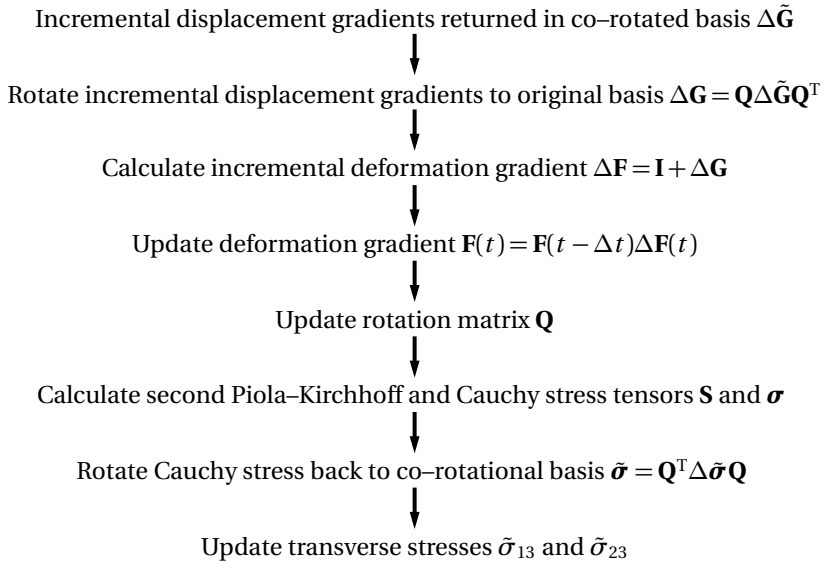

Figure 2.15: Subroutine calculation flow.

Single element tests

Using the numerical implementation described above, the mitral valve strain–energy function described by May-Newman and Yin [73] has been evaluated in a single element. Defined with the material parameters corresponding to the anterior leaflet (Table 2.8), the stress response has been calculated and compared against the analytical solution. Here a range of different stretch scenarios (uniaxial/biaxial/shear) have been evaluated (Table 2.8 and Figure 2.16).

Table 2.8: Anterior leaflet material parameters used in the single element tests. Labels: c_0 – first material parameter, c_1 – second material parameter, c_2 – third material paramaters, c – transverse shear stiffness, K – bulk modulus, and G – shear modulus

Parameter	Value
c_0 [kPa]	0.399
c_1 [–]	4.535
c_2 [–]	1446.5
c [kPa]	500
K [MPa]	100
G [MPa]	50

Table 2.9: Description of the different single element tests performed in Figure 2.16. For the definition of the associated deformation gradients and deformed configurations refer back to Equation 1.6 and Figure 1.18 on Pages 39 to 40.

Figure	Description	Stretch range
Figure 2.16a	Equal biaxial	$\lambda : 1 \rightarrow 1.2$
Figure 2.16b	Uniaxial fibre direction	$\lambda : 1 \rightarrow 1.2$
Figure 2.16c	Uniaxial cross–fibre direction	$\lambda : 1 \rightarrow 1.5$
Figure 2.16d	Shearing	$\gamma : 0 \rightarrow 0.1$

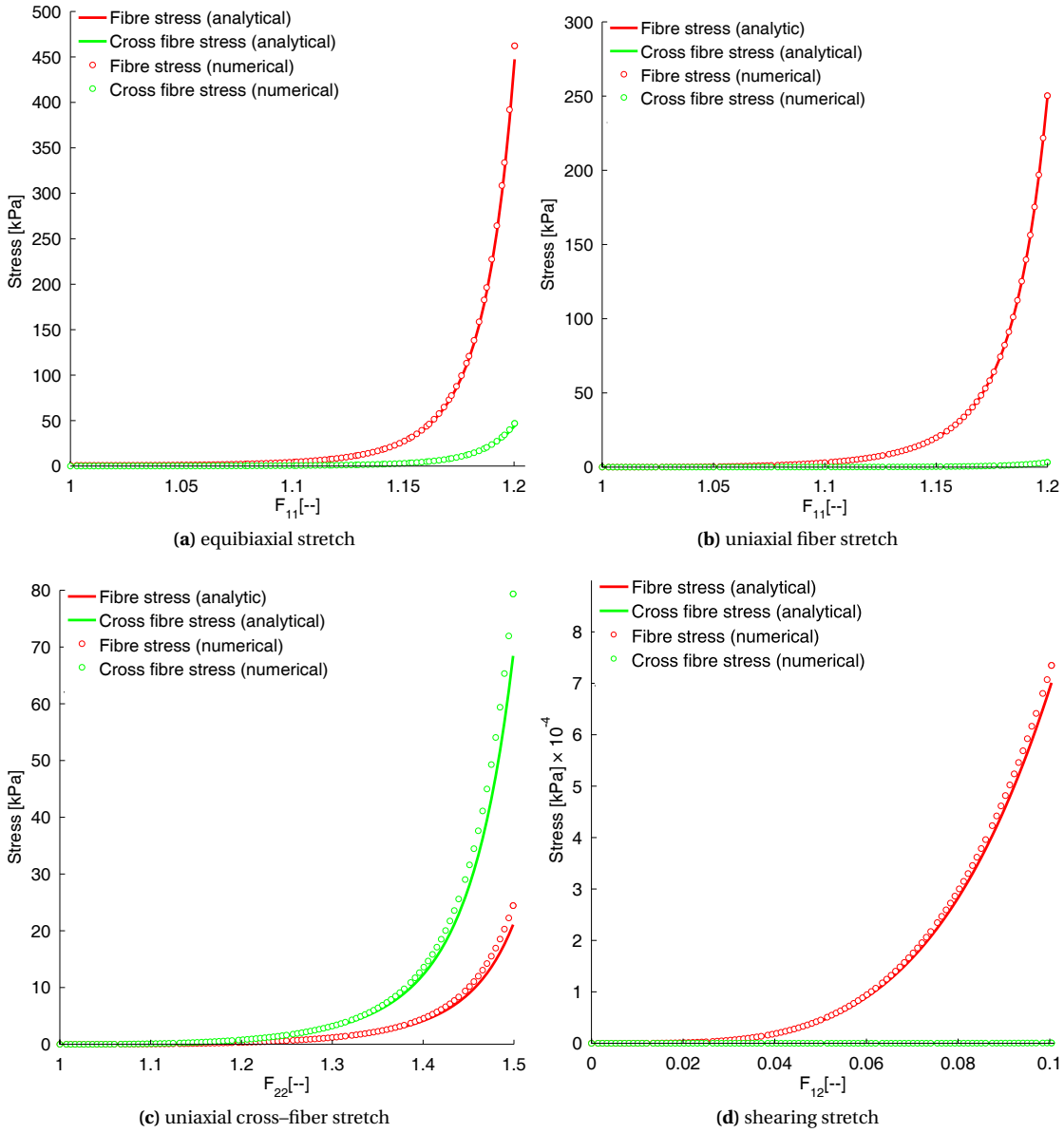

(a) equibiaxial stretch

(b) uniaxial fiber stretch

(c) uniaxial cross–fiber stretch

(d) shearing stretch

Figure 2.16: Numerical and analytical comparison of a single element under (a) equibiaxial stretch, (b) uniaxial fiber direction stretch, (c) uniaxial cross–fibre direction stretch and (d) shearing stretch. In all cases the fibre direction has been aligned with the x–axis and the cross–fibre is accordingly aligned with the y–axis. In (a) and (b) the stress are plotted against the fibre direction stretch F_{11}, whereas in (c) and (d) the stresses are plotted against the cross–fibre stretch F_{22} and the shearing stretch F_{12} respectively. Note that the units of stress are plotted with different values.

Transverse stiffness

As defined previously, the transverse stresses are updated proportionally by the parameter c which is referred to as the transverse stiffness (Equation 2.15). The value of this parameter has been suggested as 500 kPa by Einstein et al. [78], however no clear justification of this parameter's effect are detailed. Thus here the effect of this transverse stiffness term has been assessed by perturbing c by scale factors of 0.01, 0.1, 10 and 100.

In order to avoid the effects of mesh contact, this parameter has been examined in a case of simple inflation. Here a membrane sized 12 mm × 12 mm × 1 mm has been fixed spatially and a normal pressure load of 16 kPa has been applied linearly over 1s. Consisting of 144 elements, the orientation of the elemental fibre angles have been uniformly aligned with the local x–axis. The membrane has been defined with the same material parameters as in the single element tests (Table 2.8). Comparison of both the maximum principal stress and the maximum vertical displacement show that aside from 0.01,

all other scale factors of c show no significant difference (Table 2.10).

Table 2.10: Comparison of the maximum principal stresses and maximum vertical displacement in response to varying transverse stiffness.

Scale factor	Transverse stiffness [kPa]	Maximum principal stress [kPa]	Maximum vertical displacement [mm]
0.01	5	314.9384	4.132396
0.1	50	167.3721	3.306955
1	500	167.3711	3.306951
10	5000	167.3706	3.306949
100	50000	167.3705	3.306949

2.3.2 Chordal material models

In this section the different material models used to represent the chordae tendineae in the isotropic, orthotropic and hyperelastic models are described in further detail. Defined with linear and non–linear elastic moduli, standard material models have been implemented in the finite element solver LS–DYNA (Table 2.11).

Table 2.11: Comparison of the key features of the different material models used to represent the chordae tendineae.

Model	Linear	Non–linear
Isotropic	☑	☐
Orthotropic	☐	☑
Hyperelastic	☐	☑

2.3.2.1 Isotropic

In the isotropic model the marginal chordae tendineae have been defined as linearly elastic with a elastic modulus of 3 MPa. As the focus of this model was to determine the difference between structural–only and fluid–structure interaction approaches, it was chosen to approximate the material behaviour of the chordae tendineae with the simplest possible material model. This has been implemented within LS–DYNA using the standard material model `MAT_CABLE_DISCRETE_BEAM` in conjunction with the discrete cable element [79, 80]. This particular beam element was selected as it cannot generate stress under compression, only tension. The area of the beam elements has been defined as 0.6 mm^2.

2.3.2.2 Orthotropic and hyperelastic

In the orthotropic and hyperelastic models the material model used to represent the marginal, basal and strut chordae tendineae has been defined as non–linearly elastic. This has been implemented within LS–DYNA using the non–linear version of the material model `MAT_CABLE_DISCRETE_BEAM` and the discrete cable element [79, 80]. In this material model the non–linear behaviour of both the marginal and basal chordae have been defined from experimental measurements reported by Kunzelman and Cochran [67] (Figure 2.17).

The orthotropic and hyperelastic models both contain the marginal and basal chordae, however the hyperelastic model also contains strut chordae (Table 2.2). As no experimental data on the non–linear stress–strain behaviour of the strut chordae exist, the strut chordae have been defined with the same properties as the basal chordae. The cross–sectional areas of the marginal, basal/strut chordae are defined as 0.45 and 1.15 mm^2 respectively.

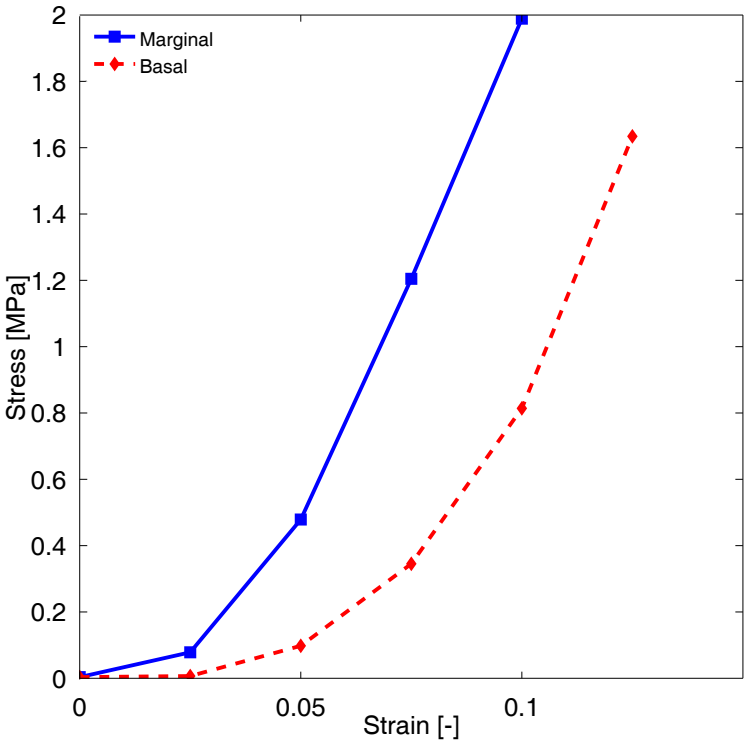

Figure 2.17: Non–linear stress–strain behaviour of the marginal and basal chordae tendineae. Data after Kunzelman and Cochran [67].

2.3.3 Fluid material model

Unlike solids, fluids generate stresses with respect to strain rates rather than strains. The strain rates are linked to the stresses via the viscosity of the fluid. Although the viscosity of blood exhibit non–linear behaviour, this typically occurs at low strain rates, thus the blood has been assumed to have constant viscosity. In LS–DYNA the fluid has been modelled using the material model `MAT_NULL`, which describes the stress response to the imposed strain rates [79, 80]. The required parameters for this material model is the density and dynamic viscoity. This material model is used in conjunction with an equation of state model which describes the pressure change in response to volumetric changes. Two equation of state models are available: `EOS_LINEAR_POLYNOMIAL` and `EOS_GRUNEISEN` [79, 80].

The change in pressure is defined using the volumetric parameter μ, density ρ and volume v (Equation 2.16). Here the subscripts 0 indicate the initial values of these variables. The pressure P calculated using this volumetric parameter μ, density ρ and the speed of sound c. Comparison of these two models over the pressure range experienced in closure and opening is shown in Figure 2.18. In expansion the two models behave identically, however differences are observed at larger compressions ratios. The `EOS_GRUNEISEN` material model has a numerical advantage as it is faster to compute than the `EOS_LINEAR_POLYNOMIAL`.

$$\mu = \frac{v_0 - v}{v} = \frac{\rho}{\rho_0} - 1 \tag{2.16}$$

$$P = \begin{cases} (\rho_0 c^2 \mu)/(1+\mu) & \text{if } \mu > 0 \\ \rho_0 c^2 \mu & \text{if } \mu < 0 \end{cases} \tag{2.17}$$

$$P = \rho_0 c^2 \mu \tag{2.18}$$

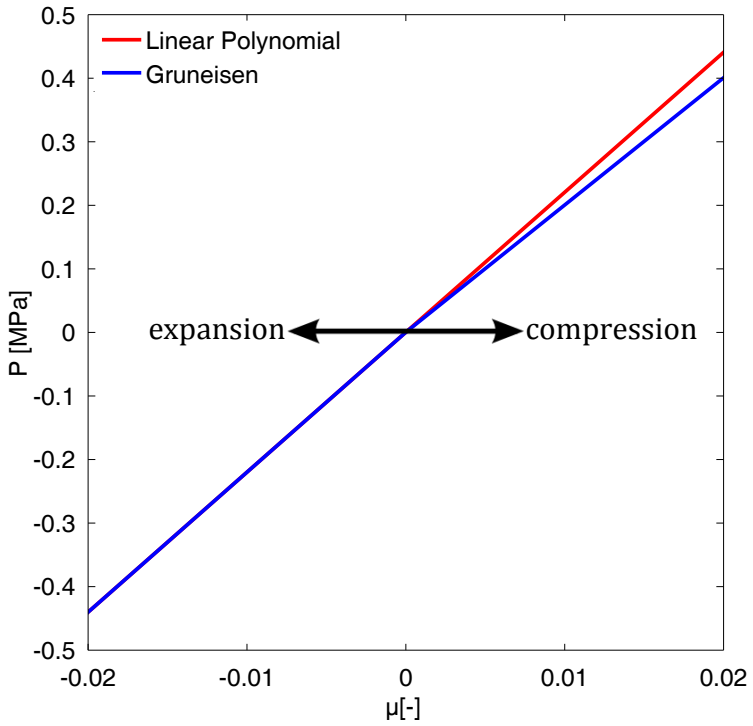

Figure 2.18: Comparison of the two equation of state models over the physiological range of pressures. Parameters used for this have been selected to be the same as in the full valve simulations: $c = 148.4\,\mathrm{m}\cdot\mathrm{s}^{-1}$ and $\rho = 1\,\mathrm{g}\cdot\mathrm{cm}^3$.

2.4 Numerical implementation

2.4.1 Structural simulations

Here the different numerical aspects of the structural simulations of the valve structure in LS–DYNA have been are summarised.

2.4.1.1 Mesh validation

The structural equations of motion are solved using the finite element method, the accuracy of the resulting solution is strongly dependent upon the size of the elements used to represent the valve structure. Here the approach taken to validate the different models are described.

Isotropic and orthotropic models

Both the isotropic and orthotropic models been validated through simulating a structural–only closure of the full valve geometry. In each model the number of elements have been increased by dividing each existing element by four, as each parent element is divided into four child elements (Figure 2.19). As all structural elements are constant stress elements shell elements, the mesh resolution is deemed to be acceptable when the predicted stress in the child element matches the parent element. Performed in an iterative fashion, both the isotropic and orthotropic models have been assessed through the maximal value of the maximum principal stress. In the isotropic and orthotropic models the meshes have been refined until the difference between successive iterations was reduced to 1% and 3% respectively.

In the case of the orthotropic mesh, the validation has been performed in closure however the application of the mesh is in valve opening. As valve opening is a transient dynamic event it is not possible to compare models with differing mesh densities as the valve is in constant motion, thus it was selected to validate the mesh density using a quasi–static simulations.

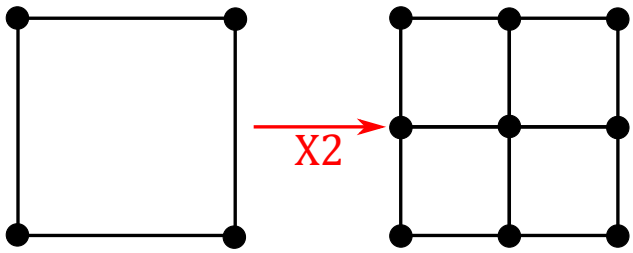

Figure 2.19: Illustration of increasing mesh density in a structural four–node shell element mesh.

Hyperelastic model

In the hyperelastic model the mesh refining procedure adopted above was found to be unsuitable in the full valve as mesh instabilities from self–contact and hourglassing (Section 2.4.1.3) were introduced from changes in the mesh sizing. Thus in order to assess the mesh size it was required to evaluate scenarios that exclude both contact and hourglass instabilities. Here the mesh sizing has been assessed by (1) in–plane stretch and (2) out–of–plane inflation of a square membrane sized 12 mm × 12 mm × 1 mm, with a fibre angle uniformly aligned with the local elemental x–axis. Three different element sizes have been assessed: 2 mm, 1 mm and 0.5 mm. The material parameters used here are the same as in the single element tests (Table 2.8).

In the stretch test, the cross–fibre direction has been held constant whilst an in–plane stretch of 1.2 has been applied in the fibre direction as a linear displacement over 1s. In the inflation test, the boundaries of the membrane are fixed spatially and a pressure load of 16 kPa as been applied normal to membrane using a linear ramp over 1s. The results of both these tests have shown that the difference in both the maximum principal stresses and maximal vertical displacements are reduced between the mesh sizings 1.0 mm and 0.5 mm (Table 2.12).

Table 2.12: Comparison of maximum principal stresses in with different mesh sizing using the user defined material model described in Section 2.3.1.3.

Test	Mesh size [mm]	Maximum Principal stress [MPa]	Maximum Vertical displacement [mm]
Stretch	2.0	251.2721	–
Stretch	1.0	251.1800	–
Stretch	0.5	251.2721	–
Inflation	2.0	181.4693	3.399927
Inflation	1.0	167.3711	3.306951
Inflation	0.5	164.4045	3.272268

2.4.1.2 Fluid effect

As the heart valves are fully immersed in fluid the dynamic motion of the structure is damped. Therefore in structural–only heart valve models it is required to approximate this damping effect. Here nodal velocity damping, mass scaling damping and mass–weighted nodal damping have been assessed and compared by using a isotropic linearly elastic square membrane of length 10 mm (Table 2.13). Fixed spatial along its boundaries, inflation of this membrane has been performed by applying a pressure of 20 kPa linearly over 1s. The resulting time dependent vertical deflection of the central node have been compared in the different simulations.

Nodal velocity dampening has been implemented in LS–DYNA by using the keyword `CONTROL_DYNAMIC_RELAXATION` [80]. At each time step, the nodal velocity $v^{n+1/2}$ is updated using the current nodal acceleration a^n and a scaled value of the previous nodal velocity $v^{n-1/2}$ (Equation 2.19). Here the scaling factor η=0.9965, a value determined from experimental measurements performed by Burriesci

et al. [111] on prosthetic valves in a left heart simulator.

$$v^{n+1/2} = \eta v^{n-1/2} + a^n \Delta t \tag{2.19}$$

In order to approximate the fluid damping effect, the mass–scaling approach increases the mass density of the structure by an appropriate factor. Following the approach adopted by Kunzelman et al. [85] and Schievano et al. [103], the density has been increased by a factor of 10. However no justification of this is reported within these studies.

An alternative mass–weighted nodal velocity approach has also been assessed. Implemented in LS–DYNA using the keyword `DAMPING_GLOBAL` [80], the acceleration of each node a^n is calculated as the sum of the forces F^n which include a damping force F_D (Equation 2.20). This damping force is defined as an appropriate factor D_s of the current nodal momentum mv (Equation 2.21). Here the constant D_s has been set to 0.01.

$$a^n = M^{-1}\left(F^n - F_D^n\right) \tag{2.20}$$

$$F_D^n = D_s m v \tag{2.21}$$

Comparison of the different damping approaches indicate that the mass scaling approach results in rapid oscillations when compared to the velocity damping methods (Figure 2.20). The mass–weighted damping approach initially shows small oscillations but eventually dissipate, however in the nodal velocity scaling approach the number of exportable data points was limited (1 per ∼15 ms on average in the nodal velocity scaling compared to 1 per 1 ms in the mass–scaled/mass–weighted approaches).

Table 2.13: Nodal/mass damping simulation parameters.

Parameter	Value
Shell thickness [mm]	1
Elastic modulus [kPa]	100
Poisson ratio [–]	0.45

2.4.1.3 Hourglass coefficients

The shell elements used in this work all utilise single Gauss point integration, also referred to as reduced integration, in order to avoid the numerical phenomenon known as “shear locking” in which elements are locked into non–physical modes [112]. Although reduced integration addresses this issue, it can result in another numerical instability known as hourglassing in which the displacement of opposing nodal pairs result in a zero net displacement (Figure 2.21). As a zero–energy mode the element easily enters this mode, increasing deformations can result in zero area as the element collapses that result in an infinite velocity. Prevention of these modes are avoided by the application of numerical forces referred to as hourglass forces which are added at the element level to the stress tensor. There are a range of hourglass models available in LS–DYNA, with the models divided between viscous and stiffness models [79, 80]. Here a mixture of the two types have been used.

2.4.2 Fluid simulations

In this section the different numerical aspects of the fluid related simulations in LS–DYNA have been summarised.

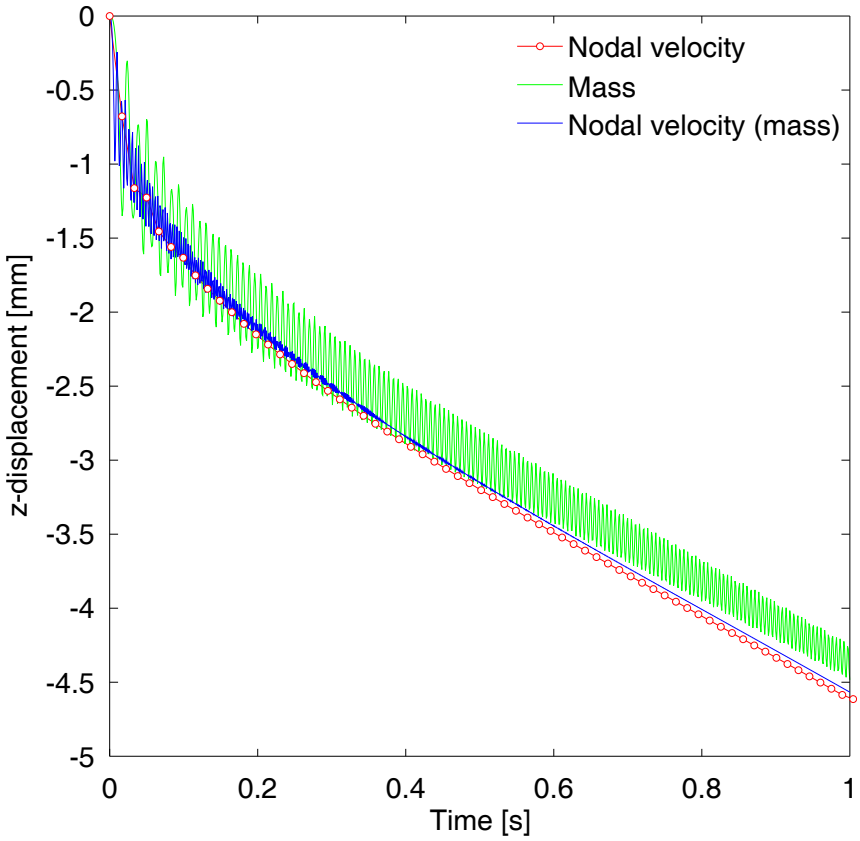

Figure 2.20: Comparison of the vertical displacement of the centre node of the square membrane against time in the nodal velocity scaled, mass scaled, and mass–weighted nodal velocity scaled damping approaches.

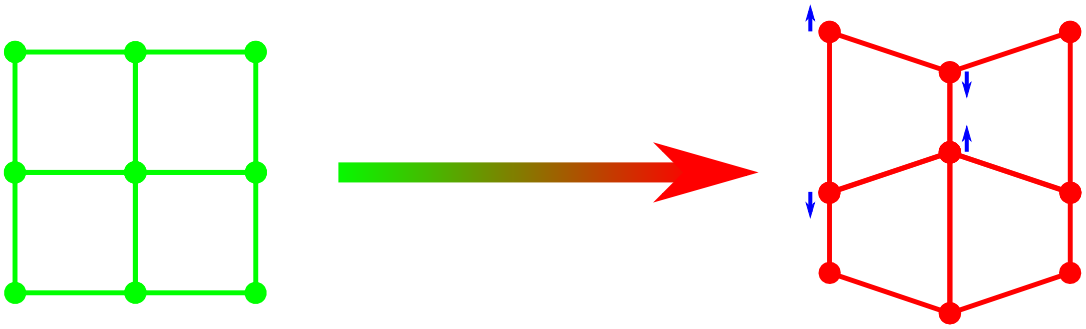

Figure 2.21: Illustration of an hourglass instability, here the blue arrows indicate the nodal displacement. As the net displacement of the nodal pairs are both zero, the increase in energy is zero.

2.4.2.1 Hydrocode

The default fluid solver in LS–DYNA is a compressible flow solver that is referred to as a hydrocode [113]. This particular approach to solving the fluid equations of motion is performed in a two–step manner, the first step involves a Lagrangian step in which the mesh is deformed subject to the applied forces. The next step requires the change in velocity and pressure (also referred to as the velocity/pressure flux) are then advected back to the fixed Eulerian mesh using monotonic advection scheme, for example the donor cell algorithm or the Van Leer MUSCL algorithm (monotone upwind scheme for conversation laws) [79]. It is this advection step that imposes the structured volume mesh requirement, as the velocity and pressure fluxes must be advected along orthogonal directions. The operational flow of this flow solver is illustrated in Figures 2.22 and 2.23. For further details regarding the operation of hydrocodes please refer to Benson [113].

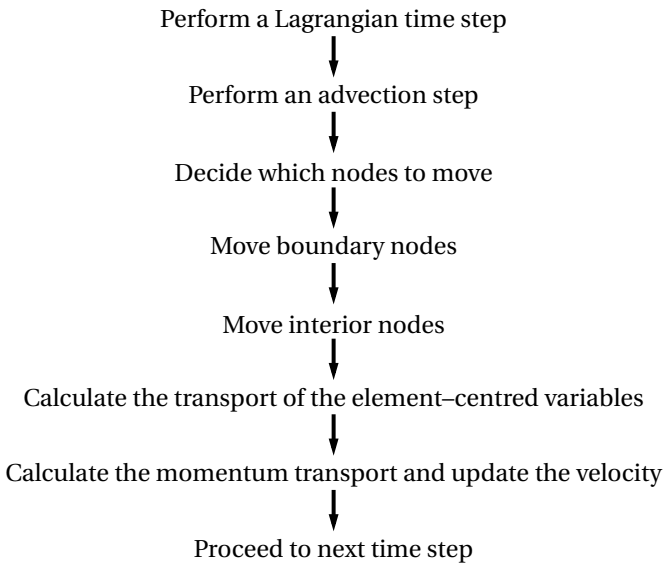

Figure 2.22: Fluid solver operational flow, details after Hallquist [79].

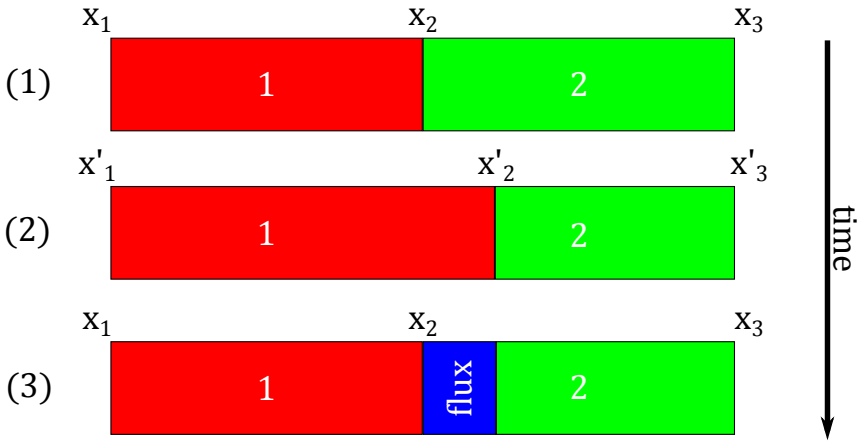

Figure 2.23: Illustration of flux advection: (1) the fluid is in its fixed Eulerian position with two adjacent elements 1 and 2. (2) the Lagrangian step results in the element 1 moving to the right, with updated nodal positions x_1',x_2' and x_3'. (3) the flux/transport of the fluid variables from element 1 to 2 is calculated and is remapped/advected from element 1 to 2.

2.4.2.2 Bulk modulus/Speed of sound

As the flow solver is compressible, the bulk modulus of the fluid must be defined. As blood is essentially an incompressible fluid, it is required to define the bulk modulus and associated speed of sound c with an appropriately high value. The speed of sound is related to the bulk modulus K, as shown in Equation 2.22. As described in Section 2.4.2.1, the fluid is solved in a two–step manner. In the Lagrangian step of the fluid motion the maximum permitted time step is governed by the smallest elemental dimension and the speed of sound which is related to the bulk modulus by the relationship shown in Equation 2.23. Thus in order to proceed with a workable time step size, the compressibility of the fluid has been reduced by adjusting the speed of sound. Although reduced, this value is still defined as with a relatively high value.

This simplification has been determined not to affect the fluid dynamics by consideration of the time scale required for a pressure wave to instantaneously reflect (from a solid interface) and travel the annular–apex distance, which has been experimentally reported as approximate 100 mm by Joudinaud et al. [44]. Using the true speed of sound, here estimated to be 1482 m·s^{-1}, and the annular–apex distance of 100 mm, the time scale required for a pressure wave to travel this is distance is of the order 1×10^{-2}

ms. In all numerical simulations the time step is of the order 1×10^{-4} ms, thus all simulations have the sufficient temporal resolution to capture fluid wave effects although defined with a reduced bulk modulus.

$$c = \sqrt{\frac{K}{\rho}} \tag{2.22}$$

$$\Delta t_{max} = \frac{\Delta l_{min}}{c} \tag{2.23}$$

2.4.2.3 Hourglass coefficient

As with the structural simulations, the solid elements are subjected to reduced integration which also require hourglass stabilisation in order to prevent zero–energy modes and numerical instabilities. For fluid simulations, it is reported in the LS–DYNA user manuals that lower hourglass coefficients are required in order to allow the fluid mesh to deform in the correct manner. In this work the recommended default hourglass model and coefficient value of 1×10^{-6} has been used.

2.4.2.4 Fluid–structure interaction

Coupling of the structure to the fluid is performed numerically within LS–DYNA using a penalty coupling method [79, 80]. Immersed within the fluid, the contact force between the fluid and structure is calculated at each time step and applied to both the structure and fluid thus coupling them together. As detailed in Section 2.4.2.1, the motion of the fluid is solved in a two–step manner in which the first step the mesh is advanced in a Lagrangian fashion (Figure 2.24). Following this step penetration of the fluid mesh into the structure is calculated and a force proportional to the distance of penetration is calculated and applied to both structural and fluid meshes, after which the fluid variables (velocity and pressure) are advected back to the fixed Eulerian mesh (Figure 2.24). This method of coupling is referred to as penalty coupling. In LS–DYNA two different contact algorithms are available, nodal and segment based. However in this work only the segment based option has been used.

This fluid–structure interaction method however has one particular insufficiency in that the structure is not able to contact itself, as the valve structure does in closure. However close the one portion of the structure approaches another portion, a gap will always remain between the two structural portions. In the Lagrangian step the fluid essentially acts as a solid stuck between two surfaces of the structure, essentially incompressible a gap proportional to a single element will always remain in between the valve in closure (Figure 2.25).

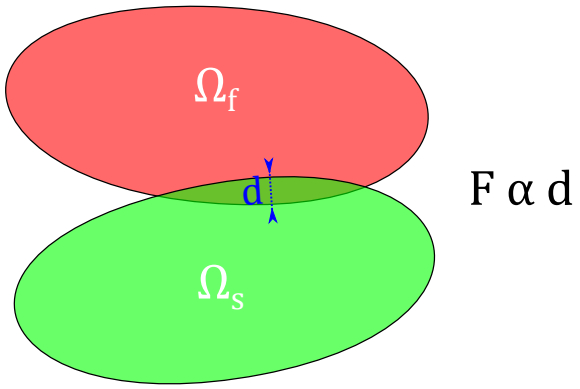

Figure 2.24: The penalty coupling fluid–structure interaction method used in LS–DYNA. The force F applied to both structural and fluid domains Ω_s and Ω_f respectively are a function of the overlap distance d.

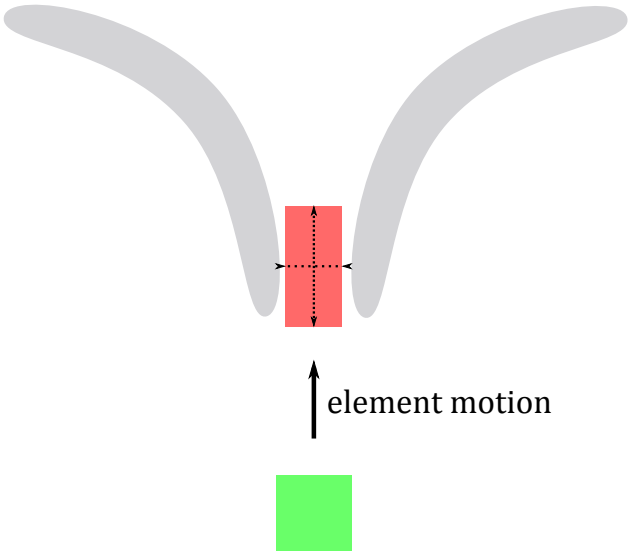

Figure 2.25: As the fluid is modelled as a compressible solid, during closure of the valve structure an artificial gap persists between the leaflets fluid element is trapped. Although this appears as a open gap, the relative velocity of the fluid element is zero and therefore fluid motion through this gap is zero.

Chapter 3

Simulation of Valvular Dynamics

The simulation and modelling of valvular dynamics, in particular that of the mitral valve, requires a method that is able to handle both the immersed nature of the heart valves within the heart and the large deformations of a complex three–dimensional structure which also involves self–contact. As detailed previously in Chapter 1, Section 1.5, published numerical models of the mitral valve can be broadly divided into structural–only or fluid–structure interaction models. As structural–only models only represent the structural domain of the valve, the effect of the haemodynamic load is approximated as a uniformly distributed pressure load over the entire surface of the valve. Fluid–structure interaction models however include both the structure of the valve and the fluid of the blood, the haemodynamic load is approximated from the interaction between the fluid and structure and vice versa resulting in a non–uniform load over the surface of the valve. Using both approaches, the following three issues related to the modelling of valvular dynamics have been examined within this chapter:

(1) Method of fluid–structure interaction – Although a commercially available finite element solver has been used, there remain several aspects of fluid–structure interaction which require user definition. Examination of the parameters relevant for the modelling of heart valve dynamics, in this and the following chapters, has been performed by comparing the results of numerical simulations to previously reported experimental results by Hart et al. [114] (Section 3.1).

(2) Effect of fluid volume geometry – Immersed within a fluid volume, existing fluid–structure interaction models of the mitral valve have simulated valve dynamics in a straight tubular fluid volume (for example see Einstein et al. [76]). Here the effect of straight and more physiological U–shaped fluid volumes upon the valvular and fluid dynamics have been assessed, with the results compared directly against structural–only methods (Section 3.2).

(3) Effect of the full cardiac cycle – Previous mitral valve models have approximated the cardiac cycle by simulating closure and opening separately using quasi–static approach. Here the valvular and fluid dynamics throughout a full cardiac cycle (open/closed/open) have been simulated in both fluid–structure interaction and structural–only models (Section 3.2).

The majority of the results presented here can be found in the paper published by this author titled "*Mitral valve dynamics in structural and fluid-structure interaction models*" [115].

3.1 Fluid–structure coupling

In this section the fluid–structure coupling approaches used in this work has been validated by comparison to the experimental data reported by Hart et al. [114]. Originally used to validate an alternative immersed boundary fluid–structure interaction approach, the dynamic motion of a simple valve–like

structure and the associated fluid field in this experimental set–up have been directly compared to the numerical results of this alternative model [114]. Here numerical simulations of the same experimental configuration have been performed, with the corresponding results used to compare qualitatively (as the quantitative data is unavailable) the different fluid–structure interaction coupling methods available in LS–DYNA Release 4.2.1 [79, 80].

3.1.1 Experimental configuration

The original experiment describes a three–dimensional channel within which a thin elastic membrane, initially at rest, is immersed in the fluid and subjected a pulsed velocity profile. Although three dimensional, the channel cross–section is constant and it has been shown that in the centre of the channel the three dimensionality of the fluid field is reduced to a two–dimensional problem (Figure 3.1). The resulting valve and fluid motion in a two–dimensional section in the centre of the channel has been recorded at different time points during the velocity pulse [114].

Using the parameters reported in this experiment (Table 3.1), a two–dimensional model which corresponds to this experiment has been created and implemented in LS–DYNA. Here the thinnest of the two thicknesses reported has been selected as this represents the membranous behaviour of the valve most closely. The structure of the valve has been modelled using the standard material model `MAT_ELASTIC` [79, 80]. Here the fluid has been modelled using the fluid material model, which is a compressible fluid model `EOS_GRUNEISEN` [79, 80]. In order to increase the maximum permittable time step the compressibility of the fluid, with no effect to the fluid behaviour, has been reduced by reducing the speed of sound to 148.4 $m{\cdot}s^{-1}$ (see Chapter 2, Section 2.4.2.2).

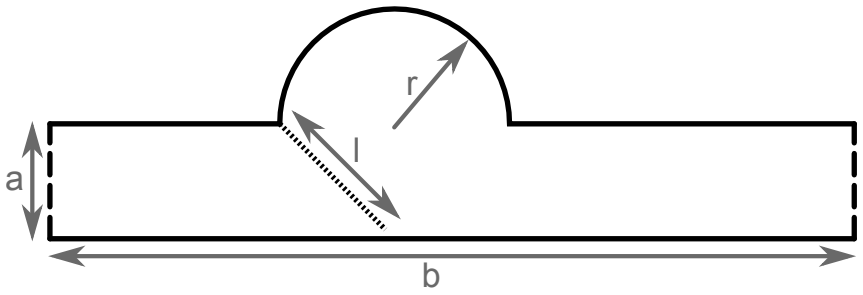

Figure 3.1: Two dimensional cross section of the channel used to describe the numerical model. Solid lines indicate the walls of the channel and have been defined with a no–slip condition, the broken lines at the left and right hand sides of the channel represent the inflow and outflow regions respectively. The dashed line in the centre of the channel is the leaflet which is initially inclined at 45° to the horizontal. The value of the dimensional parameters marked on this figure are listed in the Table 3.1.

3.1.2 Boundary conditions

The experimentally reported flow rate has been digitised, converted to a velocity and fitted to a 6–th order Fourier series (Equation 3.1). This velocity $u(t)$ is then imposed as a boundary condition to the fluid mesh and a fluid–structure interaction simulation has been performed (Figure 3.3). Using this model, aspects of the fluid–structure coupling method have been examined such as the shell element and nodal coupling approach, coupling of single/dual structural sides, the number of coupling points per shell and the bending stiffness of the structure. Here the bending stiffness has been adjusted by increasing and decreasing the number of through thickness shell integration points from 3 (bending stiffness) to 1 (no bending stiffness) [79, 80].

$$u(t) = a_0 + \sum_{n=1}^{6} a_n \cos(nwt) + \sum_{n=1}^{6} b_n \sin(nwt) \tag{3.1}$$

Table 3.1: Dimensional and experimental parameters of the channel geometry, structure and fluid reported in Hart et al. [114]. †The channel length is not reported but it has been estimated from the original figures.

Channel	Value
Length† (a) [mm]	140
Height (b) [mm]	20
Width [mm]	120
Sinus radius (r) [mm]	20

Leaflet	Value
Length [mm]	26
Thickness [mm]	0.16
Density [g·cm^{-3}]	890
Elastic modulus [MPa]	1.5
Poisson's ratio	0.49

Fluid	Value
Density [g·cm^{-3}]	1
Dynamic viscosity [kg·m^{-3}]	4.3×10^{-3}
Speed of sound [m·s^{-1}]	148.4

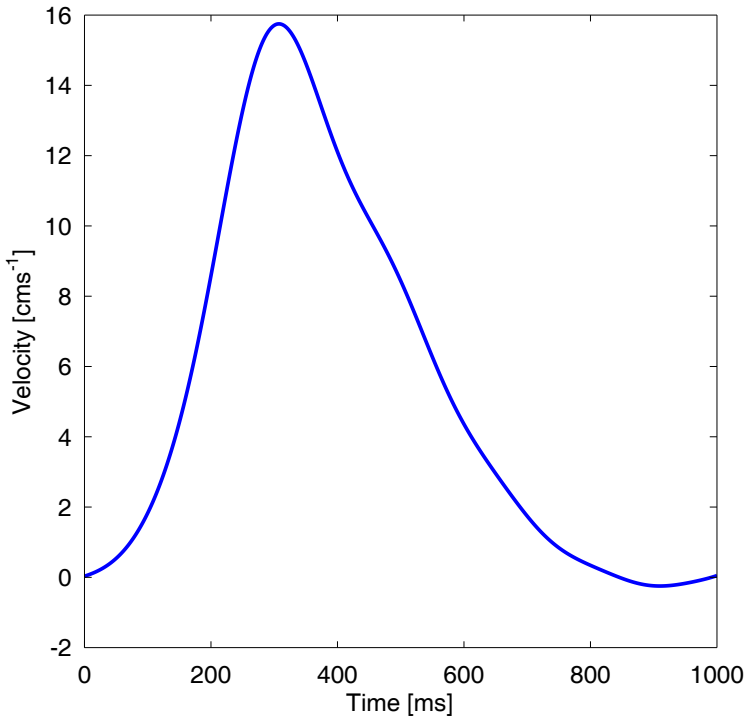

Figure 3.2: Fourier fit of the experimental inlet velocity profile The coefficients of Equation 3.1 are as follows: $a_0 = 0.05346$, $a_1 = -0.04652$, $a_2 = -0.01439$, $a_3 = 0.006251$, $a_4 = 0.003468$, $a_5 = -0.002064$, $a_6 = 0.0005004$, $b_1 = 0.05351$, $b_2 = -0.01757$, $b_3 = -0.007301$, $b_4 = 0.003373$, $b_5 = 0.0008904$, $b_6 = -0.0008609$ and $w = 0.006302$.

3.1.3 Structural dynamics

The motion of the membrane during the velocity pulse has been qualitatively compared against the experimental and numerical results of Hart et al. [114] (Figure 3.4). Here the effect of bending stiffness, the fluid–structure coupling method and coupling direction have been examined. The number of coupling points per shell element (Case E, Table 3.2) was found to have no effect on the resulting dynamics and are have therefore been omitted.

In cases A and B the the effect of modelling the valve with and without bending stiffness has been examined (membrane assumption). The results show that at the start and towards the end of the velocity pulse the deformed configurations are similar in both models (see $t = 0.35s$ and $t = 0.84s$). However

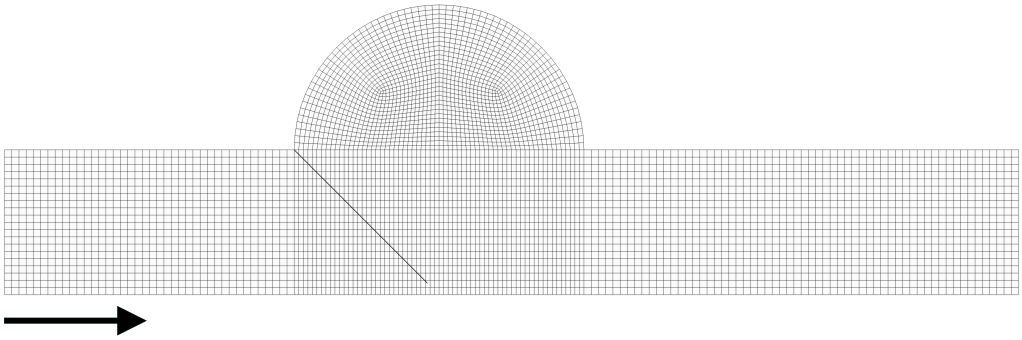

Figure 3.3: Fluid mesh with immersed structural mesh of the experimental configuration. Forward flow is defined from left to right, as indicated by the arrow. Total number of fluid and structural elements are 4816 and 26 respectively.

Table 3.2: Comparison table of the different fluid–structure simulations performed.

Case	Membrane	Coupling type		Coupling points		Coupling sides	
		Shell	Nodal	1	4	Double	Single
A	☑	☑	☐	☑	☐	☑	☐
B	☐	☑	☐	☑	☐	☑	☐
C	☑	☐	☑	☑	☐	☑	☐
D	☑	☑	☐	☑	☐	☐	☑
E	☑	☑	☐	☐	☑	☑	☐

following the peak flow rate ($t = 0.53s$)of velocity that the membrane model (case A) is able to flex more freely in the central area which corresponds better to the deformed shape. In cases A and C the two different approaches available in LS–DYNA to perform fluid–structure coupling, shell element coupling and nodal coupling, have been compared [79, 80]. Here the shell coupling approach results in a deformed configuration which is significantly closer to the deformed configuration. In the nodal coupling (case C) the valve structure does not respond to the deceleration of the fluid, remaining in the open configuration generated by the peak flow with the structure also featuring folding at the tip of the valve as the valve fails to align with the flow direction as shown in the experiment results. In cases A and D the effect of single– and double–sided fluid coupling have been examined. In the single coupled case the structure is only coupled to fluid motion approaching from the inflow direction. Uncoupled to the fluid motion in the sinus cavity, single–sided coupling results in the valve folding back upon itself in an unrealistic manner (see t=0.35s and t=0.53s in Figure 3.4). As stated previously the number of the coupling points per shell element were was found to have no effect and thus has not be included for comparison (case E).

3.1.4 Fluid dynamics

The magnitude of fluid velocity in the different simulated cases A–D are listed in Table 3.3. It can be seen that both the magnitude of the maximum velocity and the time of occurrence are similar in all cases with the exception of the nodal coupled case. Comparison of the directionality of the fluid field in the experimental and numerical results show similarities, in particular the direction of rotation in the radial cavity (Figure 3.5).

Table 3.3: Maximum velocity and time of occurrence in the different simulated cases.

Case	V_{max} [m·s^{-1}]	Time [ms]
A	0.215	282
B	0.215	283
C	0.203	466
D	0.214	293

Figure 3.4: Numerical and experimental valve deformations in response to the velocity pulse. The experimental and numerical results of Hart et al. [114] are boxed in black and shown on the left. The numerical results from LS–DYNA for cases A–D are shown to the right of this.

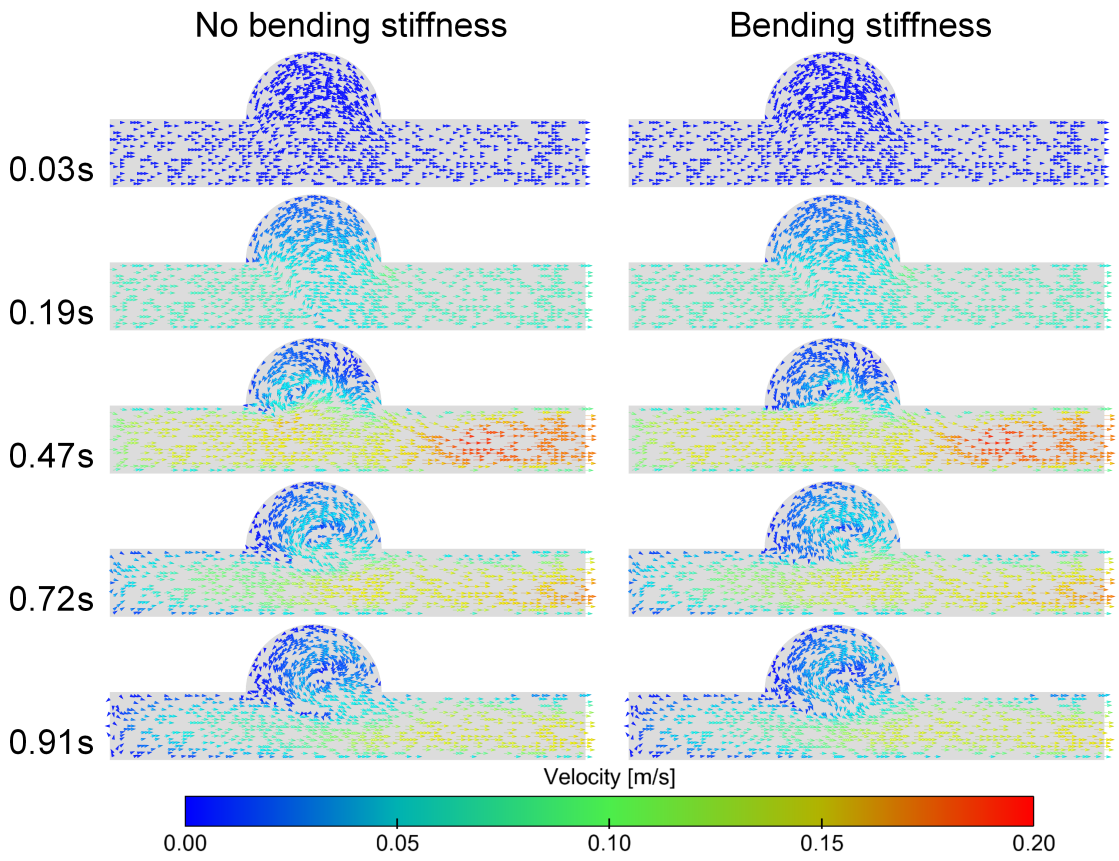

Figure 3.5: Velocity vectors in the no–bending and bending stiffness simulations, cases A and B respectively.

3.1.5 Comparison

The results of these numerical simulations have shown that the fluid–structure methods available in LS–DYNA are able to simulate the dynamic motion of a membranous structure and the associated fluid field. However some differences exist between the simulated and the original experimental results which result in the motion of the valve appearing slightly damped in comparison to the experimental results. These invariably stem from the inexact nature of comparison and the definition of the inlet velocity profile. Other causes of discrepancy are likely due to the the smaller number of elements used in the original structural model (8 beam elements against 26 shell elements), the implicit solution method and the buoyancy effect of the less dense valve material, which was originally acknowledged by Hart et al. [114].

3.1.6 Summary

By comparison with previous published experimental results by Hart et al. [114], the different fluid–structure coupling methods available in LS–DYNA have been assessed for the use of simulated valvular dynamics. The comparison of the different coupling techniques have shown that the most suitable cases for simulating valve dynamics are A (no bending stiffness) and B (bending stiffness). In this work, the simulations presented in Chapter 3 have been performed with bending stiffness (B) however the following simulations in Chapters 4 and 5 have been performed without bending stiffness (A). The decision to remove the bending stiffness was based upon two factors: the first was that no significant difference was noted between the cases A and B and the second was that by removing the in–plane/out–of–plane coupling, the complexity of the simulations were signficantly reduced (3+ integration points reduced to 1) at the cost of no signficant difference.

3.2 Full valve dynamics

As detailed in Chapter 1, Section 1.5, there are a number of different numerical studies of the mitral valve, with each examining a specific functional role in the function of the valve. The majority of these models have been described using a structural–only approach, currently the only fluid–structure interaction model of a native mitral valve currently reported is that of Einstein et al. [76] (and the subsequent iterations) in which the valve was positioned in a tubular fluid volume and the valve closure was simulated. All current comparisons between fluid–structure interaction and structural–only valve models refer to this model and are limited to comparison of the stress state, as no details of the dynamics of closure are reported.

In this section the differences between structural–only and fluid–structure interaction techniques have been quantified. Using a model of the mitral valve, comparison of the valvular dynamics in simulations of valve closure and a full cardiac cycle have been performed using structural only and fluid-structure interaction approaches in the finite element solver LS–DYNA. As previous fluid–structure interaction studies of the mitral valve have been performed solely in tubular geometries [76], the effect of the fluid volume on valve dynamics and vice versa have also been quantified by using both tubular and ventricular shaped fluid volumes. The role of the fluid volume has particular implications for the hydrodynamic testing of artificial valves as all current tests are performed in straight fluid chambers as required by current ISO regulations [116] and FDA Replacement Heart Valve Guidance [117].

3.2.1 Valve model

The model presented here is referred to as the isotropic model previously in Chapter 2 and is based upon anatomical measurements and descriptions previously reported by Sakai et al. [19] and Ho [9]. Here the annulus of the model has been defined as a static planar D–shaped orifice, the annular proportions and lengths of the different leaflet cusps have been defined from anatomical measurements of excised human valves [19]. Studies on porcine mitral valves have shown that the annular length of an intact valve is shorter than that of an excised valve [11], for this reason the annular length of each cusp segment has been adjusted from the reported excised value and scaled to the corresponding annular segment of the model. The total annular length of the model is 85.7 mm and the annular lengths of the different leaflet sections are listed in Table 3.4. The leaflets of the valve model extend outwards from the annulus towards the free margin of the leaflets, which has been defined using splines connecting the midpoint of each cusps (defined as the leaflet height) to an interface point, defined as 7.5 mm above the annular plane, between each cusp. In this model only the primary chordae tendineae, which are attached to the free margin of the leaflet, have been modelled. The number and location of these chordae have been based on anatomical descriptions [16, 19]. These chordae have been modelled as attached to a static node which represents the papillary muscle tip, positioned in a plane 20.0 to 22.0 mm above the annular plane (Figure 3.6). The location of papillary tip was adjusted to ensure coaptation of the leaflet occurs with the application of physiological pressure.

The initial geometry of the valve model was defined with the leaflets in an open configuration and in order to reduce the computational time required, only half the model was simulated. Here the plane of symmetry was defined as the anteroposterior axis of the valve, as shown in Figure 3.6.

Table 3.4: Dimensional parameters of the mitral valve model.

Leaflet	Annular length [mm]	Leaflet height [mm]	Leaflet area [mm^2]
Anterior	28.9	23.4	444.3
Commissural	7.0	8.7	46.1
Posterior (P2)	17.4	13.8	177.7
Posterior (P1/P3)	12.7	11.2	111.4

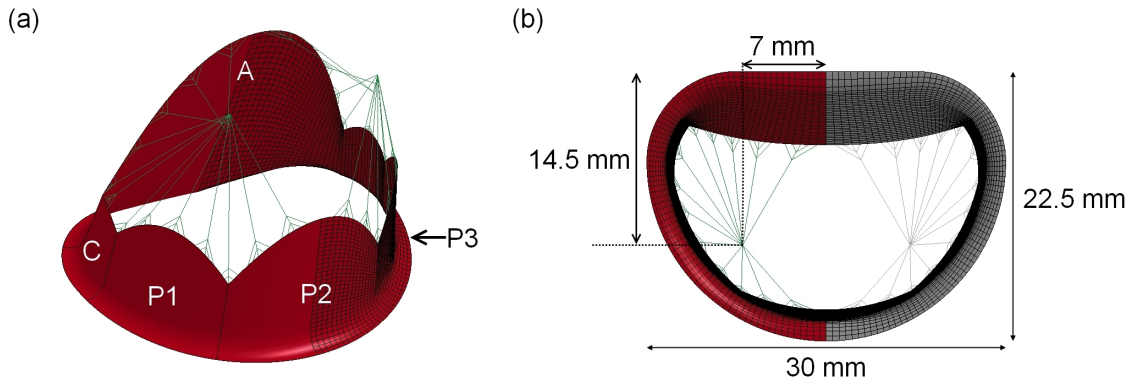

Figure 3.6: (a) Profile of the mitral valve model, with and without the finite element shell mesh; leaflet labels: A – anterior leaflet, C – commissural leaflet, P1/P3 and P2 – side and central cusps of the posterior leaflet. (b) Model profile as viewed from the left atrium with the anteroposterior (22.5 mm) and commissural (30 mm) diameters labelled; the reflected component of the geometry is represented in grey.

3.2.2 Material model

As the main aim of this work was to characterise the differences in structural and fluid–structure interaction techniques the problem has been simplified. Here the material properties of the valve leaflets and chordae tendineae have been simplified and modelled as isotropic linearly elastic materials, neglecting their non–linear elastic behaviour and anisotropy.

Implemented with the standard material model `MAT_ELASTIC`, both anterior and posterior leaflets have been defined with the same material properties. Here the chordae have been modelled as only generating force solely under tension and have defined using the standard material model `MAT_CABLE_DISCRETE_BEAM` [79, 80] (Table 3.5).

Table 3.5: Leaflet and chordae tendineae material properties.

Variable	Shell	Beam
Elastic modulus [MPa]	3	40
Poisson's ratio [–]	0.45	–

3.2.3 Valve model – finite element mesh

The geometry of the valve model was discretised into a finite element mesh of shell elements for the leaflets and beam elements for chordae tendineae. Here the leaflets have been defined using Belytschko–Lin–Tsay shell elements with a constant thickness of 0.75 mm. The chordae have been defined using discrete beam/cable elements, which collapse under compression, with a uniform cross–sectional area of 0.6 mm^2 [79, 80]. The density ρ of all structural components has been defined as $\rho = 1000\ kg{\cdot}m^{-3}$.

The independence of the finite element solution to the size of the elements in the valvular model was determined independently of the fluid model. Using the closure conditions in a structural–only analysis, the mesh sizing was determined to be sufficient by performing a mesh independence analysis (see Chapter 2, Section 2.4.1.1). The final model consisted of 2688 shell elements and 333 beam elements (Figure 3.6).

3.2.4 Fluid volumes

Fluid–structure interaction has been performed by immersing the valve model into separate overlapping tubular and ventricular shaped fluid volume. Static and rigid with a fixed volume, the geometry of these fluid volumes represent the left ventricle of the heart only and have been sized on the volumetric

measurements of the left ventricle. As the fluid–structure interaction simulations include aspects of systole and diastole, an intermediate volume of 35 cm^3 for the atrial section and 85 cm^3 for the ventricular section has been chosen. The fluid volume geometries and the surfaces used to apply the transvalvular pressures are shown in Figure 3.7.

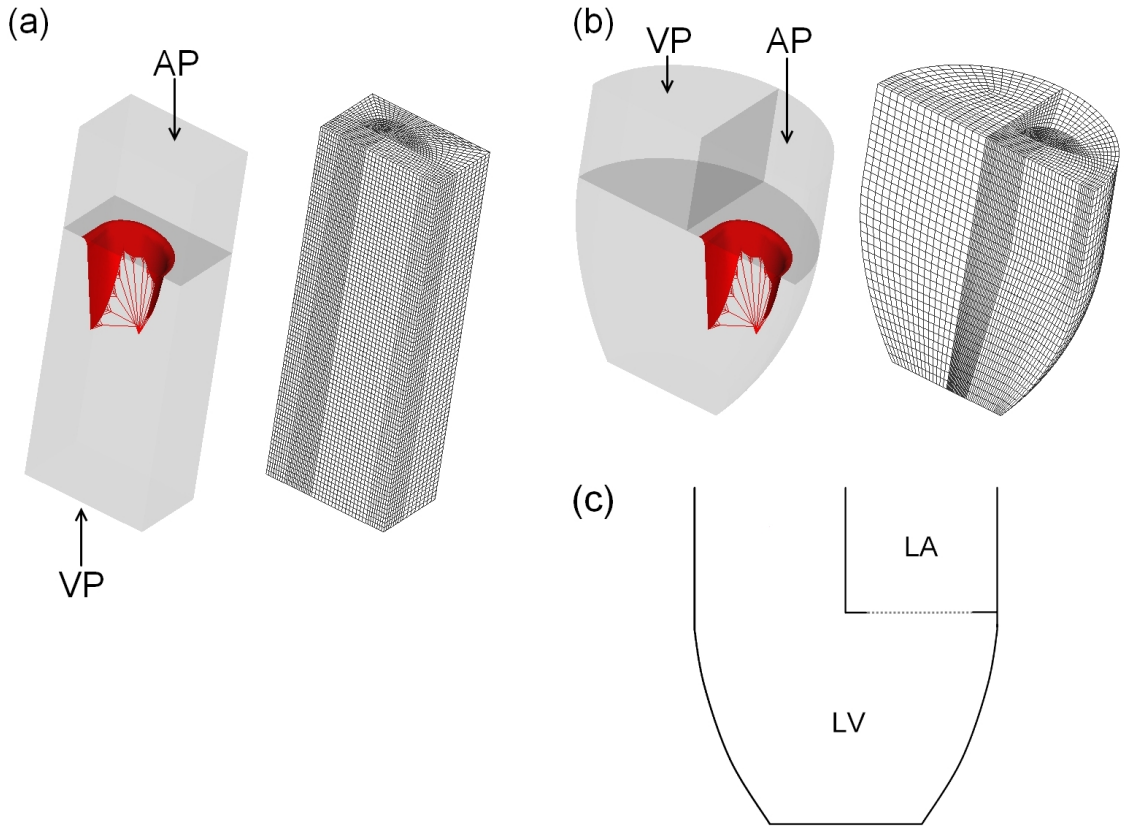

Figure 3.7: (a) tubular fluid volume and mesh and (b) ventricular fluid volume and mesh; Figure labels AP and VP denote the atrial and ventricular pressure surfaces respectively. (c) schematic outline of the ventricular fluid volume with the solid boundaries (solid lines) and annular orifice (dotted line) labelled.

3.2.5 Fluid parameters

Parameters have been chosen to reflect the higher density and dynamic viscosity of blood, which has been modelled as a Newtonian fluid (Table 3.6) Here the fluid material model `EOS_GRUNEISEN` has been used, in order to increase the maximum permittable time step the compressibility of the fluid has been reduced (see Chapter 2, Section 2.4.2.2).

Table 3.6: Newtonian fluid properties used to represent blood. Note that the bulk modulus has been reduced in order to increase the maximum permittable time step (see Chapter 2, Section 2.4.2.2).

Parameter	Value
Density [g·cm^{-3}]	1.00
Dynamic viscosity [Pa·s]	0.004
Fluid speed of sound [m·s]	148.4

3.2.6 Fluid volumes – finite element meshes

The geometry of the two fluid volumes was discretised into solid LS–DYNA ALE fluid elements, with a mesh designed such that the valvular orifice matched the shape of the valve annulus (Figure 3.7). As with the structural mesh, the element size of the fluid mesh was selected such that the independence of

the solution to the mesh was obtained. This was performed by applying a velocity boundary condition to the inlet of each model equal to $1 m \cdot s^{-1}$. The solution was considered converged when the absolute difference in the velocity between subsequent timesteps was of the order of 10^{-6}. Once stabilised, the velocity across the valve plane was compared until the difference between subsequent models was reduced to less than 5% in the region of interest. The final models of the tubular and ventricular volumes consisted of 81,920 and 43,008 solid brick elements respectively, as shown in Figure 3.7. The ventricular pressure plane (VP in Figure 3.7) was defined at the plane of the outlet of the fluid volume in both fluid–structure interaction models.

3.2.7 Transvalvular pressure difference

The pressure applied to both structural and fluid–structure interaction models has been taken from Levick [1], the reported curves have been digitised and then formatted into an appropriate format suitable for LS–DYNA (Figure 3.8). Using the structural and fluid–structure interaction models, the structural and fluid dynamics have been simulated using two different pressure loads: (1) early systolic pressure ramp simulating valve closing (ESPR in Figure 3.8) and (2) a full cardiac cycle simulating both valve opening and closing.

For the full cardiac cycle the pressure difference illustrated in Figure 3.8 is input directly as a pressure load onto the fluid volume/structural model. For the early systolic pressure ramp, the transvalvular pressure applied to the model was measured as the difference from the point of the left atrial/left ventricle pressure cross-over until the maximum of ventricular pressure. The maximum ventricular pressure was sustained for a further 22 ms, in order to ensure the valve was in a static configuration, taking the total simulation time to 200 ms.

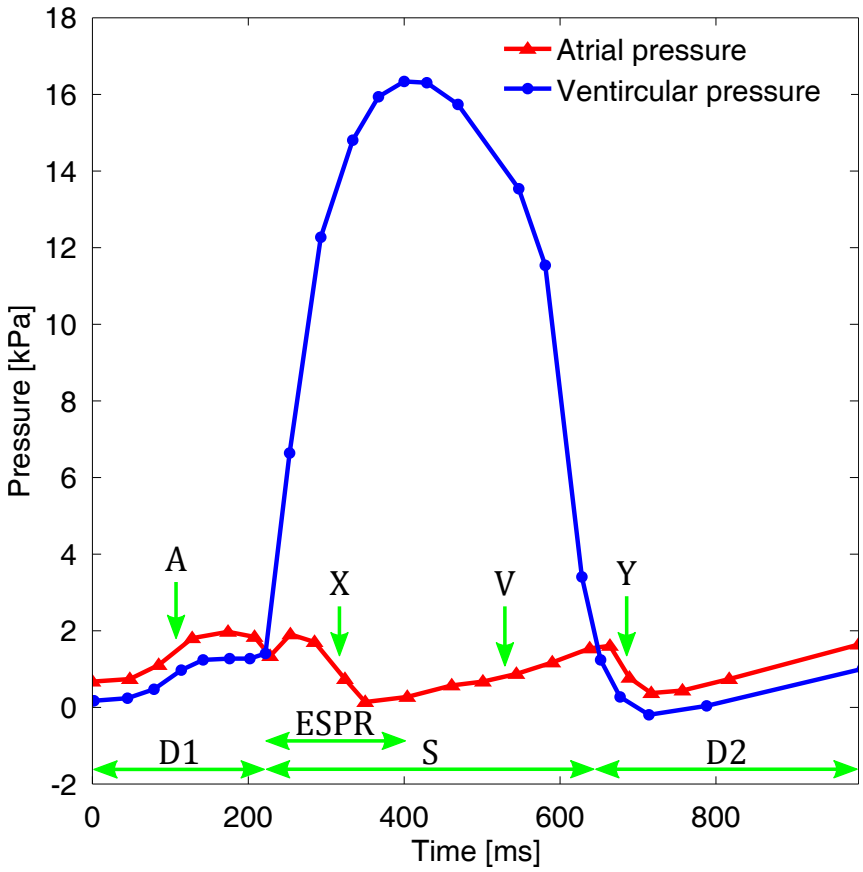

Figure 3.8: Transvalvular pressure load, values after Levick [1]. Label definitions – D1, 1st diastolic phase, valve open; ESPR, early systolic pressure ramp, valve closing; S, systolic phase, valve closed; D2, 2nd diastolic phase, valve open; A, atrial systole (A wave); X, atrial relaxation (X wave); V, atrial filling (V wave); Y, atrial emptying (Y descent).

3.2.7.1 Structural–only simulations

The transvalvular pressures described in Figure 3.8 were applied directly to the structural model as a uniform pressure load distributed over the corresponding atrial and ventricular sides of the leaflet structure. As before, the nodal velocity of the valve structure was scaled using a global damping factor of 0.9965, a value which was based on previous experience [111]. In order to model the valve as a single surface structure, a contact penalty condition was applied to all the shell elements of the model.

3.2.7.2 Fluid–structure interaction simulations

In the fluid–structure interaction simulations, the transvalvular pressure was applied to the boundaries of the fluid models (see Figure 3.7) and the resulting fluid flow has been coupled to the structure of the valve by a penalty coupling method: if the fluid contacts and penetrates the structure of the valve, a resistive force linearly proportional to the distance penetrated is applied to both the fluid and the structure, thus coupling them together [79, 80]. Under the application of the ventricular pressure ramp (ESPR) the fluid–structure coupling has only been applied to the ventricular side of the valve, as fluid only approaches from this side. In the full cardiac cycle simulation this coupling was applied to both atrial and ventricular sides of the valve, as fluid flow approaches the valve from both atrial and ventricular sides. Fluid flow was restricted to flow through the valve by applying a no-slip condition to the nodes in the plane of the valve. The boundaries of the volume, with the exception of the inflow and outflow sections (AP and VP in Figure 3.7), were also defined as no-slip.

3.2.8 Simulation details

Here a combination of different software has been used. The geometry and finite element mesh of all the models described in this work were generated using ANSYS (Release 11.0) and subsequently converted to a LS–DYNA compatible format using a custom written script. All the numerical simulations were performed on a Intel Xeon 2.66 GHz workstation operating with LS–DYNA 971 Release 3.2.1 and post–processing of the data was performed using a combination of Ensight 9.1, LS–PREPOST 2.1 and MATLAB 7.6.0.

3.2.9 Valve closure simulations

In this section the dynamic behaviour of the valve in valve closure only is presented. Under the application of the early systolic pressure ramp (ESPR) the valve leaflets coapt together and remain closed until the end of the simulation. Here the structural and fluid–structure interaction models have been analysed and compared at closure, when the structure is in a static, closed configuration. The maximum values of the principal stresses at t = 200ms and their locations in the three different models are listed in Table 3.7. The corresponding stress distribution in the valve, as viewed from the ventricular side, is presented in Figure 3.9. The configuration of the valve, represented by the nodes in the anteroposterior section, at t = 200ms is displayed in Figure 3.10.

Table 3.7: Comparision of maximum value of principal stress and valvular location at valve closure.

Model	Principal stress (kPa)	Location
Structural	566.4	P2/P3 fold
Tubular	626.3	P2/P3 fold
Ventricular	635.3	P2/P3 fold

The configuration of the valve at closure in the different models is compared in Figure 3.10. In all of the models, the leaflets have coapted and the valve has closed. The gap in the fluid–structure interaction models is a numerical artifact, which has also been noted previously by Kunzelman and et al.

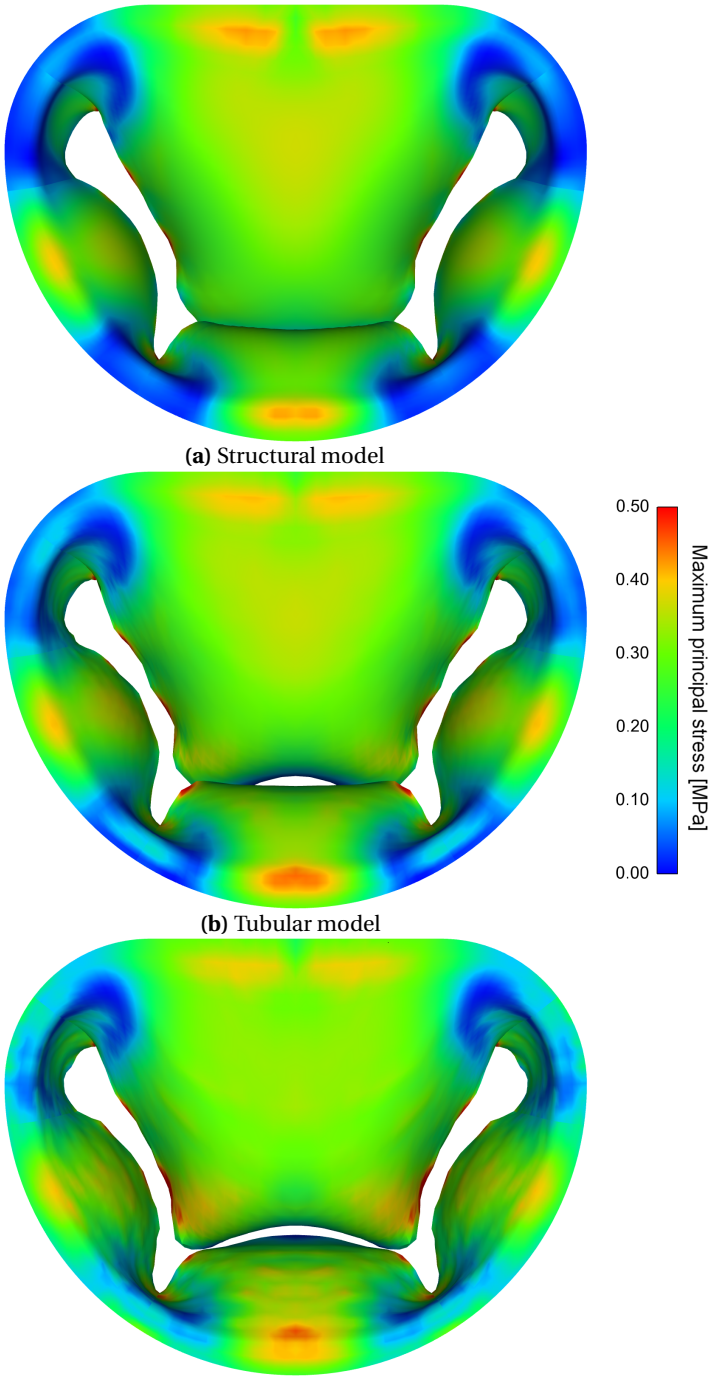

(a) Structural model

(b) Tubular model

(c) Ventricular model

Figure 3.9: Maximum principal stresses in the valve at t = 200ms in units of MPa in: (a) the structural model, (b) the tubular model and (c) the ventricular model. Stress range from 0 MPa to 0.5 MPa.

Table 3.8: Structural and FSI model simulation time for the different pressure loads.

Model	Pressure load	Approx. simulation time
Structural	Closure	6 minutes
Tubular	Closure	18 hours
Ventricular	Closure	13 hours
Structural	Cardiac cycle	50 minutes
Tubular	Cardiac cycle	90 hours
Ventricular	Cardiac cycle	65 hours

[98]. The nodal positions at the base of the valve compare well in all the models, but significant differences arise towards the leaflet tips between the structural and fluid–structure interaction models; in

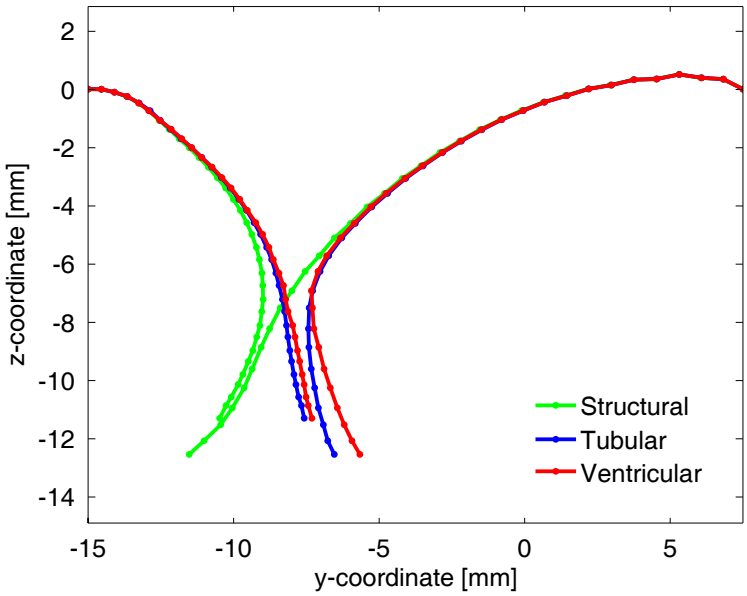

Figure 3.10: Configuration of the valve in the anteroposterior section at t = 200ms closure in the structural, tubular and ventricular models.

both these models the tips of the posterior leaflets are positioned further towards the anterior side than the structural model. This difference arises from the simplification of uniform pressure applied to the surface of the valve in the structural simulation. At the base of the valve, this assumption holds well as the pressures on each side of the valve corresponds to the pressure in the atrial and ventricular chambers. Towards the tips of the leaflets, close to the coapting surfaces, the transvalvular pressure is no longer the same as the pressure over the rest of the body and the assumption of uniform pressure no longer holds. The resulting non-uniform pressure distribution over the valve results in the difference in closure exhibited in Figure 3.10.

The corresponding distribution of local (elemental) maximum of the principal stresses are compared in Figure 3.9 and their global maxima at closure are listed in Table 3.7. Both fluid–structure interaction models presented higher maximum values of stress than the structural model, with the ventricular model with the largest value. In all models the peak stress were located at the fold of the posterior leaflet (P2/P3). From Figure 3.9 it can be seen that the distribution of stress is similar, with stress concentrations located at the base of the cusps and at the folds of the leaflet. For closure events only, structural models simulate a similar stress distribution to fluid–structure interaction models, although with a lower magnitude of stress. However structural–only models do have a clear advantage over fluid–structure interaction models in terms of the required simulation time, as shown in Table 3.8.

3.2.10 Cardiac cycle simulation

In this section the dynamic behaviour of the valve and the fluid in the full cardiac cycle is presented. In the previous section only valve closure has been simulated, here the transvalvular pressure load applied results in the simulation of opening, closing and reopening phases of the valve. This allow the examination of the opening phase following closure, a factor which has a key role in cardiac function during diastole (see Chapter 1, Section 1.3.1).

3.2.10.1 Valve dynamics

The dynamics of the valve in the two fluid–structure interaction simulations have been compared against each other and also with the structural simulation subject to the same pressure load in terms of the maximum resultant nodal velocity in the anteroposterior section of the valve during opening and clos-

ing (Table 3.9), valve configuration and nodal velocity during closure (Figure 3.11) and the change in geometric orifice area throughout the simulated cardiac cycle (Figure 3.12).

Table 3.9: Maximum anteroposterior nodal velocity during closing (C) and opening (O) phases in the structural, tubular and ventricular models, listed with the time of occurance.

Model	C/O	Time [ms]	Max. resultant velocity [ms^{-1}]
Structural	C	246	0.922
Tubular	C	254	1.202
Ventricular	C	252	1.058
Structural	O	664	0.351
Tubular	O	684	0.748
Ventricular	O	684	0.657

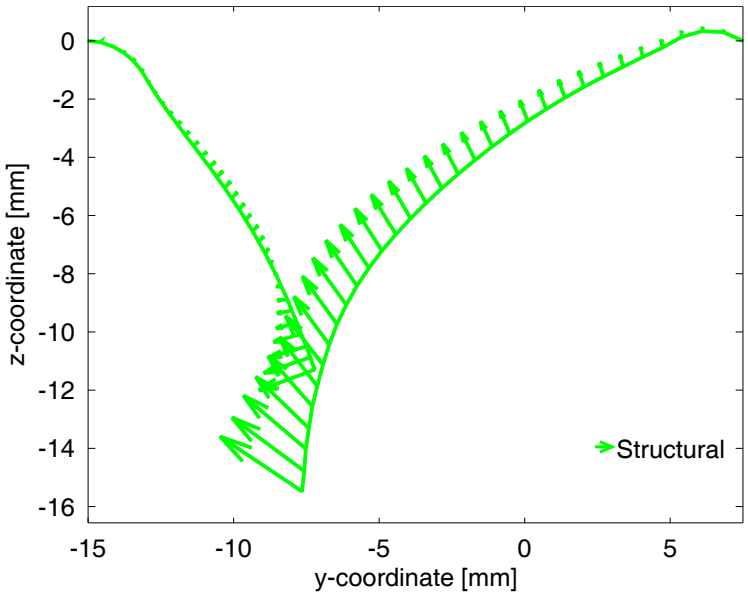

(a) Structural model

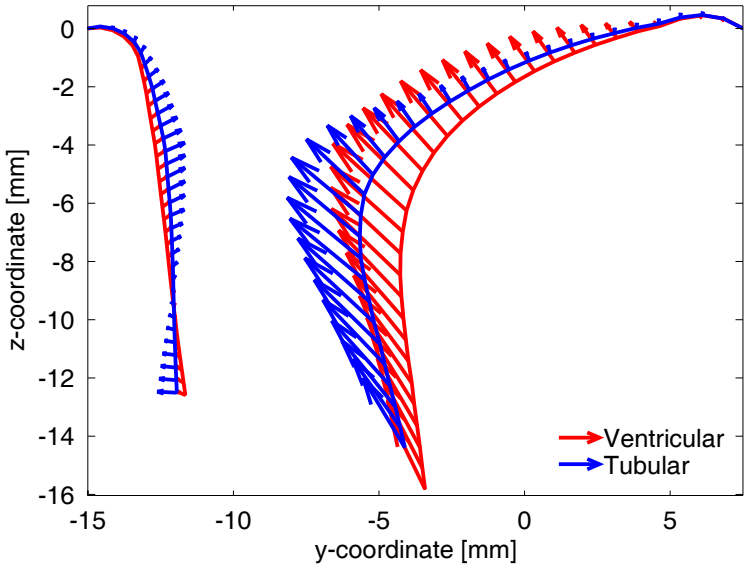

(b) Tubular and ventricular models

Figure 3.11: Valve configuration, through the anteroposterior section, at the time of maximum nodal velocity (see Table 3.9) in: (a) the structural model and (b) the tubular and ventricular models. Here the nodal positions have be drawn with the corresponding velocity vectors.

The difference in the nodal velocity of the valve structure, in the anteroposterior section, during opening and closing has been compared in Table 3.9. During closure of the valve in the S phase, the maximum nodal velocity in the structural model is comparable to the nodal velocities in the fluid–structure interaction simulations. As the valve reopens in the D2 phase, the maximum nodal velocity in the structural model is significantly lower than the fluid–structure interaction model. The nodal coordinates and corresponding velocities of the nodes in the anteroposterior section of the valve during valve opening (S phase) of the different models are presented in Figure 3.11. In the structural simulation the maximum nodal velocity occurs at the tip of the anterior leaflet when the anterior leaflet is close to impacting the posterior leaflet; whereas in the fluid–structure interaction simulations the maximum nodal velocities occur close to the centre of the anterior leaflet whilst the leaflets are still separated by a distance of approximately 5mm. From comparing the coaptation of the leaflets, subtle differences were found in the two fluid–structure interaction simulations. In the tubular model both leaflets were displaced to the centre of the orifice during closure, which resulted in the posterior leaflet making contact with the centre of the anterior leaflet. With the further application of pressure the point of coaptation then moved towards the anterior leaflet tip. In the ventricular model, the posterior leaflet sustains a smaller displacement and the anterior leaflet contacts the posterior leaflet close to the tip of the anterior leaflet and with the application of further pressure no further displacement occurs.

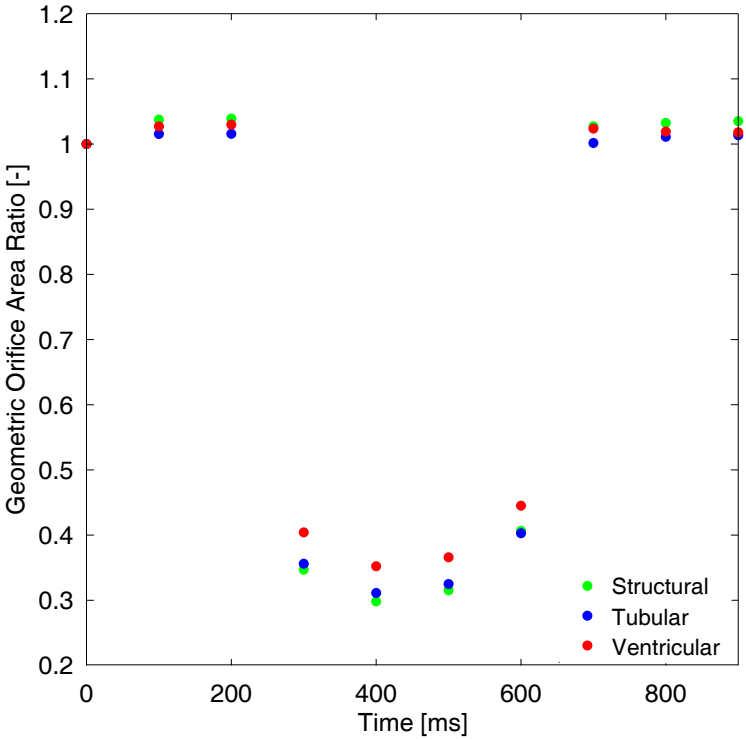

Figure 3.12: Variation in the geometric orifice area during the cardiac cycle for the structural and FSI models. This area is determined by measuring the area enclosed by the valve leaflets, relative to a plane parallel to the annulus at the height of the commissural/anterior leaflet cleft, at 100ms intervals during the cycle. The resulting area ratio is calculated relative to the initial orifice area at t = 0ms.

Variation in the geometric orifice area in both fluid–structure interaction models during the D1 and D2 phases were found to be marginally smaller than the structural model, with the ventricular model larger than the tubular model (see Figure 3.12). During the S phase the structural model presented a smaller geometric orifice area than both fluid–structure interaction models, with all models following the same trend. However the complete closure of the valve in the fluid–structure interaction models is hampered by the fluid element gap, as previously highlighted in Figure 3.10.

3.2.10.2 Fluid volume effect

The dynamics of the fluid in the two fluid–structure interaction simulations have been compared against each other in terms of the maximum fluid velocity and vorticity (Tables 3.10 and 3.11), flow field in the first open phase (Figure 3.13), particle traces during closure (Figure 3.14) and the particle traces in the second open phase (Figure 3.15).

Table 3.10: Time and maximum magnitude of the nodal z–velocity in valvular plane of the tubular and ventricular models.

Model	Time (ms)	Max. z–velocity (ms^{-1})
Tubular	255	2.738
Ventricular	254	1.857

Table 3.11: Maximum magnitude of the vorticity during closing (C) and opening (O) phases in the tubular and ventricular models in the anteroposterior plane, listed with the time of occurrence.

Model	C/O	Time (ms)	Max. of vorticity (s^{-1})
Tubular	C	257	1.21×10^3
Ventricular	C	257	0.79×10^3
Tubular	O	685	0.31×10^3
Ventricular	O	685	0.35×10^3

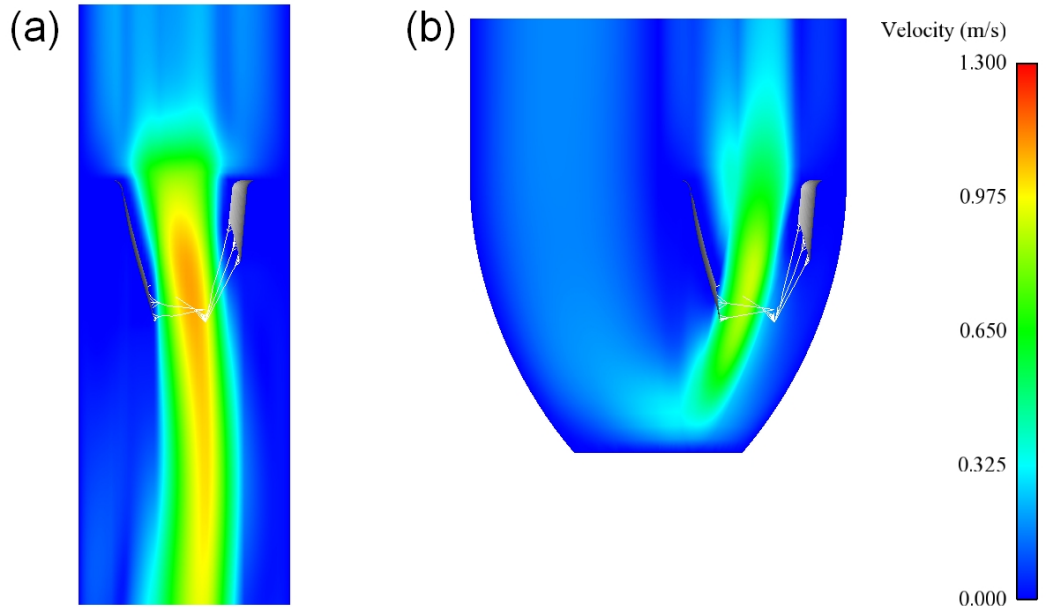

Figure 3.13: Fluid velocity during diastolic filling phase (D1) at t = 200 ms visualised in the centre of the valve model in: (a) the tubular model and (b) the ventricular model. Velocity range from 0 to 1.3 ms^{-1}.

In the D1 phase, the valve begins in an open position and flow passes through the valvular orifice into the ventricular chamber (Figure 3.13). In the tubular model the flow is directed to the posterior side by the anterior leaflet, but in the ventricular model the flow bends round the bottom of the ventricular volume towards the left ventricular outtract. Although the maximum velocity of the core of the fluid is similar between the fluid–structure interaction models, the extent of the jet is significantly smaller in ventricular model as the fluid more restricted than in the tubular model.

In the fluid domain, the change of sign in the transvalvular pressure gradient causes the flow to change direction between the D1, S and D2 phases of the pressure curve (see Figure 3.8). In the D1 phase of the cardiac cycle, the valve is open and flow passes from the atrial chamber to the ventricular chamber; the flow field during this phase (t = 200 ms) in the tubular and ventricular models, as viewed through the symmetry plane of the fluid volume, is shown in Figure 3.13.

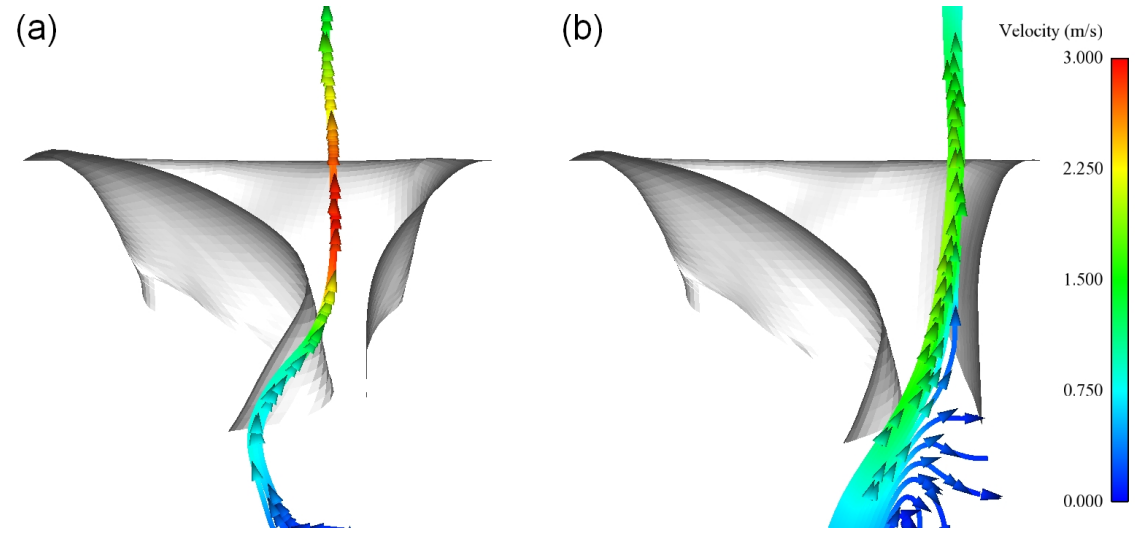

Figure 3.14: Fluid particle trace during valve closure at t = 257 ms in: (a) the tubular model and (b) the ventricular model. Velocity range from 0 to 3.0 ms^{-1}.

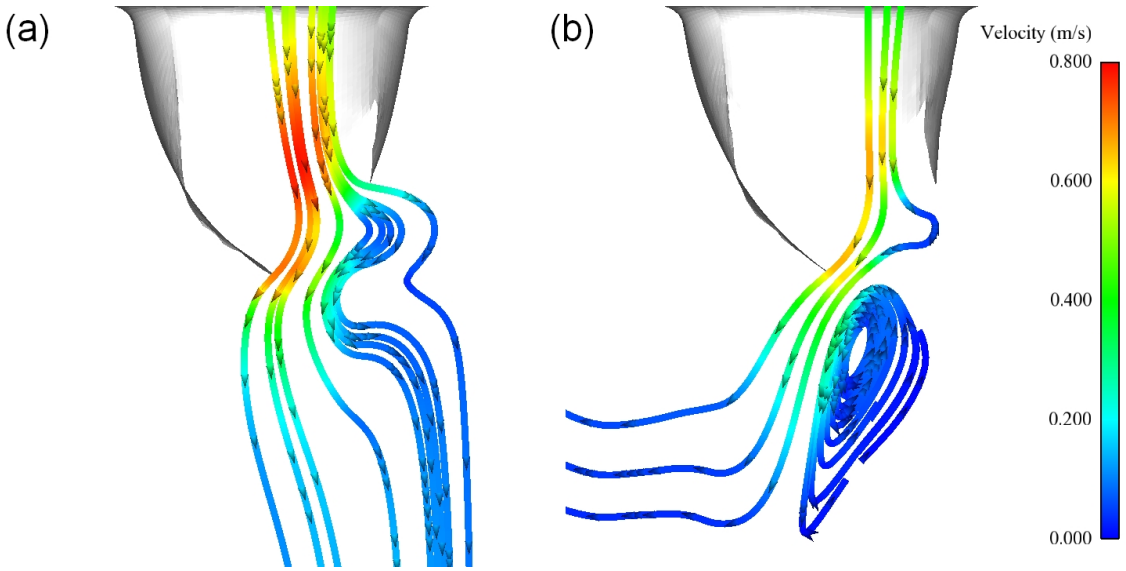

Figure 3.15: Fluid particle trace during valve opening at t = 685 ms in: (a) the tubular model and (b) the ventricular model. Velocity range from 0 to 0.8 ms^{-1}.

Following the D1 phase is the S phase, during which the flow direction reverses causing the valve to close. The closure of the valve generates a fluid jet, or dynamic regurgitation, forcing fluid back into the atrial section. The timing and maximum magnitude of the nodal z-velocity in the valvular plane in the tubular and ventricular models is listed in Table 3.10. A particle trace following the velocity field of the fluid in the tubular and ventricular models at t = 257ms is presented in Figure 3.14.

After closure of the valve in the S phase, the valve re-opens during the D2 phase. As flow enters the ventricular chamber of the fluid volume, fluid mixing generates vorticity in the flow. A particle trace following the velocity field of the fluid in the tubular and ventricular models at t = 685ms is presented in Fig. 3.15. The time points of both Figures 3.14 and 3.15 were selected to coincide with the maximum of transvalvular velocity and when the behaviour of the fluid was most evident. The corresponding maximum vorticity at both these timepoints (t = 257 ms and t = 685 ms) in both tubular and ventricular fluid geometries is listed in Table 3.11.

Following this first filling phase is the S phase during which the direction of fluid flow reverses and closes the valve. The motion of the valve during closure generates a dynamic regurgitant fluid jet in both fluid–structure interaction models. From measuring the velocity of the fluid nodes lying in the valvular

plane of the fluid volume, the maximum velocity was found to occur at approximately the same time but the magnitude in the tubular model was found to be approximately 50% greater than that of the ventricular model (Table 3.10), which correlates with the higher transvalvular flow velocities as shown in Figure 3.13. Comparison of the filling velocity compares well to values described in the literature of approximately 80cms^{-1} [118]. After the S phase comes the D2 phase, during which the valve reopens and flow passes from the atrium to the ventricle. As the valve opens a fluid jet forms, generating vorticity in the ventricular chamber of the fluid volume. Due to the faster transvalvular flow, the maximum value of the vorticity was found to be greater in the tubular model than the ventricular model (see Table 3.11). However the vorticity of the flow was found to have a larger extent in the ventricular fluid volume than the tubular volume, as highlighted in the particle traces of during reopening of the valve in Figure 3.15. Analysis of the two fluid volumes used in the fluid–structure interaction simulations has shown that the valvular dynamics, in terms of the nodal configuration at closure and the nodal velocities during opening and closing, are comparable between the fluid–structure interaction models although differences were noted in the coaptation dynamics. The effect on the coupled fluid dynamics in the fluid volumes were found to generate higher velocity flow in the tubular volume during opening and closing, along with differences in the fluid vorticity during reopening.

3.2.11 Limitations

The valvular model used in this work has been useful in analysing the differences between the structural and fluid–structure interaction modelling techniques, but it has limitations such as the uniform thickness and the linear elastic behaviour of the valve model. Although the anterior cusp and the central posterior cusp coapt successfully, the valve does not fully close in the commissural areas. Due to the expensive computational time required, the fluid–structure interaction simulations presented here have only been performed for a single cycle. The fluid volume used to represent the left atrium and ventricle have been sized using realistic volumetric measurements, but are non-physiological in that the boundaries are modelled as rigid and static; the contractility of the left ventricular chamber and the papillary muscles have been neglected. However the models incorporate aspects which have not been previously examined in heart valve modelling and offer a qualitative description of the valve behaviour under different operative conditions. The same modelling techniques can also be applied to tissue [119] and polymeric [120] valves which also undergo large deformation in response to fluid loads.

3.2.12 Summary

Here the difference between structural–only models and fluid–structure interaction models has been presented in two separate simulations, one simulating closure only and the other simulating the full cardiac cycle. From the closure simulation it has been shown that the structural model is similar to the fluid–structure interaction models in terms of the predicted stresses but not the stress magnitude or the valvular configuration. Although there are differences between the models, the numerical complexity of a fluid–structure interaction simulations highlights the suitability of structural–only simulations for the modelling of static configurations such as closed valves.

In the cardiac cycle simulation the coupled dynamics of the structure and the fluid has been examined. It was found that the behaviour of the valve varied significantly between the structural and fluid–structure interaction models due to the uniform pressure distribution in the structural model; the dynamics of the valve in the two fluid volumes were found to be similar, with subtle difference in the coaptation of the valve. Significant differences in the fluid domains of the fluid–structure interaction models were noted, with the tubular model exhibiting faster fluid velocity during both opening and closing of the valve and a reduced fluid vorticity when compared to the ventricular model.

In conclusion, structural–only models have been shown to produce similar results when consider

static/quasi–static events, but in order to accurately simulate full dynamic behaviour fluid–structure interaction models are required.

3.3 Context

Although several different numerical studies have been performed on mitral valve models, this work has characterised one of the key assumptions in these studies. Using a fluid–structure interaction method which has been evaluated against previously reported experimental results, the effect of the structural–only approximation of the haemodynamic load has been examined. Here a quasi–static simulations of closure and full cycle simulations of valve closure/reopening have been performed, previous analysis of valve dynamics have solely been quasi–static closure only or simplified full cycle simulations (for example the sinusoidal pressure load used in Kunzelman et al. [85]). Here this study has shown that the uniform pressure assumptions made in structural only models results in differences in the dynamic motion of the valve, final deformed configuration and stress distributions.

This dynamic motion has particular impact in scenarios such as the edge–to–edge repair whereby the shape of the valvular orifice is changed (see Chapter 4). During diastole the fluid loading of the valve has significantly altered from its normal uncorrected state and methods such as fluid–structure interaction are required to determine the structural load and associated stresses in the valve from the dynamic interaction of the structure and the fluid. Also, as the mitral valve regulates the flow in the heart, fluid–structure interaction models simulating normal and pathological states (such as valvular stenosis where valvular motion is restricted) are important.

Chapter 4

Valvular Repair Techniques

Complementing *in vivo* and *in vitro* experimental techniques, numerical simulation of surgical repair techniques offer additional insight into valvular function. Variables which are unmeasurable experimentally, such as the internal stresses of the valve, can be approximated in physiological scenarios through numiercal modelling methods. Here a fluid–structure interaction modelling technique has been used to address the simulation of a valvular repair technique known as the edge–to–edge surgical repair technique. Described in further detail in Section 4.1, the following two issues related to modelling the edge–to–edge repair have been examined within this chapter:

(1) Fluid–loading approximation – Previous structural–only models of this repair technique have approximated the haemodynamic loading using an approach based upon the geometric orifice area of the valve. Here this approximation has been characterised using both structural–only and fluid–structure interaction models of an edge–to–edge repaired valve (Section 4.2).

(2) Valvular repair with or without annuloplasty – There are two main approaches through which the edge–to–edge repair can be applied, through open heart surgery or percutaneously, with the key difference between the two being the option of applying annular support through annuloplasty. Using a fluid–structure interaction method, the differences between the edge–to–edge repair with and without annuloplasty have been examined in a dysfunctional model of the mitral valve (Section 4.3).

The majority of the results presented within this chapter have contributed to the paper published by this author titled: "*Fluid–structure interaction study of the edge-to-edge repair technique on the mitral valve*" [121].

4.1 Clinical background

As highlighted previously, the most common dysfunction of the mitral valve is mitral valve regurgitation which accounts for ∼70% of native mitral valve dysfunctions [3]. In mitral valve regurgitation abnormal amounts of retrograde flow enters the atrial chamber increasing the haemodynamic load in the left heart, a factor which can lead to cardiac related pathologies such as ventricular and atrial dilation, hypertrophy and atrial fibrillation [5]. The etiologies this dysfunction can be divided between structural (primary) and functional (secondary) dysfunctions. Structural dysfunctions are caused by factors which affect the tissue of the valve, resulting in a loss of biomechanical strength (i.e. myxomatous mitral tissue degeneration). Functional dysfunctions result from indirect factors which do not affect the tissue, but impact the function of the valvular subcomponents (i.e. annular dilation or papillary muscle displacement) [122]. Correction of regurgitation is performed by repairing existing valve anatomy or re-

placement by prosthetic substitute. Repair is preferred if possible, as mortality rates are reduced (2.0% against 6.1% for replacement) and other related complications such as thromboses are minimised [6].

Using the existing anatomy, repair attempts to improve compromised valvular function. The most common approach is annuloplasty, in which a prosthetic ring is implanted to reshape the annulus geometry to a functional state. A range of different options exist which include rigid/semi-rigid or flexible devices, with closed or partial ring designs. Another repair method is the edge–to–edge repair technique designed by Alfieri [122]. This technique rectifies prolapse through restoring coaptation by joining the prolapsing segment(s) to the opposing leaflets. By repairing the existing valve structure the edge–to–edge repair reduces the severity of the regurgitation during systole, improving factors such as the ejection fraction [123]. However technique reduces both the geometric and effective orifice areas of the valve during diastole, altering the normal stress state of the valve and fluid dynamics during diastolic filling.

Traditionally the edge–to–edge repair is performed via a midline sternotomy and in conjunction with annuloplasty, a factor which has had positive clinical results in particular when annular function is compromised [122, 124]. Recently less invasive approaches have been pioneered whereby this repair is performed using a clip, rather than sutures. Delivered via percutaneous access through the femoral venous transseptal path, this clip consists of two metallic arms which grip and hold the prolapsing segments of the leaflets together as the heart beats [125]. Less invasive as open access to the heart is no longer required, these methods do not allow additional supplement of an annuloplasty ring.

4.2 Edge–to–edge modelling methods

Although experimental [126] and clinical studies [127] of the edge–to–edge repair provide functional understanding of the haemodynamic properties and the clinical success rate of the procedure respectively, these studies do not provide insight into how the valve itself is affected. In order to assess the biomechanical function of the valve in such states it is required to utilise numerical modelling techniques. Due to the immersed nature of the heart valves and the resulting non–uniform haemodynamics loads throughout the cardiac cycle, numerical modelling heart valves is a complex issue. As detailed in Chapter 3, this requires an approach that is able to address the large deformation of a non–linear elastic structure and the coupling of the fluid and structural domains (fluid–structure interaction).

Although fluid–structure interaction models of the native mitral valve exist, no such models of the edge–to–edge repair have previously been reported. Prior to the work reported here, all previous models of the edge–to–edge repair have been performed using structural–only modelling [105, 104, 95] or valveless fluid–only modelling approaches [106], both of which have limitations. As detailed in Chapter 3, structural–only models simplify the haemodynamic loading upon the valve as uniform. This assumption of uniform pressure has been previously shown to affect valve dynamics in terms of its deformation and stress state, particular in dynamic event such as valve opening. Although fluid–only models yield the non–uniform pressure field across the valve, these models do not account for the deformation of the valve which in turn regulates the flow through the orifice.

Here the methodology used to simulate the haemodynamic loading during diastole in structural–only models of the edge–to–edge repair have been characterised against comparative fluid–structure interaction simulations. In previously reported structural–only models (see Dal Pan et al. [104] for example) the transvalvular pressure difference used to simulate diastole has been defined using a numerically derived relationship based upon the flow rate. Using the same flow rate in a fluid–structure simulation, the effect of this uniform pressure load on the resulting stress state and deformed configuration of the valve have been compared.

4.2.1 Mitral valve model

The geometry of the mitral valve used here is a modified version of the model described in Chapter 2 as the orthotropic model. In order to model the effect of the edge–to-edge correction, the central region of the anterior and posterior leaflet have been connected together using rigid beams by initially defining the valve in a semi–closed position (Figure 4.2). In this model the annulus has been defined with an anteropostero diameter of 24 mm and a commissural diameter of 32 mm, consistent with the 4:3 ratio described previously in Chapter 2, Section 2.1.1. The leaflets have been sized using the anatomical data reported by Sakai et al. [19], with the corresponding lengths and areas are listed in Table 4.1. Here the papillary muscle has been positioned 22 mm above the annular plane, the lateral positioning of the papillary muscle has been defined as the same as in the model described in Chapter 3, Section 3.2.1.

In order to reduce the numerical complexity the valve has been modelled as symmetrical about the anteropostero axis. The leaflets and chordae have been modelled using 952 Hughes–Liu shell elements and 658 discrete cable/beam elements respectively [79, 80]. In this model the semi–closed configuration of the valve leaflets are defined as the initial stress–free configuration.

Table 4.1: Leaflet lengths and areas of the linear orthotropic edge–to–edge repair model.

	Leaflet height [mm]	Area [mm^2]
Anterior	24.6	586.7
Posterior (P2)	13.8	188.0
Posterior (P1/P3)	11.2	310.0

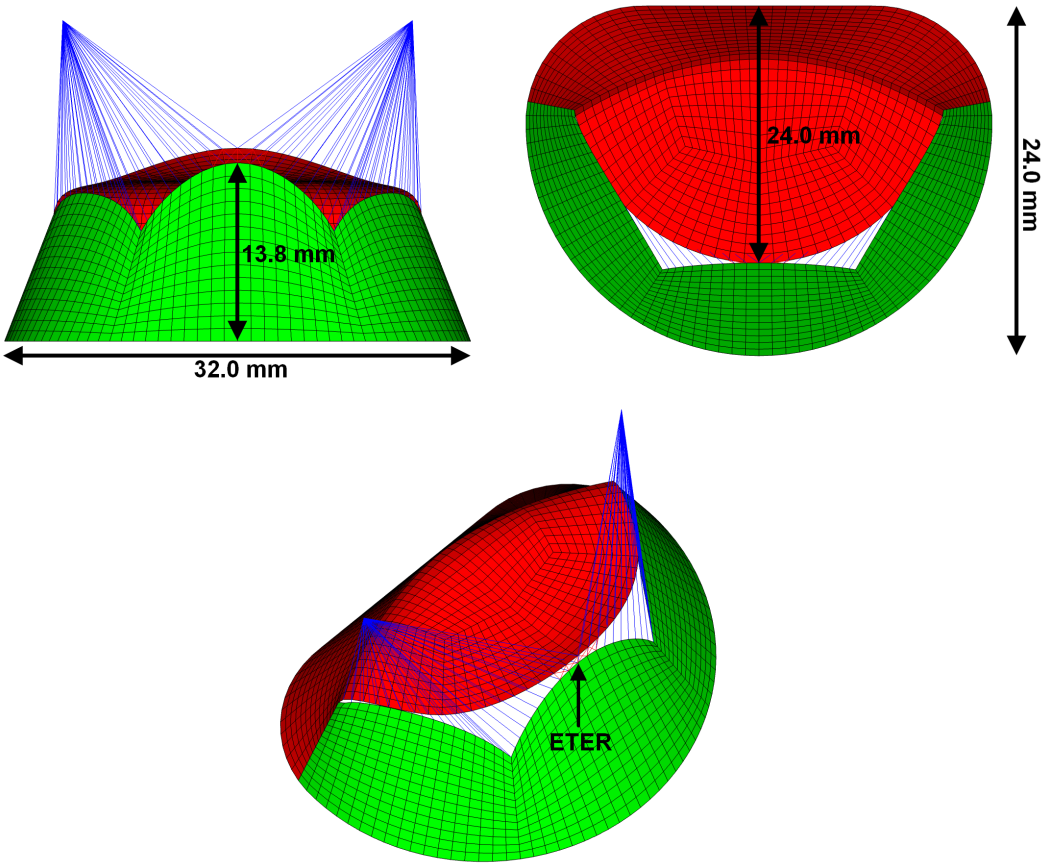

Figure 4.1: Geometry of the linear orthotropic edge–to–edge repaired model. Here the anterior leaflets are visualised in red, the posterior in green and the chordae in blue. The central anterior and posterior leaflets lengths are labelled, as are the anteroposterior and commissural diameters and the location of the edge–to–edge repair (ETER).

4.2.2 Material model

Here the material properties of the leaflets and chordae tendineae have been defined as linearly elastic materials. The anterior and posterior leaflets have been modelled as an orthotropic membrane, the stiffer fibre direction has been uniformed defined as aligned parallel to the annulus (circumferentially). The properties used here have been obtained from a previously reported study by Votta et al. [102] (Table 4.2). As before, the chordae tendeae have been modelled as beams which collapse under compression and only bear loads under tension. The elastic modulus of the chordae have been defined using the same value used previously in Chapter 3, Section 3.2 (Table 4.2). Using standard LS–DYNA material models, the leaflets and chordae tendineae have been implemented using `MAT_ORTHOTROPIC_ELASTIC` and `MAT_CABLE_DISCRETE_BEAM` respectively [79, 80].

Table 4.2: Material parameters of the leaflet shell elements and chordal beam elements. Leaflet parameters taken from Votta et al. [102]. Labels: t – leaflet thickness, v – Poisson's ratio, E_C – circumferential elastic modulus, E_R – radial elastic modulus, G_{CR} – circumferential/radial shear modulus, A – chordal cross–sectional area and E – chordal elastic modulus.

Leaflets/Chordae	Parameter	Value
Both leaflets	t [mm]	1
	v [–]	0.45
Anterior leaflet	E_C [MPa]	6.2
	E_R [MPa]	2.1
	G_{CR} [MPa]	1.4
Posterior leaflet	E_C [MPa]	2.4
	E_R [MPa]	1.8
	G_{CR} [MPa]	0.7
Chordae	A [mm^2]	0.6
	E [MPa]	40

4.2.3 Fluid model

In order to perform a fluid–structure interaction simulation, the valve model must be immersed within a fluid volume. As highlighted in Chapter 3, Section 3.2 the geometry of this fluid volume has a strong effect upon the resulting valvular dynamics. Thus in order to minimise these effects and focus upon the valve, the fluid volume used here has been described with a straight outflow section with infinite fluid boundaries (Figure 4.2). The size of the outflow section was determined by using computation fluid dynamic simulations to determine the width at which the velocity magnitude was reduced to less than 1% of the maximum fluid velocity. Using the fluid–only solver ANSYS CFX v11, a steady state analysis of the fluid field was performed using the same geometry and boundary conditions as shown in Figure 4.2. The width at which the velocity magnitude of the fluid in the symmetry plane was reduced to 1% of the maximum jet velocity was found to be 60 mm (results not shown), the dimension to which the fluid–structure interaction fluid volume was truncated to. The resulting fluid mesh consisted of 23200 solid LS–DYNA ALE fluid elements, with a mesh designed such that the valvular orifice matched the shape of the valve annulus (Figure 4.2).

4.2.4 Fluid parameters

Parameters have been chosen to reflect the higher density and dynamic viscosity of blood, which has been modelled as a Newtonian fluid (Table 4.3). Here the fluid material model `EOS_GRUNEISEN` has been used, in order to increase the maximum permittable time step the compressibility of the fluid has been reduced (see Chapter 2, Section 2.4.2.2).

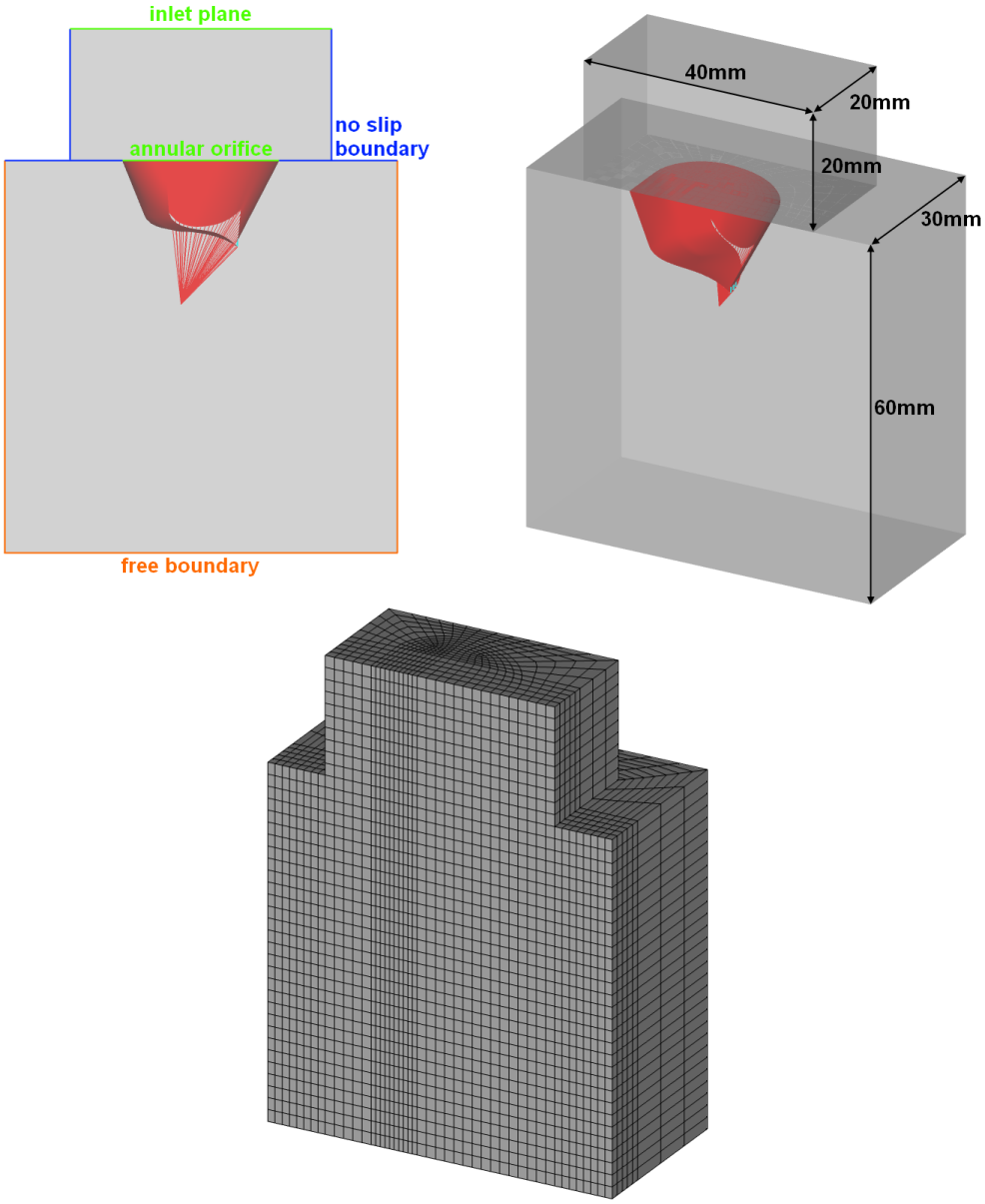

Figure 4.2: Top left – Schematic of the fluid geometry, highlighting the inlet plane, annular orifice, no–slip boundaries and free boundaries. Top right – Dimensional size of the fluid volume. Bottom – Finite element mesh of the fluid volume.

Table 4.3: Newtonian fluid properties used to represent blood. Note that the bulk modulus has been reduced in order to increase the maximum permittable time step (see Chapter 2, Section 2.4.2.2.

Parameter	Value
Density [g·cm^{-3}]	1.080
Dynamic viscosity [Pa·s]	0.0039
Fluid speed of sound [m·s]	148.4

4.2.5 Transvalvular pressure difference

In the structural–only model, the haemodynamic load of diastole has been applied as a uniform pressure. Following the approach detailed by Dal Pan et al. [104], this transvalvular pressure difference is defined as a function of the flow rate Q and the geometric orifice area A of the valve (Equation 4.1). Here the geometric orifice area refers to the visible area of the valve, which has been calculated as ∼50% of

the enclosed annular area in the initial configuration (Table 4.4).

In the fluid–structure interaction model the flow rate Q has been directly applied to the inlet plane of the fluid volume and the pressure load on the valve has been determined from the numerical coupling of the fluid and the structure, here performed using a penalty coupling method (Section 2.4.2.4). As the flow rate is constant, these simulations are quasi–static. The fluid and structural boundary conditions have been applied until the dynamic behaviour of the valve stabilises, which has occurs after ∼2s of simulation time.

$$\Delta P = 0.16 \left(\frac{Q}{A} \right)^2 \tag{4.1}$$

Table 4.4: Parameters used to calculate the transvalvular pressure drop as defined by Equation 4.1.

Parameter	Symbol	Value
Flow rate [l·min^{-1}]	Q	16
Geometric orifice area [cm^2]	A	1.97
Pressure drop [mmHg]	ΔP	10.55

4.2.6 Simulation details

As in previous structural–only simulations, the fluid effect has been approximated with the application of the global nodal dampening factor of 0.9965 (Section 2.4.1.2) [111]. For the fluid–structure interaction simulations the numerical coupling of the fluid and the structure has been performed by using a penalty coupling method (Section 2.4.2.4). All simulations and post–processing were performed on a Intel Xeon 2.66 GHz workstation with LS–DYNA 971 Release 4.2.1,LS–PREPOST 3.1, EnSight 9.1.2 and MATLAB R2010b.

4.2.7 Valve deformation

The deformation of the valve has been compared in the structural–only and fluid–structure interaction simulations (Figure 4.3). As shown previously in Chapter 3, Section 3.2.9 the deformed configuration of the valve in quasi–static states are similar in both structural–only and fluid–structure interaction simulations. Here this similarity is also noted as both open configurations of the valve are similar in profile, with the fluid–structure interaction model showing a slight increase in deformation (Figure 4.3). Inspection of the geometric orifice area, as viewed from the left ventricular side, are also similar in both structural–only and fluid–structure interaction models (Figure 4.4).

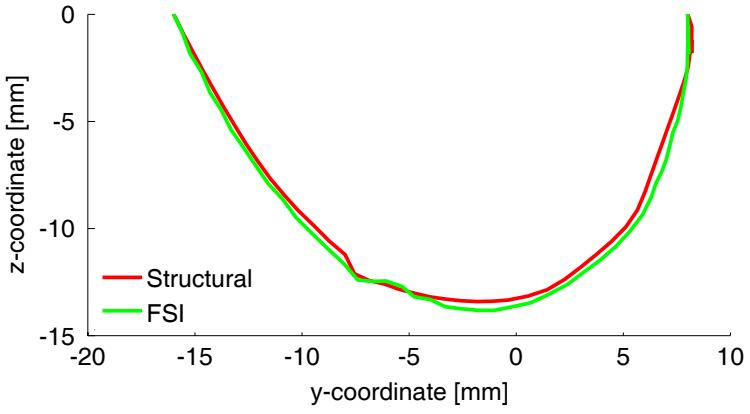

Figure 4.3: Nodal deformation in the anteropostero axis of the model in both the structural–only and fluid–structure interaction simulations.

4.2.8 Valve stresses

The distribution of the maximum principal stress of the deformed valve have been compared in the structural–only and fluid–structure interaction simulations (Figure 4.4). Comparison of the maximum magnitude of the principal stresses shows a ∼180% increase in the fluid–structure interaction case (Table 4.5). Examination of the maximum principal stress distribution show significant differences, with the fluid–structure interaction model showing larger stresses in all regions. However the peak stresses are located in the same locations in both models, at the commissural region between the two leaflets and at the location of the edge–to–edge repair.

Table 4.5: Comparison of the maximum principal stresses in the structural–only and fluid–structure interaction models.

Model	Maximum principal stress [kPa]
Structural–only	111.9
Fluid–structure interaction	324.2

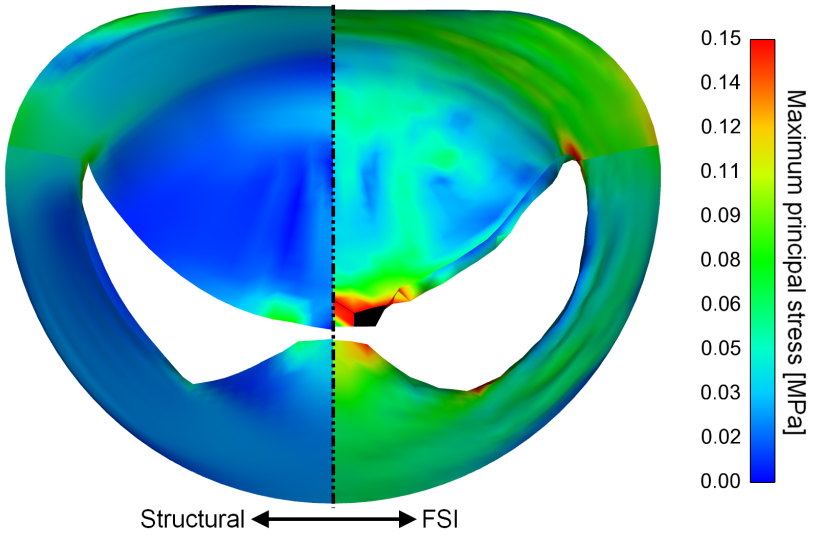

Figure 4.4: Comparison of the maximum principal stress distribution in the the valve in the structural–only (left) and fluid–structure interaction (right) simulations. Note that in the fluid–structure interction simulations, the free edge of the leaflets has aligned with the flow direction and appears as a fold in this figure. Here stress magnitudes greater than 0.15 MPa have been visualised in black.

4.2.9 Limitations

As the aim of these simulations were to assess the structural–only approach reported previously, this work is subject to several limitations. Here the material model has been simplified by describing the biomechanical response as linearly elastic, resulting in smaller deformations than in a non–linear model. The geometry of the model has also been prescribed in its repaired configuration, thus any induced stresses from this procedure have been neglected. Finally diastole has been modelled as a quasi–static event, however diastole is a dynamic event. In order to simulate the full dynamics of filling during diastole, especially in the case of a surgically corrected valve in which the fluid transport is affected, it is required to use a fluid–structure interaction method. All of these issues have been addressed in the following section, Section 4.3.

4.2.10 Summary

Here the structural–only approach based upon the transvavlvular flow rate and geometric orifice area, originally reported by Dal Pan et al. [104], has been used to simulate the edge–to–edge repair in a structural–only model. Comparison of this approach has been made against an equivalent fluid–structure interaction model defined with the same flow rate. The results of these quasi–static simulations indicate that in this model of the of edge–to–edge repair, structural–only and fluid–structure interaction methods result in similar deformed states and geometric orifice areas. However the resulting stress state is significantly greater in the fluid–structure interaction case, with increases in the maximal value of the maximum principal stress of ∼180%.

4.3 Percutanenous edge–to–edge repair

As stated previously in Section 4.2, all reported models of the edge–to–edge repair can be classified as either structural–only or fluid–only. Structural–only models have been used to examine aspects of this repair technique such as the associated stress increase in diastole from correction and the dual effect of stitch location and length. Votta et al. [95] report that during diastole a repaired valve experiences principal stresses comparable to that of systole, whereas Dal Pan et al. [104] and Avanzini [105] have shown that the lateral positioning and length of the suture both have a positive effect in reducing the magnitude of stress induced. These models have also shown that the uncorrected dilation of the annulus in a simulated dysfunctional state result in a higher value of stress during diastole. Fluid–only models have been used to study the effect of a double orifice (central leaflet correction) and an asymmetric single orifice (commissural leaflet correction) on the haemodynamic properties of diastole. The results of Redaelli et al. [106] indicate that the transvalvular pressure drop is a function of the total cross–sectional area of the repaired valve. However fluid–only approaches do not account for the presence of the valve, which in its repaired state increases the haemodynamic resistance during diastole [126].

As detailed above in the Section 4.2, the structural–only approaches used to analyse the stress state of the valve during diastole underestimate the maximum magnitude of the maximum principal stress by a factor of ∼1.8. Thus in order to correctly address the valvular and fluid dynamics of a corrected valve during diastole, it is required to use fluid–structure interaction methods. In this section a fluid–structure interaction model of a centrally corrected edge–to–edge repaired valve is presented in which both normal (with annuloplasty) and percutaneous (without annuloplasty) approaches have been examined. Using non–linear material models to represent the mitral valve, the simulation of the coupled function of the valve and blood have been performed in normal and dysfunctional states representative of functional mitral valve regurgitation. Here this dysfunctional state has been simulated by annular dilation, assuming that the biomechanical properties of both the leaflets and chordae remain constant between the normal and dysfunctional states, a factor traditionally reflective of functional regurgitation. Simulation of diastole has been performed and the resulting variation in stress states and fluid dynamics in these corrected states have been then been compared to the uncorrected valve.

4.3.1 Normal valve model

The model presented here is referred to as the orthotropic model previously in Chapter 2. The model geometry is based upon anatomical measurements reported from *in/ex vivo* sources and has been modelled as symmetric about the anteropostero axis, allowing for the computational simplification of only simulating half of the valve. The base of the model, the normal (undilated) annulus was defined as a static and planar D–shaped orifice with an anteropostero and commissural diameters of 22.5 mm and 30 mm respectively (Figure 4.5). Using the centre of the anterior leaflet as a reference point, the annular extent of the valvular cusps was defined by scaling reported data [19] to the D–shaped orifice. The

perimeter of the annulus and its enclosed area in the normal state are 8.67 cm and 5.54 cm^2 respectively.

Extending from the annulus are the cusps of the leaflets, represented here by the larger anterior and three smaller posterior cusps (Figure 4.5). Sized from anatomical measurements [11], the areas formed by the leaflets have been meshed using rectangular shell elements. Measurements of the leaflet thickness show regional differences between leaflets [54], however no detailed description of this variation exists in the literature. This variation in thickness has been simplified by modelled both leaflets as uniformly equal to 1 mm. In total the mesh consisted of 4000 Belytschko–Lin–Tsay shell elements [79, 80], the resolution was determined to be sufficient by performing a mesh independence analysis (see Chapter 2, Section 2.4.1.1).

During valve closure inversion of the valve is prevented by the chordae tendineae, structures which are classified by the anatomical position where they attach to the leaflet. Here only the marginal and basal chordae have been included, which support the free edges of the leaflets and the base of the valve near the annulus respectively. Anatomical observations indicate that the number and distribution of the chordae vary significantly, for example the number of marginal chordae attached to the anterior leaflet can range from 5 to 13 [16]. Here in this model, the distribution of the chordae has been defined in order to achieve physiological coaptation under closure conditions. In total, the chordae consist of 1666 discrete beam/cable elements [79, 80]. The cross–sectional area of the marginal and basal chordae have been taken as 0.45 mm^2 and 1.15 mm^2 respectively, as reported in Kunzelman and et al. [98]. Here the density ρ of all valvular parts has been taken as $\rho = 1\,g \cdot cm^{-3}$.

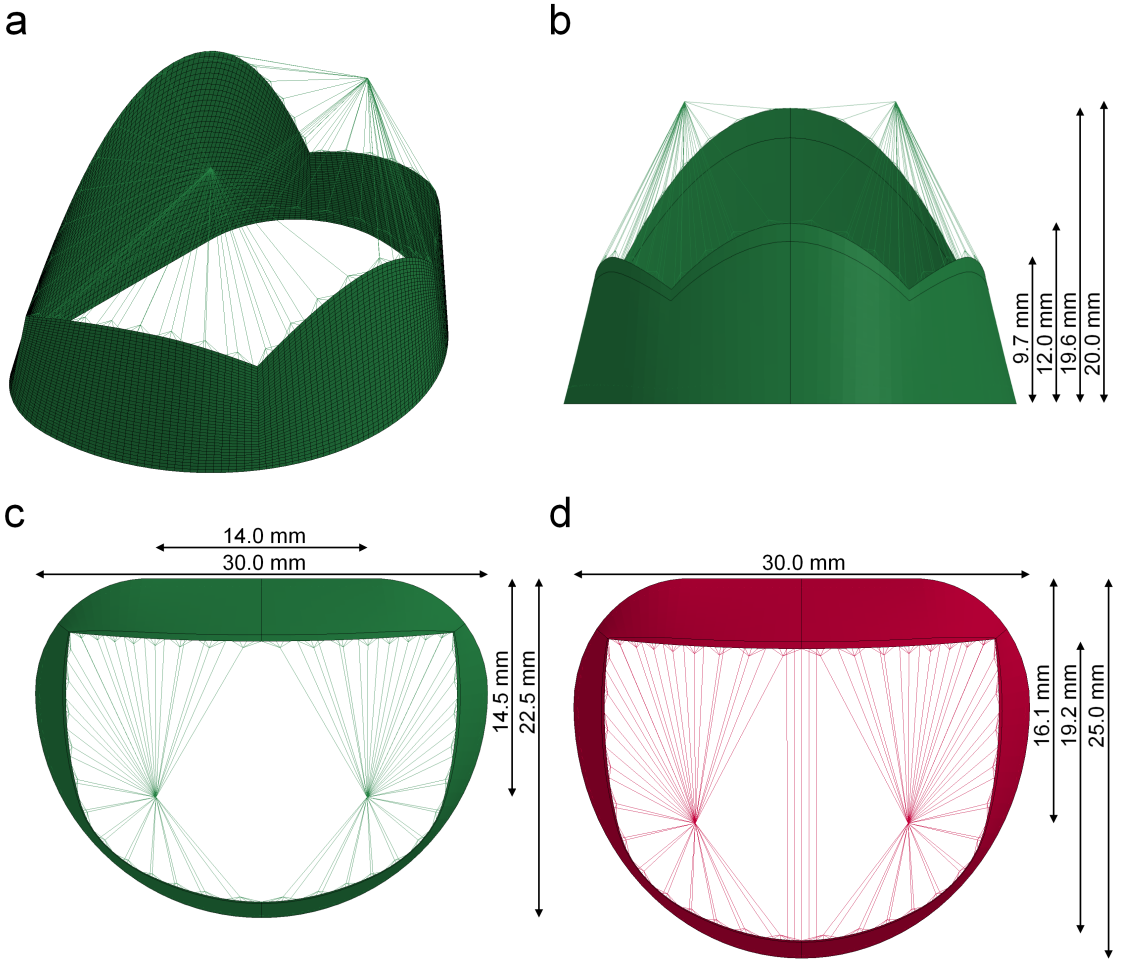

Figure 4.5: Finite element model of the mitral valve: (a) 3D view with finite element mesh superimposed , (b) front view, (c) top down view (normal) and (d) top down view (dysfunctional).

4.3.2 Dysfunctional valve model

In vivo echocardiographic comparison of human patients with both normal and regurgitant function have shown that the annulus of the valve is more dilated in this dysfunctional state [28]. Under normal conditions the annulus is a highly dynamic structure, varying in eccentricity[1] from 0.57 at mid–systole to 0.42 in mid–diastole. In dysfunctional states the annulus of the valve is less dynamic, varying from 0.50 in mid–systole from 0.42 to in mid–diastole [28].

Using the data reported by Kaplan et al. [28], a dysfunctional state was modelled by dilation of the valvular orifice in the anteropostero axis. Following this, correction was simulated in two separate scenarios in order to examine the difference between traditional and endovascular techniques for the edge–to–edge repair. Comparison of these states was performed against an undilated and uncorrected model, which is referred to as the normal state.

Here a state of functional mitral valve regurgitation has been modelled where dysfunction is generated from a change in annular dimension, whilst the function of the leaflets and chordae has been assumed to remain normal. The annulus of the model has been dilated in the anteropostero axis by a factor of 1.11 which decreases the eccentricity from 0.66 to 0.56, consistent with the average reduction in eccentricity of 15.5% during diastole as reported by Kaplan et al. [28] (see Figure 4.5). The result of this dilation increased the leaflet surface area by 3.7%, annulus length to 8.96 cm and the annular orifice area to 6.04 cm^2. This modified geometry is the reference geometry for the dysfunctional state and was defined as stress–free. Both normal and dysfunctional models have been defined using the same material model which is described in the following Section 4.3.3.

4.3.3 Material model

The biomechanical response of the anterior and posterior leaflets have been defined using the biaxial stress–strain experiments performed by May-Newman and Yin [54]. Using the reported stress–strain curves, key data points have been discretised and input into the material model `MAT_NONLINEAR_ORTHOTROPIC` in LS–DYNA [80] (Figure 4.6). Here the leaflets are modelled as membranes, thus reduced integration across the shell thickness has been defined. The biomechanical response of the chordae have been modelled as beams which generates force solely under tension. The non–linear tensile properties of the chordae have been defined from experimental data reported by Kunzelman and Cochran [67] and were input into the material model `MAT_CABLE_DISCRETE_BEAM` [80].

4.3.4 Fluid–structure interaction model

Fluid–structure interaction has been performed by immersing the valve model into an overlapping U–shaped fluid domain, volumetrically sized with left ventricular and atrial volumes of 85 and 35 ml respectively (Figure 4.7) [1]. Although the ventricle has been defined using an un–physiologically rigid volume, previous fluid–structure interaction analysis has shown that difference in valvular dynamics exist between straight and more physiological U–shaped geometries [115] (see Chapter 3). Using a structured mesh, the volume was designed to include the shape of the mitral and aortic orifices (Figure 4.7). The final meshed geometry of the fluid volume with the normal annulus consisted of 20430 LS–DYNA 8–node brick elements. In the dilated geometry the larger orifice increased the number of fluid elements, resulting in a fluid volume with 30618 elements.

Parameters have been chosen to reflect the higher density and dynamic viscosity of blood, which has been modelled as a Newtonian fluid (Table 4.6). Here the fluid material model `EOS_GRUNEISEN` has been used, in order to increase the maximum permittable time step the compressibility of the fluid has been reduced (see Chapter 2, Section 2.4.2.2). Mesh independence was verified on a series of fluid–only analyses by applying the pressure boundary condition of the full simulation up to maximum value of

[1] Eccentricity (e) is defined as $e = \frac{\sqrt{a^2-b^2}}{a}$, where a and b are the major and minor axes of the orifice.

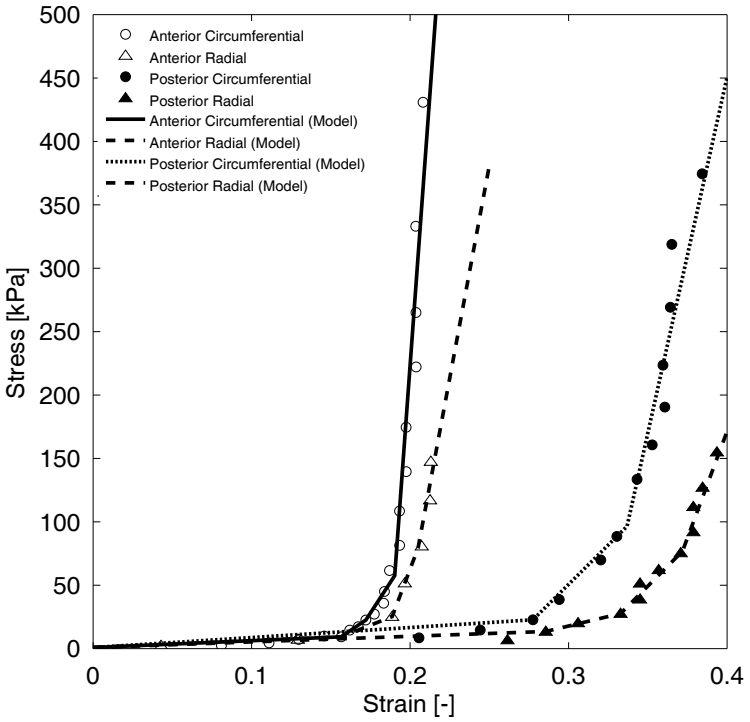

Figure 4.6: Stress–strain curves used to define the circumferential and radial elastic moduli in the anterior and posterior leaflets. Here the experimental data of May-Newman and Yin [54] is represented using the following figure labels: ○ – anterior circumferential, △ – anterior radial, ● – posterior circumferential and ▲ – posterior radial.

pressure described in Figure 4.8 (see Chapter 2, Section 2.2.2). In these simulations coupling of the fluid to the structure has been performed using a penalty coupling method [79, 80] (see Section 2.4.2.4).

Table 4.6: Newtonian fluid properties used to represent blood. Note that the bulk modulus has been reduced in order to increase the maximum permittable time step (see Chapter 2, Section 2.4.2.2).

Parameter	Value
Density [g·cm^{-3}]	1.080
Dynamic viscosity [Pa·s]	0.0039
Fluid speed of sound [m·s]	148.4

4.3.5 Simulation of diastole

Previous transient fluid–structure interaction simulations of a single cardiac cycle (∼1000ms) with the available computer equipment has been shown to require ∼100 hours of computer time [115]. Here the focus is in the diastolic component of the cardiac cycle, thus these simulations have been limited to this portion of the cycle. The transvalvular pressure difference across the valvular orifice during diastole has been represented using a 6th order Fourier series (Figure 4.8). Here the the units of pressure and time are defined as mmHg and ms respectively. In the dysfunctional states, prior to the application of this diastolic pressure difference which signifies the start of diastole, the simulation of the edge–to–edge repair is performed as detailed in the following section.

$$\Delta P(t) = a_0 + \sum_{n=1}^{6} a_n \cos(n w t) + \sum_{n=1}^{6} b_n \sin(n w t) \tag{4.2}$$

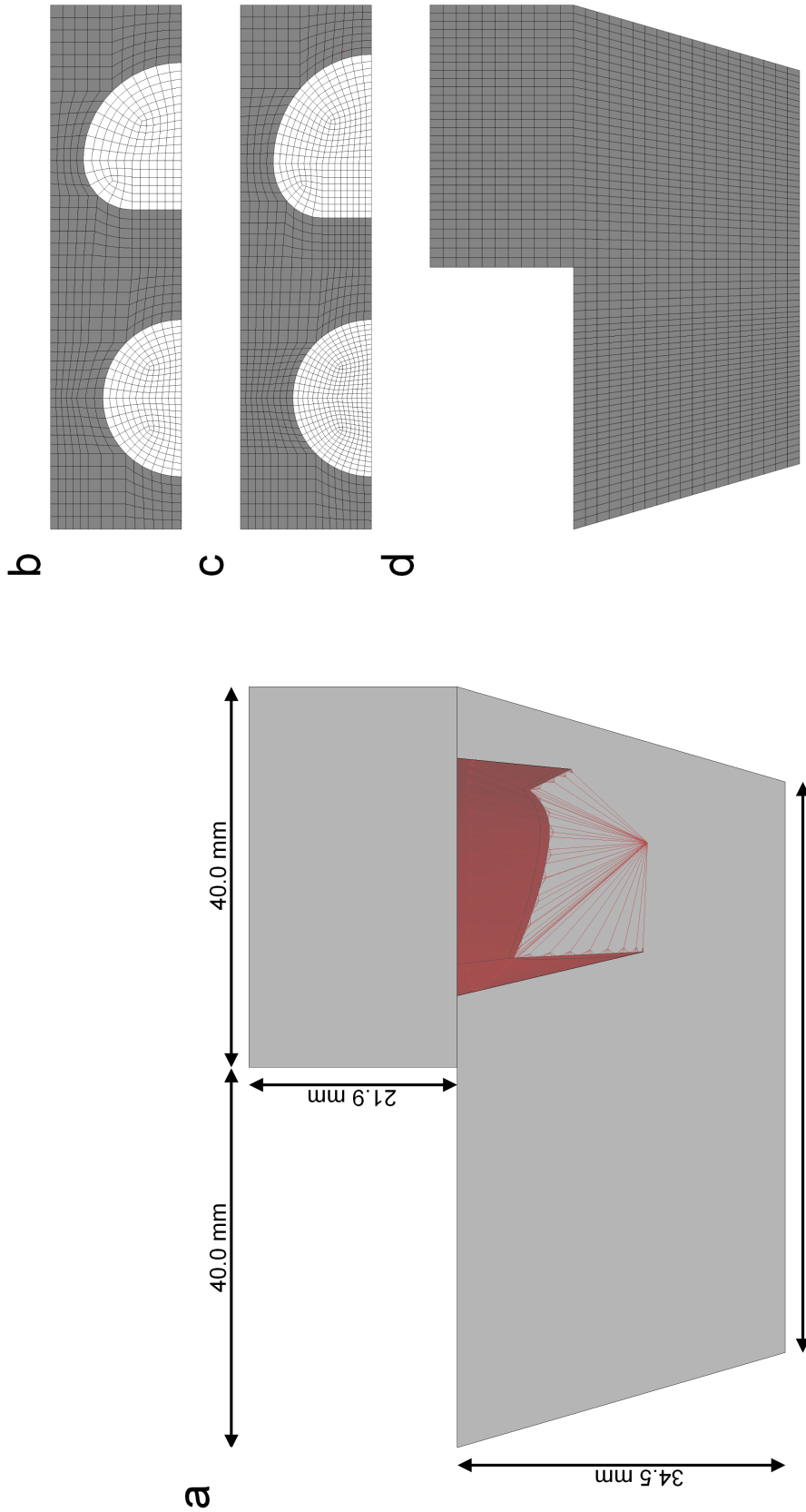

Figure 4.7: (a) Fluid volume geometry in which the mitral valve model is immersed into (highlighted in red), (b) top down view of the normal mesh with the valvular orifices highlighted in white, (c) top down view of the dilated mitral annulus model and (d) side view of the normal fluid volume mesh. The volume of the atrial and ventricular chambers were sized to 35 ml and 85 ml respectively.

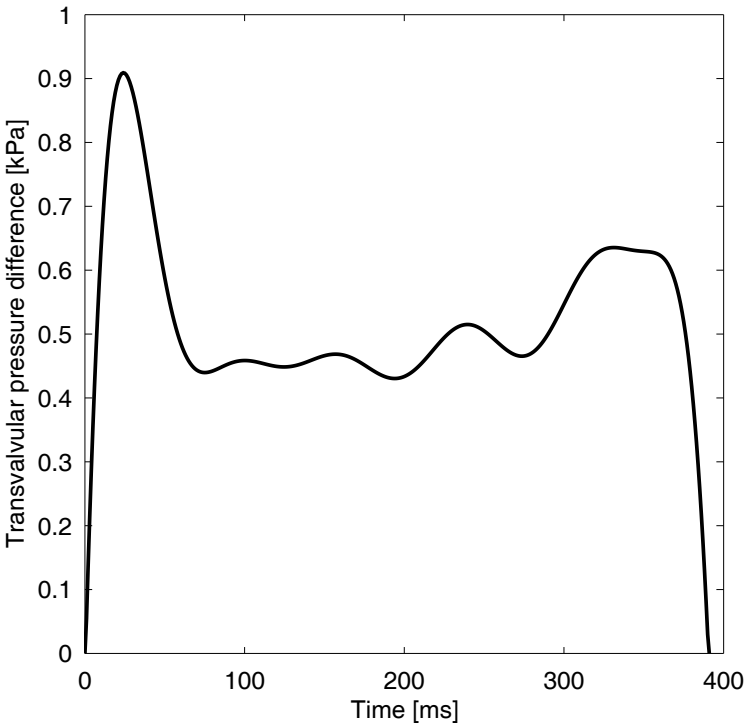

Figure 4.8: Transvalvular pressure difference between left atrium and ventricle during diastole. The zero pressure difference marks the pressure cross–over points in the cardiac cycle, indicating the start and end of diastole. Average transvalvular pressure was 0.52 kPa (3.9 mmHg). Data after Levick [1]. The coefficients of Equation 4.2 are as follows: $a_0 = -6.299$, $a_1 = -13.21$, $a_2 = 0.7083$, $a_3 = 8.703$, $a_4 = 7.035$, $a_5 = 2.608$, $a_6 = 0.2057$, $b_1 = 13.55$, $b_2 = 16.41$, $b_3 = 8.148$, $b_4 = 0.2259$, $b_5 = -1.848$, $b_6 = -1.006$ and $w = 0.01185$.

4.3.6 Simulation of valve repair

As detailed previously, here the edge–to–edge repair has been examined in two different scenarios. The first is a standard surgical approach in which annuloplasty is concurrently applied, the second is an endovascular approach in which only the edge–to–edge repair is performed as annuloplasty cannot be applied (Figure 4.9). Here the edge–to–edge repair has been defined as the central correction of the anterior and posterior leaflets. The suturing together of the opposing leaflet segments has been simulated by first connecting the two leaflets, over a width of 2 mm on both sides, with thermal beam elements. Following this, a negative thermal load (a linear ramp of -5°C over 100 ms) was used to contract these beams, virtually suturing the two edges (Figure 4.10). This single Hughes–Liu beam was defined with a density of 1 $g \cdot cm^{-3}$, an elastic modulus of 1 MPa and a thermal coefficient of expansion 1 $°C^{-1}$. The values of these parameters were set to reduce the length of the beam connecting both leaflet edges by ∼99%, ensuring the connection of the two leaflet portions.

Both repair scenarios are performed using the dysfunctional state generated though valvular dilation (see Section 4.3.2). In the percutaneous approach only edge–to–edge is applied, therefore only the thermal beams are contracted and the annulus remains dilated. In the standard case the effect of a rigid annuloplasty ring and the edge–to–edge repair are mimicked by simultaneously contracting the thermal beams and displacing the nodes of the dilated annulus back to the initial D–shape of the normal annulus. Simulated separately to the fluid–structure interaction simulation of diastole, the valve repair has been performed using structural–only simulations for computational efficiency. The dampening effect of the fluid was approximated by using a global nodal damping factor of 0.9965, based on previous experimental results [111] (see Chapter 2, Section 2.4.1.2). The final configuration (geometry and stress state) has been used as the initial state for the corresponding fluid–structure interaction simulations, prior to which the thermal beam elements were switched from deformable to rigid objects. The deformation of the valve and the resultant maximum principal stresses following the valve repair, in both cases, are shown in Figure 4.10.

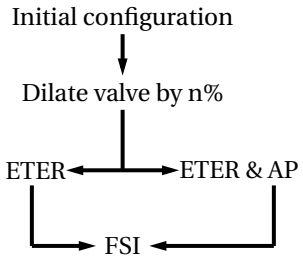

Figure 4.9: Valve correction simulation flow. Labels: ETER – edge–to–edge repair, AP – annuloplasty and FSI – fluid–structure interaction.

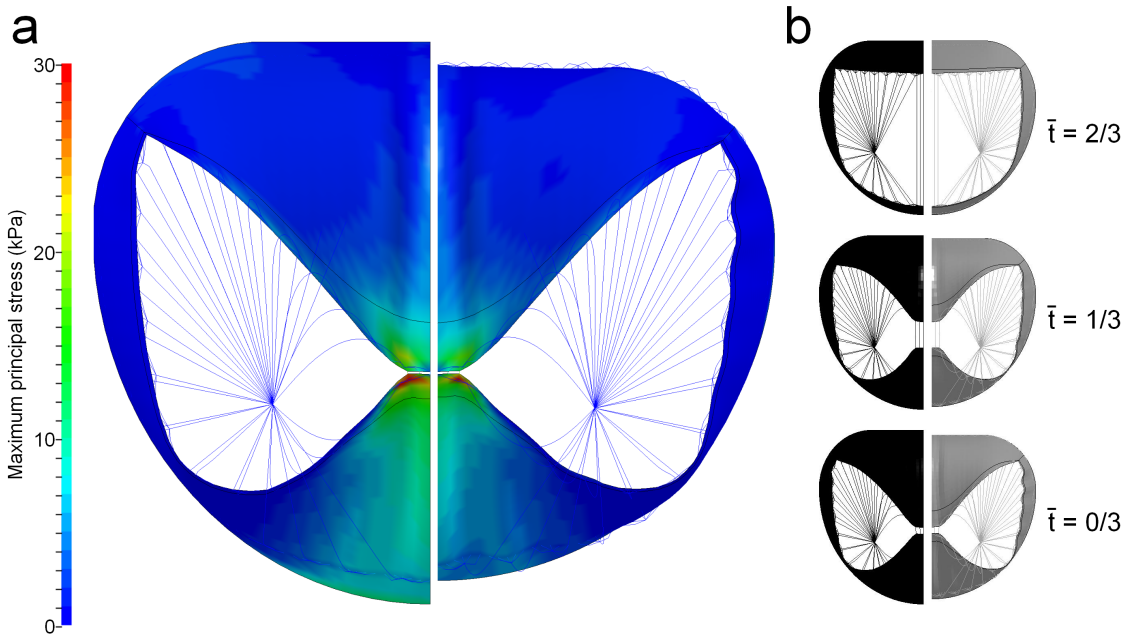

Figure 4.10: Simulation of the edge–to–edge correction in the dilated mitral valve model; (a) maximum principal stress distribution in its final state, $\bar{t} = t/t_{max} = 1$, without (left) and with (right) annuloplasty; (b) the corresponding deformation at $\bar{t} = t/t_{max} = 0/3$, $1/3$ and $2/3$, without (left) and with (right) annuloplasty.

4.3.7 Valve dynamics

Here the response of the valve in both normal and dysfunctional states are compared. The values of the maximum principal stresses induced in the normal and two dysfunctional models are listed in Table 4.7. The deformation and stress distribution in each model at its maximum principal stress is visualised in Figure 4.11.

During diastole the stresses in the uncorrected valve are small, however the effect of the edge–to–edge repair increases the maximum principal stress by ∼200% (Table 4.7). The maximum diastolic principal stresses in the repaired valves equate to 65% (edge–to–edge repair with annuloplasty) and 68% (edge–to–edge repair only) of the maximum principal stress observed in the same model during systolic closure only (∼300 kPa). Using a linear elastic orthotropic model, Votta et al. [95] performed simulations of the edge–to–edge repair, showing the maximum diastolic stress in a repaired state is comparable to the maximum systolic stress. Similar analysis by Dal Pan et al. [104] reports the maximum diastolic stress as 71% of the systolic stress. The inconsistencies of these values can be attributed to the fact that structural models are not adequate to model diastole which is a transient event, where the valve is in dynamic motion and the pressure load is non–uniform over the valve surface.

Although the magnitude of stresses are similar in both edge–to–edge repair cases, the distribution of stress differs. Comparison of stress at the local maximum of each model shows that with the edge–

to–edge repair only a concentrated stress distribution is located at the suture, compared to the edge–to–edge repair with annuloplasty case where the stresses are redistributed along the free margin of leaflets (Figure 4.11). This reduction in stress between corrected and uncorrected annular dilation has also been highlighted in previous simulations [95, 104].

Clinical results have shown that the repair of the valve without the application of an annuloplasty ring has suboptimal performance [122]. Although the etiologies of heart valve disease are numerous, it has been possible to explore in detail the effect of one factor here in this model: annular dilation. In this case it has been shown that valve correction without the application of annuloplasty induces a higher maximum stress and a more concentrated stress pattern. This has particular impact upon percutaneous techniques whereby the edge–to–edge repair is the only available option.

Table 4.7: Maximum principal stress in normal and repaired models. Labels: ETER – edge–to–edge repair and AP – annuloplasty.

Model	Max. principal stress (kPa)
Normal	69.7
ETER & AP	195.8
ETER only	205.5

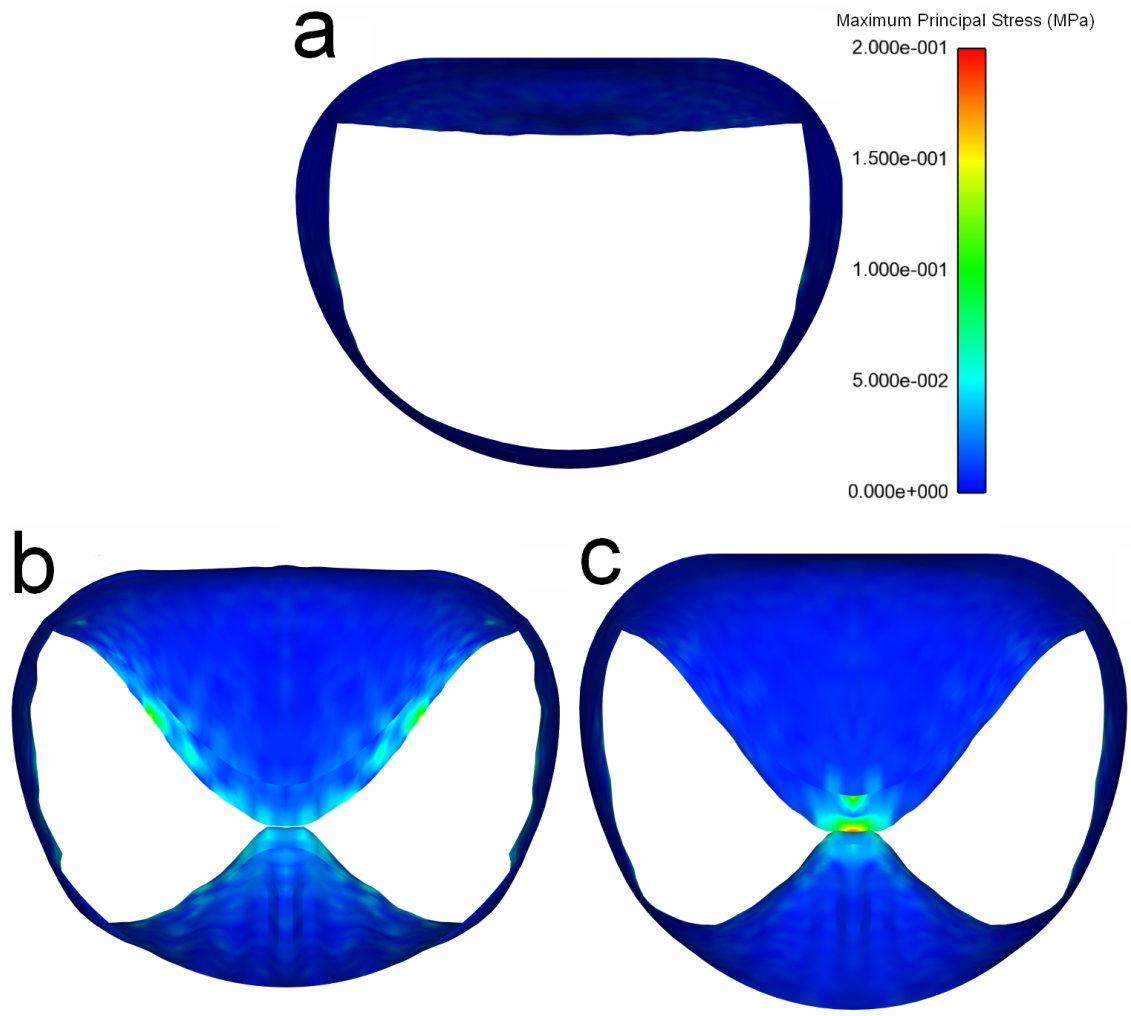

Figure 4.11: Valve deformation and maximum principal stress distribution at the local maximum of the principal stress in each model as viewed from the ventricular side of the valve in the (a) normal valve (t= 42 ms),(b) edge–to–edge repaired valve with annuloplasty (t = 340 ms) and (c) the edge–to–edge repaired only valve (t = 101 ms).

4.3.8 Fluid dynamics

Here the effect of the edge–to–edge repair on the fluid dynamics have in the dysfunctional states have been compared against the normal valve model. The flow rate through the orifice throughout the diastolic cycle in both corrected and normal models are visualised and listed in Figure 4.12 and Table 4.8 respectively. Comparison of the velocity magnitude downstream of the valve is visualised using the plane located in the centre of the valve, parallel to the anteropostero axis in Figure 4.13. The associated fluid motion through the orifice has also been analysed using particle tracing as shown in Figure 4.14.

Comparison of the flow rate shows that the edge–to–edge repair impairs the rapid fluid transport ability of the valve (Figure 4.12). The initial flow rate between the normal and repaired valves are comparative over the initial 20 ms of the diastolic simulations. Beyond this point, the difference in magnitude rises to over 100 $cm^3 \cdot s^{-1}$ as the repaired valves are unable to deform freely and increase the flow rate. This is highlighted by the location of the maximum flow rate (Figure 4.12) which occurs at ∼360 ms in the normal model (13.4 $l \cdot min^{-1}$) and ∼40 ms in the two repaired valves (7.5 and 6.8 $l \cdot min^{-1}$ for the edge–to–edge repair only and the edge–to–edge repair with annuloplasty).

Downstream of the valve, the maximum magnitude of the fluid velocity has been measured as ∼0.8 $m \cdot s^{-1}$ in all three models (Figure 4.13). This value corresponds to expected physiological values during diastole [115]. Particle traces at the maximum velocity point in the cycle highlight that the fluid field in the corrected cases contain large areas of rotation (Figure 4.14).

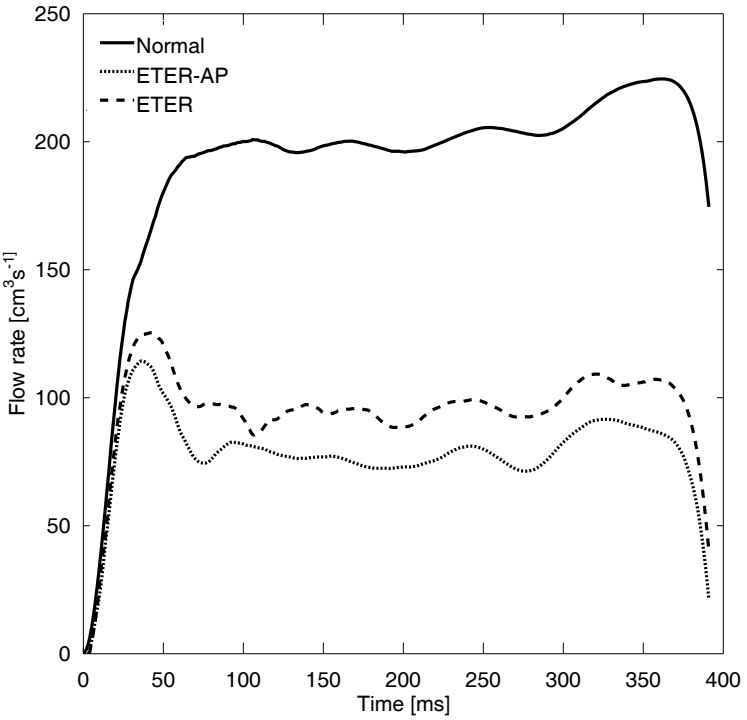

Figure 4.12: Flow rate through mitral orifice in the normal valve, edge–to–edge repaired valve with annuloplasty and the edge–to–edge repaired only valve.

Table 4.8: Maximum value of the flow rates in the normal, edge–to–edge repaired valve with annuloplasty and the edge–to–edge repaired only valve. Labels: ETER – edge–to–edge repair and AP – annuloplasty.

Model	Flow rate ($cm^3 \cdot s^{-1}$)	Flow rate ($l \cdot min^{-1}$)
Normal	224	13.4
ETER & AP	114	6.8
ETER only	125	7.5

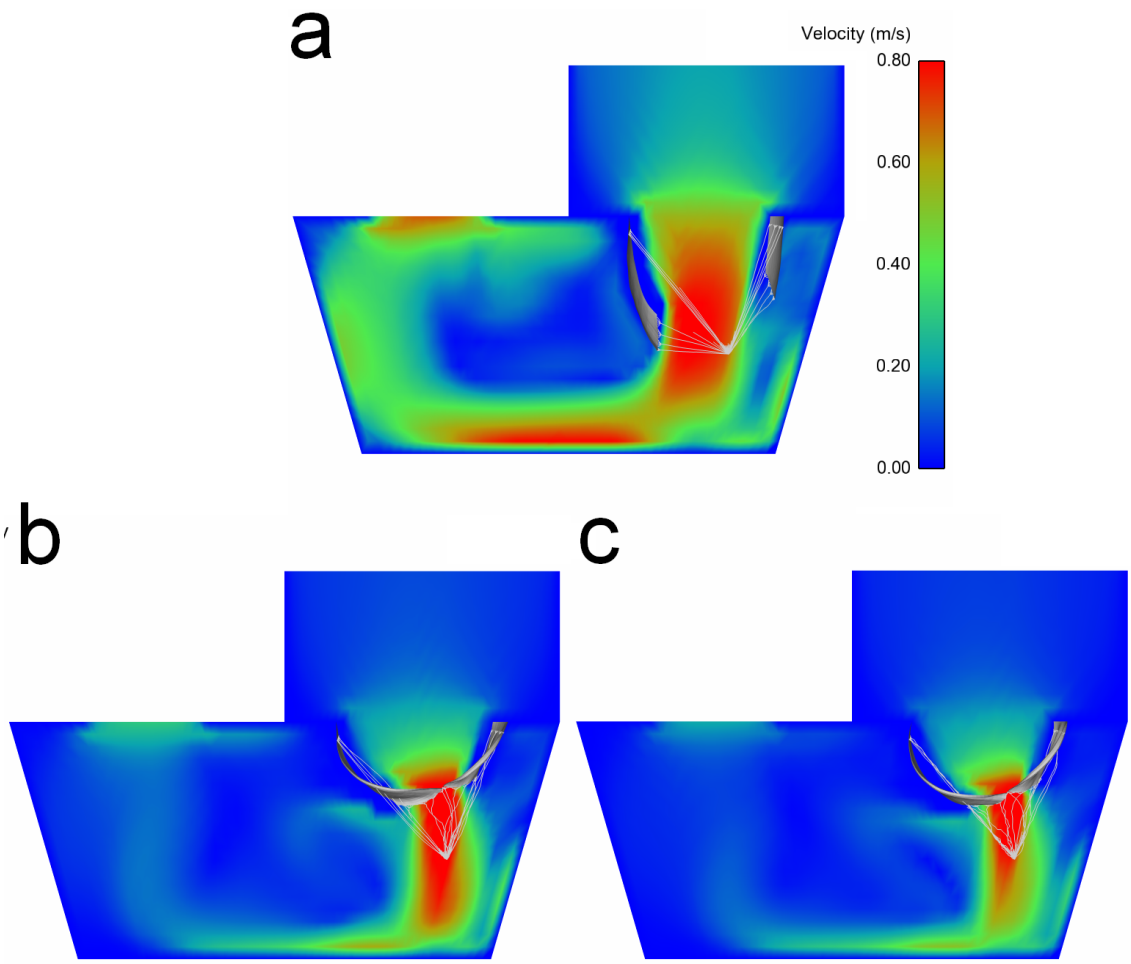

Figure 4.13: Fluid velocity distribution through a plane centred in the valve model in the (a) normal valve, (b) edge–to–edge repaired valve with annuloplasty and (c) edge–to–edge repaired only valve. All figures visualised at t = 365 ms, the point at which the global maximum fluid velocity was observed.

4.3.9 Limitations

This study only analyses the effect of a centrally located suture, lateral suture positions have not been examined. However the central suture corresponds to the most severe scenario in terms of the leaflet stress distribution as reported in previous structural analyses of the edge–to–edge repair technique [105, 104, 95]. Here the annulus of the valve was modelled as a static planar object, neglecting its dynamic motion, which adopts a 'saddle' shape in the systolic phase [12]. This has been shown to reduce stress concentrations during valve closure [89]. However, the focus of this study was the diastolic peak where the role of the annulus dynamics in the reduction of stress is reduced. In this model the biomechanical response of the functionally regurgitant valve was assumed to be identical to the normal valve. However, echocardiographic studies by Chaput et al. [128] have shown that functional mitral regurgitation results in increased valve leaflet area/volume, a change that will directly affect the biomechanical response of the valve. It is important to note that no data has been reported which has characterised the biaxial mechanical behaviour of mitral valve tissue in this state.

The fluid volume used in this analysis has several simplifications regarding its geometry and dynamics of its boundaries. Here the ventricular chamber was designed as a rigid U–shaped volume with an open aortic position, factors which are all unphysiological. Also in functional regurgitant states the left ventricular volume is dilated, a factor ignored here as this model of dysfunction only includes valvular changes.

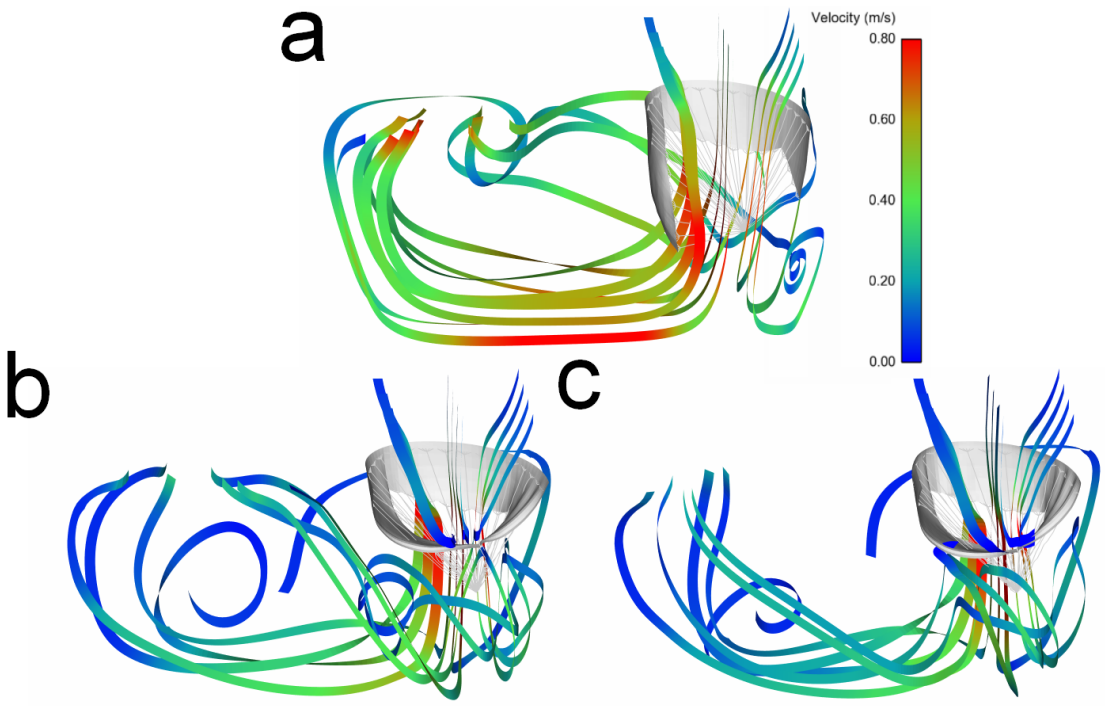

Figure 4.14: Particle traces of the fluid field taken at t = 365 ms. Particles were seeded from a plane located 10 mm above the valve orifice in the (a) normal valve, (b) edge–to–edge repaired valve with annuloplasty and (c) edge–to–edge repaired only valve.

As the valve was defined in its unstressed open configuration at the beginning of the diastole, and the motion of the ventricular wall was neglected, the results obtained during the initial phases of opening are approximated. Analysis of the stress state of the mitral valve has been performed when the valve is fully opened, when the effects of ventricular dynamics are reduced and the maximum principal stresses are constant. Previous analysis [115] of a single cardiac cycle (open–closed–open) has shown that during the second open period, when the valve is fully open, the maximum principal stresses are constant.

In the structural model of the valve the leaflets are represented by constant stress elements, in which the calculated stress is uniform over each shell. In the edge–to–edge only simulation a strong stress concentration was noted at the position of the repair (Figure 4.11), upon inspection this was found to be localised within a single element. In order to assess the exact spatial extent of this stress concentration, further simulations with increased mesh resolutions are required.

4.3.10 Summary

Here the functional response of the valve and associated fluid dynamics in a simulated dysfunctional state and subsequent surgical repair has been performed. Diastole was simulated using a fluid–structure interaction method with non–linear orthotropic material models used to described the mechanical response of the leaflets and chordae. Simulation of dysfunction has been performed by dilating the valve in the anteropostero axis to match the eccentricities reported *in vivo* in cases of functional mitral valve regurgitation and subsequently corrected in two separate simulations: edge–to–edge repair with and without annuloplasty.

The results of the fluid–structure interaction simulations have shown that the maximum principal stresses induced in both corrected cases are 200% larger in a repaired valve compared to a normal valve. Although the maximum of both corrected scenarios are similar in magnitude, the distribution of the stress between the two cases differ significantly, with high stress concentrations in the dilated model with the edge–to–edge repair only. Typically stresses in the mitral valve in this portion of the cardiac

cycle are low. Stress reduction will therefore be beneficial in minimising the detrimental effects of the edge–to–edge repair.

The fluid dynamics of filling are also affected, with highly directed flow generated by the edge–to–edge repair. Similar magnitudes of the velocity are observed downstream of the valve, however the repaired valves exhibited diminished flow rates throughout the diastolic cycle, such that the peak flow rate was shifted from the end of the simulation to the start of diastole.

4.4 Context

Although previous structural–only and fluid–only models of the edge–to–edge repair exist, this work is the first to simulate this particular valve repair technique using a fluid–structure interaction method. As shown in Section 4.2 significant differences are observed between quasi–static structural–only and fluid–structure interaction approaches to the edge–to–edge repair, with stresses ∼180% greater in the fluid–structure interaction cases. Full transient fluid–structure interaction of the edge–to–edge repair has explored in a model of valvular dysfunction in Section 4.3.6, whereby a normal valve model has been subjected to a simulated annular dilation and subsequently repaired with the edge–to–edge repair using standard and percutaneous methods. The results of these simulations indicate that there is an improved states of stress in the case of the edge–to–edge repair with annuloplasty (standard method), however at the cost of slightly reduced flow rate.

Chapter 5

Valve Remodelling and Growth

As detailed previously, the biomechanical properties of the different subvalvular components of the valve are key to correct valvular function. Although the ability to withstand the haemodyanmics load of systole and rapidly transition from closed to open in diastole are derived primarily from the collagen and elastin constituents of the leaflets [49], it is the proportions, microstructural organisation and fibre orientation of these constituents which provides these properties (see Chapter 1, Section 1.4). In normal states, cellular processes within the tissue homeostatically maintain the biomechanical properties of these constituents. However it is the gradual loss of this tissue regulation which is considered to be the cause behind valvular disease [129], such as in myxomatous degeneration where deviations in the constituent properties and organisation result in dysfunctional states which are characterised by a loss in mechanical strength and abnormal constitutive proportions and organisation. Myxomatous degeneration increases in the content of collagen (the load bearing component of the microstructure) are reported [61, 60], however the load bearing strength is deceased as the organisation of the fibrous microstructure decreases resulting in a loss of biomechanical strength [62].

The homeostatic regulation of the tissue is a complex biological process, which is typically assessed *in vitro* in cultured cell populations. However such techniques cannot truly represent the *in vivo* environment of the tissue, such as the stresses and strains induced from the cyclic loading of the cardiac cycle. Through numerical models, such as those presented here, the biological response of the tissue to the *in vivo* environment can be assessed. In order to examine the role between mechanical stimuli and the associated biological events, it is required to build abstract models that encompass the resulting biological activity (i.e. remodelling[1] or growth[2]) without including exact detail of the biological function. For example, in this work the biological response of the tissue has been simplified to be a function of mechanistic inputs (stresses/strains). Although disconnected from the exact biological function, these models can be used to gain insight into possible mechanisms through which biological function are abstractly linked to the mechanistic environment in terms of the stresses and strains.

Within the context of the mital valve, here the following two issues related to remodelling and growth have been examined:

(1) Fibre orientation remodelling – Remodelling of the microstructure, in terms of the reorientation of the fibre direction, has been performed in the anterior belly region of a full mitral valve model. Using a stress–based approach, it has been examined if an arbitrary fibre distribution can be remodelled to a more physiological distribution solely based upon the stress state. Defined initially with a uniform fibre distribution and subjected to normal systolic pressures, the fibre distribution has been remodelled relative to the first and second principal stresses with the resulting fibre distributions qualitatively compared to experimental results (Section 5.2).

[1] Remodelling is defined as a change in the existing microstructure of the tissue.
[2] Growth is defined as a change in mass of the existing structure.

(2) Leaflet growth – Growth in response to a simulated ischemic mitral regurgitation, in terms of increasing the leaflet thickness, has been performed in a partial model of the mitral valve. Using a stress–based approach, the growth response is defined using the difference between the maximum principal stresses in the normal and dysfunctional states induced during systolic closure. Following the growth phase, the resulting stress distribution is compared to the normal and dysfunctional states (Section 5.3).

To the author's knowledge, the work presented here are the first studies into growth and remodelling effects on the mitral valve.

5.1 Biological background

The leaflet tissue consists of an extracellular matrix which is divided into three layers: the fibrosa, spongiosa and the ventricularis (see Chapter 1, Section 1.4.1). The composition, organisation and orientation of the constituent components within this extracellular matrix result in a controlled biomechanical balance between the required stiffness and flexibility. Homeostatic regulation of these biomechanical properties are governed by cells referred to as valvular interstitial cells, which are embedded within the extracellular matrix. In normal states, these cells are primarily quiescent and maintain baseline levels of extracellular matrix turnover, however when required these cells are able to enter active states in which the expression of the constitutive components are increased [129]. It is this modulation between quiescent and active states that enables the valve to adapt to its operational environment for example in response to injury or increasing haemodynamic load in child/adult development [130, 131]. It is considered that the disruption of this modulation, which causes a maladaptive response of the extracellular matrix, is the origin of heart valve disease [129].

Although the link between the mechanical environment and the adaptation/maladaptation of the extracellular matrix is not a clearly understood process, this relationship has been observed *in vivo*. Animal experiments by Dal-Bianco et al. [132] have shown that ovine mitral valves subjected to abnormal mechanical loads, in the case of simulated ischemic regurgitation, respond by increasing mass and reorganisation of the leaflet microstructure. Similarly, measurements of leaflet areas in cases of functional mitral regurgitation in human subjects by Chaput et al. [128] have shown that leaflet areas are larger in dysfunctional states. In order to examine the functional link between changes in the leaflet microstructure and the stresses/strains, abstracted models of the adaptation/maladaptation process have been implemented and examined in a model of the mitral valve.

5.2 Valve remodelling

As detailed previously in Chapter 1, Section 1.4, the anisotropic, non–linear biomechanical response of the mitral valve leaflets is characterised by the predominant collagen fibre direction [54]. Experimental measurements of the fibre orientation indicate that the fibres are non–uniformly distributed and aligned towards key anatomical structures, such as the insertion of the chordae tendineae into the leaflet surface [52, 41] (Figure 5.1). In previous numerical models this fibre distribution has either been defined individually in each anatomical region, or simplified as uniformly aligned as parallel to the annulus (Table 5.1). Although numerically more efficient to implement, uniformly orientated models (for example see Votta et al. [32]) report greater maximum principal stresses than non–uniformly orientated models (for example see Prot et al. [92]) as the load is not distributed as equally.

In these non–uniform models the fibre orientation has been based upon the experimental data, of which there is only one source, reported by Cochran et al. [52]. Using this data, the orientation of the predominant fibre direction has been mapped to the geometry of the different valve models (Table 5.1).

Although defined anatomically, the orientation of these fibres in these models have been defined arbitrarily rather than functionally, i.e. based upon the functional requirements of the tissue as observed with the fibre alignment at sites of chordal insertions [41]. Using a discrete fibre model, the functional remodelling of the fibre orientation within the leaflet has been modelled using a stress–based approach as detailed below in Section 5.2.5. By comparing the induced stresses and strains, this stress–based approach has been evaluated as a possible mechanism through which functional and physiological fibre distributions are generated.

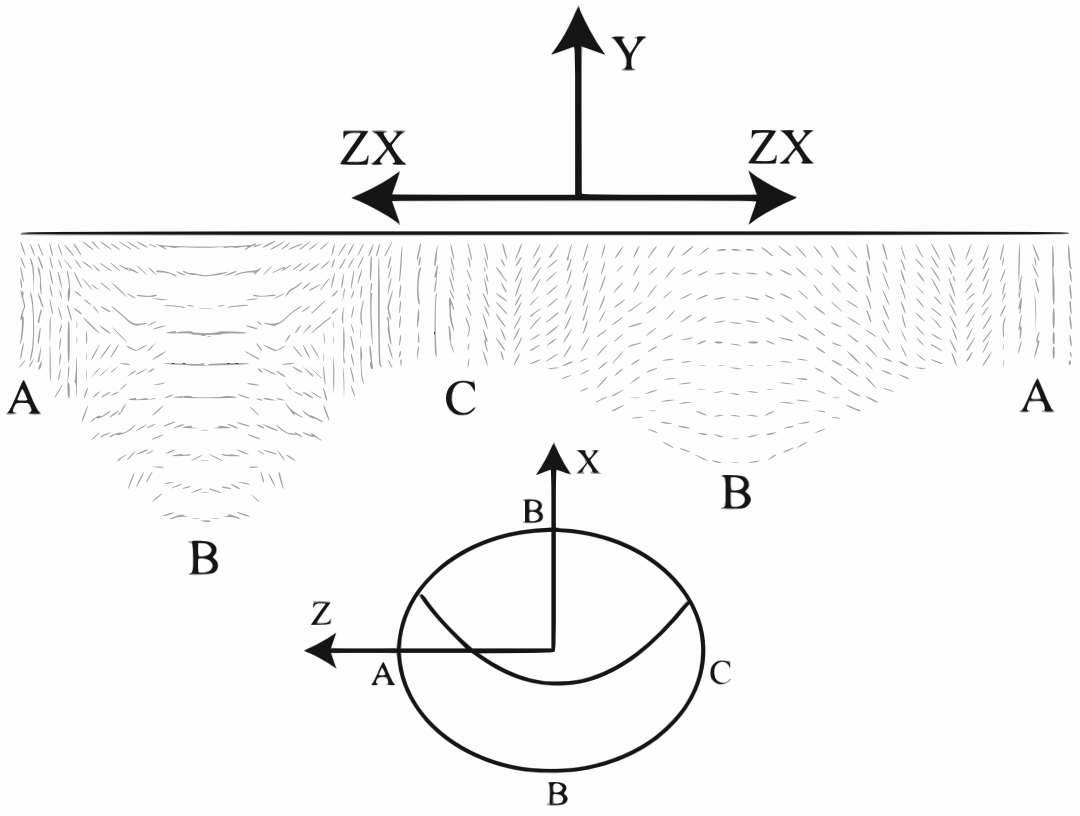

Figure 5.1: Experimental measurement of the predominant fibre orientation in the mitral valve leaflets. Image after Einstein et al. [76].

Table 5.1: Comparison of the different fibre distributions used in previous non–linearly elastic numerical studies of the mitral valve. Labels: Local fibre alignment – individually aligned, anatomically mapped fibre distributions and Global fibre alignment – uniformly aligned fibre distribution orientated parallel to the annulus.

Model	Local fibre alignment	Global fibre alignment
Einstein et al. [76]	☑	☐
Einstein et al. [96]	☑	☐
Einstein et al. [97]	☑	☐
Prot et al. [74]	☐	☑
Votta et al. [32]	☐	☑
Prot and Skallerud [91]	☑	☐
Prot et al. [92]	☑	☐
Stevanella et al. [94]	☐	☑
Prot et al. [64]	☑	☐
Skallerud et al. [93]	☑	☐

5.2.1 Valve geometry

The model presented here is referred to as the hyperelastic model previously in Chapter 2. The geometry of this valve model is based upon anatomical measurements reported from *in/ex vivo* sources. Here the valve has been modelled as symmetric about the anteropostero axis which allows for the computational simplification of only simulating half the valve.

Forming the base of this model is the annulus, here defined as a static and planar D–shaped orifice with an anteropostero and commissural diameters of 22.5 mm and 30 mm respectively. Using the centre of the anterior leaflet as a reference point, the annular extent of the valvular cusps was defined by scaling reported anatomical measurements by Kunzelman et al. [11] to the D–shaped orifice. The perimeter of the annulus and its enclosed area are 8.67 cm and 5.54 cm^2 respectively. Extending from the annulus are the anterior and posterior cusps of the leaflets. Sized from anatomical measurements by Kunzelman et al. [11], the leaflets are modelled as a continuous band of tissue. The anterior and posterior leaflets have been individually defined with a single cusp each (Figure 5.2). Experimental measurements of the leaflet thickness show regional differences between leaflets [54], however as no detailed description of this variation is reported the leaflets have been defined with a uniform thickness of 1 mm.

During valve closure, inversion of the valve is prevented by the chordae tendineae, structures which are classified by the anatomical position of leaflet attachment. In this mode the marginal, basal and strut chordae have all been included. The thinner marginal chordae support the free edges of the leaflets whereas the thicker basal and strut chordae support the base and the central anterior regions of the valve leaflets respectively. The cross–sectional area of the marginal and basal/strut chordae have been taken as 0.45 mm^2 and 1.15 mm^2 respectively, as reported in Kunzelman and et al. [98]. The chordae are connected to the papillary muscles, here represented as two static nodes positioned in a plane 20 mm above the annulus. The lateral distance between the two tips has been defined in the range 19.5 mm to 21 mm, a value scaled relative to the annular diameter from experimentally reported measurements [110]. The anteropostero position of the these tips was modified to achieve physiological coaptation under closure conditions.

5.2.2 Material model

In this model both the leaflets and chordae have both been modelled as non–linear elastic materials using a combination of standard and custom user defined LS–DYNA material models respectively.

5.2.2.1 Leaflet material model

Described in detail in Chapter 2, Section 2.3.1.3, the leaflets have been modelled as a transversely isotropic, non–linear, anisotropic, hyperelastic membrane following the numerical approach documented by Einstein et al. [78]. Based upon a finite strain approach, the stress response of this material model is defined as a function the deformation of the body. The formulation of this method is detailed in Chapter 1, Section 1.4.3, thus the exact details are omitted for brevity.

Deformation of the leaflet material is characterised through the deformation gradient $\mathbf{F}$ which describes the spatial derivative in the initial basis, of the current deformed state of the leaflets (see Figure 1.17 on Page 39). Embedded in the plane of the leaflet structure are a family of fibres, initially orientated in the direction defined by the unit vector $\mathbf{a}_0 = [a_{01}, a_{02}, 0]$. Convected with the deformation of the structure, the associated change in length of these fibres λ_f can be calculated as a function of the deformation gradient $\mathbf{F}$. Using the associated right Cauchy–Green stretch tensor, which is defined as $\mathbf{C} = \mathbf{F}^{\mathrm{T}}\mathbf{F}$, in conjunction with the square of the embedded fibre stretch λ_f^2 the anisotropic mechanical response of the leaflet tissue can be described using an exponential strain–energy function [73] (Equation (5.1). A scalar valued function, here the terms I_1 and I_4 are the first and fourth invariants of the tensor $\mathbf{C}$ which describe the volumetric deformation and the square of the fibre–direction stretch respectively (Equa-

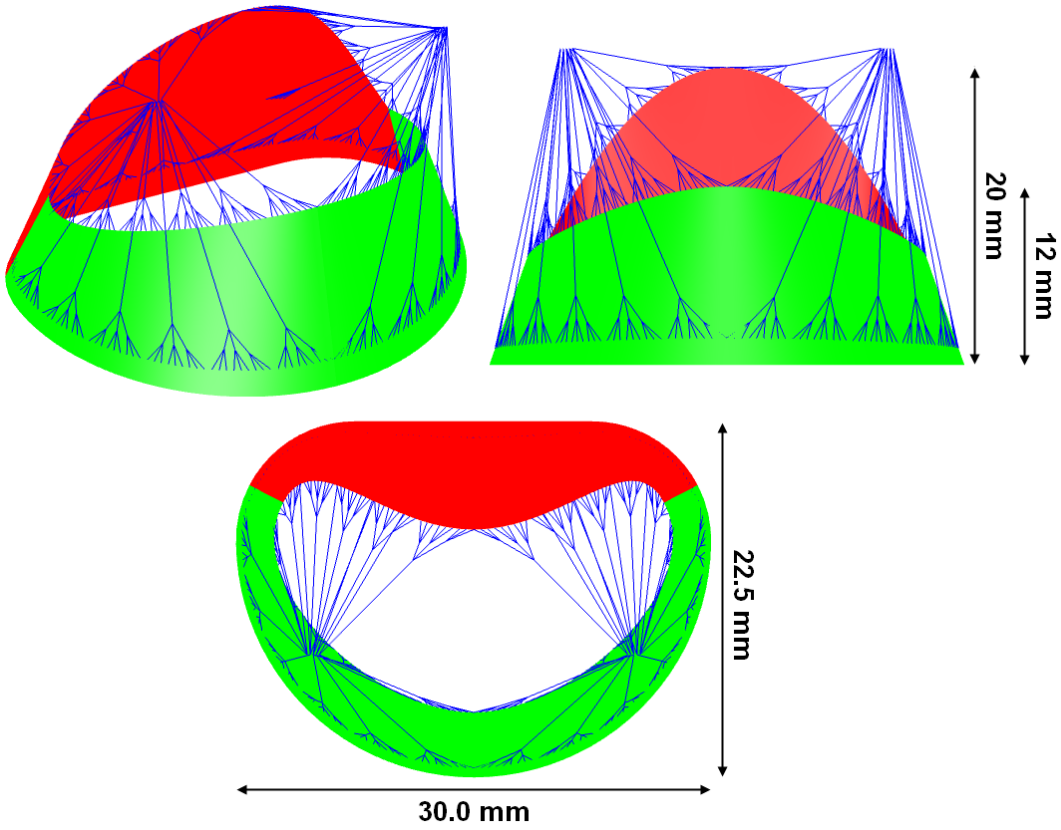

Figure 5.2: Three–dimensional, front and top views of the mitral valve model. The anterior and posterior leaflets are respectively coloured red and green. The blue beams represent the cordae tendineae. Here the leaflet lengths, anteropostero diameter and commissural diameter have been labelled. The geometry of the model has been reflected in the axis of symmetry.

tions 5.2 and 5.3). The associated parameters c_0,c_1 and c_2 for both anterior and posterior leaflets have been taken from experimental values reported in the literature [73]. Examples of the stress response of this material model under biaxial stretch, in both the anterior and posterior leaflet, are illustrated in Figures 5.3a and 5.3b.

$$\psi(I_1, I_4) = c_0 \left(\exp \left[c_1 (I_1 - 3)^2 + c_2 (\sqrt{I_4} - 1)^4 \right] - 1 \right) \tag{5.1}$$

$$I_1 = \mathrm{tr}(\mathbf{C}) = C_{11} + C_{22} + C_{33} \tag{5.2}$$

$$I_4 = \lambda_f^2 = \mathbf{a_0} \cdot (\mathbf{C}\,\mathbf{a_0}) = a_{01} C_{11} a_{01} + a_{01} C_{12} a_{02} + a_{02} C_{21} a_{01} + a_{02} C_{22} a_{02} \tag{5.3}$$

Table 5.2: Strain–energy function coefficients of Equation 5.1. Values from May-Newman and Yin [73].

Leaflet	c_0 [kPa]	c_1	c_2
Anterior	0.399	4.535	1446.5
Posterior	0.414	4.848	305.4

5.2.2.2 Chordae material model

The non–linear material response of the chordae tendineae have been modelled using the experimental measurements reported by Kunzelman and Cochran [67] (Figure 5.3c). As no experimental data on the non–linear stress–strain behaviour of the strut chordae exist, the strut chordae have been defined with the same properties as the basal chordae. The cross–sectional areas of the marginal, basal/strut chordae

are defined as 0.45 and 1.15 mm^2 respectively.

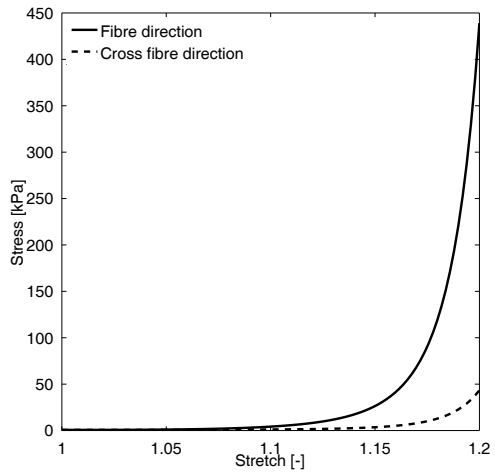

(a) Anterior leaflet

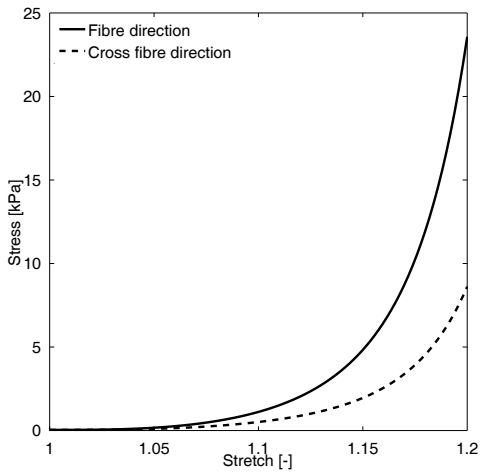

(b) Posterior leaflet

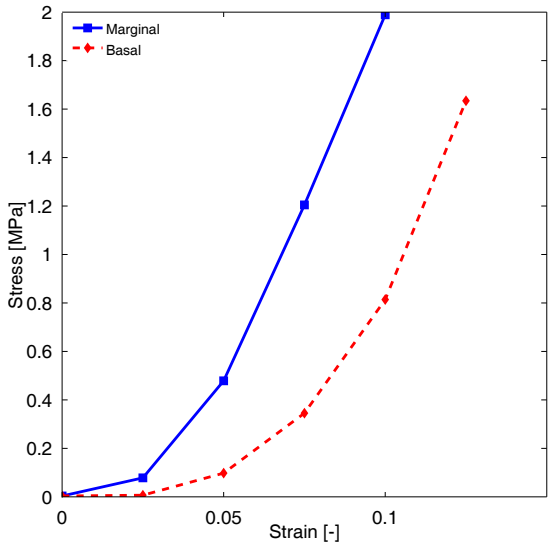

(c) Chordae tendineae

Figure 5.3: (a) and **(b)**: Mitral valve leaflet material model stress response to in–plane equibiaxial stretch λ in (a) the anterior leaflet and (b) posterior leaflet. Note the difference in the stress scale. The values of the deformation gradient are defined as $F_{11} = F_{22} = \lambda$ and $F_{33} = (F_{11}F_{22})^{-1}$, as described previously in Equation 1.6 on Page 39. **(c)**: Non–linear stress–strain behaviour of the marginal and basal chordae tendineae. Data after Kunzelman and Cochran [67].

5.2.3 Finite element mesh

The geometry of the valve leaflets and chordae tendineae have been discretised by using co–rotational Hughes–Liu shell and discrete cable elements respectively [79, 80]. The leaflets consist of 3920 co–rotational Hughes–Liu shell elements in total, with 1680 and 2240 elements used in the anterior and posterior leaflets respectively. The free margin of the leaflets are supported by the primary/marginal chordae tendineae, which have been discretised into 143 discrete cable elements. Similarly the basal and central portion of the anterior leaflet are supported by the secondary/basal and strut chordae tendineae respectively, which consist of 143 and 6 discrete cable elements respectively. In order to simplify the numerical complexity of the problem only half the valve has been simulated, with the valve modelled as symmetrical about the anteropostero axis (Figure 5.4).

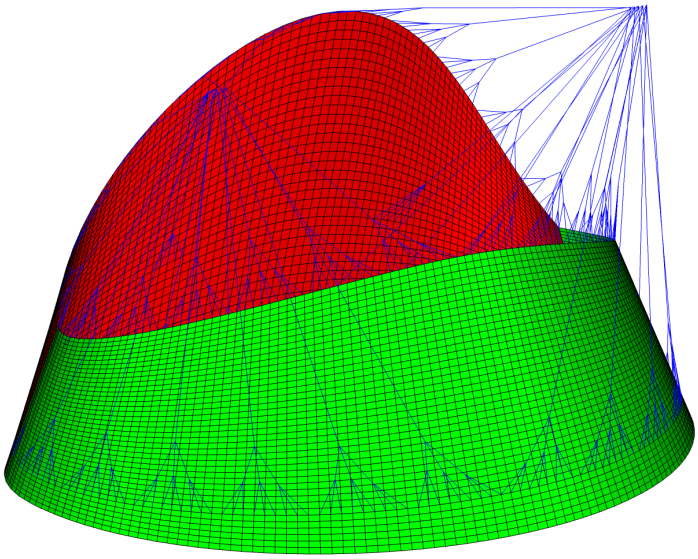

Figure 5.4: Three–dimensional view of the finite element mesh used. The anterior and posterior leaflets are respectively coloured red and green. The blue beams represent the chordae tendineae. Here the model has been reflected in its the axis of symmetry.

5.2.4 Valve closure

It has been assumed that the remodelling process occurs solely as a consequence of the stresses induced during valve closure, thus only the systolic portion of the cardiac cycle has been simulated. Structural–only simulations of closure have been performed by applying the systolic transvalvular pressure difference shown in Figure 5.5. Performed in a structural–only model this pressure load has been defined as uniform over the surface of the leaflets, a factor which has been shown previously in Chapter 3 to affect the dynamics of closure. However as it is the stress state of the leaflets which are of interest, the structural–only approach used here has been deemed an appropriate simplification.

As a structural–only model, the dampening effect of the blood has been approximated (see Chapter 2, Section 2.4.1.2) by increasing the density of the structure by a factor of ten following the approach taken by Kunzelman et al. [85] and Schievano et al. [103] ($\rho = 10.0\ \mathrm{g \cdot cm^{-3}}$).

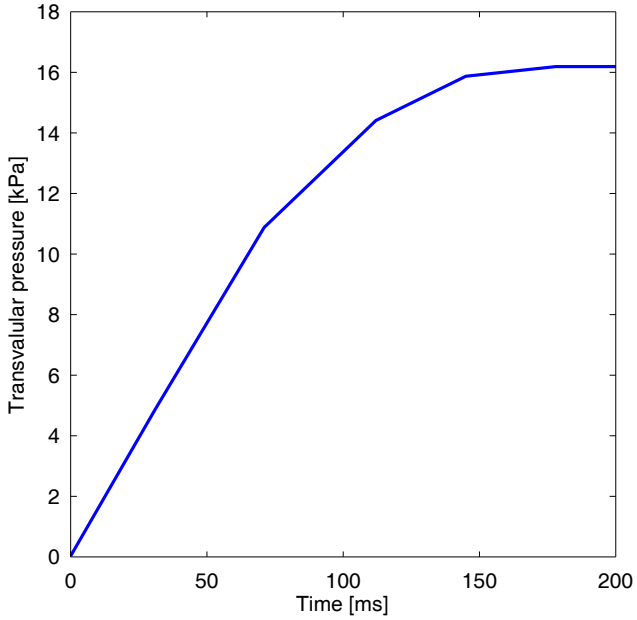

Figure 5.5: Systolic transvalvular pressure difference used to simulate closure. Data after Levick [1].

5.2.5 Fibre remodelling

The remodelling process through which the microstructure of the leaflet tissue adapts has been based upon the stress–based approach, a decision based upon the *in vitro* experiments of Merryman et al. [133] that indicate that valvular interstitial cells respond to increased levels of stress. Following the approach previously reported by Driessen et al. [134], in which remodelling of the the fibre orientation in response to closure has been performed in a structural–only model of the aortic valve, this methodology has been adapted and applied to closure of the mitral valve. The process through which the fibres are remodelled has been briefly summarised in Figure 5.6.

As described previously, the initial fibre orientation of both leaflets has been defined as uniformly orientated parallel to the annulus. The initial fibre direction $\mathbf{a_0} = [a_{01}, a_{02}, 0]$ and the orthogonal cross–fibre orientation are both illustrated in Figure 5.7. Using this initial fibre distribution, valve closure has been simulated with the resulting stress distribution at closure used to update the fibre orientation, completing a single iteration. Using this updated fibre orientation, closure is re–simulated and the fibre distributions are updated iteratively. Here the extent of remodelling has been simplified by restricting the remodelled regions to the elements which form the belly region of the anterior leaflet, as highlighted in Figure 5.9 on Page 131. This remodelling approach has been applied over two iterations.

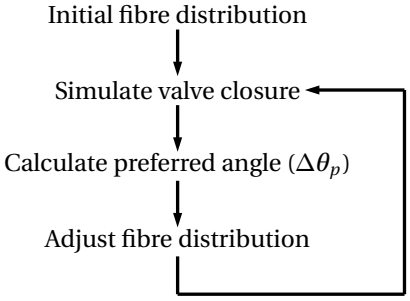

Figure 5.6: Stress based remodelling algorithm.

Remodelling algorithm

As described above, it has been assumed that remodelling of the leaflet microstructure occurs through fibre reorientation in response to the induced stresses during closure. From the stress state at closure, the variation in fibre angle $\Delta\theta$ is calculated as a function of the ratio of extra stresses in the first and second principal stress directions. The extra stresses $\tilde{\boldsymbol{\sigma}}$ are determined from subtracting the hydrostatic pressure of the material p from the the Cauchy stress tensor $\boldsymbol{\sigma}$ (Equation (5.4). As the leaflets have been defined as a membrane, the value of the hydrostatic pressure p is defined to enforce the membrane condition $\sigma_{33} = 0$ [78] (see Equation 1.18 on Page 41).

The contribution of the extra stress tensor in the first two principal stress directions ($\mathbf{v}_1$ and $\mathbf{v}_2$ respectively) is calculated in the deformed configuration and referred to as σ_1 and σ_2 (Equations 5.5 and 5.6). As only tensile stresses (i.e. $\sigma_i > 0$ where $i = 1,2$) are assumed to contribute to remodelling, the contribution of the extra stresses are defined through the response functions g_1 and g_2 (Equation 5.7). From the ratio of these two response functions the preferred fibre angle θ_p is defined, which is orientated relative to the first principal stress direction $\mathbf{v}_1$ (Equation 5.8). The change in angle orientation $\Delta\theta$ between successive iterations is defined as a function of the preferred fibre angle θ_p and the reorientation constant k, here set to unity (Equation 5.9).

The effect of this algorithm is to align the fibre angle in the direction of the largest principal stress, as illustrated by the two examples detailed in Figure 5.8. In Figure 5.8a the extra stress contributions in the two principal stress directions ($\mathbf{v}_1$ and $\mathbf{v}_2$) are of similar magnitude reflective of a biaxially loaded state of stress, as $\sigma_1 \simeq \sigma_2$. The preferred fibre direction is defined as orientated equally between $\mathbf{v}_1$

(a) Circumferential

(b) Radial

Figure 5.7: Initial fibre orientation in the anterior and posterior leaflets; (a) – fibre direction aligned in the circumferential direction parallel to the annulus. (b) – cross fibre direction aligned in the radial direction orthogonal to the circumferential direction.

and $\mathbf{v}_2$ directions and $\theta \to 45°$. In Figure 5.8b the extra stress contributions in the two principal stress directions are of unequal magnitude reflective of a uniaxially loaded state of stress, as $\sigma_1 > \sigma_2$. In this case the preferred fibre direction is orientated further towards $\mathbf{v}_1$ as $\theta \to 0°$ (or $\theta \to 90°$ in the case of $\sigma_2 > \sigma_1$).

$$\boldsymbol{\sigma} = p\mathbf{I} + \tilde{\boldsymbol{\sigma}} \tag{5.4}$$

$$\sigma_1 = \mathbf{v}_1 \cdot (\tilde{\boldsymbol{\sigma}}\, \mathbf{v}_1) \tag{5.5}$$

$$\sigma_2 = \mathbf{v}_2 \cdot (\tilde{\boldsymbol{\sigma}}\, \mathbf{v}_2) \tag{5.6}$$

$$g_i = \begin{cases} \sigma_i & \text{if } \sigma_i \geq 0 \\ 0 & \text{if } \sigma_i < 0 \end{cases} \quad \text{where } i = 1,2 \tag{5.7}$$

$$\theta_p = \arctan\left(\frac{g_2}{g_1}\right) \tag{5.8}$$

$$\Delta\theta = k\theta_p \tag{5.9}$$

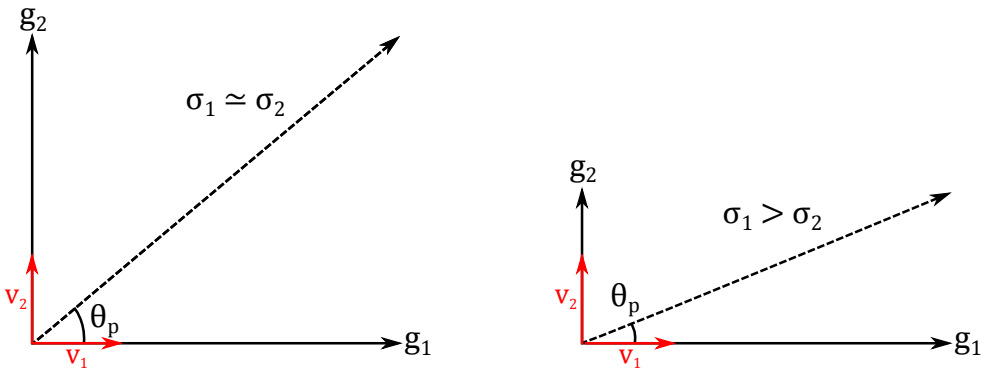

(a) Equal principal stress contributions

(b) Unequal principal stress contributions

Figure 5.8: (a) – example of the preferred fibre angle direction θ_p where $\sigma_1 \simeq \sigma_2$, here the stress contributions between the first and second principal stress directions are similar in magnitude thus the preferred angle is orientated equally between the $\mathbf{v}_1$ and $\mathbf{v}_1$ directions. (b) – example of the preferred fibre angle direction θ_p where $\sigma_1 > \sigma_2$, here the stress contributions between the first and second principal stress directions are greater in the $\mathbf{v}_1$ thus the preferred fibre angle is orientated further towards the $\mathbf{v}_1$ direction.

5.2.6 Remodelling response

Following the approach detailed previously, the fibre distribution has been remodelled over two iterations in base of the anterior leaflet of the valve using the extra stress contribution obtained at the end of closure. Here only the changes in fibre orientation are examined, the stress distributions from which this reorientation is derived from are presented below in Section 5.2.7.

The regions of greatest variation in fibre angle, over both iterations, was found to be in the central region of the anterior leaflet towards in the symmetry plane of the model (Figure 5.9). Smaller regions away from the centre of the leaflets also show large variation in fibre angle around the chordal insertion. The size of both these regions decreases between the initial and first remodelled iterations. The area of least reorientation was found to be towards the symmetry plane of the valve surrounding the strut chordae insertion, indicating the maximum principal stress direction in this region is predominantly aligned in the initial fibre direction.

Inspection of the individual fibre orientation shows that in the first remodelled iteration the majority

of fibres are perturbed towards the radial direction (Figure 5.10). The majority of fibre rotation occurs towards the base of the leaflet, in the vicinity near the symmetry plane and around the chordal insertion away from the symmetry plane. In the second iteration the majority of the fibres are perturbed further towards the radial direction such that the fibre direction is approximately aligned equally between the circumferential and radial directions. Towards the symmetry plane the elements progressively rotate towards the radial direction, such that the centre of the leaflet the fibre direction is approximately aligned in the radial direction. Similar rotations are observed at the top of the remodelled region.

Comparison with the experimentally measured fibre orientation described previously show similar features such as fibre rotations in the off–centre region of the anterior leaflet towards the insertion of the chordae as described by Chen and May-Newman [41], however the rotations shown in the model are rotated further towards the radial direction (Figure 5.1). The model also does not exhibit the circumferentially aligned fibres in the centre of the anterior region as shown experimentally. As this fibre remodelling has only been performed for two iterations it is not clear if a stable solution can be found, this is indicated by the variation in root mean squared of $\Delta\theta$ which remains approximately constant (Table 5.3).

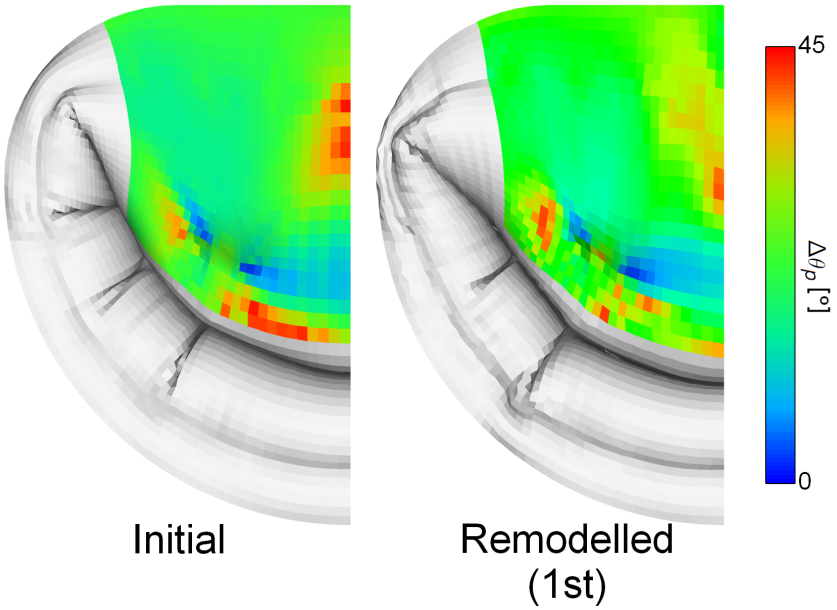

Figure 5.9: Magnitude of $\Delta\theta_p$ in anterior belly region of the valve in the first two iteration initial and remodelled (1st). Only the highlighted anterior belly elements were subjected to fibre reorientation.

Table 5.3: Root mean square variation of $\Delta\theta$ per iteration

Iteration	Root mean squared $\Delta\theta$ [°]
Initial	21.3
First	22.2
Second	20.3

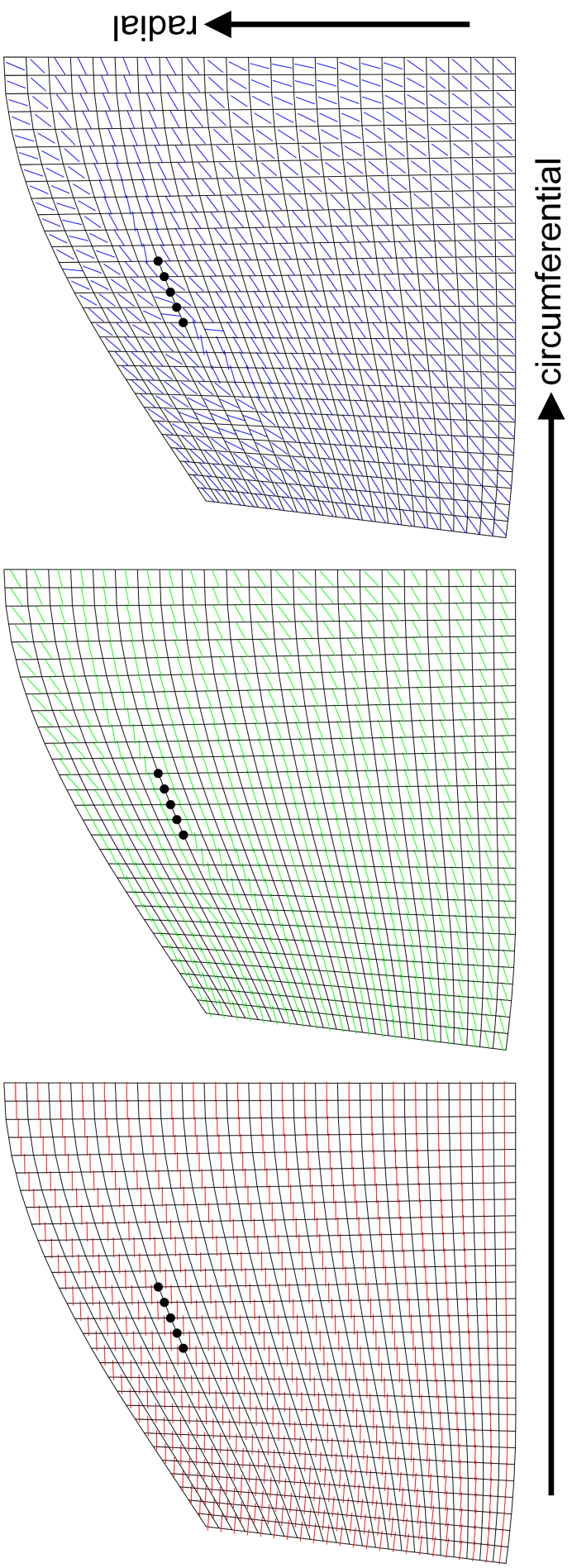

Figure 5.10: Fibre angle in the remodelled areas, insertion of the strut chordae labelled as ●. Left – initial fibre orientation, aligned circumferentially. Middle – first iteration. Right – second iteration.

5.2.7 Principal stress distribution

The maximum principal stresses induced at the end of closure in the initial and remodelled fibre distributions models are shown to be similar in magnitude in all three models (Table 5.4). Comparison of the principal stress distributions shows that the location of the maximal stress occurs in the same location in all three models, at the insertion of the strut chordae (Figure 5.11). Away from this insertion, the reorientation of the fibres alters the maximum principal stress distribution in the off–centre region of the anterior leaflet as the magnitude of the stress decreases. However this is balanced by increases in the stress magnitude observed at the annular base at the centre of the leaflet.

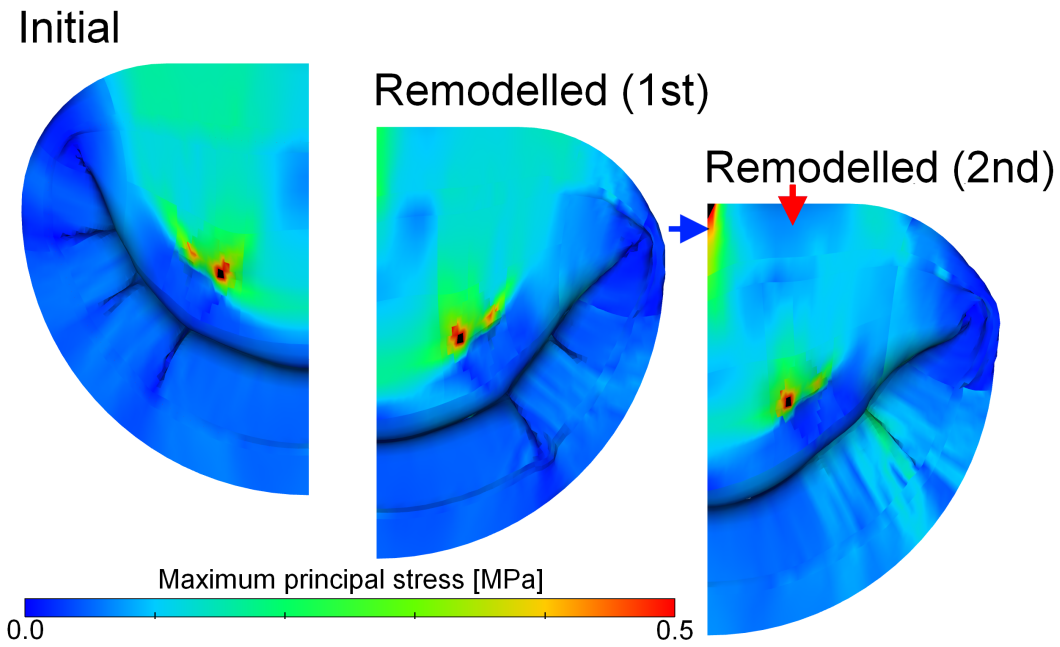

Figure 5.11: Comparison of stresses at closure with the initial (left) and remodelled (right) fibre orientation. Note that values of stress greater than 0.5 MPa are visualised with the colour black. In the 2nd remodelled case, regions of stress decrease and increase are highlighted with red and blue arrows respectively.

Table 5.4: Maximum principal stress at t=200ms.

Iteration	Maximum principal stress [MPa]
Initial	1.19
1st	1.38
2nd	1.21

5.2.8 Principal stretch distribution

The maximum principal stretches induced at the end of closure in the initial and remodelled fibre distributions models have been found to have negligible differences between iterations (Table 5.5). Similar to the principal stresses, the comparison of the principal stretch distributions shows that the peak principal stretches are located in the vicinity of the strut chordal insertions (Figure 5.12). Through remodelling of the fibre orientation the magnitude of the maximum principal stretches at the base of the anterior leaflet are reduced (Figure 5.12). This decrease in stretch results from the rotation of the stiffer fibre direction towards the direction of the greater principal stress, which increases the stiffness and therefore reduces the deformation as shown below in Section 5.2.9. However in the two remodelled iterations the area of greatest stretch surrounding the strut chordal insertion remains the same.

Table 5.5: Maximum principal stretch at closure (t=200 ms).

Iteration	Maximum principal stretch [–]
Initial	1.660
1st	1.659
2nd	1.633

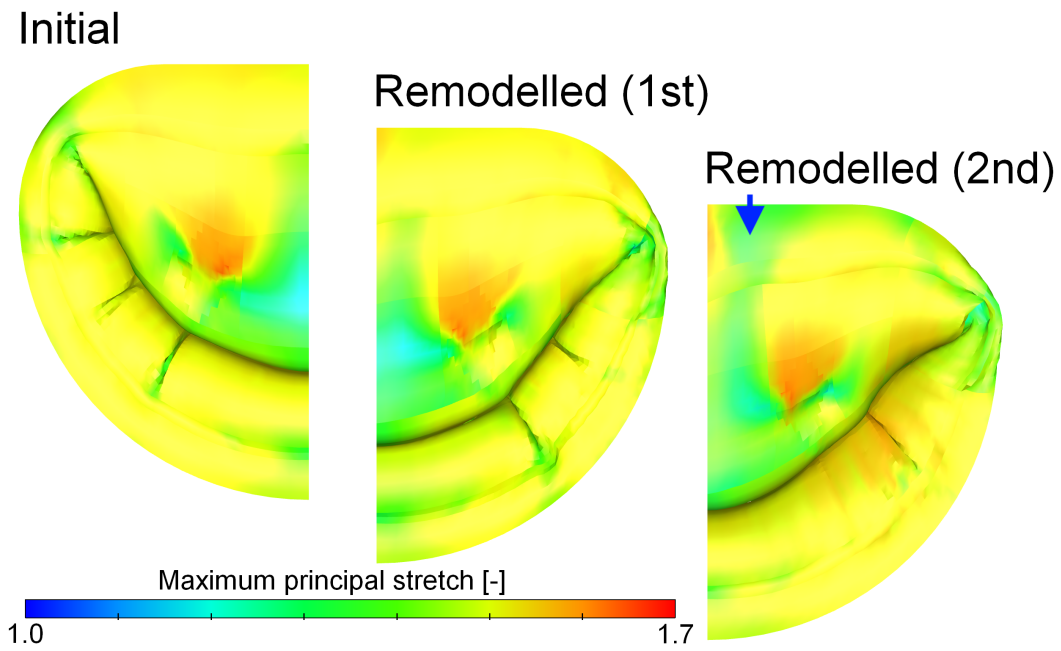

Figure 5.12: Comparison of the maximum principal stretch in the at closure with the initial (left) and remodelled (right) fibre orientation. In the 2nd remodelled case, regions of stretch decrease is highlighted a blue arrow.

5.2.9 Deformed configuration

As described in the previous section, rotation of the stiffer fibre direction towards the greater principal stress increases the stiffness of the leaflets to the applied load that results in a decreased deformation. Comparison of the deformation in the anteropostero plane shows that the anterior leaflet profile of the valve exhibits reduced displacements in the atrial direction in both the remodelled scenarios (Figure 5.13).

5.2.10 Limitations

In these simulations only the basal region of the anterior leaflet, rather than the full valve, has been subjected to the remodelling process. However as this region is the most highly loaded region, it is likely that it will exhibit the largest and most significant fibre orientation as the approach adopted here is stress–based. Extension of this method to the full model of the valve will be added in future iterations.

Here the leaflets of the valve have been modelled using a discrete fibre model in which the material properties are defined relative to the fibre direction only. More advanced material models of the mitral valve have include a continuous description of the fibres, such as the model described by Einstein et al. [76]. Following experimental measurements of the fibre dispersion, perturbations around this value have shown that with decreased fibre dispersion prolapsed states are generated [97]. Comparison of discrete and continuous fibre models by Bischoff [75] have shown that continuous models exhibit smaller deformations under biaxial loading. From the orientation response of the fibres it is clear that the state of loading is highly biaxial in the anterior leaflet. Fibre splay also has a key role in dysfunctional states such as myxomatous degeneration, in which the fibre dispersion is reported to lose all organisation [62].

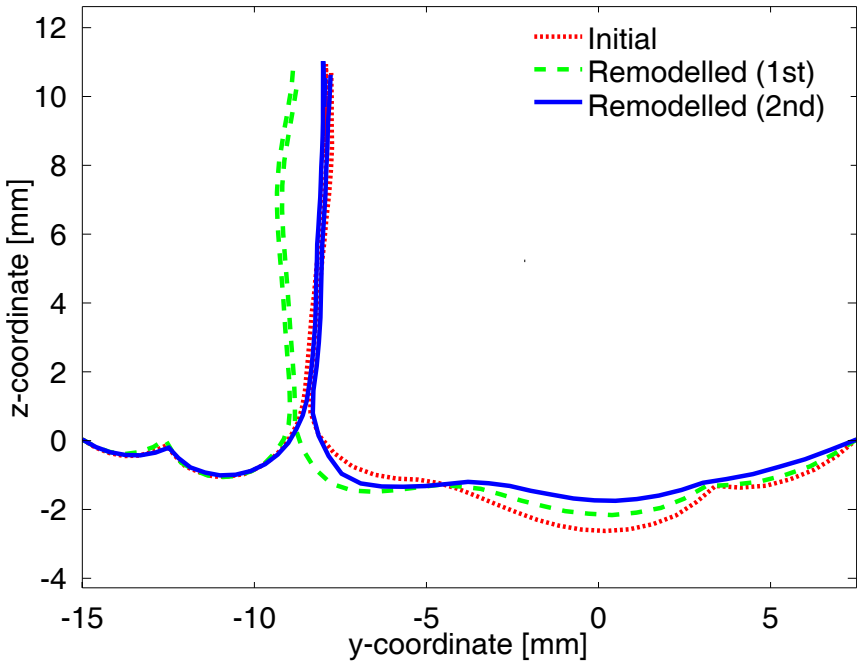

Figure 5.13: Comparison of leaflet deformation at the end of closure, nodal coordinates shown were taken in the symmetry plane of the model.

As a key feature of the leaflet microstructure in both normal and dysfunctional states, it is intended to include fibre dispersion in the remodelling process in future iterations of this work.

5.2.11 Summary

A full three–dimensional model of the mitral valve has been described using a transversely isotropic, non–linear, anisotropic, hyperelastic membrane material model. Using a stress–based approach, the fibre orientation of the basal region of the anterior region has been remodelled in response to closure. Beginning with a uniform distribution of fibre aligned parallel to the annulus, the fibre orientation has been remodelled based upon the ratio of the extra stresses in the first and second principal stress directions. Starting from this arbitrary distribution a stress–based approach to remodelleing has been implemented and examined by comparison to experimentally measured distributions.

The resulting changes in fibre distribution have shown certain features of the native leaflet fibre orientation, as the fibre were found to rotate towards the insertion of the chordae tendineae. However it was also found that in the central regions of the valve the leaflets showed significant deviation away from circumferential alignment observed in the native leaflet tissue. Examination of the magnitude of the maximum principal stress show no significant change, however some localised regions of the leaflets exhibited reduced principal stresses and stretches. Comparison of the deformed configuration in the anteropostero plane of the valve show significant variation in the protrusion of the leaflet into the left atrium.

5.3 Valve growth

As described previously, in dysfunctional states such as functional mitral regurgitation it has been experimentally noted that the area of the mitral valve is greater when compared to normal valves [128]. Further examination of functional mitral regurgitation in an ovine animal model have been subjected to papillary muscle by retraction, have also shown significant growth of the valve with increasing leaflet lengths and areas [132]. Traditionally it has been considered that the properties of the valve are unaltered in cases of functional mitral regurgitation. However these results indicate that the abnormal

mechanical environment induce a growth response in the microstructure of the valve.

In order to better understand this process, a stress–based growth model of valve adaptation in response to a simulated left ventricular ischemic event has been implemented in a numerical model of the mitral valve. Here this adaptation process has been assumed to respond to mechanical stimulii through growth whilst maintaining the initial material properties. Based upon *in vivo* measurements, a state of ischemic mitral regurgitation has been simulated through the retraction of the papillary muscle tips of the model. The resulting increases in maximum principal stresses in this dysfunctional state have been used to define the growth which is proportional to stress increment. The resulting effect of this thickness increase has then been examined in terms of the new stretches and stresses in the valve tissue.

5.3.1 Valve geometry

Using the same geometry as detailed above in Section 5.2.1, here the valve has been truncated to the anterior leaflet only (Figure 5.14). These changes have been performed in order to reduce numerical instabilities in the model arising from issues such as mesh–to–mesh contact. Although only the central portion of the anterior leaflet has been simulated, other aspects such as the primary/secondary chordae tendineae and the papillary muscle tip remain. As before, the chordae are connected to the papillary muscles which have been initially defined as two static nodes positioned in a plane 20 mm above the annulus. The lateral distance between the two tips has been defined in the range 19.5 mm to 21 mm, a value scaled relative to the annular diameter from experimentally reported measurements [110]. The anteropostero position of the these tips was modified to achieve physiological coaptation under closure conditions.

The valve model has been discretised into 1160 co–rotational Hughes–Liu shell elements which have initially been defined with a uniform thickness of 1 mm. The marginal and basal/strut chordae have been discretised into a total of 92 discrete cable elements, defined a cross–sectional area of 0.45 and 1.15 mm^2 respectively. In order to simplify the numerical complexity of the problem only half the valve has been simulated, with the valve modelled as symmetrical about the anteropostero axis. The truncated edge of the model has been simply constrained by only permitting translations in the yz–plane (Figure 5.14).

Figure 5.14: Geometry of the growth model with the anterior leaflet highlighted in red with the unmodelled geometry represented in grey. The dashed line in the middle figure shows the line along which the model was constrained in the x–direction. Left – top down view. Middle – front view. Right – three dimensional view.

5.3.2 Material model

Here the material models used to represent the leaflets and the chordae are the same as described previously in Section 5.2.2. In this model the embedded fibres have been uniformly aligned in the circumfer-

ential direction and as only the anterior leaflet is modelled, only the anterior material model parameters are required (Table 5.6).

Table 5.6: Strain–energy function coefficients of Equation 5.1. Values from May-Newman and Yin [73].

Leaflet	c_0 [kPa]	c_1	c_2
Anterior	0.399	4.535	1446.5

5.3.3 Valve closure

Simulation of valve closure has been performed in a structural–only simulation. The transvalvular pressure difference used to define systole is the same as described previously in Section 5.2.4. The dampening effect of the fluid has been approximated with a mass–weighted nodal velocity damping method with the damping constant $D_s = 0.01$ (see Equations 2.20 and 2.21 in Section 2.4.1.2 on Page 77).

5.3.4 Ischemic mitral regurgitation

Here a state of ischemic mitral regurgitation has been simulated by displacing the papillary muscles during closure. As described previously in Chapter 1, Section 1.3.5, in normal states the papillary muscle contracts in order to maintain a constant distance to the annular plane. However in states of ischemic regurgitation the contractility of the ventricle is impaired, accordingly *in vivo* measuremesnts of the distance between the annular plane and the papillary muscle tips have been shown to increase during systole (Table 5.7) [46] . From this data it can be calculated that the average papillary muscle to annulus distance increases by 9.68% and 16.91% in the anterior and posterior papillary muscle tips respectively. Here the average value of 13.29% has been used to define the displacement of the papillary muscle tips during systole. Accordingly, the papillary muscle tips are displaced in the normal direction of the annular plane, away from the atrium and towards the ventricular apex, during the simulation of closure by a distance of 2.65 mm. Initially in the same position as the normal valve model, this displacement has been defined using a linear ramp over the 200 ms of closure (Figure 5.15).

Table 5.7: Distance from anterior and posterior papillary muscles to annulus center in normal and ischemic mitral regurgitation (IMR) cases. Values from Vergnat et al. [46].

Papillary muscle	Normal [mm]	IMR [mm]
Anterior	27.9±0.9	30.6±1.3
Posterior	27.8±1.2	32.5±1.4

5.3.5 Growth algorithm

Closure of the valve has been performed in the normal and dysfunctional states with uniform thickness. Using the difference between the two stress states, the dysfunctional model has been simulated to undergo a growth response. The growth response of the leaflet tissue in the dysfunctional state is assumed to respond by increasing the leaflet thickness in response increases in the maximum principal stress. The increase in thickness Δt is defined by the ratio of the difference in stresses between the dysfunctional and normal state, σ_d and σ_n respectively, relative to the original stress state σ_n. It has been assumed that only increases in the maximum principal stresses increase the thickness of the leaflets, decreases in the stresses do not change the thickness (Equation 5.10). Following this growth phase closure is performed in the growth modified valve model (now with non–uniform thickness) subject to the same dysfunctional papillary muscle displacements. The resulting stresses are then used to update the valve thickness in an iterative manner (Figure 5.16).

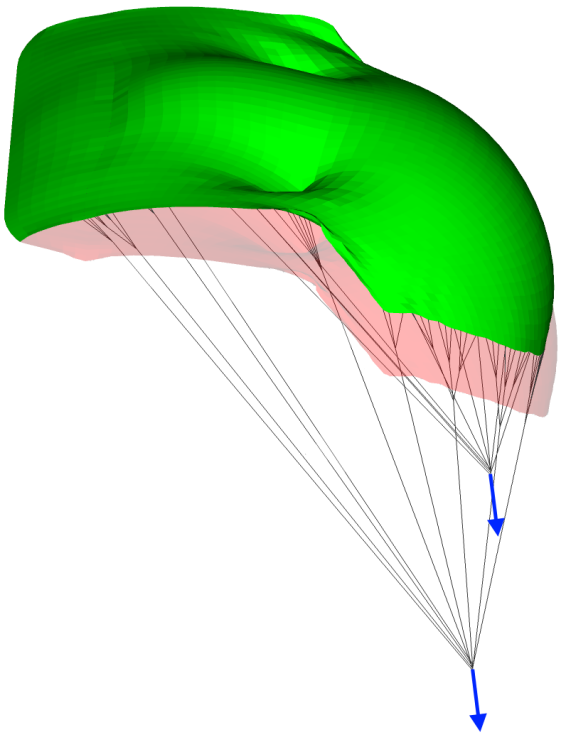

Figure 5.15: Valve configuration in the normal (green) and dysfunctional (red) states at closure. Here the blue arrows indicates the displacement the papillary muscles tips during systole in the dysfunctional case. It can be seen that the resulting leaflet configuration in the dysfunctional case is displaced further away from the atrium. For clarity, the chordae tendineae of the valve in the dysfunctional case have not been visualised.

$$\frac{\Delta t}{t} = \begin{cases} (\sigma_d - \sigma_n)/\sigma_n & \text{if } \sigma_d - \sigma_n > 0 \\ 1 & \text{if } \sigma_d - \sigma_n \leq 0 \end{cases} \tag{5.10}$$

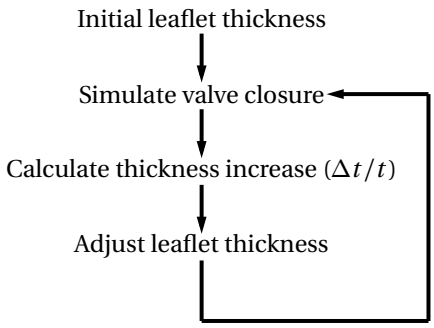

Figure 5.16: Stress based growth algorithm.

5.3.6 Growth response

Here only the the growth response in the dysfunctional state is examined, the stress distributions from which the remodelling response are calculated from are presented below in Section 5.3.7. Using the stresses at closure in the normal and dysfunctional uniform thickness models, the growth response has been calculated for a single iteration. Applying the growth algorithm illustrated in Figure 5.16 the leaflet thickness has been updated using Equation 5.10, with the resulting variation presented in Figure 5.17. Non–uniformly distributed, the effect of the growth response exhibits greater thickness increases in the basal region and the free margin of the valve. Regions toward the central free margin show the smallest (if any) increase in thickness. From the growth response, the mass of the leaflet has increased by

~13% (Table 5.8). Using the non–uniform thickness distribution, closure has been re–simulated and the stresses compared between the the normal and dysfunctional states.

Table 5.8: Mass of the anterior leaflet in the normal and growth modified leaflet models.

Iteration	Mass [g]
Initial	0.169946
Growth	0.19126

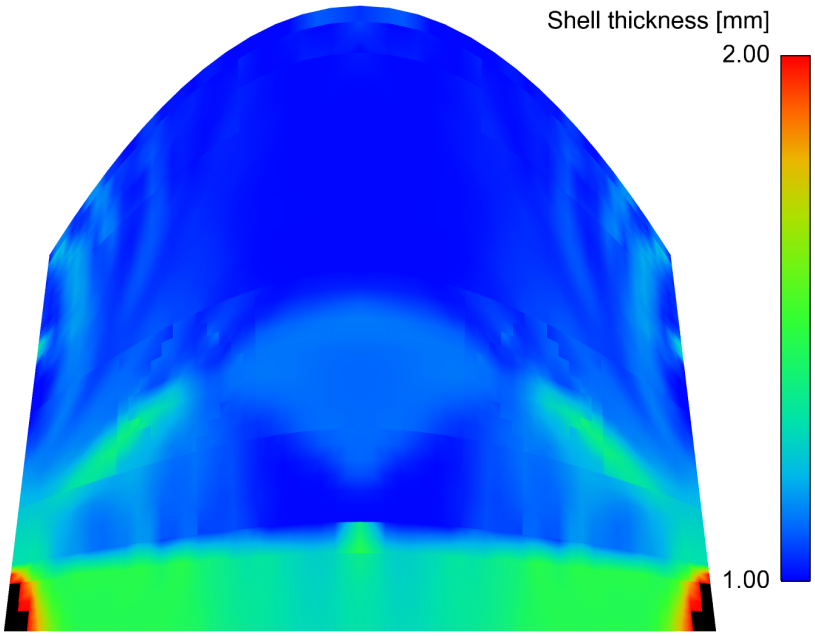

Figure 5.17: Variation in thickness following growth phase, here visualised in the valve in its initial undeformed configuration. Note that values greater than 2 mm are visualised in black.

5.3.7 Stress distribution

Here the resulting maximum principal stress distributions in the normal, dysfunctional uniform thickness and the dysfunctional non–uniform thickness models have been compared (Figure 5.18). In the normal model, peak stresses occur at the insertions of the strut chordae, similar to the full valve model described previously in Section 5.2.7. This uniform thickness model is then subjected to a simulated dysfunction in which the papillary muscle node is retracted during closure, which results in an increase of 13.2% in the maximal value of the maximum principal stress (Table 5.9). In the dysfunctional state (uniform thickness) peak stresses still occur at the insertion of the strut chordae, however regions of similar magnitude to the peak stress appear at the edge of the leaflets and towards the basal regions. The central region of the leaflet also show appreciable greater magnitude stresses than in the normal case.

Following the growth response described in Section 5.3.5 the thickness of the leaflet are updated and closure is re–simulated. This non–uniform thickness model exhibits a maximal value of the maximum principal stress that is comparable to the normal case (Table 5.9). It can be seen from the comparison of the stress distributions in the normal and the non–uniform thickness growth modified model, that the stress distribution are almost identical. The induced stress increases from simulated dysfunction have all been reduced and returned to the normal values.

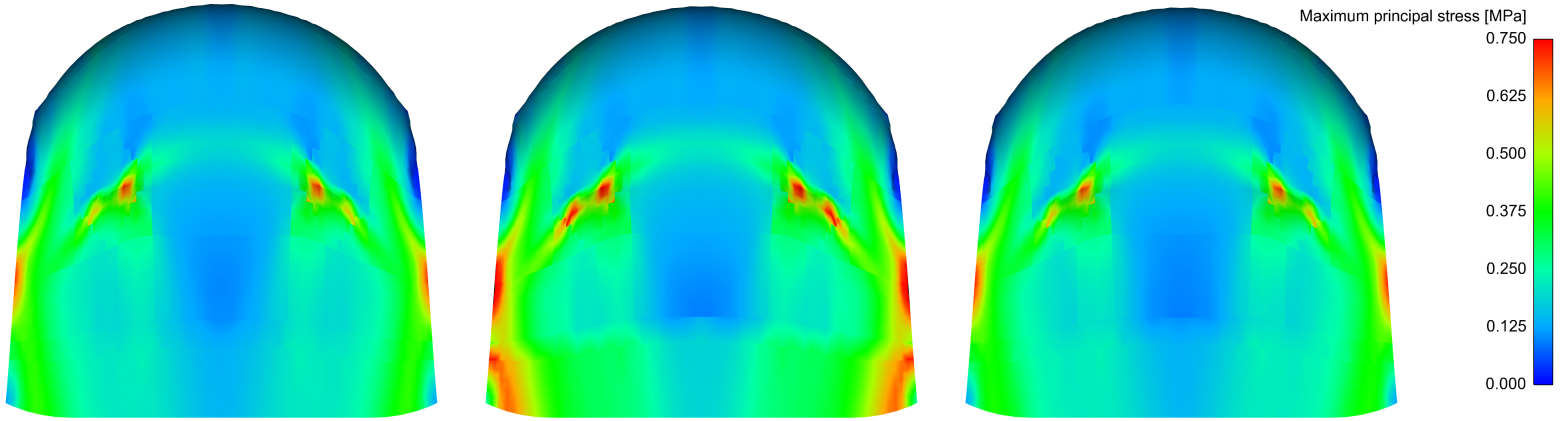

Figure 5.18: Comparison of the stresses in the normal and dysfunctional states. Left – normal model. Middle – uniform thickness model subject to papillary muscle displacement. Right – growth adapted, non–uniform thickness model subject to papillary muscle displacement. Note that the normal and the growth adapted stress distributions are almost identical.

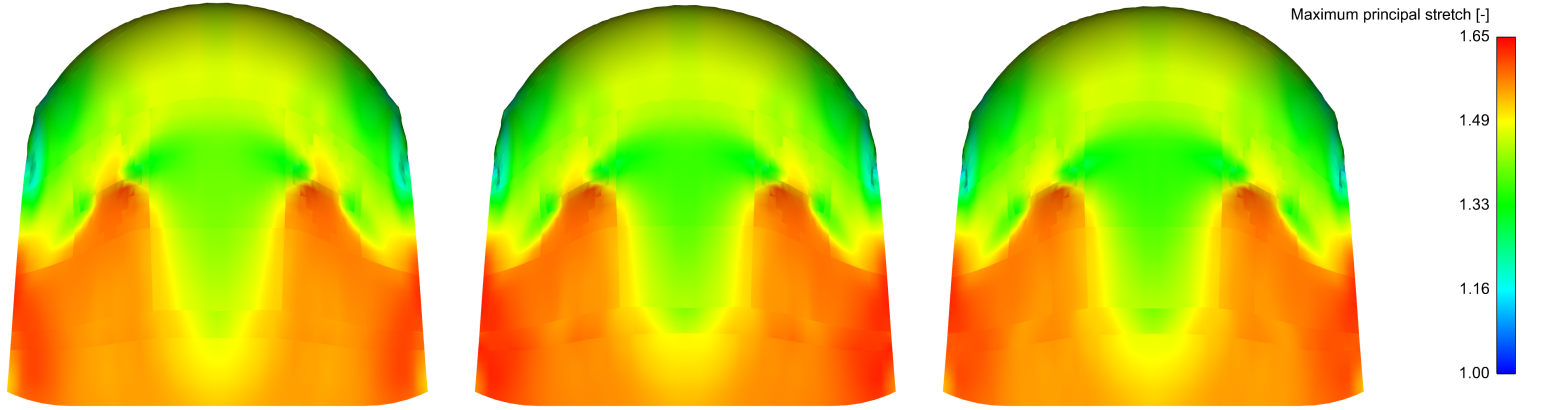

Figure 5.19: Comparison of the stretches in the normal and dysfunctional states. Left – normal model. Middle – uniform thickness model subject to papillary muscle displacement. Right – growth adapted, non–uniform thickness model subject to papillary muscle displacement. Note that all three stretch distributions are almost identical.

Table 5.9: Comparison of the maximum principal stresses in the normal and dysfunctional models

Model	Thickness	Max. principal stress [MPa]
Normal	Uniform	1.06
Dysfunctional	Uniform	1.20
Dysfunctional	Non–uniform	1.03

5.3.8 Stretch distribution

In this section the maximum principal stretches in the normal, dysfunctional uniform thickness and the dysfunctional non–uniform thickness models have been compared. Comparison of the maximal value of the maximum principal stretches between all three models show no significant difference (Table 5.10). Similar comparison of the maximal value of the fibre stretch also show no appreciable difference (Table 5.11). Examination of the principal stretch distributions show near identical distributions in all three models (Figure 5.19).

Table 5.10: Comparison of the maximum principal stretch λ_{ps} in the normal and dysfunctional models.

Model	Thickness	Max. principal stretch [–]
Normal	Uniform	1.64
Dysfunctional	Uniform	1.64
Dysfunctional	Non–uniform	1.63

Table 5.11: Comparison of the maximum fibre stretch λ_f in the normal and dysfunctional models.

Model	Thickness	Max. fibre stretch [–]
Normal	Uniform	1.21
Dysfunctional	Uniform	1.21
Dysfunctional	Non–uniform	1.21

5.3.9 Closed configuration

The deformation configuration of the valve at the end of closure in the anteropostero plane of the model has been compared in the three different models (Figure 5.20). Retraction of the papillary muscles in the dysfunctional states reduces the displacement of the leaflet into the atrium, as reported in the dysfunctional states [132]. It can be seen that the effect of the thickness growth in the valve has no appreciable difference in the deformed configuration of the model in the anteropostero plane of the valve.

5.3.10 Limitations

Here only the central anterior leaflet portion has been simulated. This region consists of only 39.0% of the full valve model presented in Section 5.2 (Table 5.12). As only the anterior leaflet of the model is represented here, the deformed state of the valve is greater than in the full model, as the posterior leaflet limits the distance which the anterior leaflet can traverse across the mitral orifice (Figure 5.21). However the largest growth response was exhibited in the basal regions of the anterior leaflet, regions which are not typically in contact with the posterior leaflet and show similar comparison to the deformed state of the full model (Figure 5.17).

Simulation of ischemic mitral regurgitation has been performed by displacing the papillary muscles away from the annular plane over the course of closure. Here this motion has been assumed to act linearly over the time course of closure, in future iterations of this model this motion will be synchronised with the dynamics of closure.

In this model growth has been assumed to be in the thickness direction only, full volumetric growth in all three dimensions has not been modelled. The experimental measurements of Dal-Bianco et al.

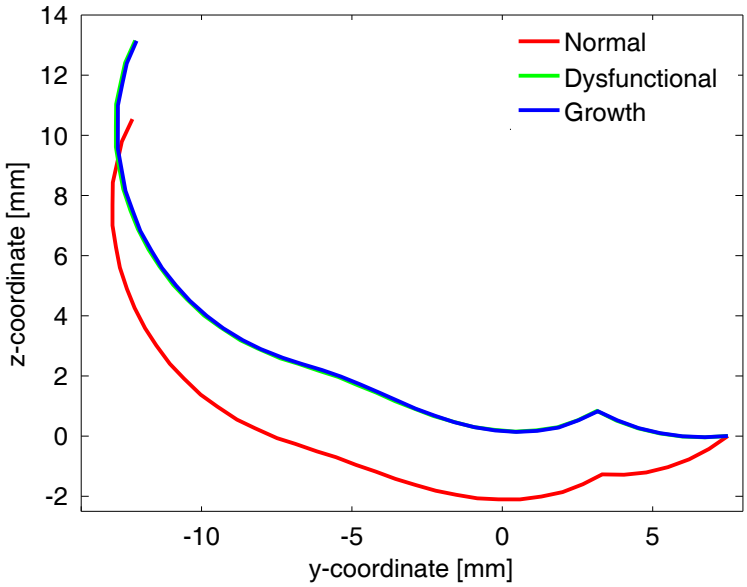

Figure 5.20: Comparison of the closed configuration in the normal and dysfunctional states at the end of closure.

[132] indicate that the growth response of the valve increases both the leaflet length, leaflet area and leaflet thickness (Table 5.13). Alternative approaches of modelling growth have been proposed and implemented by other authors for ventricles [135] and arteries [136]. Based upon the same finite strain theory used here, these studies have included full volumetric growth effects. It is planned to add similar features to future iterations of this work.

In this model the leaflets are represented by constant stress elements, in which the calculated stress is uniform over each shell. In these simulation a strong stress concentration was noted at the insertion of the chordae (Figure 5.18), upon inspection this was found to be localised within a single element. In order to assess the exact spatial extent of this stress concentration, further simulations with increased mesh resolutions are required.

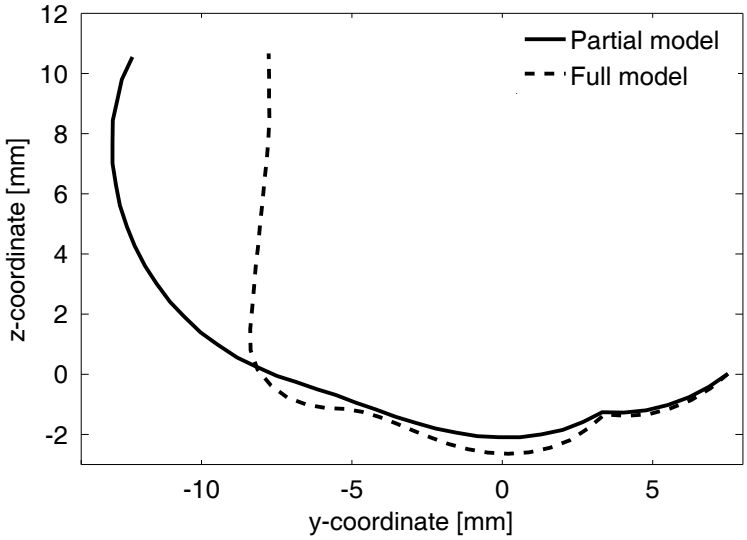

Figure 5.21: Comparison of the closed configuration in the anteropostero plane of the valve in the growth and the full model (full model data from Figure 5.13, Section 5.2.9). In both models the fibres orientation has been defined as parallel to the annulus.

Table 5.12: Full and partial model area comparisons.

Model	Area [mm^2]
Growth model	339.9
Full model (Anterior)	411.8
Full model (Total)	871.2

Table 5.13: Variation in leaflet lengths and areas as reported by Dal-Bianco et al. [132]. Labels: AL – anterior leaflet length, PL – posterior leaflet length and LA – leaflet area.

Parameter	Normal value	Dysfunctional value	Difference [±%]
AL [mm]	17.4±1.3	19.4±1.5	+11.5
PL [mm]	14.6±1.9	15.9±1.7	+8.9
LA [cm^2]	14.3±1.9	16.7±1.9	+16.8

5.3.11 Summary

Here a simplified model of the mitral valve has been subjected to a simulated case of ischemic mitral regurgitation by retraction of the papillary muscle tip during systolic closure. In a uniform thickness model of the valve, the increases in the maximum principal stresses have been calculated and used as the motivation behind thickness based growth. This non–uniform thickness growth modified model has been subjected to the same papillary muscle retraction and the stress and stretch states compared to both the normal and dysfunctional states. Results show that the stresses are reduced to the same magnitude as the normal constant thickness state.

5.4 Context

The work in this chapter has addressed the remodelling and growth of the mitral valve using a fibre aligned hyperelastic material model. The work presented here is a first step to defining a mechanically based model of tissue remodelling and growth in the context of the mitral valve. Adopted from previous efforts reported in aortic valves it is expected that the approaches used here will require some modification as loading conditions are significantly different between the aortic and mitral valves. Applied to a model of the native mitral valve in normal and dysfunctional states, the approach reported here could also be extended to the design of tissue engineered valves.

Chapter 6

Conclusions and Future Work

6.1 Conclusions

6.1.1 Simulation of Valvular Dynamics

In Chapter 3 the methodology used in this work and in the previously published finite element models of the mitral valve/heart valves have been examined. Quasi–static simulations of valve closure, in which the valve reaches a closed configuration where it is in equilibrium with the applied forces, have been performed using both structural–only and fluid–structure interaction approaches. Results show that although there are differences between structural and fluid–structure interaction simuations due to the constant pressure assumption used in the structural approach, the maximum magnitude of the principal stresses and the closure dynamics are similar in both cases. Thus for quasi–static events such as closure, simpler and faster structural–only simulations are appropiate.

However in dynamic/transient events such as valve opening following closure, where the valve is no longer in a state of equilibrium, it has been shown that structural–only approaches are inadequate. Significant differences between the two in terms of the in valvular dynamics have been noted, such as the location of the maximumal velocity which in the structural–only simulations is located at the tip, whereas in a similar fluid–structure interaction simulation it is located in the belly region of the anterior leaflet. Thus for transient events such as valve opening and closing, complex and slower fluid–structure interaction simulations are appropiate. The effect of fluid geometry upon valvular dynamics has also been investigated, comparing tubular and U–shaped fluid volumes. Results indicate significant differences due to the faster fluid flow generated in the straighter and less physiological tubular volume when compared to the U–shaped volume.

6.1.2 Valvular Repair Techniques

In Chapter 4 a fluid–structure interaction method has been used to simulate the effect of a surgical repair technique known as the edge–to–edge repair. Applied to valves which are no longer able to prevent retrograde flow during closure, the repair restores function in closure by reducing the interleaflet distance by connecting surgically connecting the prolapsing segment of the leaflets. Although function in closure is restored, valvular function in opening is modified as the shape of the valvular orifice is reduced. Affecting the flow rate through the valve, this repair also increases the induced stress in the valve due to the increased haemodynamic loads. In this work the effect of this procedure has been simulated in a dysfunctional model of the mitral valve using a fluid–structure interaction model. Using this model both an invasive and non–invasive approach to the edge–to–edge have been examined, with the resulting valvular and fluid dynamics compared to a normal valve. The results of these simulations indicate that the maximum magnitude of the principal stresses are approximately doubled when compared to

the normal valve, conversely the corresponding flow rate through the valvular orifice was found to be reduced by approximately half. Significant differences were observed between the non–invasive and invasive procedures, with the more invasive procedure resulting in a more diffuse stress distribution when compared to the localised stress concentration in the non–invasive case. Clinical studies indicate that the long–term survival of the invasive procedure is greater, here the simulated results suggested a possible stress related mechanism.

6.1.3 Valve Remodelling and Growth

In Chapter 5 the role of biomechanical forces in the growth and remodelling of the mitral valve have been examined in both normal and diseased states. Using a hyperelastic, non–linear, anisotropic, fibre aligned material model, the remodelling of fibre distribution in the anterior leaflet in response to the induced stresses during closure have been simulated. Starting with an initial distribution of uniformly distributed fibres, it has been examined if a stress based approach to fibre remodelling will result in a functional configuration which compares well to experimentally measured results. The results indicate that the remodelled fibre distributions include some aspects of experimentally reported fibre distributions, such as alignment at the insertion of the strut chordae. However the simulated fibre distributions lack alignment in other regions, exhibiting unphysiological fibre configurations. Performed a function of the discrete fibre direction only, these results suggest that in order to generate functional and physiological fibre distributions further inputs such as the fibre splay are required.

Following this, in a simplified model of the mitral valve, the growth response of the mitral valve in response to a simulated case of ischemic mitral regurgitation has been performed. In this model ischemic mitral regurgitation has been simulated by retracted the papillary muscles during closure, the resulting growth response of the leaflet thickness to the abnormal biomechanical loads have been defined as a function of the both the principal stresses in normal and dysfunctional states. After updating the thickness, the growth modified model was closed again under the same dysfunctional conditions and the resulting stresses re–evaluated. The results indicate that in the growth modified model the distribution of the maximum principal stresses show little or no significant difference to the normal case, suggesting a possible mechanism for stress reduction in dysfunctional states such as ischemic mitral regurgitation.

6.1.4 Limitations

The main limitation of this model (and all finite element models) is the inability to measure and therefore validate the predicted stress states *in vivo*. Currently the most appropriate method of validation are either *in vivo* comparison of leaflet deformation (for example see Prot et al. [92]) or *in vivo* strain–based measurements such as those reported by Sacks et al. [137]. Although the simulated stress states presented are an approximation of the *in vivo* conditions, comparisons between different iterations of each model allows for a qualitative understanding of how the stress distributions vary in the different scenarios modelled.

6.2 Future Work

6.2.1 Fluid volume geometry

Limited by the structured mesh required by the fluid solver, in this work the geometry of the ventricle has been represented as a rigid volume that is formed of cuboid elements. A gross simplification of the dynamic geometry of the ventricle, the geometric form of the ventricle is a key feature in the function of the mitral valve and the heart (see Chapter 1, Section 1.3.1).

Using an alternative approach, it will be possible to represent the ventricle as another immersed structure within a common fluid volume. With this approach it will be possible to generate more physi-

ological shaped geometries and allow the definition of the dynamic motion of the ventricular wall during filling. Using such a model of the ventricle and the mitral valve, it is planned to address issues such as valvular and filling dynamics in mitral valve stenosis and ventricular dilation.

6.2.2 Dysfunctional material properties

The application of the edge–to–edge repair is typically performed in cases of mitral valve prolapse/regurgitation whereby the tissue no longer has its native biomechanical properties (see Chapter 1, Section 1.4). Previous experimental results indicate that both the leaflet and chordal tissue exhibit a weaker biomechanical tensile strength, with the leaflet tissue also showing a less anisotropic response [62, 69].

Although previous of the edge–to–edge repair have attempted to model this state of tissue dysfunction, simplifications have been made in the material model used to represent the biomechanical properties. Also implemented using a structural–only approach, the induced stresses will have been underestimated (see Chapter 4, Section 4.2). By fitting the stress response of the the anisotropic fibre aligned material model described in this work (see Chapter 2, Section 2.3.1.3), it is planned to address the effect of the edge–to–edge repair in a degenerate case of mitral regurgitation using a the fluid–structure interaction.

6.2.3 Valve tissue remodelling

The remodelling and growth of the tissue microstructure has been modelled using a discrete fibre model and stress–based approach of tissue adaptation. As described previously, an extension of this will be implement a continuous based description of the fibre distribution that will also include the fibre splay as a parameter of investigation.

In this work the adaptation has assumed to be a stress driven process, i.e. force based. However there exists some debate on if cells interpret stresses or strains. In order to assess this a principal strain approach to remodelled of the tissue is planned. By following the directions of maximal deformation, the variation in the stress and strain distribution will be assessed.

Uniquely for valves, significant contact forces are imparted on the contact surfaces of the valves during each cardiac cycle. In dysfunctional states such as ischemic mitral regurgitation, tenting of the leaflets can reduce the contact area and thus the contact force. The role of this contact force in regulation of the tissue microstructure has yet to be addressed and is planned to be implemented in future work.

6.2.4 Patient Specific Models

In this work all the model presented have been described using idealised geometries, in reality the mitral valve has a significant degree of asymmetry (Chapter 1). In order to be of use in medical scenarios it is required to build patient specific models which incorporate the relevant patient detail. It has been shown from numerical simulations asymmetric geometrical features do affect the stress state of the valve, resulting in an asymmetric distribution [90]. Using imaging modalities such as magnetic resonance imaging (MRI) and three dimensional echocardiography, patient specific features such as the annular position & dynamic motion, papillary muscle position & motion and the leaflet length & thickness can obtained and input into the model. From the resulting simulations it will also be possible to validated the model and modelling methodology by direct comparison to clinical measurements of the valve deformation and/or fluid velocities.

Bibliography

[1] J.R. Levick. *An Introduction to Cardiovascular Physiology*. 4th edition, 2003.

[2] Ajit P Yoganathan, Zhaoming He, and S. Casey Jones. Fluid mechanics of heart valves. *Annu Rev Biomed Eng*, 6:331–362, 2004. doi: 10.1146/annurev.bioeng.6.040803.140111. URL http://dx.doi.org/10.1146/annurev.bioeng.6.040803.140111.

[3] B. Iung, G. Baron, E. G. Butchart, F. Delahaye, C. Gohlke-Bärwolf, O. W. Levang, P. Tornos, J. Vanoverschelde, F. Vermeer, E. Boersma, P. Ravaud, and A. Vahanian. A prospective survey of patients with valvular heart disease in europe: The euro heart survey on valvular heart disease. *European Heart Journal*, 24(13):1231–1243, July 2003.

[4] Julien I.E Hoffman and Samuel Kaplan. The incidence of congenital heart disease. *Journal of the American College of Cardiology*, 39(12):1890–1900, June 2002. ISSN 0735-1097. URL http://www.sciencedirect.com/science/article/pii/S0735109702018867.

[5] Subodh Verma and Thierry G Mesana. Mitral-valve repair for mitral-valve prolapse. *N Engl J Med*, 361(23):2261–2269, Dec 2009. doi: 10.1056/NEJMct0806111. URL http://dx.doi.org/10.1056/NEJMct0806111.

[6] A. C. Anyanwu, B. Bridgewater, and D. H. Adams. The lottery of mitral valve repair surgery. *Heart*, 96(24):1964–1967, Dec 2010. doi: 10.1136/hrt.2010.199620.

[7] G. Ambler, R. Z. Omar, P. Royston, R. Kinsman, B. E. Keogh, and K. M. Taylor. Generic, simple risk stratification model for heart valve surgery. *Circulation*, 112(2):224–231, Jul 2005. doi: 10.1161/CIRCULATIONAHA.104.515049.

[8] Bruce E. Keogh and Robin Kinsman. Fifth national adult cardiac surgical database report 2003. *The Society of Cardiothoracic Surgeons of Great Britain and Ireland*, 2003.

[9] S Y Ho. Anatomy of the mitral valve. *Heart*, 88:5–10, November 2002.

[10] A. Angelini, S. Y. Ho, R. H. Anderson, M. J. Davies, and A. E. Becker. A histological study of the atrioventricular junction in hearts with normal and prolapsed leaflets of the mitral valve. *Br Heart J*, 59(6):712–716, Jun 1988.

[11] K.S. Kunzelman, R.P. Cochran, E.D. Verrier, and R.C. Eberhart. Anatomic basis for mitral valve modelling. *Journal of Heart Valve Disease*, 3(5):491–496, 1994.

[12] Federico Veronesi, Cristiana Corsi, Lissa Sugeng, Victor Mor-Avi, Enrico G Caiani, Lynn Weinert, Claudio Lamberti, and Roberto M Lang. A study of functional anatomy of aortic-mitral valve coupling using 3d matrix transesophageal echocardiography. *Circ Cardiovasc Imaging*, 2(1):24–31, Jan 2009.

[13] Horia Muresian. The clinical anatomy of the mitral valve. *Clin Anat*, 22(1):85–98, Jan 2009. doi: 10.1002/ca.20692.

[14] Jason L Quill, Alexander J Hill, Timothy G Laske, Ottavio Alfieri, and Paul A Iaizzo. Mitral leaflet anatomy revisited. *J Thorac Cardiovasc Surg*, 137(5):1077–1081, May 2009. doi: 10.1016/j.jtcvs.2008.10.008.

[15] M. E. Silverman and J. W. Hurst. The mitral complex. interaction of the anatomy, physiology, and pathology of the mitral annulus, mitral valve leaflets, chordae tendineae, and papillary muscles. *Am Heart J*, 76(3):399–418, Sep 1968.

[16] J. H. C. Lam, N. Ranganathan, E. D. Wiglb, and M. D. Silver. Morphology of the human mitral valve: I. chordae tendineae: A new classification. *Circulation*, 41(3):449–458, March 1970.

[17] Alexandra A Degandt, Patricia A Weber, Hashim A Saber, and Carlos M G Duran. Mitral valve basal chordae: comparative anatomy and terminology. *Ann Thorac Surg*, 84(4):1250–1255, Oct 2007. doi: 10.1016/j.athoracsur.2007.05.008. URL http://dx.doi.org/10.1016/j.athoracsur.2007.05.008.

[18] Leon Axel. Papillary muscles do not attach directly to the solid heart wall. *Circulation*, 109(25):3145–3148, Jun 2004. doi: 10.1161/01.CIR.0000134276.06719.F3. URL http://dx.doi.org/10.1161/01.CIR.0000134276.06719.F3.

[19] T. Sakai, Y. Okita, Y. Ueda, T. Tahata, H. Ogino, K. Matsuyama, and S. Miki. Distance between mitral anulus and papillary muscles: Anatomic study in normal human hearts. *Journal of Thoracic and Cardiovascular Surgery*, 118:636–641, 1999.

[20] Jos J M Westenberg, Mike G Danilouchkine, Joost Doornbos, Jeroen J Bax, Rob J van der Geest, Gerda Labadie, Hildo J Lamb, Michel I M Versteegh, Albert de Roos, and Johan H C Reiber. Accurate and reproducible mitral valvular blood flow measurement with three-directional velocity-encoded magnetic resonance imaging. *J Cardiovasc Magn Reson*, 6(4):767–776, 2004.

[21] P. J. Kilner, G. Z. Yang, A. J. Wilkes, R. H. Mohiaddin, D. N. Firmin, and M. H. Yacoub. Asymmetric redirection of flow through the heart. *Nature*, 404(6779):759–761, Apr 2000. doi: 10.1038/35008075. URL http://dx.doi.org/10.1038/35008075.

[22] B. J. Bellhouse and F. H. Bellhouse. Fluid mechanics of the mitral valve. *Nature*, 224(5219):615–616, Nov 1969.

[23] J. G. Dumesnil and A. P. Yoganathan. Theoretical and practical differences between the gorlin formula and the continuity equation for calculating aortic and mitral valve areas. *Am J Cardiol*, 67(15):1268–1272, Jun 1991.

[24] Morteza Gharib, Edmond Rambod, Arash Kheradvar, David J Sahn, and John O Dabiri. Optimal vortex formation as an index of cardiac health. *Proc Natl Acad Sci U S A*, 103(16):6305–6308, Apr 2006. doi: 10.1073/pnas.0600520103. URL http://dx.doi.org/10.1073/pnas.0600520103.

[25] L. Hatle, A. Brubakk, A. Tromsdal, and B. Angelsen. Noninvasive assessment of pressure drop in mitral stenosis by doppler ultrasound. *Br Heart J*, 40(2):131–140, Feb 1978.

[26] Helmut Baumgartner, Judy Hung, Javier Bermejo, John B. Chambers, Arturo Evangelista, Brian P. Griffin, Bernard Iung, Catherine M. Otto, Patricia A. Pellikka, and Miguel QuiÃśones. Echocardiographic assessment of valve stenosis: Eae/ase recommendations for clinical practice. *European Journal of Echocardiography*, 10(1):1–25, January 2009. URL http://ejechocard.oxfordjournals.org/content/10/1/1.short.

[27] W. A. Zoghbi, M. Enriquez-Sarano, E. Foster, P. A. Grayburn, C. D. Kraft, R. A. Levine, P. Nihoyannopoulos, C. M. Otto, M. A. Quinones, H. Rakowski, W. J. Stewart, A. Waggoner, and N. J. Weissman. American society of echocardiography: recommendations for evaluation of the severity of native valvular regurgitation with two-dimensional and doppler echocardiography. *European Journal of Echocardiography*, 4(4):237–261, December 2003. URL http://ejechocard.oxfordjournals.org/content/4/4/237.short.

[28] S. R. Kaplan, G. Bashein, F. H. Sheehan, M. E. Legget, B. Munt, X. N. Li, M. Sivarajan, E. L. Bolson, M. Zeppa, M. Z. Arch, and R. W. Martin. Three-dimensional echocardiographic assessment of annular shape changes in the normal and regurgitant mitral valve. *Am Heart J*, 139(3):378–387, Mar 2000.

[29] Liam P. Ryan, Benjamin M. Jackson, Yoshiharu Enomoto, Landi Parish, Theodore J. Plappert, Martin G. St. John-Sutton, Robert C. Gorman, and Joseph H. Gorman III. Description of regional mitral annular nonplanarity in healthy human subjects: A novel methodology. *The Journal of Thoracic and Cardiovascular Surgery*, 134(3):644–648, September 2007. ISSN 0022-5223. URL http://www.sciencedirect.com/science/article/pii/S0022522307006228.

[30] Tomasz A Timek and D.Craig Miller. Experimental and clinical assessment of mitral annular area and dynamics: what are we actually measuring? *The Annals of Thoracic Surgery*, 72(3):966–974, September 2001.

[31] Jun Kwan, Min-Jae Jeon, Dae-Hyeok Kim, Keum-Soo Park, and Woo-Hyung Lee. Does the mitral annulus shrink or enlarge during systole? a real-time 3d echocardiography study. *J Korean Med Sci*, 24(2):203–208, Apr 2009. doi: 10.3346/jkms.2009.24.2.203.

[32] Emiliano Votta, Enrico Caiani, Federico Veronesi, Monica Soncini, Franco Maria Montevecchi, and Alberto Redaelli. Mitral valve finite-element modelling from ultrasound data: a pilot study for a new approach to understand mitral function and clinical scenarios. *Philosophical Transactions of the Royal Society A: Mathematical, Physical and Engineering Sciences*, 366(1879):3411–3434, 2008. doi: 10.1098/rsta.2008.0095.

[33] S. M. Tuladhar and P. P. Punjabi. Surgical reconstruction of the mitral valve. *Heart*, 92(10):1373–1377, Oct 2006. doi: 10.1136/hrt.2005.067421. URL http://dx.doi.org/10.1136/hrt.2005.067421.

[34] Paul Dagum, Tomasz Timek, G. Randall Green, George T. Daughters, David Liang, Jr Ingels, Neil B., and D. Craig Miller. Three-dimensional geometric comparison of partial and complete flexible mitral annuloplasty rings. *J Thorac Cardiovasc Surg*, 122(4):665–673, October 2001. URL http://jtcs.ctsnetjournals.org/cgi/content/abstract/122/4/665.

[35] J. K. Perloff and W. C. Roberts. The mitral apparatus: Functional anatomy of mitral regurgitation. *Circulation*, 46(2):227–239, August 1972. URL http://circ.ahajournals.org/content/46/2/227.short.

[36] Akinobu Itoh, Gaurav Krishnamurthy, Julia C Swanson, Daniel B Ennis, Wolfgang Bothe, Ellen Kuhl, Matts Karlsson, Lauren R Davis, D. Craig Miller, and Neil B Ingels. Active stiffening of mitral valve leaflets in the beating heart. *Am J Physiol Heart Circ Physiol*, 296(6):H1766–H1773, Jun 2009. doi: 10.1152/ajpheart.00120.2009. URL http://dx.doi.org/10.1152/ajpheart.00120.2009.

[37] Martin Misfeld and Hans-Hinrich Sievers. Heart valve macro- and microstructure. *Philosophical Transactions of the Royal Society B: Biological Sciences*, 362(1484):1421–1436, August 2007. URL http://rstb.royalsocietypublishing.org/content/362/1484/1421.abstract.

[38] M. S. Sacks, Z. He, L. Baijens, S. Wanant, P. Shah, H. Sugimoto, and A. P. Yoganathan. Surface strains in the anterior leaflet of the functioning mitral valve. *Ann Biomed Eng*, 30(10):1281–1290, 2002.

[39] Robert O Bonow, Blase A Carabello, Kanu Chatterjee, Antonio C de Leon, David P Faxon, Michael D Freed, William H Gaasch, Bruce W Lytle, Rick A Nishimura, Patrick T O'Gara, Robert A O'Rourke, Catherine M Otto, Pravin M Shah, Jack S Shanewise, 2006 Writing Committee Members, and American College of Cardiology/American Heart Association Task Force. 2008 focused update incorporated into the acc/aha 2006 guidelines for the management of patients with valvular heart disease: a report of the american college of cardiology/american heart association task force on practice guidelines (writing committee to revise the 1998 guidelines for the management of patients with valvular heart disease): endorsed by the society of cardiovascular anesthesiologists, society for cardiovascular angiography and interventions, and society of thoracic surgeons. *Circulation*, 118(15):e523–e661, Oct 2008. doi: 10.1161/CIRCULATIONAHA.108.190748. URL http://dx.doi.org/10.1161/CIRCULATIONAHA.108.190748.

[40] Daniel M Espino, Duncan E T Shepherd, David W L Hukins, and Keith G Buchan. The role of chordae tendineae in mitral valve competence. *J Heart Valve Dis*, 14(5):603–609, Sep 2005.

[41] Ling Chen and Karen May-Newman. Effect of strut chordae transection on mitral valve leaflet biomechanics. *Ann Biomed Eng*, 34(6):917–926, Jun 2006. doi: 10.1007/s10439-006-9095-7. URL http://dx.doi.org/10.1007/s10439-006-9095-7.

[42] Uri Gabbay and Chaim Yosefy. The underlying causes of chordae tendinae rupture: a systematic review. *Int J Cardiol*, 143(2):113–118, Aug 2010. doi: 10.1016/j.ijcard.2010.02.011. URL http://dx.doi.org/10.1016/j.ijcard.2010.02.011.

[43] Jeffrey J. Silbiger and Raveen Bazaz. Contemporary insights into the functional anatomy of the mitral valve. *American Heart Journal*, 158(6):887–895, December 2009. ISSN 0002-8703. URL http://www.sciencedirect.com/science/article/pii/S0002870309008060.

[44] T.M. Joudinaud, C.L. Kegel, E.M. Flecher, P.A. Weber, E. Lansac, U. Hvass, and C.M.G. Duran. The papillary muscles as shock absorbers of the mitral valve complex. an experimental study. *European Journal of Cardio-thoracic Surgery*, 32:96–101, 2007.

[45] Liam P. Ryan, Benjamin M. Jackson, Landi M. Parish, Hiroaki Sakamoto, Theodore J. Plappert, Martin St. John-Sutton, III Gorman, Joseph H., and Robert C. Gorman. Mitral valve tenting index for assessment of subvalvular remodeling. *Ann Thorac Surg*, 84(4):1243–1249, October 2007. URL http://ats.ctsnetjournals.org/cgi/content/abstract/84/4/1243.

[46] Mathieu Vergnat, Arminder S Jassar, Benjamin M Jackson, Liam P Ryan, Thomas J Eperjesi, Alison M Pouch, Stuart J Weiss, Albert T Cheung, Michael A Acker, Joseph H Gorman, and Robert C Gorman. Ischemic mitral regurgitation: a quantitative three-dimensional echocardiographic analysis. *Ann Thorac Surg*, 91(1):157–164, Jan 2011. doi: 10.1016/j.athoracsur.2010.09.078. URL http://dx.doi.org/10.1016/j.athoracsur.2010.09.078.

[47] Michael S Sacks, W. David Merryman, and David E Schmidt. On the biomechanics of heart valve function. *J Biomech*, 42(12):1804–1824, Aug 2009. doi: 10.1016/j.jbiomech.2009.05.015. URL http://dx.doi.org/10.1016/j.jbiomech.2009.05.015.

[48] Bruce Alberts, Alexander Johnson, Julian Lewis, Martin Raff, Keith Roberts, and Peter Walter. *Molecular Biology of the Cell*. Garland, fourth edition, 2002. URL http://www.ncbi.nlm.nih.gov/books/bv.fcgi?call=bv.View..ShowTOC&rid=mboc4.TOC&depth=2.

[49] K. S. Kunzelman, R. P. Cochran, S. S. Murphree, W. S. Ring, E. D. Verrier, and R. C. Eberhart. Differential collagen distribution in the mitral valve and its influence on biomechanical behaviour. *J Heart Valve Dis*, 2(2):236–244, Mar 1993.

[50] D. L. Mulholland and A. I. Gotlieb. Cell biology of valvular interstitial cells. *Can J Cardiol*, 12(3): 231–236, Mar 1996.

[51] Elizabeth H. Stephens, Tom C. Nguyen, Akinobu Itoh, Neil B. Ingels, D. Craig Miller, and K. Jane Grande-Allen. The effects of mitral regurgitation alone are sufficient for leaflet remodeling. *Circulation*, 118(14 suppl 1):S243–S249, September 2008. URL http://circ.ahajournals.org/content/118/14_suppl_1/S243.abstract.

[52] R. P. Cochran, K. S. Kunzelman, C. J. Chuong, M. S. Sacks, and R. C. Eberhart. Nondestructive analysis of mitral valve collagen fiber. *ASAIO Transactions*, 37(3):M447, July/September 1991.

[53] K. L. Billiar and M. S. Sacks. A method to quantify the fiber kinematics of planar tissues under biaxial stretch. *J Biomech*, 30(7):753–756, Jul 1997.

[54] K. May-Newman and F. C. Yin. Biaxial mechanical behavior of excised porcine mitral valve leaflets. *Am J Physiol*, 269(4 Pt 2):H1319–H1327, Oct 1995.

[55] Jonathan Grashow, Michael Sacks, Jun Liao, and Ajit Yoganathan. Planar biaxial creep and stress relaxation of the mitral valve anterior leaflet. *Annals of Biomedical Engineering*, 34(10):1509–1518, 2006. ISSN 0090-6964. URL http://dx.doi.org/10.1007/s10439-006-9183-8.

[56] R. E. Clark. Stress-strain characteristics of fresh and frozen human aortic and mitral leaflets and chordae tendineae. implications for clinical use. *J Thorac Cardiovasc Surg*, 66(2):202–208, Aug 1973.

[57] D. N. Ghista and A. P. Rao. Mitral-valve mechanics–stress-strain characteristics of excised leaflets, analysis of its functional mechanics and its medical application. *Med Biol Eng*, 11(6):691–702, Nov 1973.

[58] L. Chen, F.C.P Yin, and K. May-Newman. The structure and mechanical properties of the mitral valve leaflet–strut chordae transition zone. *Journal of Biomechanical Engineering*, 126:244–251, April 2004.

[59] Gaurav Krishnamurthy, Akinobu Itoh, Wolfgang Bothe, Julia C Swanson, Ellen Kuhl, Matts Karlsson, D. Craig Miller, and Neil B Ingels. Stress-strain behavior of mitral valve leaflets in the beating ovine heart. *J Biomech*, Jun 2009. doi: 10.1016/j.jbiomech.2009.05.018.

[60] Richard H. Davis, Benjamin Schuster, Suzanne B. Knoebel, and Charles Fisch. Myxomatous degeneration of the mitral valve. *The American Journal of Cardiology*, 28(4):449–455, October 1971. ISSN 0002-9149. URL http://www.sciencedirect.com/science/article/pii/0002914971900099.

[61] W. G. Cole, D. Chan, A. J. Hickey, and D. E. Wilcken. Collagen composition of normal and myxomatous human mitral heart valves. *Biochem J*, 219(2):451–460, Apr 1984.

[62] J. Edward Barber, F. Kurtis Kasper, Norman B. Ratliff, Delos M. Cosgrove, Brian P. Griffin, and Ivan Vesely. Mechanical properties of myxomatous mitral valves. *Journal of Thoracic and Cardiovascular Surgery*, 122(5):955–962, November 2001. ISSN 0022-5223. doi: 10.1067/mtc.2001.117621.

[63] William R Mills, J. Edward Barber, Norman B Ratliff, Delos M Cosgrove, Ivan Vesely, and Brian P Griffin. Biomechanical and echocardiographic characterization of flail mitral leaflet due to myxomatous disease: further evidence for early surgical intervention. *Am Heart J*, 148(1):144–150, Jul 2004. doi: 10.1016/j.ahj.2004.01.021.

[64] V. Prot, B. Skallerud, G. Sommer, and G. A. Holzapfel. On modelling and analysis of healthy and pathological human mitral valves: two case studies. *J Mech Behav Biomed Mater*, 3(2):167–177, Feb 2010. doi: 10.1016/j.jmbbm.2009.05.004. URL http://dx.doi.org/10.1016/j.jmbbm.2009.05.004.

[65] Jun Liao, Lauren B Priddy, Bo Wang, Joseph Chen, and Ivan Vesely. Ultrastructure of porcine mitral valve chordae tendineae. *J Heart Valve Dis*, 18(3):292–299, May 2009.

[66] C. Millington-Sanders, A. Meir, L. Lawrence, and C. Stolinski. Structure of chordae tendineae in the left ventricle of the human heart. *J Anat*, 192 (Pt 4):573–581, May 1998.

[67] K. S. Kunzelman and R. P. Cochran. Mechanical properties of basal and marginal mitral valve chordae tendineae. *ASAIO Trans*, 36(3):M405–M408, 1990.

[68] Jun Liao and Ivan Vesely. A structural basis for the size-related mechanical properties of mitral valve chordae tendineae. *Journal of Biomechanics*, 36(8):1125–1133, August 2003.

[69] J. E. Barber, N. B. Ratliff, D. M. Cosgrove, B. P. Griffin, and I. Vesely. Myxomatous mitral valve chordae. i: Mechanical properties. *J Heart Valve Dis*, 10(3):320–324, May 2001.

[70] Gerhard A. Holzapfel. *Nonlinear Solid Mechanics*. Wiley, 2000.

[71] Alan D Freed, Daniel R Einstein, and Ivan Vesely. Invariant formulation for dispersed transverse isotropy in aortic heart valves: an efficient means for modeling fiber splay. *Biomech Model Mechanobiol*, 4(2-3):100–117, Nov 2005. doi: 10.1007/s10237-005-0069-8. URL http://dx.doi.org/10.1007/s10237-005-0069-8.

[72] G.A. Holzapfel and R.W. Ogden. *Biomechanics of soft tissue in cardiovascular systems*. Courses and lectures - International Centre for Mechanical Sciences. Springer, 2003. ISBN 9783211004555. URL http://books.google.co.uk/books?id=u58XJlr5YuYC.

[73] K. May-Newman and F. C. Yin. A constitutive law for mitral valve tissue. *J Biomech Eng*, 120(1):38–47, Feb 1998. doi: 10.1115/1.2834305.

[74] V. Prot, B. Skallerud, and G. A. Holzapfel. Transversely isotropic membrane shells with application to mitral valve mechanics. constitutive modelling and finite element implementation. *International Journal for Numerical Methods in Engineering*, 71(8):987–1008, 2007. doi: 10.1002/nme.1983.

[75] Jeffrey E. Bischoff. Continuous versus discrete (invariant) representations of fibrous structure for modeling non-linear anisotropic soft tissue behavior. *International Journal of Non-Linear Mechanics*, 41(2):167–179, March 2006. ISSN 0020-7462. URL http://www.sciencedirect.com/science/article/pii/S0020746205000739.

[76] D. R. Einstein, K. S. Kunzelman, P. G. Reinhall, R. P. Cochran, and M. A. Nicosia. Haemodynamic determinants of the mitral valve closure sound: a finite element study. *Med Biol Eng Comput*, 42(6):832–846, Nov 2004.

[77] K. L. Billiar and M. S. Sacks. Biaxial mechanical properties of the native and glutaraldehyde-treated aortic valve cusp: Part ii–a structural constitutive model. *J Biomech Eng*, 122(4):327–335, Aug 2000.

[78] D. R. Einstein, P. Reinhall, M. Nicosia, R. P. Cochran, and K. Kunzelman. Dynamic finite element implementation of nonlinear, anisotropic hyperelastic biological membranes. *Computer Methods in Biomechanics and Biomedical Engineering*, 6(1):33–44, 2003. ISSN 1025-5842. doi: 10.1080/1025584021000048983.

[79] John O. Hallquist. *LS–DYNA Theory Manual*. Livermore Software Technology Corporation (LSTC), March 2006. URL http://www.lstc.com/pdf/ls-dyna_theory_manual_2006.pdf.

[80] Livermore Software Technology Corporation: LSTC. *LS–DYNA Keyword User's Manual*, 971 edition, May 2007. URL http://www.lstc.com/pdf/ls-dyna_971_manual_k.pdf.

[81] Eli J Weinberg and Mohammad R Kaazempur-Mofrad. A large-strain finite element formulation for biological tissues with application to mitral valve leaflet tissue mechanics. *J Biomech*, 39(8): 1557–1561, 2006. doi: 10.1016/j.jbiomech.2005.04.020. URL http://dx.doi.org/10.1016/j.jbiomech.2005.04.020.

[82] Eli J Weinberg and Mohammad R Kaazempur Mofrad. A finite shell element for heart mitral valve leaflet mechanics, with large deformations and 3d constitutive material model. *J Biomech*, 40(3): 705–711, 2007. doi: 10.1016/j.jbiomech.2006.01.003. URL http://dx.doi.org/10.1016/j.jbiomech.2006.01.003.

[83] Peter J Cawley, Jeffrey H Maki, and Catherine M Otto. Cardiovascular magnetic resonance imaging for valvular heart disease: technique and validation. *Circulation*, 119(3):468–478, Jan 2009. doi: 10.1161/CIRCULATIONAHA.107.742486. URL http://dx.doi.org/10.1161/CIRCULATIONAHA.107.742486.

[84] Gabriel Valocik, Otto Kamp, and Cees A Visser. Three-dimensional echocardiography in mitral valve disease. *Eur J Echocardiogr*, 6(6):443–454, Dec 2005. doi: 10.1016/j.euje.2005.02.007. URL http://dx.doi.org/10.1016/j.euje.2005.02.007.

[85] K.S. Kunzelman, R.P. Cochran, C Chuong, W.S. Ring, E.D. Verrier, and R.D. Eberhart. Finite element analysis of the mitral valve. *Journal of Heart Valve Disease*, 2(3):326–340, 1993.

[86] O.C. Zienkiewicz, R.L. Taylor, R.L. Taylor, and J.Z. Zhu. *The finite element method: its basis and fundamentals*. The Finite Element Method. Elsevier Butterworth-Heinemann, 2005. ISBN 9780750663205. URL http://books.google.co.uk/books?id=YocoaH8lnx8C.

[87] K. S. Kunzelman, M. S. Reimink, and R. P. Cochran. Annular dilatation increases stress in the mitral valve and delays coaptation: a finite element computer model. *Cardiovascular Surgery*, 5 (4):427–434, July 1997. ISSN 0967-2109. doi: http://dx.doi.org/10.1016/S0967-2109(97)00045-8.

[88] Karyn S. Kunzelman, David W. Quick, and Richard P. Cochran. Altered collagen concentration in mitral valve leaflets: biochemical and finite element analysis. *The Annals of Thoracic Surgery*, 66 (6, Supplement 1):S198–S205, December 1998. ISSN 0003-4975.

[89] Ivan S. Salgo, III Gorman, Joseph H., Robert C. Gorman, Benjamin M. Jackson, Frank W. Bowen, Theodore Plappert, Martin G. St John Sutton, and Jr Edmunds, L. Henry. Effect of annular shape on leaflet curvature in reducing mitral leaflet stress. *Circulation*, 106(6):711–717, 2002.

[90] Khee Hiang Lim, Joon Hock Yeo, and Carlos M G Duran. Three-dimensional asymmetrical modeling of the mitral valve: a finite element study with dynamic boundaries. *Journal of Heart Valve Disease*, 14(3):386–392, May 2005.

[91] V. Prot and B. Skallerud. Nonlinear solid finite element analysis of mitral valves with heterogeneous leaflet layers. *Comput. Mech.*, 43:353–368, 2009.

[92] V. Prot, R. Haaverstad, and B. Skallerud. Finite element analysis of the mitral apparatus: annulus shape effect and chordal force distribution. *Biomechanics and Modeling in Mechanobiology*, 8(1): 43–55, February 2009.

[93] B. Skallerud, V. Prot, and I. S. Nordrum. Modeling active muscle contraction in mitral valve leaflets during systole: a first approach. *Biomech Model Mechanobiol*, 10(1):11–26, Feb 2011. doi: 10.1007/s10237-010-0215-9. URL http://dx.doi.org/10.1007/s10237-010-0215-9.

[94] Marco Stevanella, Emiliano Votta, and Alberto Redaelli. Mitral valve finite element modeling: implications of tissues' nonlinear response and annular motion. *J Biomech Eng*, 131(12):121010, Dec 2009. doi: 10.1115/1.4000107. URL http://dx.doi.org/10.1115/1.4000107.

[95] Emiliano Votta, Francesco Maisano, Monica Soncini, Alberto Redaelli, Franco M Montevecchi, and Ottavio Alfieri. 3-d computational analysis of the stress distribution on the leaflets after edge-to-edge repair of mitral regurgitation. *Journal of Heart Valve Disease*, 11(6):810–822, Nov 2002.

[96] D.R. Einstein, K.S. Kunzelman, P.G. Reinhall, M.A. Nicosia, and R.P. Cochran. Non–linear fluid–coupled computational model of the mitral valve. *Journal of Heart Valve Disease*, 14(2):376–385, March 2005.

[97] Daniel R Einstein, Karyn S Kunzelman, Per G Reinhall, Mark A Nicosia, and Richard P Cochran. The relationship of normal and abnormal microstructural proliferation to the mitral valve closure sound. *J Biomech Eng*, 127(1):134–147, Feb 2005.

[98] K.S. Kunzelman and et al. Fluid-structure interaction models of the mitral valve: function in normal and pathological states. *Philosophical Transactions of the Royal Society B*, 362:1393–1406, 2007.

[99] M. S. Reimink, K. S. Kunzelman, E. D. Verrier, and R. P. Cochran. The effect of anterior chordal replacement on mitral valve function and stresses. a finite element study. *ASAIO J*, 41(3):M754–M762, 1995.

[100] M. S. Reimink, K. S. Kunzelman, and R. P. Cochran. The effect of chordal replacement suture length on function and stresses in repaired mitral valves: a finite element study. *J Heart Valve Dis*, 5(4):365–375, Jul 1996.

[101] K. Kunzelman, M. S. Reimink, E. D. Verrier, and R. P. Cochran. Replacement of mitral valve posterior chordae tendineae with expanded polytetrafluoroethylene suture: a finite element study. *J Card Surg*, 11(2):136–45; discussion 146, 1996.

[102] Emiliano Votta, Francesco Maisano, Steven F Bolling, Ottavio Alfieri, Franco M Montevecchi, and Alberto Redaelli. The geoform disease-specific annuloplasty system: a finite element study. *Ann Thorac Surg*, 84(1):92–101, Jul 2007. doi: 10.1016/j.athoracsur.2007.03.040. URL http://dx.doi.org/10.1016/j.athoracsur.2007.03.040.

[103] Silvia Schievano, Karyn Kunzelman, Mark A Nicosia, Richard P Cochran, Daniel R Einstein, Sachin Khambadkone, and Philipp Bonhoeffer. Percutaneous mitral valve dilatation: single balloon versus double balloon. a finite element study. *J Heart Valve Dis*, 18(1):28–34, Jan 2009.

[104] F. Dal Pan, G. Donzella, C. Fucci, and M. Schreiber. Structural effects of an innovative surgical technique to repair heart valve defects. *Journal of Biomechanics*, 38(12):2460 – 2471, 2005. doi: 10.1016/j.jbiomech.2004.10.005.

[105] A Avanzini. A computational procedure for prediction of structural effects of edge-to-edge repair on mitral valve. *J Biomech Eng*, 130(3):031015, Jun 2008. doi: 10.1115/1.2913235.

[106] A. Redaelli, G. Guadagni, R. Fumero, F. Maisano, and O. Alfieri. A computational study of the hemodynamics after "edge-to-edge" mitral valve repair. *J Biomech Eng*, 123(6):565–570, Dec 2001.

[107] David M. McQueen and Charles S. Peskin. Heart simulation by an immersed boundary method with formal second-order accuracy and reduced numerical viscosity. *Mechanics for a New Millennium, Proceedings of the International Conference on Theoretical and Applied Mechanics*, 2000.

[108] D. M. McQueen, C. S. Peskin, and E. L. Yellin. Fluid dynamics of the mitral valve: physiological aspects of a mathematical model. *Am J Physiol*, 242(6):H1095–H1110, Jun 1982.

[109] Torsten Schenkel, Mauro Malve, Michael Reik, Michael Markl, Bernd Jung, and Herbert Oertel. Mri-based cfd analysis of flow in a human left ventricle: Methodology and application to a healthy heart. *Annals of Biomedical Engineering*, 37(3):503–515, March 2009. URL http://dx.doi.org/10.1007/s10439-008-9627-4.

[110] Henrik Jensen, Morten Ø Jensen, Steffen Ringgaard, Morten H Smerup, Thomas S Sorensen, Won Y Kim, Erik Sloth, P. Wierup, J. Michael Hasenkam, and Sten L Nielsen. Geometric determinants of chronic functional ischemic mitral regurgitation: insights from three-dimensional cardiac magnetic resonance imaging. *J Heart Valve Dis*, 17(1):16–22; discussion 23, Jan 2008.

[111] G. Burriesci, I. C. Howard, and E. A. Patterson. Influence of anisotropy on the mechanical behaviour of bioprosthetic heart valves. *J Med Eng Technol*, 23(6):203–215, 1999.

[112] O.C. Zienkiewicz and R.L. Taylor. *The Finite element method: Solid mechanics*. Number v. 2 in The Finite Element Method: Solid Mechanics. Butterworth-Heinemann, 2000. ISBN 9780750650557. URL http://books.google.co.uk/books?id=MhgBfMWFVHUC.

[113] David J. Benson. Computational methods in lagrangian and eulerian hydrocodes. *Computer Methods in Applied Mechanics and Engineering*, 99(2-3):235–394, September 1992. ISSN 0045-7825. URL http://www.sciencedirect.com/science/article/B6V29-47XFB59-T2/2/adc6d5946275fd214d1ca25290a51450.

[114] J. De Hart, G. W. Peters, P. J. Schreurs, and F. P. Baaijens. A two-dimensional fluid-structure interaction model of the aortic valve [correction of value]. *J Biomech*, 33(9):1079–1088, Sep 2000.

[115] K. D. Lau, V. Diaz, P. Scambler, and G. Burriesci. Mitral valve dynamics in structural and fluid-structure interaction models. *Med Eng Phys*, 32(9):1057–1064, Nov 2010. doi: 10.1016/j.medengphy.2010.07.008. URL http://dx.doi.org/10.1016/j.medengphy.2010.07.008.

[116] ISO5840:2005–Cardiovascular Implants: Cardiac Valve Prostheses.

[117] Draft Guidance for Industry and FDA Staff: Heart Valves - Investigational Device Exemption (IDE) and Premarket Approval (PMA) Applications.

[118] Marc Thiriet. *Biology and Mechanics of Blood Flows. Part II: Mechanics and Medical Aspects*. Springer New York, 2008.

[119] G. Burriesci, F. Cavallo Marincola, and C. Zervides. Design of a novel polymeric heart valve. *J Med Eng Technol*, 34(1):7–22, Jan 2010. doi: 10.3109/03091900903261241. URL http://dx.doi.org/10.3109/03091900903261241.

[120] Hossein Ghanbari, Helene Viatge, Asmeret G Kidane, Gaetano Burriesci, Mehdi Tavakoli, and Alexander M Seifalian. Polymeric heart valves: new materials, emerging hopes. *Trends Biotechnol*, 27(6):359–367, Jun 2009. doi: 10.1016/j.tibtech.2009.03.002. URL http://dx.doi.org/10.1016/j.tibtech.2009.03.002.

[121] K. D. Lau, V. Díaz-Zuccarini, P. Scambler, and G. Burriesci. Fluid-structure interaction study of the edge-to-edge repair technique on the mitral valve. *J Biomech*, 44:2409–2417, Jul 2011. doi: 10.1016/j.jbiomech.2011.06.030. URL http://dx.doi.org/10.1016/j.jbiomech.2011.06.030.

[122] O Alfieri and M. D. Bonis. The role of the edge-to-edge repair in the surgical treatment of mitral regurgitation. *J Card Surg*, 25(5):536–541, Sep 2010. doi: 10.1111/j.1540-8191.2010.01073.x.

[123] Tim D Kinnaird, Bradley I Munt, Andrew P Ignaszewski, James G Abel, and R. Christopher Thompson. Edge-to-edge repair for functional mitral regurgitation: an echocardiographic study of the hemodynamic consequences. *J Heart Valve Dis*, 12(3):280–286, May 2003.

[124] Francesco Maisano, Alessandro Caldarola, Andrea Blasio, Michele De Bonis, Giovanni La Canna, and Ottavio Alfieri. Midterm results of edge-to-edge mitral valve repair without annuloplasty. *J Thorac Cardiovasc Surg*, 126(6):1987–1997, Dec 2003. doi: 10.1016/S0022. URL `http://dx.doi.org/10.1016/S0022`.

[125] T. Feldman, S. Kar, M. Rinaldi, P. Fail, J. Hermiller, R. Smalling, P. L. Whitlow, W. Gray, R. Low, H. C. Herrmann, S. Lim, E. Foster, D Glower, and E. V. E. R. E. S. T. Investigators. Percutaneous mitral repair with the mitraclip system: safety and midterm durability in the initial everest (endovascular valve edge-to-edge repair study) cohort. *J Am Coll Cardiol*, 54(8):686–694, Aug 2009.

[126] Liang Shi and Zhaoming He. Hemodynamics of the mitral valve under edge-to-edge repair: an in vitro steady flow study. *J Biomech Eng*, 131(5):051010, May 2009. doi: 10.1115/1.3118772. URL `http://dx.doi.org/10.1115/1.3118772`.

[127] F. Maisano, L. Torracca, M. Oppizzi, P. L. Stefano, G. D'Addario, G. La Canna, M. Zogno, and O. Alfieri. The edge-to-edge technique: a simplified method to correct mitral insufficiency. *Eur J Cardiothorac Surg*, 13(3):240–5; discussion 245–6, Mar 1998.

[128] Miguel Chaput, Mark D Handschumacher, Francois Tournoux, Lanqi Hua, J. Luis Guerrero, Gus J Vlahakes, and Robert A Levine. Mitral leaflet adaptation to ventricular remodeling: occurrence and adequacy in patients with functional mitral regurgitation. *Circulation*, 118(8):845–852, Aug 2008. doi: 10.1161/CIRCULATIONAHA.107.749440. URL `http://dx.doi.org/10.1161/CIRCULATIONAHA.107.749440`.

[129] Robert B Hinton and Katherine E Yutzey. Heart valve structure and function in development and disease. *Annu Rev Physiol*, 73:29–46, Mar 2011. doi: 10.1146/annurev-physiol-012110-142145. URL `http://dx.doi.org/10.1146/annurev-physiol-012110-142145`.

[130] Elena Rabkin-Aikawa, Mark Farber, Masanori Aikawa, and Frederick J Schoen. Dynamic and reversible changes of interstitial cell phenotype during remodeling of cardiac valves. *J Heart Valve Dis*, 13(5):841–847, Sep 2004.

[131] Elena Aikawa, Peter Whittaker, Mark Farber, Karen Mendelson, Robert F Padera, Masanori Aikawa, and Frederick J Schoen. Human semilunar cardiac valve remodeling by activated cells from fetus to adult: implications for postnatal adaptation, pathology, and tissue engineering. *Circulation*, 113(10):1344–1352, Mar 2006. doi: 10.1161/CIRCULATIONAHA.105.591768. URL `http://dx.doi.org/10.1161/CIRCULATIONAHA.105.591768`.

[132] J. P. Dal-Bianco, E. Aikawa, J. Bischoff, J. L. Guerrero, M. D. Handschumacher, S. Sullivan, B. Johnson, J. S. Titus, Y. Iwamoto, J. Wylie-Sears, R. A. Levine, and A. Carpentier. Active adaptation of the tethered mitral valve: insights into a compensatory mechanism for functional mitral regurgitation. *Circulation*, 120(4):334–342, Jul 2009. doi: 10.1161/CIRCULATIONAHA.108.846782. URL `http://dx.doi.org/10.1161/CIRCULATIONAHA.108.846782`.

[133] W. David Merryman, Inchan Youn, Howard D Lukoff, Paula M Krueger, Farshid Guilak, Richard A Hopkins, and Michael S Sacks. Correlation between heart valve interstitial cell stiffness and transvalvular pressure: implications for collagen biosynthesis. *Am J Physiol Heart Circ Physiol*,

290(1):H224–H231, Jan 2006. doi: 10.1152/ajpheart.00521.2005. URL http://dx.doi.org/10.1152/ajpheart.00521.2005.

[134] Niels J B Driessen, Martijn A J Cox, Carlijn V C Bouten, and Frank P T Baaijens. Remodelling of the angular collagen fiber distribution in cardiovascular tissues. *Biomech Model Mechanobiol*, 7 (2):93–103, Apr 2008. doi: 10.1007/s10237-007-0078-x. URL http://dx.doi.org/10.1007/s10237-007-0078-x.

[135] Edward K. Rodriguez, Anne Hoger, and Andrew D. McCulloch. Stress-dependent finite growth in soft elastic tissues. *Journal of Biomechanics*, 27(4):455–467, April 1994. ISSN 0021-9290. URL http://www.sciencedirect.com/science/article/pii/0021929094900213.

[136] Larry A. Taber and Jay D. Humphrey. Stress-modulated growth, residual stress, and vascular heterogeneity. *J. Biomech. Eng.*, 123(6):528–535, December 2001. URL http://link.aip.org/link/?JBY/123/528/1.

[137] Michael S Sacks, Yoshiharu Enomoto, Jeffrey R Graybill, W. David Merryman, Ahmad Zeeshan, Ajit P Yoganathan, Robert J Levy, Robert C Gorman, and Joseph H Gorman. In-vivo dynamic deformation of the mitral valve anterior leaflet. *Ann Thorac Surg*, 82(4):1369–1377, Oct 2006. doi: 10.1016/j.athoracsur.2006.03.117. URL http://dx.doi.org/10.1016/j.athoracsur.2006.03.117.

[138] A. Carpentier, J. Guerinon, A. Deloche, J.N. Fabiani, and J. Relland. Pathology of the mitral valve. In *The Mitral Valve: A Pluridisciplinary Approach*, chapter 7, pages 65–77. Edward Arnold, 1976.

[139] POV–Ray 3.6.1. *User Documentation*. URL http://www.povray.org/documentation/.

Appendix A

Anatomical Data

A.1 Annulus

Table A.1: Annular dimensions, all units in mm. Labels: I – intact, E – excised, H – human, P – porcine, TL – total annular length, AL – total anterior annular length, PL – total posterior annular length, PLA – posterior leaflet anterior cusp annular length, PLC – posterior leaflet central cusp annular length, PLP – posterior leaflet posterior cusp annular length, CA – anterior commissural cusp annular length and CP – posterior commissural cusp annular length.

Reference	[15] (H)	[11] (H)	[11] (P)	[19] (H)	[138] (H)
TL (I)	–	82±7	79±7	–	–
TL (E)	80–120	99±8	106±7	93.2±11	116±3.5
AL (I)	–	30±5	31±3	–	–
AL (E)	24–45	32±4	32±4	32±4	32±1.3
PL (I)	–	52±6	50±5	–	–
PL (E)	23–41	67±8	74±7	–	–
PLA (E)	–	–	–	14.1±3.6	–
PLC (E)	–	–	–	19.3±4.1	–
PLP (E)	–	–	–	13.6±3.3	–
CA (E)	–	–	–	7.7±2.1	12±3.3
CP (E)	–	–	–	7.2±2.1	17±0.8

A.2 Leaflets

Table A.2: Leaflet dimensions, all units in mm. Labels: E – excised, H – human, P – porcine, AFM – anterior leaflet free margin length, PFM – posterior leaflet free margin length, ALH – anterior leaflet height, PLM – posterior leaflet height, PLAH – posterior leaflet anterior cusp height, PLCH – posterior leaflet central cusp height, and PLPH – posterior leaflet posterior cusp height.

Reference	[15] (H)	[11] (H)	[11] (P)	[19] (H)	[138] (H)
AFM (E)	–	45±6	46±4	–	–
PFM (E)	–	75±12	94±3	–	–
ALH (E)	18–32	20±2	20±4	23.4±2.9	23±0.9
PLH (E)	8–25	12±1	12±2	–	–
PLAH (E)	–	–	–	11.2±2.3	9±1
PLCH (E)	–	–	–	13.8±2.9	14±0.9
PLPH (E)	–	–	–	11±2.3	10±1.2
CAH (E)	–	7±1	7±1	8.7±2.4	8±1
CPH (E)	–	7±1	7±1	8.3±2	8

A.3 Chordae tendineae

Table A.3: Measurements of chordae lengths, all units in mm. Labels: H – human, P – porcine, ALM – anterior leaflet marginal chordae, ALB – anterior leaflet basal chordae, PLM – posterior leaflet marginal chordae, PLB – posterior leaflet basal chordae, APM – anterolateral papillary muscle, PPM – posteromedial papillary muscle, ALMC – anterior leaflet main chordae, ALPC – anterior leaflet paramedial chordae, ALCC – anterior leaflet paracommissural chordae, PLCT – posterior leaflet cleft chordae, CAC – anterior commissural cusp chordae and CPC – posterior commissural cusp chordae.

Reference	[11] (H)	[11] (P)	[19] (H)	[138] (H)
ALM (APM)	13±2 mm	14±1	–	–
ALB (APM)	17±3 mm	18±2	–	–
PLM (APM)	12±2 mm	12±2	–	–
PLB (APM)	16±2 mm	16±2	–	–
ALM (PPM)	13±2 mm	15±3	–	–
ALB (PPM)	18±3 mm	20±3	–	–
PLM (PPM)	12±2 mm	12±2	–	–
PLB (PPM)	16±2 mm	16±2	–	–
ALMC (APM)	–	–	17.2±3.9	19±0.4
ALPC (APM)	–	–	16.2±3.7	15±0.5
ALCC (APM)	–	–	15.5±3.0	17±0.3
ALMC (PPM)	–	–	17.9±4.3	17±0.2
ALPC (PPM)	–	–	16.8±3.4	–
ALCC (PPM)	–	–	17.5±4.0	–
PLCT (APM)	–	–	14.5±3.2	13±3.7
PLCT (PPM)	–	–	14.9±3.2	13±3.7
CAC	–	–	12.3±3.6	13±0.2
CPC	–	–	13.8±3.9	15±0.05

A.4 Papillary muscle

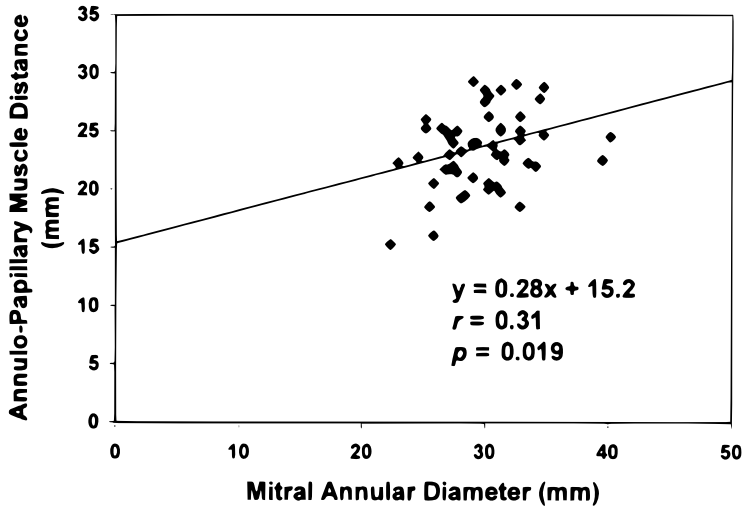

Figure A.1: Measurement of mean papillary muscle distance from the mitral annulus. Image after Sakai et al. [19].

Appendix B

Numerical Methods

LS–DYNA is a numerical code which provides a continuum approximation of the non–linear dynamic of structures (or fluids) using the finite element method. Here the technical details of the numerical approach adopted in LS–DYNA are reviewed. The information presented in this chapter has been obtained directly from the theory and user manuals [79, 80].

B.1 Structural dynamics

Defined in a moving Lagrangian frame of reference, the dynamics of the structure are solved by approximating the solution to the conservation of mass and momentum equations using the finite element method as detailed in the following sections.

B.1.1 Problem definition

Consider a body within a fixed Cartesian coordinate system in which a point is initially located at X_α (where α=1, 2, 3) and subsequently moves to the point x_i (where i=1, 2, 3) in the same coordinate system (Figure B.1). Using a Lagrangian formulation the deformation of this point can be described in terms of the initial coordinates X_α (Equation B.1). At the time t=0 the this point is located at X_α with velocity V_i (Equations B.2 and B.3). Here the notation $\dot{x}$ is the first time derivative of the point coordinate, i.e. the velocity $v_i = \dot{x} = dx/dt$.

$$x_i = x_i(X_\alpha, t) \tag{B.1}$$

$$x_i(X_\alpha, 0) = X_\alpha \tag{B.2}$$

$$\dot{x}_i(X_\alpha, 0) = V_i(X_\alpha) \tag{B.3}$$

B.1.2 Governing Equations

The Lagrangian dynamics of the solid are governed by the conservation of momentum (Equation B.4) which satisfies the traction boundary condition on the boundary ∂b_1 (Equation B.5), the displacement boundary condition on the boundary ∂b_2 (Equation B.6) and the contact discontinuity along the interior boundary ∂b_3 where $x_i^+ = x_i^-$ (Equation B.7). Here the notation $\ddot{x}$ is the second time derivative of the point coordinate, i.e. the acceleration $a_i = \ddot{x} = d^2x/dt^2$. The comma used in the index notation denotes covariant spatial differentiation, i.e. $\sigma_{ij,j} = \partial\sigma_{ij}/\partial x_j$. Conservation of mass is trivially satisfied in the Lagrangian form (Equation B.8). Here σ_{ij} is the Cauchy stress tensor, ρ is the current density, ρ_0 is the

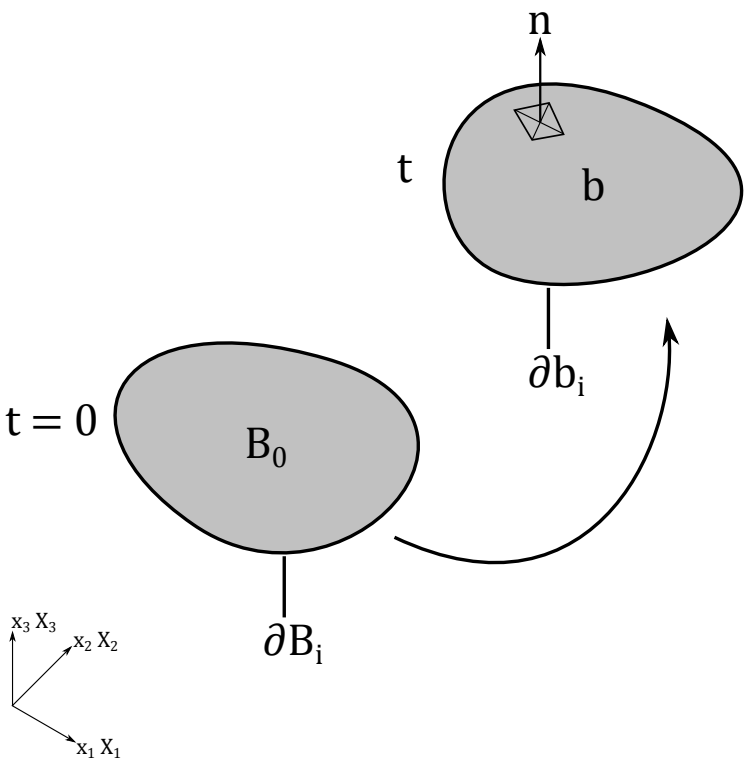

Figure B.1: Problem definition.

initial/reference density, n_i is the unit outward normal to boundary element ∂b_i, f_i is the body force density and V is the current volume ratio defined relative to the initial volume V_0.

$$\sigma_{ij,j} + \rho f_i = \rho \ddot{x}_i \tag{B.4}$$

$$\sigma_{ij} n_i = t_i(t) \tag{B.5}$$

$$x_i(X_\alpha, t) = D_i(t) \tag{B.6}$$

$$\left(\sigma_{ij}^{+} - \sigma_{ij}^{-}\right) n_i = 0 \tag{B.7}$$

$$\rho V = \rho_0 \tag{B.8}$$

Conservation of energy is can be defined as follows (Equation B.9), here the terms s_{ij}, p and q are the deviatoric stresses, pressure and bulk viscosity respectfully (Equations B.10 and B.11). Here δ_{ij} is the Kronecker delta, i.e. $\delta_{ij} = 1$ if $i = j$ else $\delta_{ij} = 0$.

$$\dot{E} = V s_{ij} \dot{\epsilon}_{ij} - (p+q)\,\dot{V} \tag{B.9}$$

$$s_{ij} = \sigma_{ij} + (p+q)\,\delta_{ij} \tag{B.10}$$

$$p = -\frac{1}{3}\sigma_{ij}\delta_{ij} - q = -\frac{1}{3}\sigma_{kk} - q \tag{B.11}$$

B.1.3 Weak formulation

The weak formulation of the problem is defined by integrating the conservation of momentum over the current geometry (Equation B.12). Here δx_i satisfies all the boundary conditions upon ∂b_2

$$\int_v \left(\rho \ddot{x}_i - \sigma_{ij,j} - \rho f_i\right) \delta x_i \, dv + \int_{\partial b_1} \left(\sigma_{ij} n_j - t_i\right) \delta x_i \, ds + \int_{\partial b_3} \left(\sigma_{ij}^+ - \sigma_{ij}^-\right) n_j \delta x_i \, ds = 0 \tag{B.12}$$

This equation is simplified by first applying the divergence theorem to the volume integral shown in Equation B.13. Following this the product rule is then applied to the same terms (Equation B.14).

$$\int_v \left(\sigma_{ij} \delta x_i\right)_{,j} dv = \int_{\partial b1} \sigma_{ij} n_j \delta x_i \, ds + \int_{\partial b_3} \left(\sigma_{ij}^+ - \sigma_{ij}^-\right) n_j \delta x_i \, ds \tag{B.13}$$

$$\left(\sigma_{ij} \delta x_i\right)_{,j} = \sigma_{ij,j} \delta x_i + \sigma_{ij} \delta x_{i,j} \tag{B.14}$$

Combining Equations B.13 and B.14 gives Equation B.15, which is then substituted into Equation B.12 to give the weak formulation of the momentum equation (Equation B.16).

$$\int_v \sigma_{ij} \delta x_{i,j} \, dv = \int_v -\sigma_{ij,j} \delta x_i \, dv + \int_{\partial b1} \sigma_{ij} + n_j \delta x_i \, ds + \int_{\partial b3} \left(\sigma_{ij}^+ - \sigma_{ij}^-\right) n_j \delta x_i \, ds \tag{B.15}$$

$$\delta \pi = \int_v \rho \ddot{x}_i \delta x_i \, dv + \int_v \sigma_{ij} \delta x_{i,j} \, dv - \int_v \rho f_i \delta x_i \, dv - + \int_{\partial b1} t_i \delta x_i \, ds = 0 \tag{B.16}$$

B.1.4 Finite element method

Here the solid is represented by a mesh of k interconnected nodes, in which the coordinates of the points x_i are described as a function of the shape functions ϕ_j, parametric coordinates (ξ, η, ζ) and the nodal coordinates of the j–th node in the i–th direction x_i^j (Equation B.17). Summing over the n elements, $\delta\pi$ can be approximated (Equation B.18).

$$x_i(X_\alpha, t) = x_i\left(X_\alpha(\xi, \eta, \zeta), t\right) = \sum_{j=1}^{k} \phi_j(\xi, \eta, \zeta) \, x_i^j(t) \tag{B.17}$$

$$\delta \pi = \sum_{m=1}^{n} \delta \pi_m = 0 \tag{B.18}$$

The weak formulation can then be written as shown in Equation B.19, in which the ϕ_i^m are the shape functions for the associated k nodes of the element (Equation B.20). Note that here the integrals are performed over the individual volumes of the elements, v_m.

$$\sum_{m=1}^{n} \left\{ \int_{v_m} \rho \ddot{x}_i \phi_i^m \, dv + \int_{v_m} \sigma_{ij}^m \phi_{i,j}^m \, dv - \int_{v_m} \rho f_i \phi^m{}_i \, dv - \int_{\partial b1} t_i \phi_i^m \, ds \right\} = 0 \tag{B.19}$$

$$\phi_i^m = \left(\phi_1, \phi_2, \ldots, \phi_k\right)_i^m \tag{B.20}$$

In matrix form the weak formulation is given as shown in Equation B.21, where N is the interpolation matrix, σ the stress vector $\sigma^{\mathrm{T}} = (\sigma_{xx}, \sigma_{yy}, \sigma_{zz}, \sigma_{xy}, \sigma_{yz}, \sigma_{zx})$, B the strain–displacement matrix and a the nodal acceleration vector. Given that the body forces, internal stresses, etc. are all known varibles, the only remaining unknown is the acceleration.

$$\sum_{m=1}^{n}\left\{\int_{v_m}\rho N^{\mathrm{T}}N a\,dv+\int_{v_m}B^{\mathrm{T}}\sigma\,dv-\int_{v_m}\rho N^{\mathrm{T}}b\,dv-\int_{\partial b1}N^{\mathrm{T}}t\,ds\right\}^{m}=0 \tag{B.21}$$

B.2 Time integration

Using the acceleration a defined above from the weak formulation of the momentum equation, the motion of the dynamics of the solid body are defined by integrating the accelerations and resulting velocities. In LS–DYNA time integration is performed using an explicit method, which staggers the velocity with respect to the displacement in time. Using central finite difference, this staggered velocity/displacement scheme ensures second order accuracy in time.

Using the nodal displacement at the current time step $t = n+1$ and the velocities at an intermediate time step $t = n+1/2$, the nodal displacement at the next time step is determined (Equation B.22). The velocity at this intermediate time step is determined by equating the acceleration $t = n$ to the velocities at times $t = n-1/2$ and $t = n+1/2$ using the central finite difference scheme (Equation B.23), with the acceleration at time $t = n$ determined from the nodal forces and masses (Equation B.24).

$$d^{n+1} = d^n + v^{n+1/2}\Delta t \tag{B.22}$$

$$v^{n+1/2} = v^{n-1/2} + a^n\Delta t \tag{B.23}$$

$$v^{n+1/2} = v^{n-1/2} + \frac{F^n}{M}\Delta t \tag{B.24}$$

The force at time $t = n$ can be divided into external (body forces, contact forces, etc.) and internal forces (Equation B.25). The internal forces is calculated from the transpose of the strain displacement matrix B^{T} multiplied with the stress σ (Equation B.26). This stress σ is determined from the selected material model (linear, non–linear, solid, fluid, etc.)

$$F^n = F^n_{int} + F^n_{ext} \tag{B.25}$$

$$F^n_{int} = \int_V B^t\sigma^n\,dv \tag{B.26}$$

B.3 Fluid dynamics

Defined in a moving Lagrangian frame of reference, the dynamics of the fluid are solved by approximating the solution to the conservation of mass and momentum equations using the finite element method as detailed previously. Following this, the fluid variables are advected to a fixed Eulerian frame of reference as detailed in Section B.3.5.

B.3.1 Governing equations

Defined a Lagrangian frame of reference, the governing equations of motion for the fluid are the same as described previously in Section B.1.2. However in a fluid the stresses are generated in response to strain rates and not strains as detailed below in Section B.3.4.

B.3.2 Weak formulation

As the governing equations are the same as the structural case, the weak formulation follows the approach detailed in Section B.1.3 above.

B.3.3 Finite element method

As the weak formulation is the same as the structural case, the finite element implementation follows the approach detailed in Section B.1.4 above.

B.3.4 Material model

Unlike solids, in fluids the stresses induced in the Lagrangian frame of reference are generated in response to strain rates rather than strains. In LS–DYNA the fluid material model `MAT_NULL` must be used, in this model the the deviatoric stresses σ' are proportional to the shear strain rate $\dot{\varepsilon}'$ rather than the shear strain. For Newtonian fluids the coefficient of proportionality is the dynamic viscosity of the fluid μ (Equation B.27). The internal pressure is defined using an equation of state, which is a function of the volumetric deformation and the speed of sound C of the material (Equation B.28). Here δ_{ij} is the Kronecker delta, i.e. $\delta_{ij} = 1$ if $i = j$ else $\delta_{ij} = 0$.

$$\sigma_{ij} = -P\delta_{ij} + \sigma' = -P\delta_{ij} + 2\mu\dot{\varepsilon}' \tag{B.27}$$

$$P = \rho C^2 \frac{\Delta V}{V} \tag{B.28}$$

B.3.5 Hydrocode

Numerical simulations of fluid motion using a Lagrangian approach only can result in severe mesh distortion. In order to avoid numerical instabilities arising from this, approaches have been developed in which the changes in the fluid variables of velocity and pressure following the Lagrangian motion of the mesh (in the distorted state) are advected back to the original fixed mesh (here referred to as Eulerian). Following this the updated Eulerian mesh is then used as in the next time step.

This particular method of fluid dynamic simulation is referred to as a "split operator" method and this class of fluid solver is referred to as a "hydrocode". As defined in Section 2.4.2.1, the fluid motion is first solved in a Lagrangian sense. Following this, the transport (or flux) of velocity and pressure resulting from the Lagrangian motion of the mesh is calculated relative to the initial fixed Eulerian configuration. This change is then advected back to the Eulerian configuration using a monotonic advection scheme.

B.4 Contact Algorithms

Contact of the structure with the structure and fluid with the structure is handled in the same manner in LS–DYNA. Penetration of a pre–defined structural component (referred to as the master) by either a fluid or structural node (referred to as the slave) is penalised by applying a resistive force. Following this the two different penalty formulations used within this work are detailed.

B.4.1 Standard penalty formulation

In the standard penalty formulation, contact is first determined if a slave node penetrates a master surface. This is determined by calculation of l (see Equation B.29); n_i is the normal of the master surface s_i and vectors t and r are vectors from an arbitrary origin to the slave node and master segement (see Figure B.2). Penetration is deemed to occur when $l < 0$, contact is then simulated by the application of an interface force vector to the slave node (f_s) and to the four nodes of the master segment (f_m^i); the stiffness factor k_i is based upon the bulk modulus K_i, shell element area A_i and an interface stiffness scale factor (defaulted to 0.1). Various different options exist for calculation of this contact stiffness parameter; the default contact stiffness is based on the minimum of the master segment and slave node,

but it is possible to base this stiffness on the master segment alone, the slave node, the slave node (area or mass weighted) or inversely proportional to the shell thickness instead of the area.

$$l = n_i \cdot [t - r(\xi, \eta)] < 0 \tag{B.29}$$

$$f_s = -l\, k_i\, n_i \tag{B.30}$$

$$f_m^i = \phi_i(\xi_c, \eta_c) f_s \tag{B.31}$$

$$k_i = \left(f_{si} K_i A_i\right) / \max[l_{shell\,diagonal}] \tag{B.32}$$

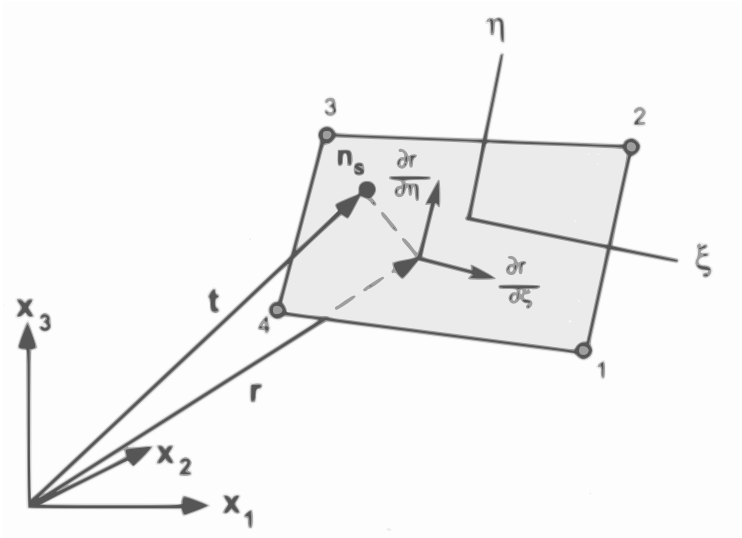

Figure B.2: Contact definition of the master segment and slave node. Image after Hallquist [79]

B.4.2 Segment Based Penalty Formulation

An alternative to the master segment/slave node method is the segment based contact penalty algorithm. This algorithm utilises segmental masses rather than nodal masses in the calculation of the contact stiffness k_{cs}. Here the variables $SLSFAC$, SFS and SFM are the contact force scale factors. The time step factor Δt_c is set to the initial time step size, however it is only updated if the solution time step increases by more than 5%.

$$k_{cs}(t) = 0.5 \cdot SLSFAC \cdot m^* \cdot (\mathrm{SFS/SFM}) \left(\frac{m_1 m_2}{m_1 + m_2}\right) \left(\frac{1}{\Delta t_c(t)}\right)^2 \tag{B.33}$$

B.5 User defined material

Custom user defined materials can be are added to LS–DYNA by amending `FORTRAN` subroutines provided by LSTC [80]. Note that this code is written in the `FORTRAN77` format, thus lines of text must not exceed 73 characters or they cannot be parsed by the compiler. Also note that variables beginning with the letters `I` to `N` have implicitly been defined as the data type `INTEGER`. Listed below is the code required to implement the transversely isotropic, anisotropic, non–linear, hyperelastic membrane model described by Einstein et al. [78] in Chapter 2, Section 2.3.1.3. Consisting of two subroutines, the first subroutine `URMATS` assembles the local strain increments (Listing B.1) which is then followed by the second subroutine `UMAT48` which calculates and returns the local elemental stress (Listing B.2).

Listing B.1: FORTRAN source code for `urmats` subroutine. This subroutine collects together the relevant parameters for the user material subroutine `umat` (Listing B.2). The code shown here has been modified from the default LS–DYNA subroutine to include the memory block `aux32loc` which includes the local incremental strains for the co–rotational Hughes–Liu element (`ELFORM=11`).

```
      subroutine urmats(lft,llt,cm,capa,mt,crv,ipt,rcoor,scoor,tcoor,
     . nnm1,nconstp)
c
c     user defined shell subroutine modified by kevin lau
c     acknowlegment and thanks to daniel einstein
c
c     approach detailed in: 'dynamic finite element implementation
c     of nonlinear, anisotropic hyperelastic biological membranes
c     by einstein et al. in comp. meth. in biomech. and biomed.
c     eng. 2003, vol. 6(1), pp.33-44, doi:10.1080/1025584021000048983
c
      include 'nlqparm'
#include "bk07.inc"
#include "bk13.inc"
      include 'bk19.inc'
      include 'iounits.inc'
      include 'memaia.inc'
#include "dynmem.inc"
C_TASKCOMMON (aux2loc)
C_TASKCOMMON (aux8cloc)
C_TASKCOMMON (aux14loc)
C_TASKCOMMON (aux19loc)
C_TASKCOMMON (aux33loc)
C_TASKCOMMON (bk36loc)
C_TASKCOMMON (failuloc)
C_TASKCOMMON (failcmloc)
C_TASKCOMMON (hourgloc)
C_TASKCOMMON (shloptloc)
C_TASKCOMMON (soundloc)
C_TASKCOMMON (subtssloc)
c
      common/aux2loc/e1(nlq),e2(nlq),d3(nlq),e4(nlq),e5(nlq),e6(nlq),
     1 wzzdt(nlq),wyydt(nlq),wxxdt(nlq),einc(nlq)
      common /aux8cloc/
     & d1(nlq),d2(nlq),d4(nlq),d5(nlq),d6(nlq),
     & dfg11(nlq),dfg21(nlq),dfg31(nlq),dfg12(nlq),dfg22(nlq),
     & dfg32(nlq),dfg13(nlq),dfg23(nlq),dfg33(nlq),stg5(nlq),
     & stg6(nlq),a11(nlq),a12(nlq),a21(nlq),a22(nlq)
      common/aux14loc/
     & sig1(nlq),sig2(nlq),sig3(nlq),sig4(nlq),
     & sig5(nlq),sig6(nlq),epsps(nlq),hsvs(nlq,142)
      common/aux19loc/
     1 sign0(nlq),sign1(nlq),sign2(nlq),sign3(nlq),sign4(nlq),
     2 sign5(nlq),sign6(nlq)
      common/aux33loc/
```

```
     1 ix1(nlq),ix2(nlq),ix3(nlq),ix4(nlq),ixs(nlq,4),mxt(nlq)
      common/bk36loc/index
      common/failcmloc/ifail(nlq)
      common/failuloc/sieu(nlq),fail(nlq)
      common/hourgloc/ym(nlq),gm(nlq),ifsv(nlq)
      common/shloptloc/ibelyt
c
      common/bk01/itherm,itemp,ntmp0,ntmp1,itempan,itempdr,itmpe(44)
      common/bk26/nintcy
      common/bk28/summss,xke,xpe,tt,xte0,erodeke,erodeie
      logical failur
      common/failcm/failur
      common/numcpu/ncpu,ncpua,ncpub,lenvec(8)
      common/shlopt/istrn,istupd,ibelyts,miter
      common/soundloc/ss(nlq),sndsp(nlq),diagm(nlq),sarea(nlq),
     . dxl(nlq)
      common/thropt/itopaz(101)
      common/umatss/ibulkp(60),nusrcn(60),iorien(60),nusrmt,ishrmp(60),
     . ivectr(60),ihyper(60)
      common/subtssloc/dt1siz(nlq)
c
      dimension cm(*),crv(lq1,2,*),nconstp(*)
      dimension eps(6),sig(6),hsv(142),temps(nlq)
      dimension thhsv(nlq,100),thhsvi(100)
      logical failel,failels(nlq)
c
      data temps/nlq*0.0/
c
c     common statement added to access the members of the
c     local displacement gradient for ELFORM = 11 only
c
      common/aux32loc/dxy(nlq),dyx(nlq),dyz(nlq),dzy(nlq),
     & dzx(nlq),dxz(nlq)
c
c     common statement has been added to access the transformation
c     matrix
c
       common/aux40loc/
     1 aa11(nlq),aa12(nlq),bb13(nlq),aa21(nlq),aa22(nlq),bb23(nlq),
     2 aa31(nlq),aa32(nlq),bb33(nlq),s11(nlq),s12(nlq),s13(nlq),
     3 s21(nlq),s22(nlq),s23(nlq),s31(nlq),s32(nlq),s33(nlq)
c
c     variable list
c
c     g1cr - dudx in corotational basis
c     g2cr - dvdx in corotational basis
c     g4cr - dudy in corotational basis
c     g5cr - dvdy in corotational basis
c     g1ob - dudx in original basis
```

```
c      g2ob - dvdx in original basis
c      g4ob - dudy in original basis
c      g5ob - dvdy in original basis
c      f1ob - f11 in original basis
c      f2ob - f21 in original basis
c      f4ob - f12 in original basis
c      f5ob - f22 in original basis
c          c1ob - c11 in original basis
c      c2ob - c21 in original basis
c      c4ob - c12 in original basis
c      c5ob - c22 in original basis
c          n1 - x-component corotational/original basis vector
c          n2 - y-component corotational/original basis vector
c
       dimension ww11(nlq),ww21(nlq),ww12(nlq),ww22(nlq)
       dimension g1cr(nlq),g2cr(nlq),g4cr(nlq),g5cr(nlq)
       dimension g1ob(nlq),g2ob(nlq),g4ob(nlq),g5ob(nlq)
       dimension f1ob(nlq),f2ob(nlq),f4ob(nlq),f5ob(nlq)
       dimension c1ob(nlq),c2ob(nlq),c4ob(nlq),c5ob(nlq)
       dimension zz1(nlq),zz2(nlq)
c
c      processing elements
c
       mx=48*(mxt(lft)-1)
       gm(lft)=cm(mx+abs(ishrmp(mt)))
       bk=cm(mx+ibulkp(mt))
       pr=(3.*bk-2.*gm(lft))/(2.*(3.*bk+gm(lft)))
       ym(lft)=2.*(1.+pr)*gm(lft)
       ss(lft)=ym(lft)/(1.-pr*pr)
c
c      determining number of requested history variables
c
       no_hsvs=nconstp(mxt(lft))
       if (lenvec(5) .eq.1) no_hsvs=no_hsvs-6
       if (iorien(mt).ne.0) no_hsvs=no_hsvs-2
       if (ihyper(mt).ne.0) no_hsvs=no_hsvs-9
c
c      initializing indeces
c
       if (iorien(mt).ne.0) then
         if (ihyper(mt).ne.0) then
           ind_defgrad=1+no_hsvs
           ind_ortho=ind_defgrad+9
         else
           ind_ortho=1+no_hsvs
         endif
         ind_q1=ind_ortho
         ind_q2=ind_ortho+1
         ind_last=ind_q2
```

```
c
      else
        if (ihyper(mt).ne.0) then
          ind_defgrad=1+no_hsvs
          ind_last=ind_defgrad+8
        else
          ind_last=no_hsvs
        endif
      endif
c
      if (ind_last.gt.142) then
        write(iotty,900) lqfmiv(mxt(lft))
        write(iohsp,900) lqfmiv(mxt(lft))
        write(iomsg,900) lqfmiv(mxt(lft))
        call adios(2)
      endif
c
      num_nods=4
      if (ibelyt.eq.0) then
        num_nods=8
        do 10 i=lft,llt
        sign0(i)=sign3(i)+ym(lft)*d3(i)
        sign3(i)=sign0(i)
 10     continue
      endif
c
c     reset hsv variables
c
        if (tt.eq.0.0.and.nintcy.eq.0) then
          do i=lft,llt
            hsvs(i,1)=1.
            hsvs(i,2)=0.
            hsvs(i,3)=0.
            hsvs(i,4)=1.
            hsvs(i,5)=1.
            hsvs(i,6)=0.
            hsvs(i,7)=1.
            hsvs(i,8)=0.
            hsvs(i,9)=0.
            hsvs(i,10)=1.
            hsvs(i,11)=1.
            hsvs(i,12)=0.
            hsvs(i,13)=hsvs(i,ind_q1)
            hsvs(i,14)=hsvs(i,ind_q2)
            hsvs(i,15)=0.
c
            hsvs(i,16)=0.
            hsvs(i,17)=0.
            hsvs(i,18)=0.
```

```
            hsvs(i,19)=0.
            hsvs(i,20)=0.
            hsvs(i,21)=0.
c
            hsvs(i,22)=0.
            hsvs(i,23)=0.
c
          enddo
        endif
c
c
      if (iorien(mt).ne.0.and.ihyper(mt).ge.0) then
c
c     G is provided in the corotation element system
c     it must be rotated back to the original basis
c     in order to assemble F
c
        do i=lft,llt
c
          g1cr(i)=e1(i)
          g2cr(i)=dyx(i)
          g4cr(i)=dxy(i)
          g5cr(i)=e2(i)
c
c         shell thinning
c
          d3(i)=(1./((g1cr(i)+1.)*(g5cr(i)+1.)-g2cr(i)*g4cr(i)))-1.
c
          zz1(i)=hsvs(i,5)
          zz2(i)=hsvs(i,6)
c
          ww11(i)=zz1(i)*g1cr(i)-zz2(i)*g4cr(i)
          ww12(i)=zz2(i)*g1cr(i)+zz1(i)*g4cr(i)
          ww21(i)=zz1(i)*g2cr(i)-zz2(i)*g5cr(i)
          ww22(i)=zz2(i)*g2cr(i)+zz1(i)*g5cr(i)
c
          g1ob(i)=zz1(i)*ww11(i)-zz2(i)*ww21(i)
          g2ob(i)=zz2(i)*ww11(i)+zz1(i)*ww21(i)
          g4ob(i)=zz1(i)*ww12(i)-zz2(i)*ww22(i)
          g5ob(i)=zz2(i)*ww12(i)+zz1(i)*ww22(i)
c
          f1ob(i)=hsvs(i,1)
          f2ob(i)=hsvs(i,2)
          f4ob(i)=hsvs(i,3)
          f5ob(i)=hsvs(i,4)
c
          hsvs(i,1)=(g1ob(i)+1.)*f1ob(i)+g4ob(i)*f2ob(i)
          hsvs(i,2)=g2ob(i)*f1ob(i)+(g5ob(i)+1.)*f2ob(i)
          hsvs(i,3)=(g1ob(i)+1.)*f4ob(i)+g4ob(i)*f5ob(i)
```

```
            hsvs(i,4)=g2ob(i)*f4ob(i)+(g5ob(i)+1.)*f5ob(i)
c
            hsvs(i,7)=hsvs(i,1)*hsvs(i,1)+hsvs(i,2)*hsvs(i,2)
            hsvs(i,8)=hsvs(i,1)*hsvs(i,3)+hsvs(i,2)*hsvs(i,4)
            hsvs(i,9)=hsvs(i,1)*hsvs(i,3)+hsvs(i,2)*hsvs(i,4)
            hsvs(i,10)=hsvs(i,3)*hsvs(i,3)+hsvs(i,4)*hsvs(i,4)
c
            hsvs(i,11)=hsvs(i,1)/sqrt(hsvs(i,7))
            hsvs(i,12)=hsvs(i,2)/sqrt(hsvs(i,7))
c
            d1(i)=e1(i)
            d2(i)=e2(i)
            d4(i)=e4(i)
            d5(i)=e5(i)
            d6(i)=e6(i)
c
          enddo
c
c       element local strains
c
        else
          do i=lft,llt
            d1(i)=e1(i)
            d2(i)=e2(i)
            d4(i)=e4(i)
            d5(i)=e5(i)
            d6(i)=e6(i)
          enddo
        endif
c
        if (ishrmp(mt).lt.0) then
          call usr_temps (a(ntmp0+1),a(n19),itemp,temps,lft,llt,ix1,ix2,
     .     ix3,ix4,ixs,ixs(1,2),ixs(1,3),ixs(1,4),num_nods,itopaz,
     .     nnm1,rcoor,scoor,tcoor)
        endif
c
c       Get thermal history variables from thermal
c       user material
c
        call get_thhsv(nthhsv,thhsv,itemp,lft,llt,
     1 num_nods,itopaz,nnm1,rcoor,scoor,tcoor)
c
c       energy calculations
c
        do 33 i=lft,llt
        einc(i)=d1(i)*sig1(i)+d2(i)*sig2(i)+d4(i)*sig4(i)+d5(i)*sig5(i)
     1         +d6(i)*sig6(i)
 33     continue
c
```

```
c       vectorization flag
c
        ivect=ivectr(mt)
c
        mte40=mt-40
c
c       scalar umat
c
        if (ivect.eq.0) then
          do 120 i=lft,llt
c
c         gathering of variables
c
          index=i
          dt1=dt1siz(i)
          eps(1)=d1(i)
          eps(2)=d2(i)
          eps(3)=d3(i)
          eps(4)=d4(i)
          eps(5)=d5(i)
          eps(6)=d6(i)
          sig(1)=sig1(i)
          sig(2)=sig2(i)
          sig(3)=sig3(i)
          sig(4)=sig4(i)
          sig(5)=sig5(i)
          sig(6)=sig6(i)
          epsp=epsps(i)
          temper=temps(i)
          failel=.false.
c
          if (no_hsvs.gt.0) then
            do j=1,no_hsvs
              hsv(j)=hsvs(i,j)
            enddo
          endif
          if (ihyper(mt).ne.0) then
            do j=1,9
              hsv(no_hsvs+j)=hsvs(i,ind_defgrad-1+j)
            enddo
          endif
          if (nthhsv.gt.0) then
            do j=1,nthhsv
              thhsvi(j)=thhsv(i,j)
            enddo
          endif
c
c         call user developed subroutines here
c
```

```
      go to (41,42,43,44,45,46,47,48,49,50), mte40
   41 call umat41 (cm(mx+1),eps,sig,epsp,hsv,dt1,capa,'shell',tt,
     . temper,failel,crv)
      go to 60
   42 call umat42 (cm(mx+1),eps,sig,hsv,dt1,capa,'shell',tt,crv,
     . temper)
      go to 60
   43 call umat43 (cm(mx+1),eps,sig,epsp,hsv,dt1,capa,'shell',tt,
     . temper,failel,crv)
      go to 60
   44 call umat44 (cm(mx+1),eps,sig,epsp,hsv,dt1,capa,'shell',tt,
     . temper,failel,crv)
      go to 60
   45 call umat45 (cm(mx+1),eps,sig,epsp,hsv,dt1,capa,'shell',tt,
     . temper,failel,crv)
      go to 60
   46 call umat46 (cm(mx+1),eps,sig,epsp,hsv,dt1,capa,'shell',tt,
     . temper,failel,crv,thhsvi,nthhsv)
      go to 60
   47 call umat47 (cm(mx+1),eps,sig,epsp,hsv,dt1,capa,'shell',tt,
     . temper,failel,crv)
      go to 60
   48 call umat48 (cm(mx+1),eps,sig,epsp,hsv,dt1,capa,'shell',tt,
     . temper,failel,crv)
      go to 60
   49 call umat49 (cm(mx+1),eps,sig,epsp,hsv,dt1,capa,'shell',tt,
     . temper,failel,crv)
      go to 60
   50 call umat50 (cm(mx+1),eps,sig,epsp,hsv,dt1,capa,'shell',tt,
     . temper,failel,crv)
c
c     scattering of variables
c
 60   if (no_hsvs.gt.0) then
        do j=1,no_hsvs
          hsvs(i,j)=hsv(j)
        enddo
      endif
c
      d3(i) =eps(3)
      if (failel) then
        sig1(i)=0.
        sig2(i)=0.
        sig3(i)=0.
        sig4(i)=0.
        sig5(i)=0.
        sig6(i)=0.
        failur=.true.
        ifail(i)=1
```

```
            fail(i)=0.
          else
            sig1(i)=sig(1)
            sig2(i)=sig(2)
            sig3(i)=sig(3)
            sig4(i)=sig(4)
            sig5(i)=sig(5)
            sig6(i)=sig(6)
          endif
          epsps(i)=epsp
 120      continue
c
c       vector umat
c
        else
c
c         assume no failed elements
c
          do i=lft,llt
            failels(i)=.false.
          enddo
c
c         call user developed subroutines here
c         first history variable is the one requested
c
          if (mt.eq.41) then
            call umat41v(cm(mx+1),d1,d2,d3,d4,d5,d6,sig1,sig2,
     .       sig3,sig4,sig5,sig6,epsps,hsvs,lft,llt,
     .       dt1siz,capa,'shell',tt,temps,failels,nlq,crv)
          elseif (mt.eq.42) then
            call umat42v(cm(mx+1),d1,d2,d3,d4,d5,d6,sig1,sig2,
     .       sig3,sig4,sig5,sig6,epsps,hsvs,lft,llt,
     .       dt1siz,capa,'shell',tt,temps,failels,nlq,crv)
          elseif (mt.eq.43) then
            call umat43v(cm(mx+1),d1,d2,d3,d4,d5,d6,sig1,sig2,
     .       sig3,sig4,sig5,sig6,epsps,hsvs,lft,llt,
     .       dt1siz,capa,'shell',tt,temps,failels,nlq,crv)
          elseif (mt.eq.44) then
            call umat44v(cm(mx+1),d1,d2,d3,d4,d5,d6,sig1,sig2,
     .       sig3,sig4,sig5,sig6,epsps,hsvs,lft,llt,
     .       dt1siz,capa,'shell',tt,temps,failels,nlq,crv)
          elseif (mt.eq.45) then
            call umat45v(cm(mx+1),d1,d2,d3,d4,d5,d6,sig1,sig2,
     .       sig3,sig4,sig5,sig6,epsps,hsvs,lft,llt,
     .       dt1siz,capa,'shell',tt,temps,failels,nlq,crv)
          elseif (mt.eq.46) then
            call umat46v(cm(mx+1),d1,d2,d3,d4,d5,d6,sig1,sig2,
     .       sig3,sig4,sig5,sig6,epsps,hsvs,lft,llt,
     .       dt1siz,capa,'shell',tt,temps,failels,nlq,crv,
```

```
     .       thhsv,nthhsv)
           elseif (mt.eq.47) then
             call umat47v(cm(mx+1),d1,d2,d3,d4,d5,d6,sig1,sig2,
     .       sig3,sig4,sig5,sig6,epsps,hsvs,lft,llt,
     .       dt1siz,capa,'shell',tt,temps,failels,nlq,crv)
           elseif (mt.eq.48) then
             call umat48v(cm(mx+1),d1,d2,d3,d4,d5,d6,sig1,sig2,
     .       sig3,sig4,sig5,sig6,epsps,hsvs,lft,llt,
     .       dt1siz,capa,'shell',tt,ipt,a(n8),a(n9))
           elseif (mt.eq.49) then
             call umat49v(cm(mx+1),d1,d2,d3,d4,d5,d6,sig1,sig2,
     .       sig3,sig4,sig5,sig6,epsps,hsvs,lft,llt,
     .       dt1siz,capa,'shell',tt,ipt,temps)
           elseif (mt.eq.50) then
             call umat50v(cm(mx+1),d1,d2,d3,d4,d5,d6,sig1,sig2,
     .       sig3,sig4,sig5,sig6,epsps,hsvs,lft,llt,
     .       dt1siz,capa,'shell',tt,temps,failels,nlq,crv)
           endif
c
c          check for failure
c
           do i=lft,llt
             if (failels(i)) then
               sig1(i)=0.
               sig2(i)=0.
               sig3(i)=0.
               sig4(i)=0.
               sig5(i)=0.
               sig6(i)=0.
               failur=.true.
               ifail(i)=1
               fail(i)=0.
             endif
           enddo
         endif
c
c        energy calculations
c
         do 130 i=lft,llt
         einc(i)=d1(i)*sig1(i)+d2(i)*sig2(i)+d4(i)*sig4(i)+d5(i)*sig5(i)
        1        +d6(i)*sig6(i)+einc(i)
  130    continue
c
         return
  900    format(/' ***Error User defined material in part',i12,
     .       ' exceeds the current limit'/
     .       10x,'of history variables for shells.')
         end
```

Listing B.2: `FORTRAN` source code for `umat48` subroutine. This subroutine calculates the local elemental stress within each shell element, input variables passed from `urmats` subroutine (Listing B.1).

```
      subroutine umat48 (cm,eps,sig,epsp,hsv,dtl,capa,etype,tt,
     1 temper,failel,crv)
c
c     user material subroutine modified by kevin lau
c     acknowlegment and thanks to daniel einstein
c
c     approach detailed in: 'dynamic finite element implementation
c     of nonlinear, anisotropic hyperelastic biological membranes
c     by einstein et al. in comp. meth. in biomech. and biomed.
c     eng. 2003, vol. 6(1), pp.33-44, doi:10.1080/1025584021000048983
c
c     variable list
c
c     cm(1)   - bulk modulus
c     cm(2)   - shear modulus
c     cm(3)   - sef option
c     cm(4)   - stress scale factor, default output kPa
c     cm(5)   - 1st material parameter
c     cm(6)   - 2nd material parameter
c     cm(7)   - 3rd material parameter
c     cm(8)   - 4th material parameter (transverse modulus)
c     cm(9)   - reset deformation switch (1/0 = true/false)
c     eps(1)  - local/rotated xx strain increment
c     eps(2)  - local/rotated yy strain increment
c     eps(3)  - local/rotated zz strain increment
c     eps(4)  - local/rotated xx strain increment
c     eps(5)  - local/rotated xx strain increment
c     eps(6)  - local/rotated xx strain increment
c     sig(1)  - local x  stress
c     sig(2)  - local y  stress
c     sig(3)  - local z  stress
c     sig(4)  - local xy stress
c     sig(5)  - local yz stress
c     sig(6)  - local zx stress
c     hsv(1)  - F1OB, F(1,1)
c     hsv(2)  - F2OB, F(2,1)
c     hsv(3)  - F4OB, F(1,2)
c     hsv(4)  - F5OB, F(2,2)
c     hsv(5)  - n1 CR/OB @ t
c     hsv(6)  - n2 CR/OB @ t
c     hsv(7)  - C1OB, C(1,1)
c     hsv(8)  - C2OB, C(2,1)
c     hsv(9)  - C4OB, C(1,2)
c     hsv(10) - C5OB, C(2,2)
c     hsv(11) - n1, CR/OB @ t+1
c     hsv(12) - n2, CR/OB @ t+1
```

```
c     hsv(13) - cos(beta)
c     hsv(14) - sin(beta)
c     hsv(15) - p
c     hsv(16) - sig(1) local
c     hsv(17) - sig(2) local
c     hsv(18) - sig(3) local
c     hsv(19) - sig(4) local
c     hsv(20) - sig(5) local
c     hsv(21) - sig(6) local
c     hsv(22) - max in-plane principal stretch
c     hsv(23) - fibre stretch
c
      include 'nlqparm'
      include 'iounits.inc'
      common/bk06/idmmy,iaddp,ifil,maxsiz,ncycle,time(2,30)
      dimension cm(*),eps(*),sig(*),hsv(*),crv(lq1,2,*)
      character*5 etype
      logical failel
c
c     subroutine variables

      real*8 f1,f2,f4,f5
      real*8 c1,c2,c4,c5,c9
      real*8 vrc1,vrc2,vrc4,vrc5,vrc9
      real*8 a01,a02
      real*8 v1,v4
      real*8 p,q,sefi1,sefi4
      real*8 s1,s2,s4,s5
      real*8 bb11,bb12,bb21,bb22
      real*8 sig1,sig2,sig4
      real*8 yy1,yy2
      real*8 cc11,cc12,cc21,cc22
c
c     shell element check
c
      if(etype.eq.'shell')then
c
c     document user material number in log
c
      if(ncycle.eq.1)then
        write (iotty,2100)
        write (iohsp,2100)
        write (iomsg,2100)
        write (iotty,2101)
        write (iohsp,2101)
        write (iomsg,2101)
        write (iotty,2102)
        write (iohsp,2102)
        write (iomsg,2102)
```

```
        write (iotty,2103)
        write (iohsp,2103)
        write (iomsg,2103)
        write (iotty,2104)
        write (iohsp,2104)
        write (iomsg,2104)
        write (iotty,2105)
        write (iohsp,2105)
        write (iomsg,2105)
        write (iotty,2106)
        write (iohsp,2106)
        write (iomsg,2106)
        write (iotty,2107)
        write (iohsp,2107)
        write (iomsg,2107)
        write (iotty,2108)
        write (iohsp,2108)
        write (iomsg,2108)
 2100   format(/' ************************************ ')
 2101   format(' *** USING CUSTOM MATERIAL UMAT48  *** ')
 2102   format(' *** FOLLOWING PARAMETERS REQUIRED *** ')
 2103   format(' ***     LMC = 9                    *** ')
 2104   format(' ***     NHV = 23                   *** ')
 2105   format(' *** IORTHO = 1                    *** ')
 2106   format(' *** IHYPER = 0                    *** ')
 2107   format(' *** ELFORM = 11                   *** ')
 2108   format(' ************************************ '/)
      endif
c
c     right Cauchy Green tensor and its inverse (C and C^-1)
c
      f1=hsv(1)
      f2=hsv(2)
      f4=hsv(3)
      f5=hsv(4)
c
      yy1=hsv(5)
      yy2=hsv(6)
c
      c1=hsv(7)
      c2=hsv(8)
      c4=hsv(9)
      c5=hsv(10)
      c9=1/(c1*c5-c4*c2)
c
      vrc1=c5*c9;
      vrc2=-c2*c9
      vrc4=vrc2
      vrc5=c1*c9
```

```
      vrc9=c1*c5-c4*c2
c
c     fibre direction vectors a0, taken from beta angle
c
      a01=hsv(13)
      a02=hsv(14)
c
c     deformation invarients I1 and I4
c
      v1=c1+c5+c9
      v4=a01*(c1*a01+c4*a02)+a02*(c2*a01+c5*a02)
      if(v4.lt.1.)then
        v4=1.
      endif
c
c     strain energy functions
c
      q=cm(6)*((v1-3.)**2.)+cm(7)*(((v4**0.5)-1.)**4.)
      sefi1=(2.*cm(5)*cm(6))*(v1-3.)*exp(q)
      sefi4=(2.*cm(5)*cm(7)*(((v4**0.5)-1.)**3.)*(1./(v4**0.5)))*exp(q)
c
c     Pressure Lagrange multiplier
c
        p=-2.*sefi1*c9
        hsv(15)=p
c
c     2nd Piola-Kirchhoff stress tensor, S, in kPa
c
      s1=2.*sefi1+2.*sefi4*a01*a01+p*vrc1
      s2=2.*sefi4*a01*a02+p*vrc2
      s4=s2
      s5=2.*sefi1+2.*sefi4*a02*a02+p*vrc5
c
c     push forward to Cauchy stress
c
      bb11=f1*s1+f4*s4
      bb12=f2*s1+f5*s4
      bb21=f1*s2+f4*s5
      bb22=f2*s2+f5*s5
c
      sig1=f1*bb11+f4*bb21
           sig2=f2*bb12+f5*bb22
           sig4=f1*bb12+f4*bb22
c
      sig1=cm(4)*sig1
      sig2=cm(4)*sig2
      sig4=cm(4)*sig4
c
c     rotate forward to element basis
```

```
            cc11=yy1*sig1+yy2*sig4
            cc12=-yy2*sig1+yy1*sig4
            cc21=yy1*sig4+yy2*sig2
            cc22=-yy2*sig4+yy1*sig2
c
            sig(1)=yy1*cc11+yy2*cc21
          sig(2)=-yy2*cc12+yy1*cc22
            sig(4)=yy1*cc12+yy2*cc22
c
c       membrane assumption
c
          sig(3)=0.
c
c       transverse stresses calculated in element basis
c
            sig(5)=sig(5)+capa*cm(4)*cm(8)*eps(5)
            sig(6)=sig(6)+capa*cm(4)*cm(8)*eps(6)
c
c       history variables
c
          hsv(16)=sig(1)
          hsv(17)=sig(2)
          hsv(18)=sig(3)
          hsv(19)=sig(4)
          hsv(20)=sig(5)
          hsv(21)=sig(6)
c
          hsv(22)=0.5*((c1+c5)+sqrt(c1*c1+c5*c5-2.*c1*c5+4.*c4*c2))
          hsv(23)=sqrt(v4)
c
c       update the n1,n2 with new n1,n2
c
          hsv(5)=hsv(11)
          hsv(6)=hsv(12)
c
          else
            write (iotty,20) etype
            write (iohsp,20) etype
            write (iomsg,20) etype
            call adios(2)
          endif
c
   20   format(/
     1   ' ***Error element type ',a,' can not be',
     2   '           run with the current material model.')
c
          return
          end
```

Appendix C

Three–Dimensional Visualisation

C.1 Edge–to–edge repair

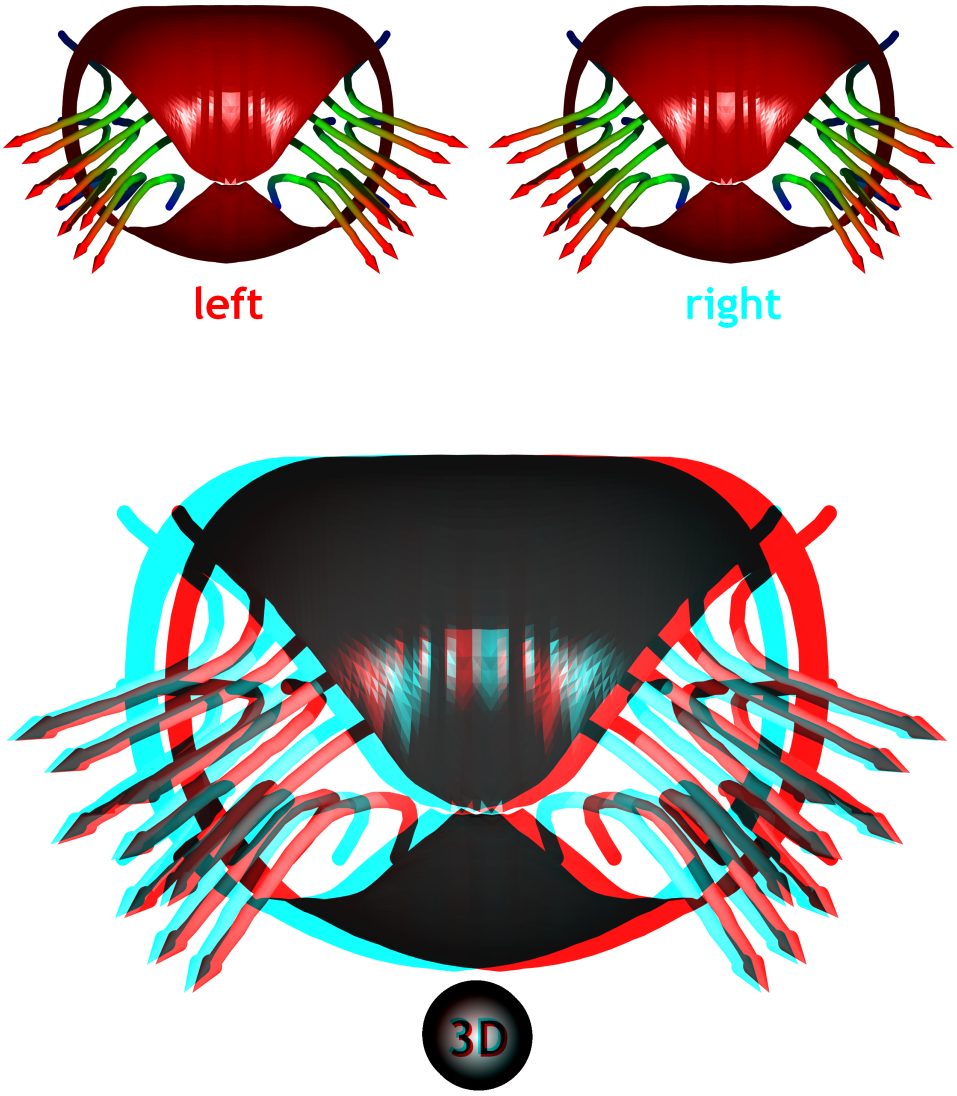

Figure C.1: Stereoscopic visualisation of the edge–to–edge repair. Best viewed in the digital version. Rendered using POV–Ray 3.6.1 [139].

Appendix D

Published Papers

In the follow pages the two published papers from this thesis have been attached, please note there are no page numbers from this point forward. The rights to reuse these papers in this thesis have been obtained from the publisher.